



# University of HUDDERSFIELD

## University of Huddersfield Repository

Airede, Yusuf Okahamame

Intrusive and Non-intrusive Methods for Fluid Diagnostics and Flow Condition Monitoring in a Control valve

### Original Citation

Airede, Yusuf Okahamame (2019) Intrusive and Non-intrusive Methods for Fluid Diagnostics and Flow Condition Monitoring in a Control valve. Doctoral thesis, University of Huddersfield.

This version is available at <http://eprints.hud.ac.uk/id/eprint/35221/>

The University Repository is a digital collection of the research output of the University, available on Open Access. Copyright and Moral Rights for the items on this site are retained by the individual author and/or other copyright owners. Users may access full items free of charge; copies of full text items generally can be reproduced, displayed or performed and given to third parties in any format or medium for personal research or study, educational or not-for-profit purposes without prior permission or charge, provided:

- The authors, title and full bibliographic details is credited in any copy;
- A hyperlink and/or URL is included for the original metadata page; and
- The content is not changed in any way.

For more information, including our policy and submission procedure, please contact the Repository Team at: [E.mailbox@hud.ac.uk](mailto:E.mailbox@hud.ac.uk).

<http://eprints.hud.ac.uk/>

**Intrusive and Non-intrusive Methods for Fluid  
Diagnostics and Flow Condition Monitoring in a  
Control valve**

---

**Airede Yusuf Okahamame**

A thesis submitted to the University of Huddersfield  
in partial fulfilment of the requirements for the degree of  
Doctor of Philosophy.

University of Huddersfield

**July 2019**

## ABSTRACT

---

Process control systems consist of numerous control loops, linked together in producing a particular product to be used for carrying out experiments or to be sold. For each of these loops, they are designed to ensure that significant flow parameters such as temperature, velocity, pressure, level, flow, etc. operate within a set range to ensure end product quality. Signal and disturbances for external control loops are sent to these control loops, or sometimes, generate their own internal disturbances, adversely affecting these variables. After measurement, comparison and calculation, the strategy that has been selected by the specific controller such as (Proportional, Proportional Integral, Proportional Integral Derivative, etc.) must be implemented by a final control element.

One common FCE (final control element) largely used in the industry for process control is the control valve. The manipulation of the flowing fluid, such as water, chemical compounds, steam, gas, etc., are done by the control valve for load disturbance to be compensated, and ensure that the process variable and the desired set point are as close as possible. Due to its importance in a flow loop, it is very important to know the control valve flow characteristics. Because of the fast development in simulating flow and using numerical technique for flow diagnostics, understanding flow inside the valve has become possible for the valve performance to be estimated.

This thesis investigates methods for diagnosing flow for both single phase and multiphase flow under various flow conditions and probe designs.

This thesis reports the results of experiments on the control valve flow characteristics using a range of statistical parameters obtained from: airborne acoustic signal microphone, vibration signal from an accelerometer on the valve body and fivehole multihole probes (MHP) placed ingeniously inside the valve at different sections of the valve inlet and outlet. An assessment on the behaviour of the fluid using these three methods has been presented.

For the multihole probe (MHP), different probe lengths and heights have been used to obtain local flow parameters and analyse how these parameters vary at different sections from inlet to outlet.

Detailed experimental investigations were conducted for diagnosing the valve flow behaviour. The signatures from these sensors (vibration and acoustic) have been analysed by making use of different statistical parameters including peak amplitude, kurtosis, RMS (root mean square), variance and Peak-to-Peak. In addition, both signals from the vibration and acoustic sensors were then transformed to frequency domain and analysed using Fast Fourier Transform (FFT) and mean frequency. Analyses for both signals in frequency domain were also carried out under various ranges of frequency. The results revealed that vibration technique gives a clearer picture into how the signal changes with different flow and valve behaviour. This research also found that frequency range between 0 to 1 KHz was more sensitive in determining the valve behaviour at various conditions. Concerning this research, it can be suggested that lower frequency range sensors (vibration and accelerometer) can be used to capture the behaviour of the control valve and detect any form of fault, which are cheaper than higher frequency range sensors.

The results also reveal that the combination of all of these techniques could be applied to increase the reliability of the valve and fault detection. The combination of all experimental methods can be considered robust, providing detailed information about the valve performance and flow diagnostics, hence, assisting in prolonging the valve life and protect the control system from any emergency shutdown.

## **DECLARATION**

---

No portion of the work presented in this thesis has been submitted in support of an application for another degree or qualification of this or any other university or other institute of learning.

The author of this thesis owns any copyright in it and has given the University of Huddersfield the right to use such Copyright for any promotional, administrative, educational and/or for the purpose of teaching.

Any section from this thesis, either in extracts or in full, may only be made in accordance with the University Library regulations. The regulation details can be obtained from the University Librarian. A copy from this declaration page must form part of any of such made copies.

Any designs, patents, trademarks that have been referenced in this thesis, and any or all other rights of intellectual property (IP) except, or any copyright works reproductions (e.g., graphs and tables) that has been described in this thesis, may not be owned by the author but may be owned by third parties. Such Reproductions and IP Rights cannot and must not be used without first, a written permission from the relevant Reproductions and/or IP rights owner(s).

## TABLE OF CONTENTS

ABSTRACT .....	ii
DECLARATION .....	iv
LIST OF FIGURES.....	ix
LIST OF TABLES.....	xx
NOMENCLATURE.....	xxi
SYMBOLS.....	xxiv
ACKNOWLEDGEMENTS .....	xxv
CHAPTER ONE.....	1
1.0 INTRODUCTION AND BACKGROUND .....	1
1.1 INTRODUCTION .....	2
1.2 BACKGROUND OF STUDY .....	3
1.2.1 THE CONTROL VALVE.....	3
1.2.2 SOME TYPES OF VALVE.....	10
1.2.3 CAVITATION.....	14
1.3 PERFORMANCE CHARACTERISTICS OF CONTROL VALVES.....	21
1.4 PRESSURE PROBES.....	23
1.4.1 STATIC PRESSURE PROBES .....	24
1.4.2 STAGNATION PRESSURE PROBES.....	24
1.4.3 FLOW DIRECTION MEASUREMENT .....	25
1.5 CONDITION MONITORING .....	28
1.5.1 CONVENTIONAL TECHNIQUES FOR CONDITION MONITORING .....	29
1.5.2 SIGNAL ANALYSIS TECHNIQUES .....	35
1.6 RESEARCH MOTIVATION.....	38
1.7 RESEARCH AIM .....	40
1.9 THESIS ORGANISATION .....	40
1.10 SUMMARY.....	42
CHAPTER TWO .....	43
2.0 LITERATURE REVIEW FOR PRESSURE PROBES AND VIBO-ACOUSTIC BASED FLOW DIAGNOSTICS TECHNIQUES.....	43
2.1 INTRODUCTION .....	44
2.2 FLOW DIAGNOSIS AND ANALYSIS INSIDE A CONTROL VALVE .....	44
2.3 MULTI-HOLE PRESSURE PROBES .....	61
2.3.1 PRESSURE PROBE CALIBRATION.....	64

2.3.2 PRESSURE PROBES APPLICATION.....	72
2.4 EXPERIMENTAL INVESTIGATION ON CONTROL VALVE CONDITION MONITORING USING ACOUSTIC AND VIBRATION FOR FAULT DETECTION .....	84
2.5 RESEARCH OBJECTIVES .....	89
2.6 LITERATURE SUMMARY .....	89
CHAPTER THREE .....	91
3.0 NUMERICAL AND EXPERIMENTAL DESIGN METHODOLOGY.....	91
3.1 INTRODUCTION TO CFD.....	92
3.1.1 WORKING OF CFD CODES.....	92
3.1.2 GEOMETRY .....	94
3.1.3 MESHING .....	94
3.1.4 SELECTION OF PHYSICAL MODELS.....	96
3.1.5 SOLVER SETTINGS.....	98
3.1.6 CONVERGENCE CRITERIA BOUNDARY CONDITIONS .....	99
3.1.7 SCOPE OF NUMERICAL WORK.....	100
3.2 EXPERIMENTAL SET UP .....	101
3.2.1 METHOD IN FINDING THE VALUES FOR C .....	103
3.2.2 THE SPECIFIC TRIM USED .....	103
3.3 TEST SET UP.....	104
3.4 DIFFERENT SENSORS USED FOR CONDITIONING MONITORING .....	108
3.4.1 FIVE-HOLE PROBE DESIGN.....	109
3.4.2 VIBRATION SENSOR.....	113
3.4.3 MICROPHONE (ACOUSTIC SENSOR) .....	114
3.4.4 MICROPHONE PRE-AMPLIFIER.....	115
3.4.5 PRESSURE TRANSDUCER .....	115
3.4.6 WATER FLOW METER.....	116
3.4.7 AIR FLOW METER.....	117
3.4.8 THERMOMETER .....	118
3.4.9 POWER SUPPLY .....	119
3.4.10 DATA ACQUISITION SYSTEM.....	119
3.5 SENSORS AND INSTRUMENTS CALIBRATION .....	121
3.5.1 FIVE HOLE PROBE CALIBRATION .....	121
3.5.2 PRESSURE SENSOR CALIBRATION .....	128
3.5.3 MICROPHONE AND ACCELEROMETER.....	131

3.5.3 FLOW METER.....	131
3.6 UNCERTAINTY AND REPEATABILITY ANALYSIS .....	132
3.6.1 UNCERTAINTY ANALYSIS.....	132
3.6.2 REPEATABILITY ANALYSIS.....	134
3.7 RISK ASSESSMENT OF THE RESEARCH .....	135
3.8 SUMMARY .....	135
CHAPTER FOUR.....	136
4.0 INTERNAL FLOW CHARACTERISTICS INSIDE THE CONTROL VALVE USING A FIVE- HOLE PRESSURE PROBE FOR SINGLE PHASE CONDITION .....	136
4.1 INTRODUCTION .....	137
4.2 NUMERICAL ANALYSIS .....	137
4.2.1 MESH INDEPENDENCE TEST .....	137
4.2.1 MODEL VALIDATION .....	138
4.2.3 PROBE HEADS COMPARISON.....	138
4.3 EXPERIMENTAL ANALYSIS.....	142
4.3.1 EXPERIMENTAL SINGLEPHASE INVESTIGATION ON THE CONTROL VALVE .....	144
4.3.2 ESTABLISHING GLOBAL AND LOCAL FLOW PARAMETERS BETWEEN HEALTHY AND FAULTY VALVE CONDITION AT DIFFERENT FLOW RATES AND VOPs.....	195
4.4 SUMMARY .....	199
CHAPTER FIVE .....	201
5.0 VIBRATION BEHAVIOUR OF THE CONTROL VALVE UNDER VARIOUS FLOW CONDITIONS FOR SINGLE PHASE AND MULTIPHASE FLOW .....	201
5.1 ADVANTAGES AND DISADVANTAGES OF USING VIBRATION TECHNIQUE.....	202
5.2 DEVELOPMENT OF VIBRATION INDICATOR FOR SINGLE PHASE FLOW CONDITION INSIDE A HEALTHY CONTROL VALVE .....	202
5.2.1 TIME DOMAIN ANALYSIS.....	202
5.2.2 ANALYSIS IN FREQUENCY DOMAIN .....	209
5.3 DEVELOPMENT OF VIBRATION INDICATORS FOR MULTIPHASE FLOW CONDITION INSIDE A HEALTHY CONTROL VALVE .....	214
5.3.1 TIME DOMAIN ANALYSIS.....	214
5.3.2 FREQUENCY DOMAIN ANALYSIS.....	218
5.4 DEVELOPMENT OF VIBRATION INDICATOR FOR SINGLE PHASE FLOW CONDITION INSIDE A FAULTY CONTROL VALVE .....	223

5.4.1 TIME DOMAIN ANALYSIS.....	223
5.4.2 ANALYSIS IN FREQUENCY DOMAIN.....	225
5.5 DEVELOPMENT OF VIBRATION INDICATOR FOR MULTIPHASE FLOW CONDITION INSIDE A FAULTY CONTROL VALVE.....	228
5.5.1 TIME DOMAIN ANALYSIS.....	228
5.5.2 ANALYSIS IN FREQUENCY DOMAIN.....	230
5.6 SUMMARY.....	235
CHAPTER SIX.....	236
6.0 ACOUSTIC BEHAVIOUR OF THE VALVE UNDER VARIOUS FLOW CONDITIONS FOR SINGLE PHASE AND MULTIPHASE FLOW.....	236
6.1 ADVANTAGES AND DISADVANTAGES OF USING ACOUSTIC TECHNIQUE.....	237
6.2 ESTABLISHING FLOW CHARACTERISTICS FOR SINGLE PHASE FLOW CONDITION INSIDE A HEALTHY CONTROL VALVE.....	237
6.2.1 TIME DOMAIN ANALYSIS.....	237
6.2.2 ANALYSIS IN FREQUENCY DOMAIN.....	243
6.3 DEVELOPMENT OF ACOUSTIC INDICATORS FOR MULTIPHASE FLOW CONDITION INSIDE A HEALTHY CONTROL VALVE.....	249
6.3.1 TIME DOMAIN ANALYSIS.....	249
6.3.2 FREQUENCY DOMAIN ANALYSIS.....	253
6.4 DEVELOPMENT OF ACOUSTIC INDICATOR FOR SINGLEPHASE FLOW CONDITION INSIDE A FAULTY CONTROL VALVE.....	258
6.4.1 TIME DOMAIN ANALYSIS.....	259
6.4.2 ANALYSIS IN FREQUENCY DOMAIN.....	260
6.5 DEVELOPMENT OF ACOUSTIC INDICATORS FOR MULTIPHASE FLOW CONDITION INSIDE A FAULTY CONTROL VALVE.....	264
6.5.1 TIME DOMAIN ANALYSIS.....	264
6.5.2 ANALYSIS IN FREQUENCY DOMAIN.....	266
6.6 SUMMARY.....	270
CHAPTER SEVEN.....	271
7.0 CONCLUSION AND FUTURE WORK.....	271
7.1 SYNOPSIS TO THE RESEARCH PROBLEMS.....	272
7.2 MAIN AIM AND ACHIEVEMENTS REVIEW.....	272
7.3. THESIS CONCLUSIONS.....	275
7.4. THESIS CONTRIBUTION.....	282
7.5. FUTURE WORKS.....	285

REFERENCES .....	287
APPENDICES .....	296
APPENDIX A.....	296
APPENDIX B.....	303
APPENDIX C .....	305
APPENDIX D.....	306
APPENDIX E .....	307
APPENDIX F .....	308
APPENDIX G.....	309
APPENDIX H .....	310

## **LIST OF FIGURES**

---

Figure 1.1: Plug valve of the Romans .....	4
Figure 1.2: Typical Industrial control valve [41] .....	6
Figure 1.3: Example of a valve trim in the lab .....	8
Figure 1.4: a valve disk with four-flow path .....	9
Figure 1.5: a typical ball valve .....	11
Figure 1.6: Example of a butterfly valve.....	11
Figure 1.7: a gate valve .....	12
Figure 1.8: a globe valve .....	13
Figure 1.9: a plug valve .....	13
Figure 1.10: a diaphragm valve .....	14
Figure 1.11: Cavitation effect in some valve part .....	16
Figure 1.12: Distribution of pressure in the control valve .....	17
Figure 1.13: determining the cavitation coefficient $X_{FZ}$ [6] .....	18
Figure 1.14: A 5-hole truncated pyramid probe .....	25
Figure 1.15: Three hole Wedge Probe for pitch and yaw angle measurement .....	25
Figure 1.16: Five-hole truncated cone probe .....	27
Figure 1.17: Five-hole truncated pyramid probe.....	27
Figure 1.18: Four-hole wedge probe for pitch and yaw angles measurement .....	28
Figure 1.19: General usage of various monitoring techniques [61] .....	29
Figure 1.20: Trend Monitoring Record [66] .....	30
Figure 2.1: (a) the globe valve model (b) stem and the disk sketch .....	45
Figure 2.2: Mean side load against mean transvers force pressure drop for the different VOPs .....	46
Figure 2.3; Variations of flow variables within the trim at 1,000kPa differential pressure and 10% valve opening position (a) Static Pressure (b) Flow Velocity [15] .....	48
Figure 2.4: Variations in $C_v$ Trim of the trim at various valve opening positions and differential pressures .....	49
Figure 2.5 (a): Valve schematic      Figure 2.5(b): the cage structure model .....	50

Figure 2.6; test system setup [21].....	50
Figure 2.7: Resistance coefficient result [21] .....	51
Figure 28: Normalized intensity for hydrophone and visualization signals for both valve openings (left-1: fully open, right-2: half-open) [7] .....	53
Figure 2.9; Normalized intensity for hydrophone and visualization signals as a function of flow rate for both valve openings (left-1: fully open, right-2: half-open). [7].....	54
Figure 2.10; Comparison of two methods of detecting cavitation [7].....	55
Figure 2.11; X-Stream Trim Disc .....	56
Figure 2.12; (a) Velocity Contours (m/s) for Modified Geometry (left) (b) Original Geometry (right) .....	57
Figure 2.13 (a) Static Pressure Contours (Pa) for Modified Geometry (left) (b) Original Geometry (right) .....	58
Figure 2.14: Oil volume fraction distribution [51] .....	60
Figure 2.15: Effect of sampling frequency of on conductivity probe [53] .....	61
Figure 2.16: Schematic representation of a five-hole probe [48] .....	65
Figure 2.17: Non-dimensional probe pressures for chamfer angle of 300 .....	66
Figure 2.18: Sector map of five-hole probe .....	67
Figure 2.19: Velocities profile along diametric chords [50] .....	69
Figure 2.20: Response of surface pressures [51] .....	70
Figure 2.21: Five-hole probe schematic and velocity resolution [52] .....	70
Figure 2.22: Velocity vector plot of a tip vortex in the cross plane [52] .....	71
Figure 2.23; The dynamic response characteristics for the theoretical and experimental results for a pressure probe that shows the acoustic attenuation and the phase distortion between measured dynamic pressure and the sensor pressure.....	73
Figure 2.24: Flow angle and Mach number for transients during uneven start [33] .....	74
Figure 2.25: Flow angularity pressure probe comparison and that of the pitot and static probe Mach number calculation in their flow field .....	75
Figure 2.26: (a) Conical head probe; (b) Hemispherical head probe; (c) Pressure tap designation [33] .....	76
Figure 2.27: Computational domain and the boundary conditions [33] .....	77

Figure 2.28: Static pressure profile along flow axis (a) upstream and (b) downstream of the probes [33] .....	77
Figure 2.29: Y-velocity profile along flow axis (a) upstream and (b) downstream of the probes [33] .....	77
Figure 2.30: Z-velocity profile along flow axis (a) upstream and (b) downstream of the probes [33] .....	78
Figure 2.31: Five-hole probe location inside the automotive wheel arch [30] .....	79
Figure 2.33: CFD geometry of the single-axle vehicle model investigated [30] .....	80
Figure 2.34: Geometry of five-hole probe [30] .....	81
Figure 2.35: Comparison of experimental and CFD pressure values measured at the five taps (Pa) [30] .....	82
Figure 2.36: Contours of pressure coefficient ( $C_p$ ) on longitudinal (X-Y) plane at $0^\circ$ without the probe [3] .....	82
Figure 3.37: Contours of pressure coefficient ( $C_p$ ) on longitudinal (X-Y) plane with the probe at $0^\circ$ .....	83
Figure 2.38: Contours of longitudinal velocity component ( $U_x$ ) at $270^\circ$ inside wheel arch on longitudinal (X-Y) plane without the probe .....	83
Figure 2.39: Measured coefficient of sigma against VOP and the valve calibration curve..	85
Figure 2.40: Valve noise measurements against VOP and the characteristics of the valve noise .....	85
Figure 2.41: Pressure ratios and flow pattern regarding the sound mutation.....	86
Figure 2.42: AE valve leakage signal characteristics for the 25.4mm ball valve in frequency domain at the change of leakage rate. (a) Compressed air leakage and (b) fresh water leakage .....	87
Figure 2.43: Valve type effect on acoustic emission RMS value .....	88
Figure 3.1: CAD model of control valve showing side and top view .....	94
Figure 3.2: Numerical geometric model of the control valve .....	94
Figure 3.3: Meshing of the flow domain .....	95
Figure 3.4: Surface finish of an SLM trim [54] .....	98
Figure 3.5: 4 inch BV500 Globe Control Valve [54] .....	101
Figure 3.6: Specific control valve trim [54] .....	104

Figure 3.7: Experimental Schematic Design setup .....	106
Figure 3.8: Air injection device .....	107
Figure 3.9: Air mass flow meter (Omega FMA 1700/1800) .....	107
Figure 3.10: Schematic for the Single and Multiphase flow loop design .....	107
Figure 3.11: Fluid flow loop lab .....	108
Figure 3.12: Five-hole probe .....	109
Figure 3.13: (a) Entire newly built test section for the calibration (b) Transverse mechanism for the calibration .....	112
Figure 3.14: Actual MHP with hemispherical head used for the calibration .....	113
Figure 3.15: The piezoelectric accelerometer sensor [98] .....	113
Figure 3.16: Microphone Acoustic sensor .....	114
Figure 3.17: Microphone Preamplifier .....	115
Figure 3.18: Pressure transducer (IMP pressure transmitter) .....	116
Figure 3.19: OMEGA-WE-SDC pulse emitter water turbine flow meter .....	117
Figure 3.20: FMA 1700/1800 OMEGA air flow meter series .....	118
Figure 3.21: Thermometer .....	118
Figure 3.22: Rapid Power supply unit .....	119
Figure 3.23: YE6232 16 channel DAQ from GST .....	120
Figure 3.24: NI USB X series DAQ .....	121
Figure 3.25: Fivehole pressure probe taping numbering [97] .....	122
Figure 3.26: Angles defining the orientation of a probe with respect to the free stream Velocity [97] .....	123
Figure 3.27: Calibration surface for $CP_{total}$ .....	124
Figure 3.28: Calibration surface for $CP_{static}$ .....	125
Figure 3.29: Calibration surface for $CP_{\alpha}$ .....	125
Figure 3.30: Calibration surface for $CP_{\beta}$ .....	126
Figure 3.31: Pressure transducers used for the calibration .....	128
Figure 3.32: Calibration pipe .....	129

Figure 3.33: Schematic for calibrating the pressure calibration procedure .....	129
Figure 3.34: Curve data for the calibrated pressure transducer .....	131
Figure 4.1: Comparison of the pressure difference ( $\Delta P$ ) between CFD and experimental results .....	138
Figure 4.2: Pressure comparison between Conical head and Hemispherical head geometry .....	138
Figure 4.3: Global pressure distribution comparison between conical head and hemispherical head geometry.....	140
Figure 4.4: Velocity comparison between conical head and Hemispherical head geometry .....	141
Figure 4.5: Global velocity profile of the valve between Conical head and Hemispherical head geometry .....	141
Figure 4.6: Pitch angle validation from 5hole pressure probe .....	142
Figure 4.7: Yaw angle validation from 5hole pressure probe .....	143
Figure 4.8: Control valve cross-section showing with inlet and outlet flow area .....	144
Figure 4.9: Single-phase experimental procedure flow chart .....	146
Figure 4.10: Pressure locations taken from the valve experimentation .....	147
Figure 4.11: Pressure drop variation for different VOP and for various flow rates .....	148
Figure 4.12: Valve Cv variation for different VOPs and for various flow rates .....	149
Figure 4.13: Valve Cv variation for different VOPs .....	149
Figure 4.14: Local pressure variation for different flow rates and VOPs for the different height positions (a) Height 1 (b) Height 2 (c) Height 3 (d) Height 4 (e) Height 4 (f) Height 6 (g) Height 7 .....	151
Figure 4.15: Pressure drop variation for different VOPs and for various flow rates for position 1 .....	154
Figure 4.16: Valve Cv variation for different VOPs at various flow rates for position 1...155	
Figure 4.17: Valve Cv variation for different VOPs for position 1 .....	155
Figure 4.18: Average velocity increase validation for the different probe measurement positions for different flow rates .....	157

Figure 4.19: Velocity profile for the valve across the different heights at the probe inlet position (0.5D) for the different VOPs (a) 800LPM (b) 900 LPM (c) 1000 LPM (d) 1100 LPM (e) 1200 LPM .....	158
Figure 4.20: Velocity profile for the valve across the different heights at the probe outlet position (0.9D) for the different VOPs(a) 800LPM (b) 900 LPM (c) 1000 LPM (d) 1100 LPM (e) 1200 LPM .....	161
Figure 4.21: Local pressure variation for different flow rates and VOPs for the different height positions (a) Height 1 (b) Height 2 (c) Height 3 (d) Height 4 (e) Height 4 (f) Height 6 (g) Height 7 .....	163
Figure 4.22: Pressure drop variation for different VOPs and for various flow rates for position 2 .....	166
Figure 4.23: Valve Cv variation for different VOPs and for various flow rates for position 2 .....	166
Figure 4.24: Valve Cv variation for different VOPs for position 2 .....	167
Figure 4.25: Velocity profile for the valve across the different heights at the probe inlet position (0.5D) for the different VOPs (a) 800LPM (b) 900 LPM (c) 1000 LPM (d) 1100 LPM (e) 1200 LPM .....	168
Figure 4.26: Velocity profile for the valve across the different heights at the probe outlet position (0.9D) for the different VOPs (a) 800LPM (b) 900 LPM (c) 1000 LPM (d) 1100 LPM (e) 1200 LPM .....	171
Figure 4.27: Local pressure variation for different flow rates and VOPs for the different height positions (a) Height 1 (b) Height 2 (c) Height 3 (d) Height 4 (e) Height 4 (f) Height 6 (g) Height 7 for position 3 .....	173
Figure 4.28: Pressure drop variation for different VOPs and for various flow rates for position 3 .....	175
Figure 4.29: Valve Cv variation for different VOPs and for various flow rates for position 3. ....	176
Figure 4.30: Valve Cv variation for the different VOPs for position 3 .....	177
Figure 4.31: Velocity profile for the valve across the different heights at the probe inlet position (0.5D) for the different VOPs (a) 800LPM (b) 900 LPM (c) 1000 LPM (d) 1100 LPM (e) 1200 LPM for position 3 .....	179
Figure 4.32: Velocity profile for the valve across the different heights at the probe outlet position (0.9D) for the different VOPs (a) 800LPM (b) 900 LPM (c) 1000 LPM (d) 1100 LPM (e) 1200 LPM for position 3 .....	181

Figure 4.33: Pressure drop comparison for different flow rates and VOPs for the different probe positions (a) 10% (b) 20% (c) 40% (d) 60% (e) 80% .....	183
Figure 4.34: Cv comparison for different flow rates and VOPs for the different measurement positions .....	185
Figure 4.35: Pressure comparison for different flow rates and VOPs for the different probe positions (a) 10% (b) 20% (c) 40% (d) 60% (e) 80% .....	186
Figure 4.36: Pressure ratio comparison for different flow rates and VOPs for the different probe positions (a) 10% (b) 20% (c) 40% (d) 60% (e) 80% .....	187
Figure 4.37: Cp comparison for different flow rates and VOPs for the different probe positions (a) 10% (b) 20% (c) 40% (d) 60% (e) 80% .....	188
Figure 4.38: Cv comparison for different VOPs at the different probe positions .....	190
Figure 4.39: Varying Cv total for the control valve system across the different VOPs....	191
Figure 4.40: Varying K value for the different sections of the control valve body at different flow rates across the different VOPs (a) 10% (b) 20% (c) 40% (d) 60% (e) .....	192
Figure 4.41: Average K value for the different sections of the control valve body across the different VOPs .....	193
Figure 4.42: Effect of K value as a function of Reynolds number at different VOPs (a)10% VOP, (b) 20% VOP, (c) 40% VOP (d) 60% VOP (e) 80% VOP.....	194
Figure 4.43 Global pressure drop comparison for healthy and faulty valve at different flow rates for (a) 60% (b) 80% VOPs .....	196
Figure 4.44: Global Cv comparison for healthy and faulty valve at different flow rates for (a) 60% (b) 80% VOPs .....	197
Figure 4.45: Single value global Cv comparison for healthy and faulty valve at different flow rates for 60 and 80% VOPs .....	198
Figure 4.46: Local sectional pressure drop comparison using the MHP for healthy and faulty valve at different flow rates for (a) 60% (b) 80% VOPs .....	198
Figure 4.47: Local sectional Cv comparison for healthy and faulty valve at different flow rates for (a) 60% (b) 80% VOPs .....	199
Figure 4.48: Single value Local sectional Cv comparison for healthy and faulty valve at different flow rates for 60 and 80% VOPs .....	200
Figure 5.1: Vibration signals for various probe height for the same probe position .....	204

Figure 5.2: Vibration signal amplitude similarities for same probe height and different probe lengths .....	205
Figure 5.3: Single-phase raw vibration signals for varying flow rates at different VOP...208	
Figure 5.4: RMS variation for various flow rates at the different VOPs (a) 10% VOP (b) 20% VOP (c) 40% VOP (d) 60% VOP (e) 80% VOP .....	209
Figure 5.5. Vibration signal spectrum for the valve at different flow rates at 10%, 20%, 40%, 60% and 80% VOPs.....	213
Figure 5.6. Mean frequency for the valve at different flow rates (a) 10% (b) 20% (c) 40% (d) 60% (e) 80%.....	214
Figure 5.7. Multiphase RMS variation for the different flow rates at (a) 10% (b) 20% (c) 40% (d) 60% (e) 80% VOP .....	216
Figure 5.8. Multiphase vibration amplitude variation for the different flow rates at 80% VOP for water flow rate of (a) 60% (b) 80% VOP .....	219
Figure 5.9. Multiphase vibration signal spectrum for the valve at different flow rates for 19.8LPM, 28.8LPM and 38.8 LPM (a) 60% (b) 80% VOP .....	221
Figure 5.10: Vibration mean frequency for the valve at different flow rates for (a) 60% VOP, (b) 80% VOP .....	223
Figure 5.11: RMS value comparison between healthy and faulty valve at different flow rates for (a) 60% VOP (b) 80% VOP .....	225
Figure 5.12. Vibration signal spectrum for the faulty and healthy valve at different flow rates (a) 60% (b) 80% .....	228
Figure 5.13. Mean frequency for the valve at different flow rates (a) 60% (b) 80% ....	229
Figure 5.14: RMS value comparison between healthy and faulty valve at different water flow rates for (a) 60% VOP (b) 80% VOP at 19.8, 28.8 and 38.8 LPM airflow rate .....	230
Figure 5.15: FFT for 19.8LPM airflow, comparing healthy and faulty valve at different water for 60% VOP .....	233
Figure 5.16: FFT for 28.8LPM airflow, comparing healthy and faulty valve at different water for 80% VOP .....	234
Figure 5.17. Mean frequency comparison for healthy and faulty valve condition at different flow rates (a) 60% (b) 80% .....	235
Figure 6.1: Acoustic signals for various probe height for the same length 1 probe position (a) Height 1 (b) Height 2 (c) Height 3 (d) Height 4 (e) Height 6 (f) Height 7 .....	239

Figure 6.2: Acoustic signal amplitude similarities for same probe height and different probe lengths (a) length 1 (b) length 2 (c) length 3 .....	240
Figure 6.3: Single-phase raw acoustic signals for varying flow rates at different VOP .....	242
Figure 6.4: RMS variation for various flow rates at the different VOPs (a) 10% VOP (b) 20% VOP (c) 40% VOP (d) 60% VOP (e) 80% VOP .....	243
Figure 6.5. Acoustic signal spectrum for the valve at different flow rates (a) 10% (b) 20% (c) 40% (d) 60% (e) 80% .....	248
Figure 6.6. Mean frequency for the valve at different flow rates (a) 10% (b) 20% (c) 40% (d) 60% (e) 80% .....	249
Figure 6.7. Multiphase RMS variation for the different flow rates at (a) 10% (b) 20% (c) 40% (d) 60% (e) 80% VOP .....	251
Figure 6.8. Multiphase acoustics amplitude variation for the different air flow rates for water flow rate of (a) 60% (b) 80% VOP .....	254
Figure 6.9. Multiphase vibration signal spectrum for the valve at different flow rates for 19.8LPM, 28.8LPM and 38.8 LPM (a) 60% (b) 80% VOP .....	256
Figure 6.10: Acoustic mean frequency for the valve at different flow rates for (a) 60% VOP, (b) 80% VOP .....	258
Figure 6.11: RMS value comparison between healthy and faulty valve at different flow rates for (a) 60% VOP (b) 80% VOP .....	260
Figure 6.12. Acoustic signal spectrum for the faulty and healthy valve at different flow rates (a) 60% (b) 80% .....	263
Figure 6.13. Acoustic mean frequency for faulty and healthy valve at different flow rates (a) 60% (b) 80% .....	264
Figure 6.14: RMS value comparison between healthy and faulty valve at different water flow rates for (a) 60% VOP (b) 80% VOP at 19.8, 28.8 and 38.8 LPM airflow rate .....	266
Figure 6.15: FFT for 19.8LPM airflow, comparing healthy and faulty valve at different water for 60% VOP .....	268
Figure 6.16: FFT for 28.8LPM airflow, comparing healthy and faulty valve at different water for 80% VOP .....	269
Figure 6.17. Mean frequency for the valve at different flow rates (a) 60% (b) 80% .....	270
Figure H1: Pressure regulator .....	311
Figure H2: PLC unit .....	311

Figure H3: PLC to DOP4 data transmission .....	312
Figure H4: Command view window .....	312
Figure H5: The Sequence command window .....	313
Figure H6: The Runtime sequence Log .....	313
Figure H7: Window for saving the data .....	314
Figure H8: Repeating of the test procedure .....	315
Figure H9:.csv excel data .....	315
Figure H10: Creating timing interval at 0.1 sec .....	315
Figure H11: Turbine flow meter calibration curve .....	316

## LIST OF TABLES

---

Table 2.1 Their CFD result validation .....	48
Table 2.2 Capacities calculated from CFD simulation results .....	58
Table 2.3: Statistical summary of all combinations of data reduction and pressure normalization techniques .....	68
Table 2.4 Pressure Probe design parameters for their design .....	72
Table 2.5: Outline of influence of the probe at the investigated locations (d = probe diameter) .....	84
Table 3.1: Material Properties .....	97
Table 3.2: Operating conditions .....	97
Table 3.3: System Boundary conditions .....	100
Table 3.4: Inlet and outlet probe positions .....	109
Table 3.5: Calibration nomenclature .....	110
Table 3.6: Mean uncertainty value for all the sensors .....	148
Table 3.7: Repeatability values at different flow rates for all the different sensors.....	149
Table 1: Accelerometer sensor specification [98] .....	296
Table 2: Specifications for the microphone sensor [99] .....	296
Table 3: Microphone YG-201 ICP preamplifier specifications [100] .....	297
Table 4: Pressure transducer specification .....	298
Table 5: Turbine flow meter technical specification for the OMEGA-WE-SDC series ...	298
Table 6: Technical specification for the FMA air mass flow meter series .....	299
Table 7: Power supply unit specification .....	299
Table 8: The YE6232 -16 CHANNEL DAQ Technical specifications .....	300
Table 9: NI DAQ technical specification .....	300

## NOMENCLATURE

---

CAD	Computer Aided Design
IP	Intellectual Property
ISA	International Society of Automation
FCI	Fluid Control Institute
IEC	International Electrotechnical Commission
LDV	Laser-Doppler Velocimetry
HWA	Hot-Wire Anemometry
PIV	Particle-Image Velocimetry
BS EN	British Standard European Norm
RMS	Root mean square
SD	Standard deviation
Sdr	Developed interfacial area ratio
FFT	Fast Fourier Transform
CCCS	Conductance and Capacitance Combination Sensor
CFD	Computational Fluid dynamics
SLM	Selective laser melting
EDM	Electron discharge machining
CFX	Computational fluid Explicit
Cv	Valve flow coefficient
(Cp)	Pressure coefficient
$D_{pipe}$	Pipe nominal diameter (m)

$D_{\text{valve}}$	Control valve body nominal size (m)
$P$	local static pressure (Pa)
$P_{\infty}$	Static pressure at free stream (Pa)
$q_{\infty}$	Dynamic pressure at free stream (Pa)
$U_{\infty}$	Velocity at free stream (m/s)
ECT	Electrical Capacitance tomography
$F_L$	Liquid pressure recovery factor
$F_k$	Ratio of specific heat factor
FRT	Total regional flow rate
$F_p$	Piping geometry factor
$F_c$	Liquid critical pressure ratio factor
$Ge^*$	Dimensionless Conductance
K	Ratio of specific heat capacitance of gas
PDE	Partial differential equation
$P_{\text{dyn}}$	Dynamic pressure (Pa)
$\bar{P}$	Average pressure (Pa)
$P_{\text{stat}}$	Static pressure (Pa)
$P_{\text{total}}$	Total pressure (Pa)
$P_v$	Fluid vapour pressure (Pa)
$CP_{\text{total}}$	Total pressure coefficient
$CP_{\text{static}}$	Static pressure coefficient
$CP_{\beta}$	Yaw angle coefficient
$CP_{\alpha}$	Total pressure coefficient
q	Pseudo-dynamic pressure (Pa)
P1	Upstream pressure (Pa)
P2	Downstream pressure (Pa)

QCV	Quick closing valve
A	Area of flow (m <sup>2</sup> )
Pa	Pascal
Qm	Mass flow rate in Kg/hr
LPM	Litres per Minute
GPM	Gallon Per minute
r/D	non-dimensional radial position for flows without and with swirl
SIMPLE	Semi-Implicit Method for Pressure Linked Equations
TAC	Twin-array capacitance
IEPE	Integrated electronics Piezo-Electric
N <sub>1</sub>	Numerical constant depending on the units to be used
F <sub>R</sub>	Reynolds number factor
F <sub>P</sub>	Piping geometry factor
V <sub>r</sub>	Radial velocity (m/s)
V <sub>z</sub>	Axial velocity (m/s)
V <sub>θ</sub>	Azimuthal velocity (m/s)
V <sub>x</sub> , V <sub>y</sub> , V <sub>z</sub>	Velocity components (m/s)
X <sub>eff</sub>	Effective pressure drop ratio across valve (Pa)
X <sub>FZ</sub>	Cavitation Coefficient
X <sub>T</sub>	Pressure drop ratio factor
Y	Expansion factor
C <sub>p</sub>	Pressure coefficient
Δp	Change in the upstream (P1) and downstream (P2) pressure (Pa)
P <sub>B</sub> /P <sub>5</sub>	Pressure at bottom hole (Pa)
P <sub>C</sub> /P <sub>1</sub>	Pressure at centre hole (Pa)
P <sub>L</sub> /P <sub>3</sub>	Pressure at left hole (Pa)

$P_R/P_2$	Pressure at right hole (Pa)
$P_T/P_4$	Pressure at top hole (Pa)
P	Proportional
PI	Proportional Integral
PID	Proportional Integral Derivative
VOP	Valve opening position
MHP	Multihole Probe
SVM	Support vector machine
SOFM	Self-organizing feature map

## SYMBOLS

---

$\alpha$	Pitch angle ( $^{\circ}$ )
$\beta$	Yaw angle ( $^{\circ}$ )
$\rho_0$	Relative water Density ( $\frac{kg}{m^3}$ )
$\rho_1$	Working fluid Density ( $\frac{kg}{m^3}$ )
$\sigma$	Cavitation number
$\varepsilon$	permittivity (F/m)
$\mu$	Dynamic Viscosity (Ns/m <sup>2</sup> )
$\xi$	Stream wise vorticity (rotation/sec)

## ACKNOWLEDGEMENTS

---

Firstly, I want to thank ALLAH for His infinite mercies over me, for His protection, guidance and blessings that enabled me complete this thesis.

Secondly, I would like to express my unreserved appreciation to Professor Rakesh Mishra, who is PhD research supervisor for the impact, encouragement, support, expertise and sense of direction rendered during the course of this research. His understanding and kindness ensured that a robust theoretical framework was pursued in a manner that guided me perform all of my experiments to the highest standard. My utmost gratitude cannot be explained in words as I forever remain in his debt.

I would also like to acknowledge the support of some of my colleagues at the University of Huddersfield EEERG (Energy, Emissions and Environment Research group), especially Dr Dharminder Singh (my co-supervisor) for his insights on flow diagnoses and direction in the analysis of some of my experimental data.

Also would like to thank my Mother, Hajia Sametu Airede, my sisters, Hajia Hauwa Sadiq Adamu and Hajia Jemila Mustafa-lecky and their loving Husbands for their moral and financial support during the course of my study. Also, to my late father, Alhaji D.M Airede who has groomed and taught me all the life lessons a son could ever wish for.

And finally, to my lovely wife, Mrs Aminat Yusuf Airede, my daughter Haleena Yusuf Airede and my son, Idrees Yusuf Airede for their support, patience, endurance and love throughout the journey of my PhD.

# CHAPTER ONE

## 1.0 INTRODUCTION AND BACKGROUND

---

*This chapter provides an overview of history and types of control valves and their many applications. This chapter also gives an insight into the control valve development as a key final control element in modern process industry, and presents the motivation for the research, the main aim and objectives. The concluding part for this chapter gives an outline for the thesis content and structure.*

## 1.1 INTRODUCTION

In process industry systems, valves are very common and a major key component. In controlling the fluid flow, temperature, pressure, level, etc., the control valve is used widely in flow processing industries. They are a major part of a typical control loop [1]. They had played, over the last few decades, an important role in various industrial application, for example, as a hydraulic device for fluid flow control. Various valve types have various applications in which they can be used for [2]. In flow control systems, valves are mostly used for safety purposes, where the valve dynamics has to match the control flow system dynamics. One of the most common component for fluid control in the industrial production process is the control valves where system parameters such as flow, pressure, etc., are controlled, especially in thermal plants, oil and gas, chemical industry, nuclear power and other similar industries [3]. Because of their fast response and high precision capabilities, they directly affect the performance level of the entire flow system.

The relationship that exists between the position of the valve and the piping system makes the relationship between the flow rate and pressure drop non-linear. Therefore, it is very important in understanding flow of fluid inside the control valve when engineers/researcher want to improve the valve performance, making it very difficult to predict their properties. However, there are CAD and CFD tools for the valve design, much of these designs mostly rest on the experiments and on experience [4]. Since either single or multiphase phenomena have been known to researchers, there have been significant developments in flow measurement techniques, which have allowed for the development of various measuring devices, though these devices have different mechanisms of how they measure the flow properties. These devices can be categorized into two groups:

- ***Intrusive techniques*** in which there is disturbance of the flow while measuring the flow properties.
- ***Non-intrusive techniques*** in which the flow properties are measured without disturbing the actual flow.

Both techniques can be applied in measuring either the flow properties of the continuous phase or that of the dispersed phase of the said flow and have thus, been implemented for the control valves.

## **1.2 BACKGROUND OF STUDY**

There have been some detailed research carried out on the control valve in the past. However, a well-detailed research about flow measurements inside the complex valve passages is very difficult and sometimes, almost impossible to carry out. It is therefore, important to design and create means to accurately take these measurements during experimentation. Numerical methods can also complement these experimental studies and provide additional information or data regarding the flow pattern and measurement results inside the control valves.

One major concern on the use of control valves in the production process is the impact by the fluid on the valve wall due to fluid high-pressure, which leads to the generation of noise and vibration on the body of the valve [3]. If the natural frequency of the valve body and that being produced because of the vibration are the same, excitation of the frequency resonance will occur on the body, causing a reduction in the valve work performance, and reduce the control valve life span, causing a significant influence (negative) on the entire industrial system [3].

The subsection 1.2.1 looks at the control valve, the history, types and its parts, to better understand their importance and functions.

### **1.2.1 THE CONTROL VALVE**

Dissipation of energy is the sole purpose of a control valve. Control valves controls flow conditions including the pressure drop, flow rate etc. by controlling how much the valves opens or closes. The valve actuator controls the closing and opening by comparing their set positions to a process variable.

Therefore, more importance should be given when considering the energy cost in evaluating the control scheme effects on the general running and profitability of the entire flow process [5].

#### **1.2.1.1 CONTROL VALVE HISTORY**

The control valve history is one story of an engineer, which was quite innovative, that developed the control valve and the intrepid companies who gave support to his effort. The control valves concepts goes as far back as the bronze plug cocks, which were used by the Romans in the aqueducts [6]. For centuries now, there have been need to move fluid (water) to populated regions from rivers. The Egyptians and the Greeks followed similar practice but it was during the Romans age that key important developments in

fluid flow networks occurred. James Watt introduced this concept of an automatic moving-stem valve in the late 18<sup>th</sup> century, which he developed in regulating his steam engine speed. Other control valve with similar application were then developed during the 19<sup>th</sup> century. Late in the 19<sup>th</sup> century, self-contained level and pressure regulators were applied to much larger steam boilers in power stations. Pressure from the process was then used in moving the stem of the valve of the pressure regulator through the valve diaphragm; the level regulator stem was moved to a ball float by a mechanical linkage. One of the first valves used by the Romans for their fluid network can be seen in figure 1.1 consisting of a plug, inserted on the valve body. The plug could rotate about 90 degree for the valve to either open or close. The material used was bronze, which facilitated the plug rotation with anti-corrosive properties. Some evidence has also suggested that Romans at that time had used primitive forms of angular, diaphragm, check and mixing valves [7].



Figure 1.1: Plug valve of the Romans

It was during the industrial revolution that the developments of modern design of valves started. When Thomas Newcomen invented the steam machine in 1705, valves were required in controlling the steam engine process. During the second half of the 18<sup>th</sup> century, an engineer named James Watt developed, for his machines, an improved valve design. Control valves later became commonly used late in the 19<sup>th</sup> century in fluid networks for power stations in controlling their entire process.

William Fisher in 1880, who was an engineer, invented the first pressure regulator valve by working constantly in ensuring that constant discharge pressure is maintained on a water pump that is steam-driven. With this development, Fisher established a company named Fisher Controls in order to manufacture regulators. By 1907, the valves regulators became popular all over the world, in Asia, Europe, etc. [6].

Mason Regulator Co, was a company established by William B. Mason in 1882. He invented in 1885, the steam pressure reducing valve and in 1886, the pump pressure regulator. This regulator, for many years, was used on the U.S Navy ships in securing higher steam operating pressure efficiencies.

When the oil and gas industry, during the turn of the century, began to spread all over, demand for massive increase in the consumption of oil for transportation and electricity production then started at this time. For this to be sustained, more power consumption rates, together with much bigger valves, became necessary. However, more energy is required from these bigger valves in moving the plug as pressure drop remained moderate. Because of this reason, the development of the pilot operated regulator was essential in response to meet the needs of increasing demand of energy as more power was needed to be supplied to the valve plug for proper control.

At the beginning of 20<sup>th</sup> century, temperature and pressure capacities increased due to the demand for larger valves, requiring more improved mechanisms for powerful positioning and construction materials. During this time, the smaller regulators were still made of bronze and the larger ones were of cast iron with disk that opens quickly and integral seats that can achieve with minimum lift, maximum flow. The oversizing and the quick opening of the disk resulted in the valve instability, which were periodic, and prompted the need for valves with slow opening characteristics to be manufactured, which compensated for the disk oversizing. The Hanlon Walter Company pioneered this development, making various contributions to valve technology developments in 1920s and 30s in the refinery and went on to become full valve manufacturing company. Mason Regulator Co. developed a new double-seated valve design that led to increase in the dynamic forces stability on the plug and the assembly by guiding the plug.

In 1920s, cracking crude oil process at a very high pressure and temperature was developed. During this period, Thomas Neilan Company was founded in serving the need of the oil and gas industry. The company developed remarkable valves regulators and introduced sophisticated temperature and pressure actuators. They produced control

valves with cast irons and heavy flanging for refineries. By the 1930s, what we have come to know today as control valve was designed. New valve innovations sprung up including but not limited to different shapes of plug in achieving different characteristic of control, or using multi stage trims to gradually reduce pressure [8].

Next section discussed the components of the control valve and their importance.

### 1.2.1.2 TYPICAL INDUSTRIAL CONTROL VALVE DESCRIPTION

Control valves are of different types, with the main differences being narrowed to the plug shape and manner in which the device is operating. Figure 1.2 shows the control valve structure and its major parts.

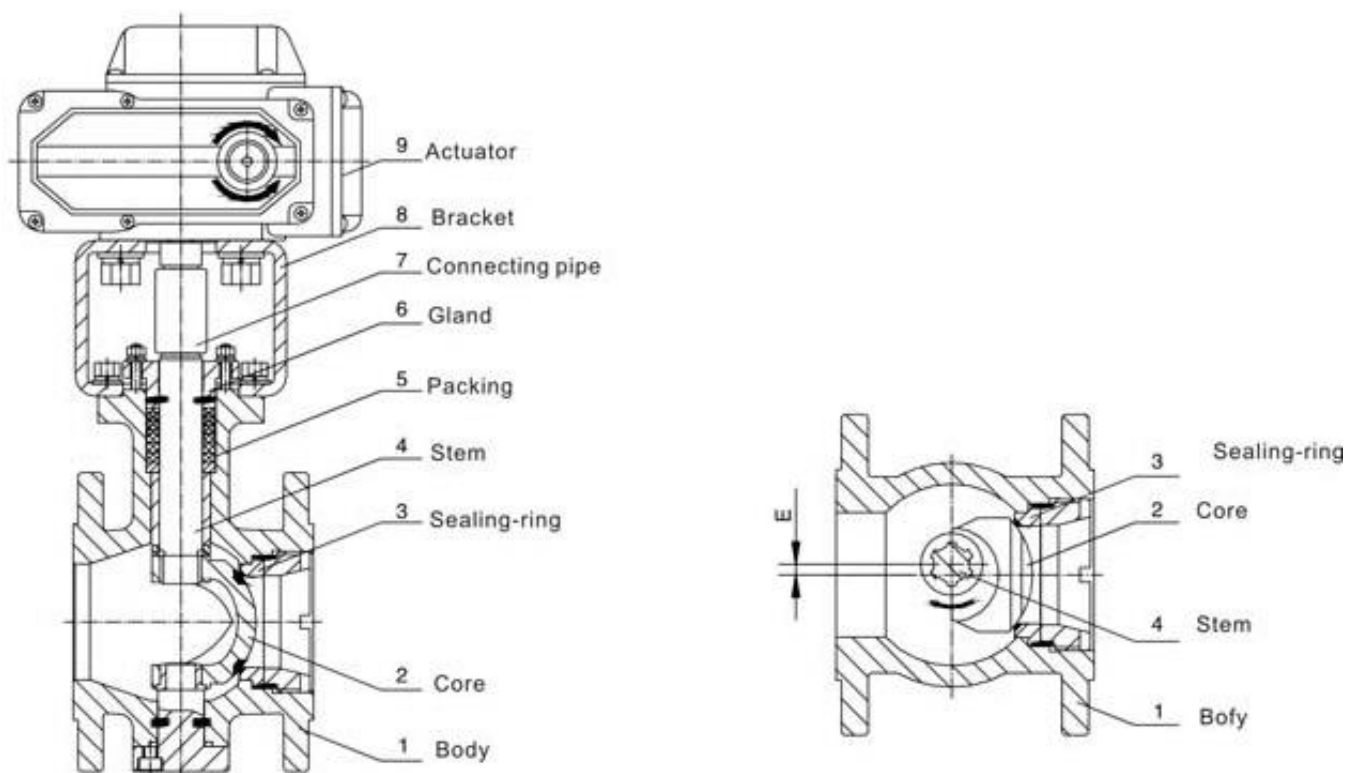


Figure 1.2: Typical Industrial control valve [5]

- **The Body**-This part of the valve allows the passage of processed fluid and the part that allows for fluid to be manipulated. As the body is in contact with the process fluid, the body material choice to be used needs to be considered carefully. It also connects to the pipe ends, creating the fluid passageway, and gives supports to the seating surfaces.

- **Plug**-They control and regulate the process fluid as they are at the stem-contoured end. It comes with several shapes such as spherical, cylindrical, etc. The plug contour determines the characteristics of the flow.
- **Stem**-This is the part of the plug, which has the linear sliding movement. Stem, such as the ball valves, can also be rotational.
- **Seat**-It is in a ring-like form that have its inner face closely following the plug contour, into which the plug fits. The closer the plug to the seat, the smaller the flow area, the farther the plug is from the seat, the greater the flow passage.
- **Actuator Stem**-It is a metal shaft of short length, with one end fixed to the drive mechanism of the valve while the other end is attached to the stem. The valve motor movement is transferred to both the plug and stem.
- **Actuator**- An actuator can be hydraulic, pneumatically or electrically powered device, supplying force and motion to close and open the valve. Usually called the valve motor. The motor could be a diaphragm, a squirrel cage electric box, etc., which converts to linear motion from rotary motion [5].
- **Stem connector**- They connect the actuator stem firmly to the stem of the valve. It connects two separately assembled control valve parts to make a complete functional unit.
- **Airset**- It manages and controls the supply of pressure to the valve actuator and all of the valve auxiliaries.
- **Bonnet**- It is the valve part that provides the stem some guidance. It also provides the main opening to the body cavity of the valve for the internal parts assembly. It provides attachments for the actuator to the valve body.
- **Cage**- It is the control valve trim part that surrounds the closure member, which provide also, the characterization of the flow and/or a seating surface. It can provide also, some alignment, balance, guiding and stability and facilitate other assembly valve trim parts.
- **Capacity**- The rate, under specific conditions, at which flow goes through the control valve.
- **Closure member**- This is a moveable part of the control valve that is positioned specifically in the flow path, in order to modify the flow rate that flows through the valve.

- **Flow coefficient-** Also known as the Cv. It is a constant value, which is related to the control valve geometry for a specified amount of valve travel, where the flow rate of the valve can be predicted.
- **Valve positioner-** It is mechanically connected to the valve actuator. They adjust their output pressure automatically to the valve actuator in maintaining the desired position, which allows a relationship that is predetermined, to that of the input signal.
- **Valve seat-** This is the contact area between the valve-mating surface and valve closure component that establishes the valve shut-off.
- **Stem guide-** The part is fitted closely to what is called the valve stem. It also aligns with the seat of the valve.
- **Travel-** It is the closure member movement from close position to a rated intermediate or full open position.
- **Vena contracta-** This is that location inside the control valve where the velocity of the fluid is at its maximum during flow, while the static pressure of the fluid and the flow cross-sectional area are at their lowest minimum at that particular location. Inside the valve, the vena contracta occur just after of the actual physical valve restriction.
- **Trim-** It is the heart of any control valve. It is the part of the valve that is normally exposed to the process fluid. They are subjected to wear and degradation, making them replaceable. Parts including the stem, closure member, etc. are known as the “valve trim”. Since they vary in their designs, their choice of material body needs to be carefully considered. Figure 1.3 shows a sample of the trim currently being used for this research [5].

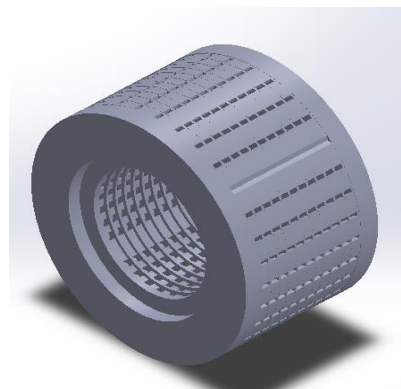


Figure 1.3: Example of a valve trim in the lab

The corrosive and erosive nature of the process fluid are key factors in the analysis of the valve trim. The trim design affects the forces that the actuator demands. To choose a valve trim, the following steps should be considered [9];

- The service life of the trim as to whether the type of the fluid is corrosive or erosive.
- Some specific criteria needs to be considered, like the trim servicing, extreme temperature, allowing no leakages on the stem.
- Generation of noise that can be because of aerodynamic noise or due to cavitation.
- Serviceability, depending on how frequently the trim is used and how much cleaning is needed or if it needs to be replaced.
- The requirement of the leakage consideration whether total shutoff is required.
- The flow characteristic of the valve to know what needs to be the installed in order to be able to control the valve gain.

Inside the trims, there are disk stacks, one on top of the other. The disk modulates the flow inside the trim, depending on its orientation. Figure 1.4 shows a disk of the valve that have four flow paths. What occurs in one flow path similarly occurs in another flow path.

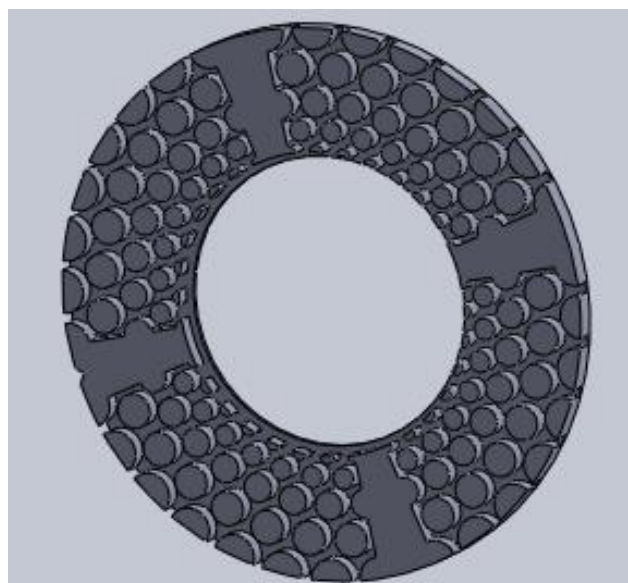


Figure 1.4: a valve disk with four-flow path

#### 1.2.1.4 REASONS WHY CONTROL VALVE FAILS AND HOW TO OVERCOME THEM

When predictive maintenance are carried out on the control valve, they become very dependable and their performance improves. However, like other machines, they occasionally fail, but when failure becomes premature, proper investigation needs to be conducted and corrected. These failures can occur because of;

- Damage due to Cavities.
- Trim erosion and corrosion.
- Valve plug resonance.
- Trim wire drawing, i.e. actual material cutting away from trim, including swarfs, when machining.

In minimizing these failures,

- Select a valve that has a trim with low-pressure recovery, or to relocate the valve to a position more favourable, or to install a secondary flow restrictor.
- Hot or wet steam condensates, which often eats away the valve body material. Stainless or alloy steel should be chosen as material for the valve body.
- Reversing the direction of flow can eliminates, at times, some specific problems.
- Using the corrosion table, better selection of valve construction material can be made [5].

Listed above are some of the problems that can affect the valve and best possible ways to overcome them. These can help to eliminate some of the problems even before they occur in order for the valve to run a smooth operation. [5]

Before selecting the valve for a particular application, proper valve sizing needs to be carried out to ensure efficient valve performance.

#### 1.2.2 SOME TYPES OF VALVE

Valves come in various designs depending on their mode of operation. Some examples of valves are further explained;

- **Ball Valves**

Figure 1.5 shows an example of a ball valve structure.

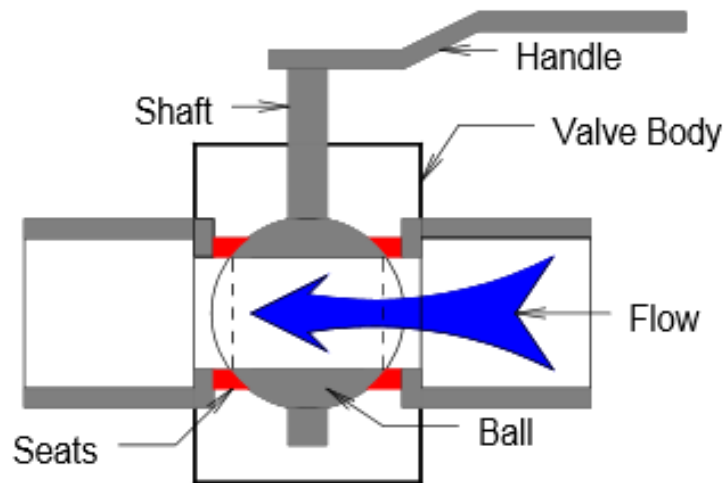


Figure 1.5: a typical ball valve [10]

As the name implies, it has a ball with a drilled hole through the centre swivel that is mounted on the body of the valve. A full flow rate occurs when the orientation of the ball hole is in the same direction as the pipe in which the fluid flows. As the ball hole orientation moves away from the pipes direction, the flow rate will begin to restrict until it cuts off completely when it reaches 90 degree [10].

- **Butterfly valve**

It operates on a similar principle with the ball valve. But instead of the valve having a ball mounted on the valve body, a butterfly, which is a circular disk is used. The name is as a result of the fact that it has two half circles that appears like wings, around the vertical shaft [10]. Figure 1.6 shows an example of a typical butterfly valve.



Figure 1.6: Example of a butterfly valve [10]

- **Gate valve**

It is a valve that moves in linear motion used to either stop or start a fluid flow. It however does not throttle or regulate the flow. The name “gate” given to this kind of valve is derived from the disk appearance in the flow stream. The gate valve disk is removed completely from the flow stream when it is fully open. There is no any flow resistance when the valve is fully open. When it is fully closed, disk-to-seal ring contact surfaces exist for the full 360 degree providing a very good sealing. With a very good disk sealing, it gives room for little or no leakage to occur [10]. Figure 1.7 shows a structured, well detailed example of a gate valve.

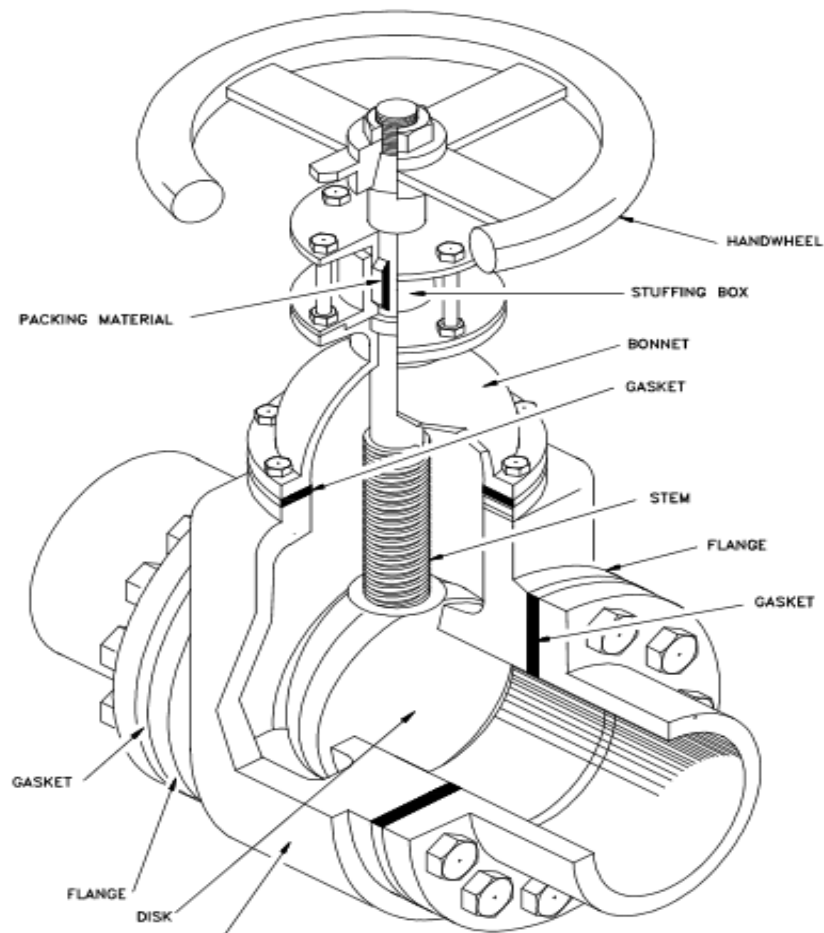


Figure 1:7: a gate valve [10]

- **Globe valves**

There are three globe valve body designs available. They are the X-body, Z-body and Angle. The simplest and most common design type is the Z-body. They consist of a disk type element which is moveable and a ring seat which is stationary in regulating pipework flow. They are named for the spherical shaped body with two

body halves separated by an inside baffle. A seat is formed in which a moveable plug can be screened to either open or shut the valve [10]. Figure 1.8 shows an example of a globe valve.

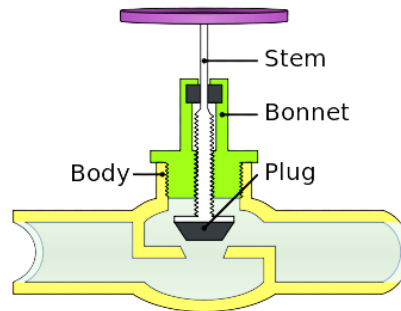


Figure 1:8: a globe valve [10]

- **Plug valves**

A rotational motion valve is used to either start or stop a fluid flow. It is so named, as the disk shape resembles that of a plug. The petcock is the simplest plug valve form. The plug valve body is made in such a way to receive the cylindrical or tapered plug. Its disk is in the form of a solid plug with a bored passage that is at right angle to the plug longitudinal axis. To open the valve, the plug passages lines up with both the outlet and inlet port of the body of the valve. When there is 90 degree turn of the plug from this open position, the plug solid part blocks this port which in turn will stop the flow of fluid [10]. Figure 1.9 shows a detailed structure of a plug valve.

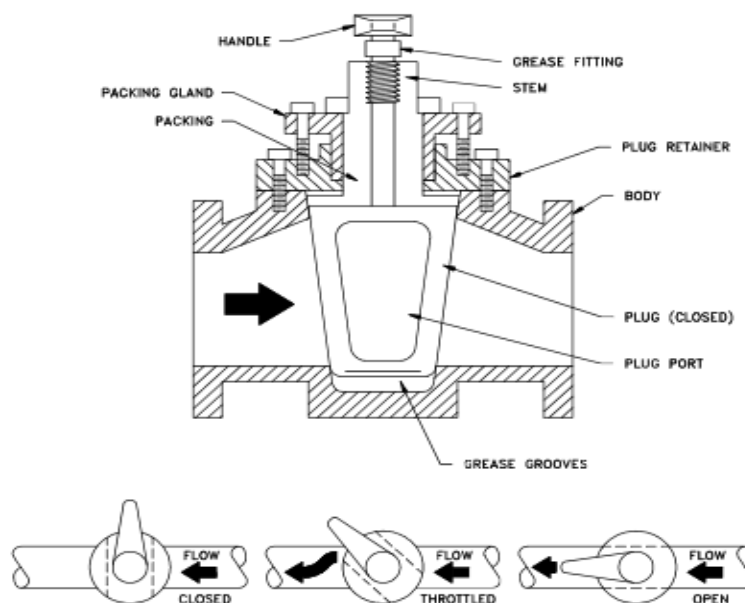


Figure 1.9: a plug valve [10]

- **Diaphragm valve**

It is also a valve with linear motion that is used to start, regulate and then stop the flow of fluid. Its name diaphragm from the fact that it has a disk that is flexible that mate with the valve body seat, as a result, forms a seal. They are very common and ideal for flows that are restrictive or for flow control applications such as to close the valve half way in order to reduce its flow rate. A flexible diaphragm is connected by a stud, which is modelled into the diaphragm to a compressor. This compressor is moved up and down thereby also causing the diaphragm to move, causing it to open or close the flow path. The valve body of this type of valve are of two types, the straight through type and the Weir type.

This action of the diaphragm can be actuated or operated manually or using the pneumatic actuator with the valve body base remaining the same [10]. Figure 1.10 shows an example of a diaphragm valve and its parts.

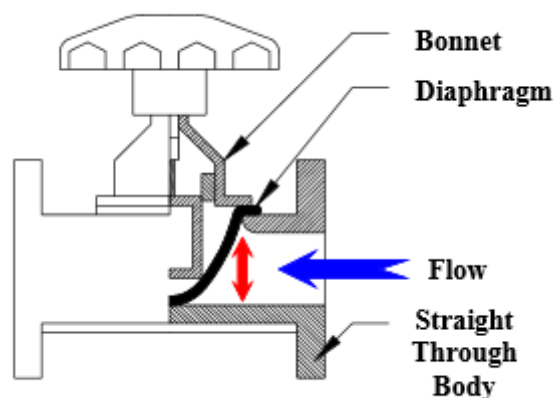


Figure 1:10: a diaphragm valve

Various types of valves have been discussed. One key defects that affect most valves is cavitation as it reduces the valves' efficiency and life span. A detail look at the cavitation is explained in the next section.

### 1.2.3 CAVITATION

Cavitation is defined as the formation of vapour bubbles of a flowing fluid in a section where the fluid pressure falls below the fluid vapour pressure. This bubble condensation does not only results in vibration that affects the surrounding structure, resulting in noise generation, but also results in the stress occurrence that are localized in the connecting

pipe walls and the body of the valve which can lead to severe pitting [11]. Cavitation poses a potential danger, particularly in pumps and valves. The damage caused by cavitation to the valve may occur quite rapidly which can sometimes results in vibration, noise and rapid valve trim deterioration that which can lead to the prevention of further operation of the valve [12]. Erosion because of cavitation is considered a key reason for damages done on the surface of hydromachine in cases where corrosion and abrasion have little influence [13]. Therefore, cavitation monitoring is of both economic and efficient process importance. The trim of the valve is usually damaged early, but the body of the control valve and that of the pipe can also be hugely affected even as far as about more than 20 diameters in the downstream of the control valve. These cavitation effects because of such pressure fluctuations can be analysed [14]. Cavitation erosion is generally because of bubble collapse near the solid wall [13] [14]. Many researches investigating erosion caused by cavitation have been carried out, due to how important they are to life, on mechanical heart valves [15].

Cavitation is a purely liquid flow phenomena as gases cannot cavitate. Cavitation has been a phenomenon that is quite familiar, particularly in shipping industry. In 1917, Lord Rayleigh, who was a British physicist, was asked to investigate the cause of the quick erosion of a fast-rotating ship propellers. He however, discovered that the effect of cavitation, which was already been proven in 1894 by Reynolds, was the cause. Although several investigations have followed regarding cavitation, many effects because of cavitation are yet to be explained completely. Cavitation can occur in a fluid because of the energy input. For example, plasma in liquids are created by a laser beam, which causes the liquid to evaporate, and by so doing, creating cavity [15].

In addition, pressure drop in hydrodynamic flows can lead to cavitation. This effect from cavitation can be regarded as a phenomenon that is quite destructive. Control valves, in addition to the rotors of the pump, are exposed to this problem as the vena contracta static pressure, even at reasonable operating conditions, can reach levels that is sufficient for cavitation in liquids to occur.

The consequences of cavitation for valve are given below, which along with the entire control process, vary and can be very destructive:

- Loud noise.

- Strong vibrations in the affected plant sections.
- Vapour formation causing choked flow.
- Fluid properties changes.
- Valve components erosion.
- Control valve destruction.
- Complete or partial shutdown of the plant.

In figure 1.11, some of the effects caused by cavitation to some valve parts can be seen.



Figure 1.11: Cavitation effect on this valve part

### 1.2.3.1 THE CAVITATION COEFFICIENT, $X_{FZ}$

Béla [16] defined the coefficient of cavitation, denoted as  $X_{FZ}$ , as the ratio that exist between the pressure drop in the valve at which cavitation begins to occur and the pressure difference between the vapour and the inlet pressure of the said application. The maximum allowable  $\Delta p$  (pressure difference between P1 and P2), before the start of cavitation is;

$$\Delta p = X_{FZ} (P_1 - P_v) \dots \dots \dots 1.1.$$

Where P1 is the inlet pressure or upstream pressure and  $P_v$  is the fluid vapour pressure. As the value of  $F_L$  (Liquid pressure recovery factor) and  $X_{FZ}$  drops, the probability of cavitation occurring then increases.

In general, the damage caused by cavitation occurs always at the downstream of the vena contracta when the valve pressure recovery causes the temporary cavities (voids) to collapse. The destruction that occurs inside the valve is due to the bubble implosions that would generate shock waves of very high pressure in the non-compressible stream. The moment when these shock waves strike the valves' solid metal surface or of the

downstream piping, it causes damages that gives an appearance that is cinder-like. When cavitation occurs, it comes with a sound and vibration resembling fragments of gravel or rock that flows through the control valve. In cases of inviscid or less viscous flows of liquid around streamlined bodies, its internal friction, when compared to that of the pressure, are often neglected. This type of velocity distribution can be calculated based on the potential theory, in the assumption that the flow conditions are known. Along the valve body contour, the distribution of pressure is derived from Bernoulli's equation in accordance to equation (1.2), showing the relationship between the minimum pressure  $P_{min}$  and that of the critical pressure.

Potential theory cannot be used in determining the minimum pressure in cases where the flow, as they occur, needs to be stalled in the control valve. Instead, Bo-Suk et al [17] showed that the cavitation coefficient  $X_{FZ}$  will prove useful. Figure 1.12 shows the distribution of pressure inside the control valve along its length.

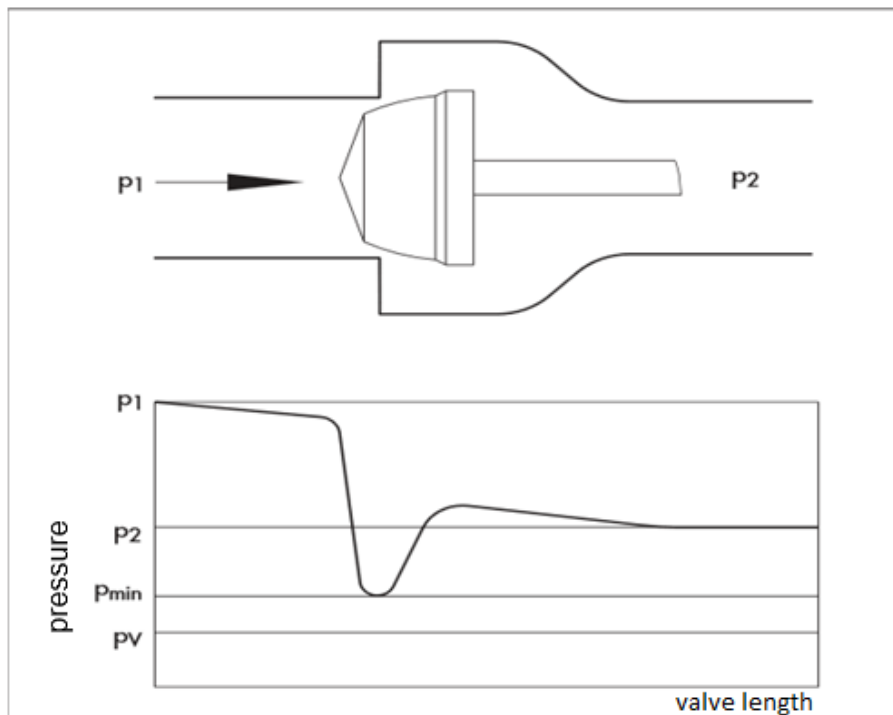


Figure 1.12: Distribution of pressure in the control valve

It is based on the principle that the ratio of the difference in external pressure ( $P1-P2$ ) to that of the difference in internal pressure ( $P1-P_{min}$ ) in the control valve, for all operating states that will ensure cavitation not to occur, equals a specific valve value  $X_{FZ}$  as seen from figure 1.12.

$$X_{FZ} = \frac{P1 - P2}{P1 - P_{min}} \dots \dots \dots 1.2$$

Though it is in the unsteady vortex cores that is downstream of the restriction is where minimum pressure occurs, direct measurement cannot determine the cavitation coefficient value. Figure 1.13 shows a curve on how the cavitation coefficient can be determined.

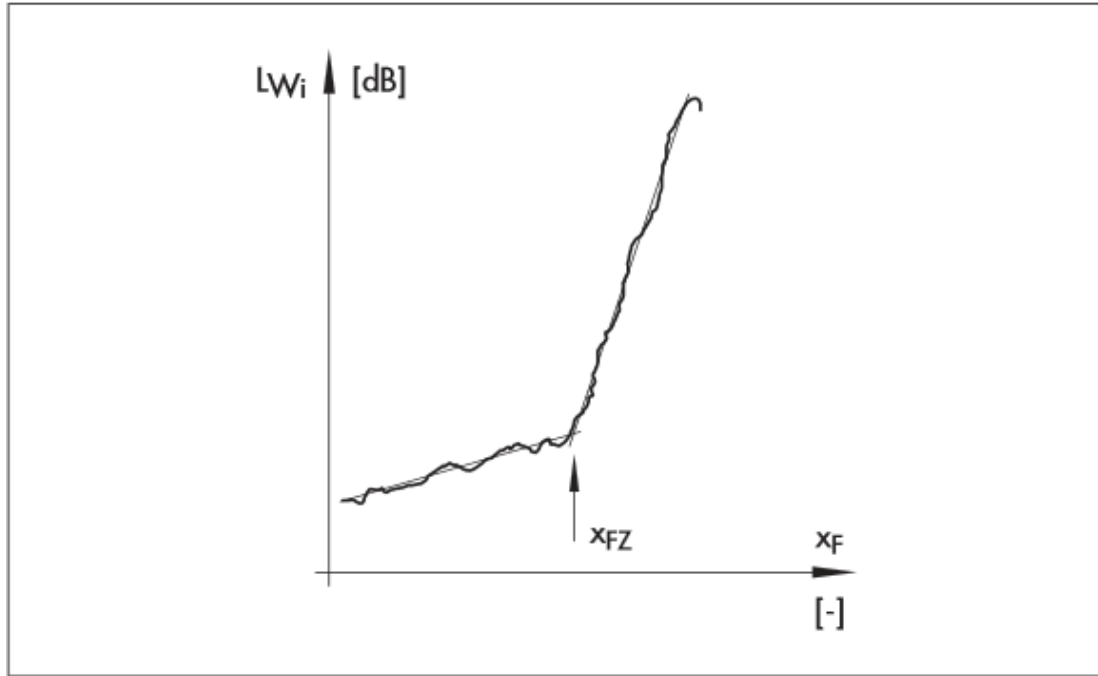


Figure 1.13: determining the cavitation coefficient  $X_{FZ}$  [6]

Where  $LW_i$  is the cavitation noise from the valve. The coefficient of cavitation  $X_{FZ}$  is determined by measurements of noise between that of the sound generated and that of the pressure ratios  $X_F$ . It is assumed therefore that when  $P_{min}$ , which is the minimum pressure, equals that of  $P_V$ , which is the fluid vapour pressure, cavitation noise would begin, which thus determines the cavitation coefficient  $X_{FZ}$  as a function of valve load (in form of pressure) by means of measuring the noise as seen from figure 1.13 [1]. If the  $X_{FZ}$  values over the entire valve travel range are known, it can therefore be determined for all of the operating pressure ratios in advance, if the effect of cavitation would be expected.

$$X_{FZ} = \frac{\Delta p}{P_1 - P_V} \dots \dots \dots 1.3$$

In cases where the operating pressure ratio  $X_F < X_{FZ}$ , there would be no danger of any form of cavitation occurring. In addition, when  $X_F \geq X_{FZ}$ , there would be a build-up of a zone of stationary cavitation whose expansion would roughly be proportional to their difference ( $X_F - X_{FZ}$ ).

Having conducted some background research based on the research topic about control valves and its deficiencies, it became necessary for further investigation to be carried to be able to address the aims of this research that will be developed. The motivation for this research is thus explained in the next section.

### **1.2.3.2 CAVITATION ELIMINATION/PREVENTION PRINCIPLE**

Cavitation phenomenon is such a complex research area that causes great damage due to high impact pressure bubbles. In this case, a liquid/vapour mixture occurs at the narrowest point inside the valve in the throttling area that have a mean density different from that of the liquid. There are ways in which cavitation can be eliminated. The issue with these methods is changing the process condition, which will have to be done before they can take effect. Process condition is however already determined before the decision of what type and capacity of valve to use. Trying to change this condition is not feasible as they are other ways in which this can be done. Because there are no known material that can indefinitely withstand any permanent damage caused by severe cavitation to the valve, the one definite solution is to eliminate cavitation. A dense liquid that has high surface tension (e.g., mercury or water) causes the greatest damage when cavitation occurs [16].

This cavitation prevention can be done in two ways, changing the operating condition of the flow process or using alternative measures while leaving these conditions constant. To eliminate cavitation by changing the process conditions, reducing the operating temperature of the valve can lower sufficiently, the vapour pressure thereby, eliminating cavitation [16]. Likewise, increasing the pressures at the downstream and upstream, without affecting  $\Delta p$ , or having a reduction in the  $\Delta p$ , can both get rid of cavitation [16]. Hence, control valves that are more likely to experience cavitation should be installed in such a way that it is at the lowest elevation possible in the piping flow system, which is also operated at minimum pressure difference ( $\Delta p$ ).

In addition, moving the control valve very close to the flow system pump will serve to increase both the pressures at the upstream and downstream. If all these cavitating conditions becomes inevitable, increasing the operating temperature or decreasing the pressure at the outlet, flashing rather than cavitation occurs, where the downstream pressure is equal or below the vapour pressure.

Where change the operating conditions of the valve cannot be effected, modifications can be made to the flow path of the valve that can result to high  $F_c$  (liquid critical pressure ratio factor) and  $F_L$  (Liquid pressure recovery factor) coefficients. In addition, using high recovery valves like the butterfly, ball and gate, which have a low  $F_L$  and  $F_c$  coefficients should be avoided. Take for example, in the design of the Swiss cheese type valve, small holes, on opposite sides of the valve cage centreline, are arranged in pairs. The Labyrinth-type control valves can be made to avoid cavitation by having at each turn, series of right-angle turns having negligible pressure recovery factor. Cavitation could be avoided also in multiple or multistep valves in series, by replacing the vena contracta with several other small vena contracta points, to ensure even distribution of the pressure drop between these several ports that are working in series. This would work if and only if the process fluid vapour pressure is below that of the outlet pressure  $P_2$  of the control valve [16].

Cavitation can be alleviated in the control valve by introducing into the area/region air or nitrogen [16] where one can anticipate that cavitation would occur. This gas can be reintroduced into the valve through the shaft of the valve or through the downstream taps that is on either sides of the pipe that is in line with the shaft, and also very close to the control valve as one can get. The gas can also absorb some of these pressure drops in restricted orifice section, partially open block or choked section of the valves.

Damage as a result of cavitation is proportional to the 3<sup>rd</sup> power of pressure drop or the 6<sup>th</sup> power of flow velocity [16]. This is the reason why reducing  $\Delta P$  by a factor of 2 will amount to an eight-fold reduction in the destruction caused by cavitation. A fixed-opening single choke fitting is only applicable when there is a constant flow rate process. The chokes that discharge into the tank vapour space can also minimize the damage caused by cavitation. This is because there would be no bubble collapse near wall of the valve.

While there is no known material that will withstand the damage caused by cavitation, some of these materials last longer than others. One of the best-known overall material selections for the resistance of cavitation is the Stellite 6B. This type of material is a wrought material that can also be welded to form various sizes of valve trims of up to 75mm (3 inches) [16].

### 1.3 PERFORMANCE CHARACTERISTICS OF CONTROL VALVES

After decades of research as to how fluid flow through the control valves, a resolution on the sizing of the valve came with design parameter development, which was derived experimentally in the late 1930's by Ralph Rockwell. Al Hanssen, who was the standardization committee Chairman for the section of control valve for the FCI (Fluid Controls Institute) in 1950, began an effort in standardizing the procedure in determining valve flow coefficient (Cv) or flow capacity.

In 1952, the facilities to test these standards was sited at Fisher (a major manufacturer of Control valve). The fluid control institute standard issued a recommendation in 1958, a voluntary standard for determining the Control Valve Capacity. This standard was the foundation for the testing of control valve, and ever since, it has been adapted and revised for later incorporation into the standard at ISA (International Society of Automation), and subsequently into an harmonised European standard, the IEC BS EN (International Electrotechnical Commission British Standard European Norm) standard 60534-2-1 [18]. The fundamental parameter now used in the control valve sizing is the Cv. Depending on what type of fluid flow through the control valve, whether compressible or incompressible, the mathematical formulation for the Cv varies. The Cv formula can be calculated for an Incompressible fluid as given in equation 1.4:

$$Cv \frac{(2 \times 10^{-7} m^3)}{s \sqrt{Pa}} = Q \times \sqrt{\frac{\rho_1 / \rho_0}{P_1 - P_2}} \dots \dots \dots 1.4$$

where;

Q = Volumetric flow rate in US GPM (Gallons per minute) through the valve

$\rho_1$  = the working fluid Density in  $kg/m^3$

$\rho_0$  = Relative water density at 15°C in  $kg/m^3$

P1= Pressure at the valve inlet in psi

P2 = Pressure at the valve outlet in psi

The expression above have been derived from the Daniel Bernoulli principles, who stated in his Hydrodynamics publication [19] that an increase in the velocity of the fluid results in a decrease in the fluids' pressure for an inviscid flow. This is known as Bernoulli's principle when referring to control valves and is given in equation 1.5:

$$\frac{P_1}{\rho g} + \frac{v^2}{2g} = \frac{P_2}{\rho g} + \frac{v^2}{2g} + K \frac{v^2}{2g} \dots \dots \dots 1.5$$

$\rho$  = the working fluid Density in  $\text{kg}/\text{m}^3$

$g$  = Acceleration due to gravity in  $\text{m}/\text{sec}^2$

$v$  = velocity of the fluid  $\text{m}/\text{sec}$

$P_1$  = Pressure at the valve inlet in Pa

$P_2$  = Pressure at the valve outlet in Pa

$K$  = A constant which represents losses with the valve

Assuming that the valve sections at both the inlet and outlet have exactly the same dimensions geometrically, and both the outlet and the inlet sections of the valve are of same elevation.

Equation 1.5 can be re-written in order to obtain the control valve equation for the Cv as seen in equation 1.6.

$$\frac{P_1}{\rho g} - \frac{P_2}{\rho g} = \frac{v^2}{2g} - \frac{v^2}{2g} + K \frac{v^2}{2g} \dots\dots\dots 1.6$$

$$\frac{P_1 - P_2}{\rho g} = K \frac{v^2}{2g} \dots\dots\dots 1.7$$

Since  $v = \frac{Q}{A}$

Where velocity is represented by  $v$ , flow rate is represented by  $Q$  and  $A$  in the Area,

$$\frac{P_1 - P_2}{\rho g} = K \frac{Q^2}{2gA^2} \dots\dots\dots 1.8$$

$$Q = \sqrt{\frac{2A^2(P_1 - P_2)}{K\rho}} \dots\dots\dots 1.9$$

Or,

$$Q = \text{constant} \sqrt{\frac{(P_1 - P_2)}{\rho}} \dots\dots\dots 1.10$$

Similarly,

$$Q = \text{constant} \sqrt{\frac{(P_1 - P_2) / \rho_0}{\rho / \rho_0}} \dots\dots\dots 1.11$$

Where  $\rho_0$  is the density of water.

Hence,

$$Q = \text{constant} \sqrt{\frac{P_1 - P_2}{\rho / \rho_0}} \dots\dots\dots 1.12$$

The constant seen in equation 1.12 could be replaced with Cv, and this Cv depends on the area. After the Cv for the process conditions has been analysed, the manufacturer of the

valve then need to, for this process, supply the kind of valve that can achieve the Cv requirements. The control valve itself restricts flow. Therefore, pressure drop across the valve always occur even at 100% valve VOP (valve opening position). The valve can also be said to have its own Cv, which can be calculated as accumulation for each of the restricting elements Cv's, which are three, for the entire valve, i.e.:

- The trim of the valve
- The seat of the valve
- The body of the valve

All of these restrictions Cv adds up to give the valve total Cv, defined as:

$$\frac{1}{Cv_{valve}^2} = \frac{1}{Cv_{Body}^2} + \frac{1}{Cv_{Trim}^2} + \frac{1}{Cv_{Seat}^2} \dots\dots\dots 1.13$$

Equation 1.13 can be rearranged as

$$Cv_{valve} = \frac{1}{\sqrt{\frac{1}{Cv_{Body}^2} + \frac{1}{Cv_{Trim}^2} + \frac{1}{Cv_{Seat}^2}}} \dots\dots\dots 1.14$$

As seen in equation 1.9 where the loss constant and the area were replaced with a single constant value, Cv where the Cv relation to the area is given as:

$$Cv = A \times K \dots\dots\dots 1.15$$

So,

$$A \times K = Q \sqrt{\frac{\rho/\rho_0}{P_1 - P_2}} \dots\dots\dots 1.16$$

Therefore, with a given set of process conditions with known area, K value can be determined for each valve element. These individual Cv values for the different valve element can then be substituted into equation 1.13 to determine the overall Cv of the valve.

**1.4 PRESSURE PROBES**

Within a stream of fluid, pressure probes is used in measuring the static pressure, the stagnation pressure, and the flow angle at impact. When a pneumatic probe used in flow measurements is being designed, the frequency response, blockage effects, pressure hole geometry and size, Reynolds number and the relative scale of the phenomena being investigated must all be addressed. Generally, a much better accuracy can be obtainable if smaller transducers and probes are used [20] though as a result, there may be compromise in the mechanical integrity as the time of response becomes longer and also,

problems with dirt inside the fluid (especially in water) can occur. Because of this reason, the blockage effects, especially for incompressible flow, becomes greatest [20].

#### **1.4.1 STATIC PRESSURE PROBES**

This type of probe can sometimes be used to obtain the static pressure measurement of the flow. This type of probe can be a cylindrical tube, simply placed in parallel to the fluid flow with static tapings situated on its probe body. There are variety of probes with nose configurations used on the tubes. They include the cone probes, wedge probes, disc probes and Prandtl tube [20]. For all the probe types listed, the readings obtained from the static pressure are influenced by some factors such as probe length, probe diameter, etc., just like the wall static tapings.

For the measurement from the static pressure probes to be accurate, the probe axis has to be placed in parallel with the flow, as their use inside flow fields are restricted in domains where the turbulence and gradients are quite small. Such conditions are hardly fulfilled in research rigs for turbomachinery except at the test sections inlet. For such condition, the stagnation pressure tubes are combined often with the static tubes in order to determine the flow velocity and stagnation pressure [20].

#### **1.4.2 STAGNATION PRESSURE PROBES**

The flow stream stagnation pressure can be measured at a point if any tube that is half-opened is placed in such a way that its open end faces the direction of the flow stream [20]. This probe certainly disturb the flow, close to the point of measurement, the flow. For steady flow that is uniform though, the stagnation occur quite rapidly in the areas close to the nose of the probe as frictional and heat transfer effects can be ignored. Any shape or size of the tube can measure the stagnation pressure correctly as long as its axis is aligned with the flow direction. However, in a situation where the pressure probe is in a stagnation-pressure field that is quite steep, for example, inside the boundary layer, the flow streamlines are then deflected towards the region of lower velocities. This type of deflection causes the pressure probe to indicate a higher stagnation pressure compared to the probe centre location [20].

When the probe axis is not parallel to the direction of flow, measurement error occurs. The shape of the probe nose determines the amount of error. Cylindrical type probes have little tolerance to misalignment. Kiel type probes can withstand up to 45-degree flow angle variations. A Pitot probe that is deeply bevelled can remain insensitive over a 25-degree angle to within 1% of the dynamic pressure.

### 1.4.3 FLOW DIRECTION MEASUREMENT

In turbomachines, there is a direct relationship between changes in the direction of flow and the work interchange. Therefore, a precise knowledge of the direction of flow is very important. For this purpose, sensitive pressure probes to such flow direction are used. The probes are generally calibrated in determining their orientation effect on the measurement to the flow. The probe calibration is most often performed by the placement of the probe in a known field. In determining the yaw and pitch effects, the test probe is rotated about its own axes. Figures 1.14 and 1.15 defines the angles of the yaw and pitch.

Some common probes that are pressure sensitive include the wedge, the cobra, the cylindrical and the five-hole probes are described. For the design of all of the probes listed, one or two pairs of pressure tapings that are symmetrically constructed are inclined with respect to the stream of flow. 2-D flow direction measurements can be obtained when just one pair of pressure tapings is used. For 3-D measurements, two pairs are used. Figure 1.14 shows a five hole pyramid probe that is truncated.



Figure 1.14: A 5-hole truncated pyramid probe

The flow direction can be determined using two methods. The first method is called the null method. In using this method, an actuator is used in mounting the probe, and the angle of flow is determined by equalising the reading of the pressure acquired on the two

opposite static tapings. In using the second method, the mounting of the probe is in fixed position while measuring the individual static pressures. By the calibration of these probes, the flow direction can be determined. The latter method can only be used when the probe is fixed and cannot be rotated while keeping the probe tip at a fixed spatial location.

The cobra probe is constructed usually using three tubes, facing the flow stream and soldered together side-by-side. It is used in determining only one angle of flow (usually the yaw angle). The tube at the centre is used in measuring the stagnation pressure, with the forward tip of the outside tubes cut off at 45-degree angle. All the tubes of the cobra probe lie in single plane. The cobra probe is used widely for studying flow angle due to their low blockage and simple manufacturing process. In determining the dynamic pressure or inference of the static pressure, the cobra probe should not be used for such purpose because the difference in pressure between the centre hole and either of the two side holes as they comprise of a relatively small fraction of the dynamic head.

Figure 1.15 depicts a wedge probe, which is a rugged, simple 2D or 3D probe consisting of a prismatic, triangular probe. The wedge probe can measure the static pressure, unlike the cobra probe. It can be made with various angles, with  $8^\circ$  and  $30^\circ$  being the most popular. The useful operating upper limit range for Mach numbers is a function of flow pitch and yaw angle for airflow. These values are lower for probes having increased included angles. Wedges that are narrower are however less sensitive to the angle of flow and have higher static pressure measurement accuracy.

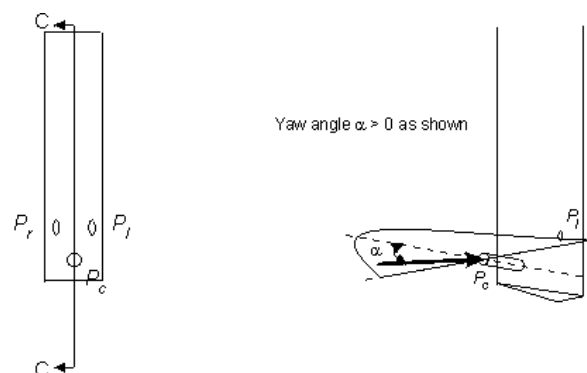


Figure 1.15: Three-hole Wedge Probe for pitch and yaw angle measurement

Pressure probes with five holes are developed using three-hole cobra and two-hole Conrad probes. They measure flow yaw and pitch angles, the total and static pressure. Due to this measurements, sufficient data can be provided to specify fully, the pressure and velocity fields with a known fluid density. Only very few flow fields in turbomachinery are not 3-dimensional. Figure 1.16 and 1.17 shows a fivehole truncated cone and pyramid probe respectively.

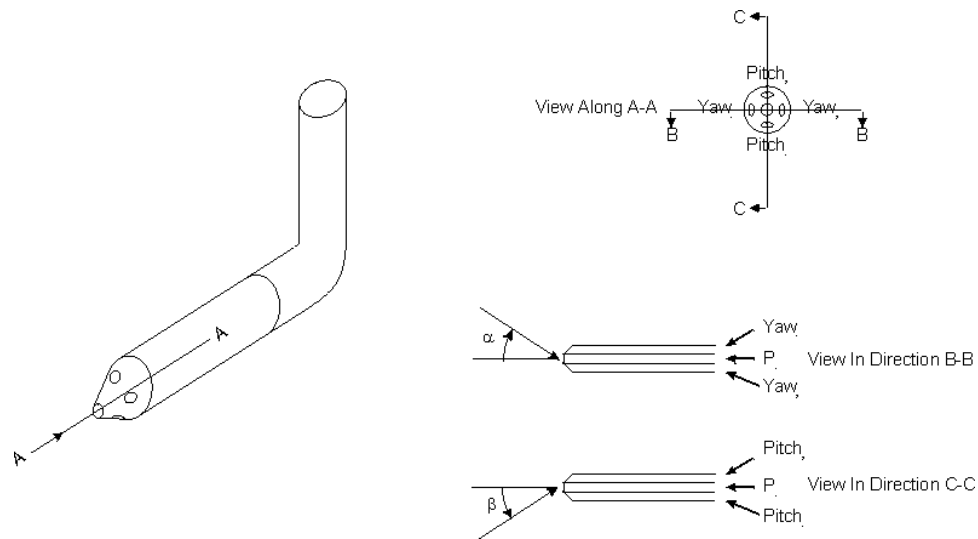


Figure 1.16: Five-hole truncated cone probe

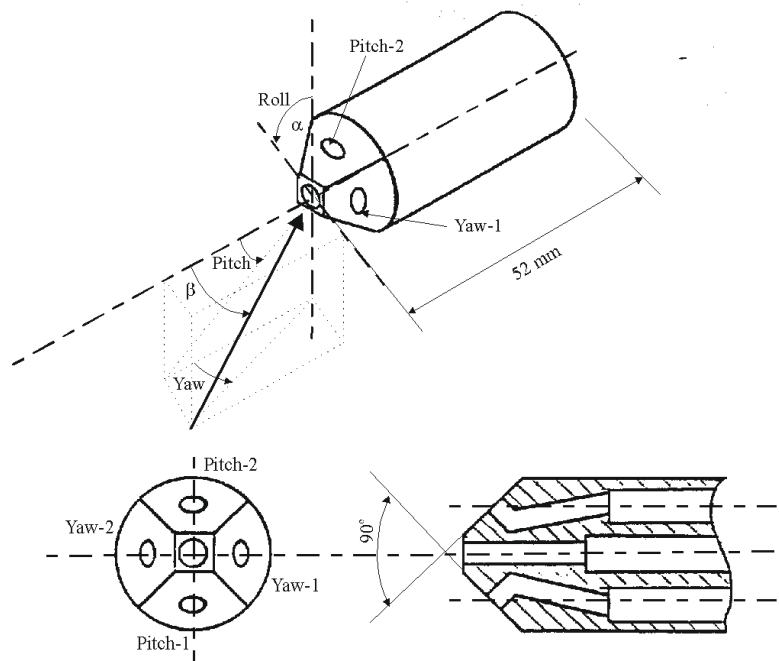


Figure 1.17: Five-hole truncated pyramid probe

Figures 1.16 and 1.17 shows geometries for a typical fivehole pressure probe. Normally, the probe nose included angle varies between 60 and 120 degrees. When the included angle are higher, it becomes more sensitive to changes in the angle of flow and less sensitive to dynamic pressure measurements. Ideally, a 90° angle can provide a more reasonable compromise.

Ideally, it only takes four-hole pressure measurements in determining the total and static pressures, and both flow angles (yaw and pitch). Figure 1.18 shows a four-hole wedge probe that can measure both pressures and flow angles.

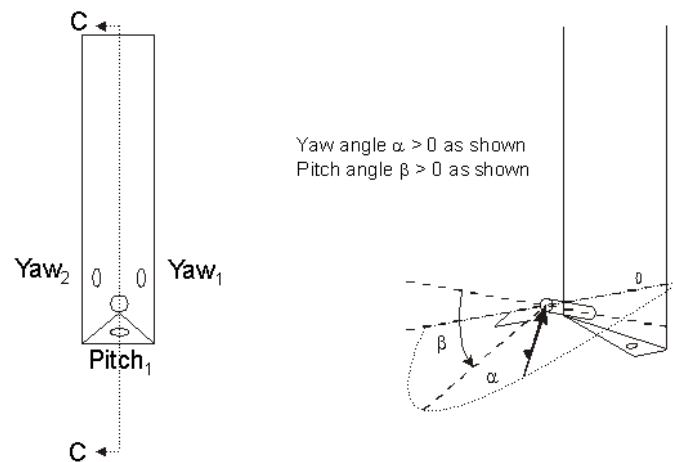


Figure 1.18: Four-hole wedge probe for pitch and yaw angles measurement

## 1.5 CONDITION MONITORING

Nowadays, mechanical industrial machineries play key roles in designing a more complex system in delivering a better functionality and flexibility. This progress, together with the need for increased life-cycle of the equipment, improved quality of production, greater need for safety in human and adversely reducing their impacts on the environment, have all attributed for the increasing need for new techniques used in their maintenance. Maintenance that are well planned when using on-line testing can be a very inexpensive measure when compared to either waiting for the total breakdown of the equipment before addressing the problem or the machines routinely taken out of production irrespective of the actual machine condition [21]. Modern techniques for machine condition monitoring makes use of technologies in evaluating the health of the machine and predicting how likely the machine would fail and therefore, maximising the

profitability of the machine [21]. Predictive monitoring, for example, is an effective technique for machine maintenance that is based on monitoring closely, certain actual condition of the machines' physical characteristics.

### 1.5.1 CONVENTIONAL TECHNIQUES FOR CONDITION MONITORING

In 2002, between March and May, a survey conducted by the Plant Maintenance Resource Centre on non-destructive testing (NDT) and CM technologies showed that the method commonly used is the human senses, with vibration and lubricating oil analysis [21] following closely. Figure 1.19 shows a pie chart, illustrating how often, some of the techniques for CM techniques are used in researches as referenced in literature [21]. Some of these CM techniques will be further explained in details in the next section [21, 22].

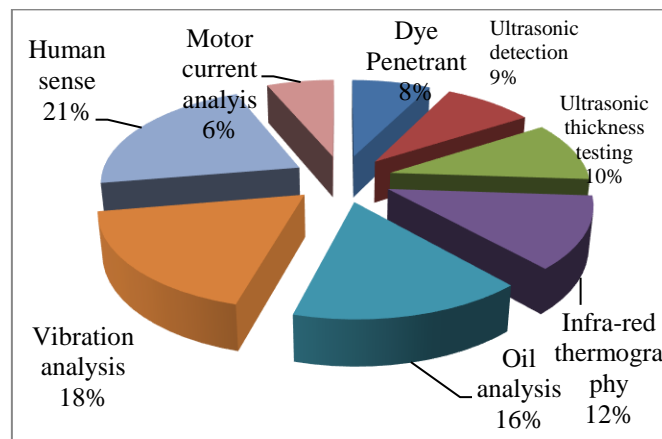


Figure 1.19: General usage of various monitoring techniques [21]

#### 1.5.1.1 TREND MONITORING

Technique for monitoring trend is based on the repeated metrics measurement including pressure, temperature, electric current, torque, noise, etc., plotted in real time. If such plots fall within an operating thresholds already predefined, the equipment/machine is said to be in a healthy state [23]. Otherwise, any readings change can be compared against a set of reference/initial parameters in identifying changes in the machine condition and by so doing, detecting any abnormalities in the machine with figure 1.20 depicting an example of this technique. If as a result, the readings goes beyond the limits already pre-specified, corrective measures would then need to be taken [24, 25].

Figure 1.19 shows a parameter variation throughout the entire life cycle of a particular machine [26]. Once any machine enters their supposed 'final life' state, they become, at any time, significantly prone to faults and failure. As a result, maintenance structures are put in place in extending the working life of the machine, which would require accurate gathering of data [21, 23].

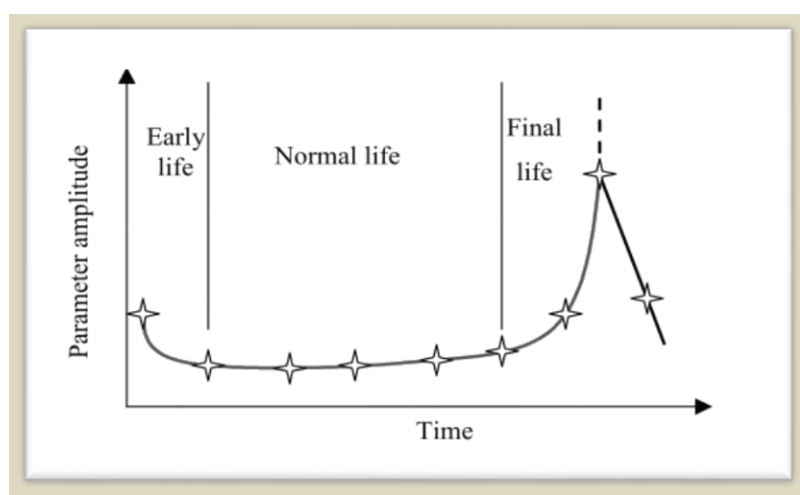


Figure 1.20: Trend Monitoring Record [26]

### 1.5.1.2 THERMAL CM

This can also be referred to as thermography. It is a well-known technique for CM where temperatures around various parts of the machine, using infra-red cameras, in identifying thermal patterns that occurs on the machine are recorded [25, 27]. This type of technique can increase the prediction of the machines component failure before causing injury to personnel, or worse, operation breakdown. This technique uses thermal signature from the machine to indicates whether the machine is healthy as any thermal deviation can be considered as a likelihood of fault occurring [21]. This monitoring technique can be used to locate faulty areas rather than finding what caused a particular fault, though the generated excess heat will have to reach the machine's surface before the heat can be detected.

Thermal CM techniques can be used on different machines such as valves, pumps, drives, motors, pulleys, bearing, etc. However, ambient temperature changes must be taken into consideration as they can directly influence the measurement accuracy [28-29].

### 1.5.1.3 VISUAL INSPECTION CM

Visual inspection for CM is a powerful, yet simple technique. It is usually supplemented by the human sense including hearing for changes in the noise of the machines, touch for increasing vibration levels and changes in temperatures of the machine surface, and sometimes smell in cases of burning as a result of electrical faults. Instant evaluation using the human senses can be used to determine the condition of the machine. Also, an experienced or skilled operator can easily detect faults such as cracks, corrosion, subsurface defects and leakage on the machine [30].

Endoscopes, stethoscope or even magnifying glasses can be used in improving this technique further [31]. However, one main drawback of this technique is the involvement of the human bias and also the dependence of the experience and skills level of the operator which can have an influence that directly affects the final conclusion, which can vary from person to person, resulting in varying diagnoses [31]. Accurate evaluation of impending failures can be done using the human senses.

### 1.5.1.4 CORROSION MONITORING

One problem that faces most mechanical systems, especially the control valve is corrosion. It results when a component of the system is exposed to an environment that is corrosive, leading to the machine's infrastructure failure [32, 33]. One common tool for corrosion CM is the weight loss analysis, where a component is removed from the system, and their weight checked before and after all the corroded parts have been taken out. If any, the loss in weight can then be considered as an average rate of corrosion indication [32, 33].

This type of method allows for earlier detection of damages caused by corrosion and help in locating fault so that corrective measures can be taken on time in order for the extension of the lifespan of the machine, preventing any extra cost and machine breakdown. Furthermore, any corrosion that occur internally can possibly cause contamination to other components, while external corrosion such as leaks can pollute the environment, which can be hazardous and cause safety issues [32, 33]. It is worth mentioning that this CM technique demands for planned equipment shutdowns, thereby incurring costs by replacing materials and production loss.

### 1.5.1.5 WEAR DEBRIS AND OIL ANALYSIS MONITORING

Oil and Water debris analysis is a commonly used technique for CM where the condition of the machine is assessed by investigating if any wear element can be found in a sample of the lubricant [34]. The quality of the lubricant can be found using this method based on the three lubrication oil main components; the lubricant additives, the base oil and contaminants. The former is used as a measure for continuous wear rate, reflecting on the performance of the machine. Early detection about the machines health can be done using the oil CM method, even earlier than using the vibration CM method. However, one disadvantage using this method is that it can be insensitive to the components physical size that has been exposed to an unusual wear [23, 32].

### 1.5.1.6 ACOUSTIC SOUND CM (AS)

Machine CM using acoustic-based methods have been applied widely for many years in mechanical systems maintenance. It is an established fact that machines generates noise and vibrations while in operation. Special microphones are used in picking up such acoustic signals and are analysed using the correct techniques for processing the signal in providing information on the machines health. Such methods are non-invasive and the microphones used are inexpensive and can be easily mounted. This type of technique is usually considered an ideal CM choice for most mechanical systems including the control valve [35]. This technique can directly provide indication of machines source of noise [36]. However, one major limitation using this method is contamination from background noise, especially those noise emanating from outside sources of the mechanical system [35].

Over the last few decades, CM of machines using acoustic technique has been a research subject quite popular amongst researchers. One particular research using this method was developed by Li *et al.* [37] for diesel engines in detecting injection timing, misfiring and tappet clicks faults. In the technique, signal-processing techniques, including discrete wavelet transform (DWT), have been used.

Airborne noises, during propagation are pressure waves propagated in sequence over a compressible medium, such as air. The sound waves, within the medium, can either refract or reflect by the use of other bodies, which can disrupts or tapering the incoming

sound signals. If the sources of the sound are located in a space that is enclosed, any boundary reflection can disrupt the sound source characteristics, making the diagnostics of fault using this technique quite difficult.

With several research work carried out using this method, acoustic signals contamination by noise from the background has caused problems that are still unresolved. Due to this reason, addressing the influence of the acoustic environment of the machines when using acoustic measurements for the purpose of CM is vital. Above all, investigation of the detection of fault characteristics when the level of noise from the machine being monitored is lower than or equal to the background noise becomes paramount.

#### **1.5.1.7 ACOUSTIC EMISSION CM (AE)**

Elastic waves transiently generated from the release of swift strain energy caused by damage or deformation on or within a material surface is called acoustic emission. The propagation of this energy is done through a fluid or structure-borne (gas or liquid) waves [38]. In most machines, acoustic emission can emanate from friction, turbulence, cavitation, material losses, leakage and impacts. RMS, Amplitudes, kurtosis and crest factor are traditionally the most common parameters for measuring AE diagnosis [35]. Due to the miniscule nature of AE technique, its properties and that of broadband signal are similar, making it a holistic tool in detecting incipient faults or damages.

Acoustic emission often has a 100 kHz to 1 MHz frequency range, making their acoustic signatures less possible to be influenced by noises from the background, which is below 1000Hz. Comparing with vibration technique, AE technique for CM of machine offers an advantage to earlier detection of failures or faults because of the sensitivity of the AE technique. However, this type of technique has its disadvantages including overcoming problems in the processing, classification and interpretation of the gathered information during the acquisition of the data. Another disadvantage of this technique for CM is that the sensor would have to be placed very close to the source of AE as the signal attenuates rapidly.

### 1.5.1.8 VIBRATION MONITORING

Every machine generates some form of vibration or another. Many researches have covered this type of technique in developing CM tool for diagnosing early fault and trouble-shooting the faults in mechanical machines, including the control valve. This monitoring technique is commonly considered as a very confident CM techniques, forming the foundation of several other programs for predictive maintenance [39, 40]. It is a general opinion that this technique is one of the most effective means in preventing failure and can be applied online to the monitoring of a wide range of mechanical components [41, 42]. This statement is true as each fault in most machines produces a unique vibration signature at specific frequencies, making it possible to be exactly mapped to faulty conditions of the machine [43]. In a valve for example, the vibration signals carries the distinct fault signatures, especially when cavitation occurs, making their detection easily realised via analysis using different methods for signal processing.

In equipment/machines, the response (measured system signal) can be monitored using vibration techniques. The response from the vibration sensor can then be processed to obtain a more holistic understanding on the health of the machine [23]. In general, accelerometers (vibration sensor) are used in acquiring vibration data having wide-range of operating frequency. The data can then be analysed using different signal processing methods including peak to peak, RMS, crest factor, FFT, peak values, spectral analysis, etc. [27]

The generated vibration signal for machines in general are an accumulation of the signals originating from every components integral to the machine and also the structures to which the vibration sensors are attached. Vibration signal might not only be as a result of the sum of both the non-stationary and non-linear sources as they could be affected also by the medium of transmission. In addition, some defects in machines might not cause substantial change to the vibration signal when compared to the baseline vibration signal, making vibration CM technique not suitable for all monitoring applications [36]. Because of this drawback, it can be said that vibration technique will not always be the solution to problems of CM [36].

In conditioning monitoring systems, processing of the signal involves analysing the data and transforming the retrieved data from the machines being monitored. For this section of this chapter, pertinent techniques used for processing the signal has been discussed in order to provide an improved understanding for data interpretation collected for CM and faults diagnosis. Techniques for signal processing are used to extract useful information from the measured signal and assess accurately, the machine condition being monitored.

Analysis in time domain is a very simple form of signal processing to measure and record, as a function of time, the magnitude of the incoming raw signal. Techniques trend analysis and visual inspections are all based on this type of analysis. In addition, analysis carried out in time domain shows the current against the previous measurement values and a predetermined threshold comparison. Amplitude of the signal changes with time, contains vital information that can help determine how the machine or equipment behave on certain conditions. The signal variation can be converted from time to frequency domain as spectrum analysis in frequency domain is becoming more useful and a common CM technique for signal processing [33]. For machinery CM, several other conditions can lead to changes in the measured signal including changes in the environment, not just faults. However, spectral analysis can be effective, particularly when applied to steady state periodic signals in situations where there is gradual development of the fault [32].

A number of researchers have thus, developed numerous techniques in carrying out non-stationary signal analysis. These techniques can be able to provide time-frequency representations for non-stationary signals, and used in faults related features extraction, which can be present in the monitored machines.

Current available methods used in signal processing are analysed based on the three major techniques, which include time-frequency, time and frequency domain.

## **1.5.2 SIGNAL ANALYSIS TECHNIQUES**

### **1.5.2.1 TIME DOMAIN ANALYSIS**

This analysis can be achieved by plotting the signal amplitude with regards to time. Statistical features including kurtosis, RMS, peak, crest factor, SD (standard deviation),

peak-to-peak, skewness, etc. of the amplitude can be used to describe the characteristics of the signal.

A widely used data collection technique is the TSA (time synchronous average) [30]. The purpose of using TSA is to use the raw signal averages to either remove or reduce non-synchronous signal and all other noise sources in order to enhance the components of the interested signal.

One major advantage of analysing signal in time-domain is the provision of a measure and information of the machine condition when faults occurs based on changes in the baseline in any statistical parameters feature. Time domain analysis can be easy in implementing because of the simplicity to represent the different statistical parameters in a single value.

As fault increases, so do the condition index, indicating the deterioration of the condition of the control valve. Below are some details of the different statistical parameters.

#### 1.5.2.1.1 Root Mean Square (RMS)

Root mean square is a second central moment of the signal SD that is normalized. The RMS of a vibration signal is a measure of the overall energy, taking into account, the signal time history. The amplitude value of the RMS for any given signal can be expressed as [34]:

$$RMS = \sqrt{\frac{1}{N} \sum_{i=1}^N x_i^2} \dots \dots \dots 1.17$$

Where N denotes the number of signal samples, for a discrete distribution  $x_1 \dots \dots \dots x_N$ .

Root mean square is the most common and simplest measure used in vibration/acoustic condition monitoring in measuring the signal overall intensity over a wide-band, and in also providing an averaging effect that helps in reducing the effect of incidental impulses.

#### 1.5.2.1.2 The Crest Factor (CF)

The ratio of the crest value of the signal crest (maximum positive peak) to the overall RMS measurement is called the Crest factor, which helps detect any changes due to impulsive

vibration force. Ideally, if the control valve develops a distinct fault, it generates an impulsive signal. Further increase in the damage will cause the vibration peak level to also increase. Also, the overall acceleration RMS level will only change a little due to the fact that the impulse signal has a very short span [38]. Analysis of the crest factor is normally used on the raw signal.

$$CF = \frac{\text{Peak Value}}{RMS} = \frac{\sup|x(n)|}{\sqrt{\frac{1}{N} \sum_{i=1}^N x_i^2}} \dots\dots\dots 1.18$$

where,  $\sup|x(n)|$  denotes the signal maximum absolute value.

### 1.5.2.1.3 Kurtosis

Kurtosis is the statistical calculation of the “peakedness” of any signal which measures how sharp the signal and the peaks amplitude is. A random noise that follows a Gaussian distribution has a kurtosis value of 3. The kurtosis values can be more than 3, like in control valves, where the peaks amplitude spectrum protudes more than the Gaussian distribution. Higher kurtosis values tends to mean that the peaks are extremely infrequent rather than a frequently sized modestly peaks. If the kurtosis value is lesser than 3.0, then the spectrum becomes flatter compared to the Gaussian.

Mathematically, the signal normalized fourth moment is called kurtosis [35]. Because of its fourth power, the signal peakedness becomes easily detected by kurtosis.

$$Kurtosis = \frac{1}{N} \sum_{i=1}^N \left[ \frac{(x_i - \bar{x})^4}{\sigma^4} \right] = \frac{1}{N} \sum_{i=1}^N \left[ \frac{(x_i - \bar{x})}{\sigma} \right]^4 \dots\dots\dots 1.19$$

Where  $\sigma$  is the standard deviation and  $\bar{x}$  is the mean.

As the onset of fault begins to sets in, kurtosis begins to increase, suggesting that the signal distribution is no longer Gaussian. This is attributed mainly to impulses (high amplitude isolated peaks) generated by faults in the valve or any other mechanical components. However, this feature is of little or no use once the faults goes from being incipient to quite severe. As a result, the peakedness of the signal begins to decrease, causing kurtosis to reduce down to a normal level found in valve with an acceptable condition [35].

### 1.5.2.2 FREQUENCY DOMAIN ANALYSIS

Analysis carried out in frequency domain has been and always will be a dominant and beneficial analysis technique for signals in establishing the signal characteristics and in diagnosing or detecting faults in machines [36, 37]. This technique converts the signal to frequency domain from time domain. The spectral content of the measured signal when compared to analysis in time-domain can be a useful technique to determine the machine condition. Because of the complexity of the signal in time-domain, frequency domain analysis can breakdown the signal into several frequency components. Researchers have shown that when these frequencies are focused more on, it can make it easier and useful to diagnose and detect faults [36] produced over a band of frequencies. The spectrum of the frequency is determined by the occurrence of the signal over a wide number of frequency bands. One common method used for machine CM is the FFT, transforming signals from time to frequency domain.

### 1.6 RESEARCH MOTIVATION

Inside the control valve, fluid flow properties in water application and production process or even in the oil and gas industry have been difficult to measure due to the complexities associated to this regard. It is therefore imperative, for these flow parameters to be measured and stored for analysis as the flow progresses.

Within these industries (oil and gas, water, etc.), it is believed that both multi and single-phase flow measurements, when readily obtained, can lead to higher efficiencies in monitoring the production, flow quality assurance and control, and production costs effectiveness. Improving the performance of mechanical devices such as the control valve can be difficult to achieve due to several reasons. Some of such reasons includes the impacts caused by the turbulent flow inside the valve, unsteady behaviour of the flow and because of cavitation.

The latter phenomenon of cavitation especially, causes many problems in the valve including valve performance deterioration, erosion inside the valve material and increase in the vibration and noise level. Because of such problems that occurs inside the control valve, this study has become very necessary to help understand the valve behaviour when they occur. Investigations into flow behaviour inside the control valve are necessary in order to carryout scheduled preventative maintenance plan that can lead to increase in

the control valve operational span. Analysing the behaviour of the control can help detect abnormalities that can help improve the maintenance and enhance the valve reliability. Early detection of such anomalies can enhance the valves' life expectancy by the adoption of different preventative actions that if conducted properly, can decrease from about 12-16 years to nearly 2 years [39]. Therefore, continuous condition monitoring needs to be conducted to increase the control valve life and by so doing, decrease the maintenance cost. Where there is a fault or damage to the control valve, many problems can occur. Such problems can include leakage, high noise and vibration level, damage to some parts of the valve that can lead to the entire system breakdown and in turn, lead to significant loss of financial value and time. Such analysis of this behaviour will be analysed and discussed in this research study.

There are various invasive and non-invasive devices/sensors and measurement techniques that exist in measuring these flow properties for both single and multiphase flow systems as the system operating conditions changes. Applying a holistic integrated measurement flow system, a more precise and clearer understanding of the fluid dynamics of the flow system inside the control valve can be obtained using the proposed experimental techniques.

- Five hole pressure probe measuring technique; due to the complex geometry of the control valve, resulting to limited space making it very difficult in inserting measuring devices. The multi hole probe is robust and can sustain harsh flow conditions such as in opaque fluid and it is easier to use and less expensive. Another reason is that this type of measuring device can obtain the 3D flow measurement that other flow measuring devices cannot give.
- Vibration analysis technique: The method is very effective as they can indicate the condition of the control valve, fault behaviour and diagnosis. The vibration analysis is fundamental in any predictive maintenance program as they are widely used is fault monitoring and early detection in the control valve, especially the ones caused by cavitation/flashing. Furthermore, the vibration signals are very not complex in their analysis, as codes are not difficult to write are readily available.
- Acoustic analysis technique: Acoustic monitoring give a more global analysis on the condition of the control valve. This technique has been chosen because when

faults occur in a control valve, the noise level changes and the variation in this changes can be analysed to detecting or monitoring such faults, hence, condition monitoring.

This research would involve the evaluation of all of these three techniques and study how information and flow parameters obtained from these techniques relates to one another in order for a broader and holistic flow diagnostics of the control valve to be achieved in the detection of any form of flow anomalies.

### 1.7 RESEARCH AIM

The specific aims of this research have been formulated and described in this section whereas the research objectives from each aim will be discussed further after an extensive literature review have been conducted in the next chapter. Based on the research study motivation, the aims for this research have been combined into one:

*“The Investigation and Establishment of flow characteristics and detection of fault on the control valve under various flow and operating conditions using intrusive and non-intrusive techniques”.*

### 1.9 THESIS ORGANISATION

**Chapter 1:** This chapter discusses the introductory review and background principles of control valves and the important role it plays in our environment. It provides many different applications where they are commonly used and the different problems they are likely to face. This chapter also lists and explains the parts of the control valve, the types and the phenomenon of cavitation that greatly cause damages to the valves. The different measurement and monitoring techniques used for analysing the flow behaviour inside the valve have also been discussed.

**Chapter 2:** This chapter discusses elaborate reviews of previous works done in control valve measurement and flow that have been developed by several researchers using various techniques. The chapter provides reviews done on several previous works by many different researchers on MHP probe design, calibration and application techniques, other methods of using invasive and non-invasive methods of flow diagnostics on both pipes and control valves, various numeric and experimental analysis on detecting faults

on valves and condition monitoring investigation for control valves. In order for the knowledge gaps to be bridged regarding this research study, the research scope for this thesis have been determined, whilst the research objectives have been formulated.

**Chapter 3:** This chapter describes the design of the experimental set up and the design made on the control valve, such as the drilling of the valve and pipes where the fivehole probe is inserted for local flow measurements, in order to accurately measure the flow. This chapter also presents the description of the sensors and instruments used, the data acquisition system, as well as the system measurements procedures used in monitoring and diagnosing the behaviour of the control valve used for this setup. Also, the calibration method for all the sensors and devices which include the pressure sensors, the five-hole pressure probe, the acoustic and vibration sensors have all been discussed and best practices for applying such instrument on the rig test facility have all been presented. Finally, CFD techniques used in mimicking the flow field, as close as possible to the experimental rig, in validating some of the results obtained experimentally from the fivehole probe have all been presented. Due to this reason, a suitable set of boundary conditions and solver settings have been presented only for the single-phase flow condition.

**Chapter 4:** This chapter discusses in details, the analysis of the results obtained during experimentation of the five-hole pressure probe regarding the behaviour of the control valve. Both qualitative and quantitative analyses have been conducted to understand the flow behavioural structure inside the control valve under single phase and multiphase conditions. The investigation focuses also on different probe lengths at the inlet and outlet across the valve and at several different height positions. Semi empirical correlation for the different length and height of the probe have been developed.

**Chapter 5:** This chapter discusses all measurements and analysis of the vibration signals that have been obtained experimentally from the control valve. It further provides analysis on different statistical parameters in understanding the behaviour of the flow inside the valve both for single and multiphase conditions in time domain. The statistical features considered here are Peak to peak, RMS, standard deviation, variance and kurtosis values. These vibrations signals for the different flow conditions are then

converted, using FFT, into frequency domain in order for more information regarding the flow behaviour to be obtained within the control valve.

**Chapter 6:** This chapter discusses the Acoustic techniques that have been used experimentally in diagnosing the behaviour of the fluid within the control valve. This chapter provides the measurements and the analysis of the acoustic signals that were obtained from the control valve at different operating and flow conditions, which is similar to the technique used in chapter 5. Furthermore, it discusses the evaluation of the method being utilised in diagnosing the fluid behaviour of the control valve.

**Chapter 7:** This chapter discusses conclusion of the results obtained during the course of this research thesis and summarises the knowledge contribution of the research. It also provides recommendation for future researches in this chosen field.

## 1.10 SUMMARY

This chapter gives an explanation of the motivation for carrying out this specific research and the reason for concentrating on these specific areas of study. Information has been presented about control valves and the need for their use and engineering demand, in addition to the functions of each part of the valve and the different types of valve there are. Also, a summary explanation of the causes of failures of the control valves and the effects they have on the entire system. Furthermore, a brief review of some traditional techniques used for condition monitoring of mechanical systems have been presented. Finally, the research aims and motivation are presented and the organisation of the thesis summarised.

## CHAPTER TWO

### 2.0 LITERATURE REVIEW FOR PRESSURE PROBES AND VIBO-ACOUSTIC BASED FLOW DIAGNOSTICS TECHNIQUES

---

*In this chapter, literature review of diagnostic techniques used for signal processing( Pressure, Vibration and Acoustics) in monitoring the behaviour and condition of control valves has been presented. Some techniques relevant to this research would be briefly discussed in assisting with the understanding of the results that would be presented in subsequent chapters of this research thesis.*

## 2.1 INTRODUCTION

A look at various literatures covering the aspect of this research would be discussed. The major part of this session is on the different type of sensors, especially on the pressure probes (5-hole) and various vibro-acoustic techniques that has been employed to determine the behaviour of the control valve at different operating conditions, which will be a fundamental part of this research. A major part in this chapter of this thesis is to see how these different types of signal behave when faults have been detected. A broad look at this processes and techniques would be discussed in this section.

## 2.2 FLOW DIAGNOSIS AND ANALYSIS INSIDE A CONTROL VALVE

In this section, other type of tools used in fluid diagnosis will be discussed. Such tools include CFD (computational fluid dynamics) and other type of intrusive and non-intrusive techniques. The main aim of using all of these tools is to detect a fault, be it cavitation, flashing, erosion, corrosion or some electrical or mechanical faults.

J Ferrari et al [44] carried out side load measurements on a 2" globe valve by making the stem heavily instrumented in order to allow, in every direction, force measurements. They ran their experiments using cavitation conditions, different VOPs and flow rates. In their experimental setup, they modified the stem to allow for deflection that can occur during their experiment in order for these deflections to be measured accurately by the gauges. They fixed 12 strain gauges to the stem at several location for the resultant force and moment to be measured accurately. Experiments were conducted at 2mm, 3mm, 4mm, 6mm and 16mm when it is fully open. Conditions were stabilized for 30 seconds and data measured at 200Hz. Figure 2.1 depicts the model of the globe valve used and the sketch of both the stem and the disc used in their experiment. Figure 2.2 depicts the result obtained from their experiment. Their results showed that the transverse force, which is normal to the stem, could reach the order of axial force making it impossible to be ignored. It was also observed that this force was weakly dependent on the levels of cavitation. They concluded that at 2mm for figure 2.2(a), the curves stay linear from pressure difference ( $\Delta P$ ) viewpoint, the influence due to cavitation was not significantly observed. From the view point of  $Q^2$ , (square of the flow rate) as seen if figure 2.2 (b), as the flow rate is impeded by the flow choke, the curves from the downstream pressure are seen to shift towards the left as cavitation effect is seen due to the increase in the transverse force.

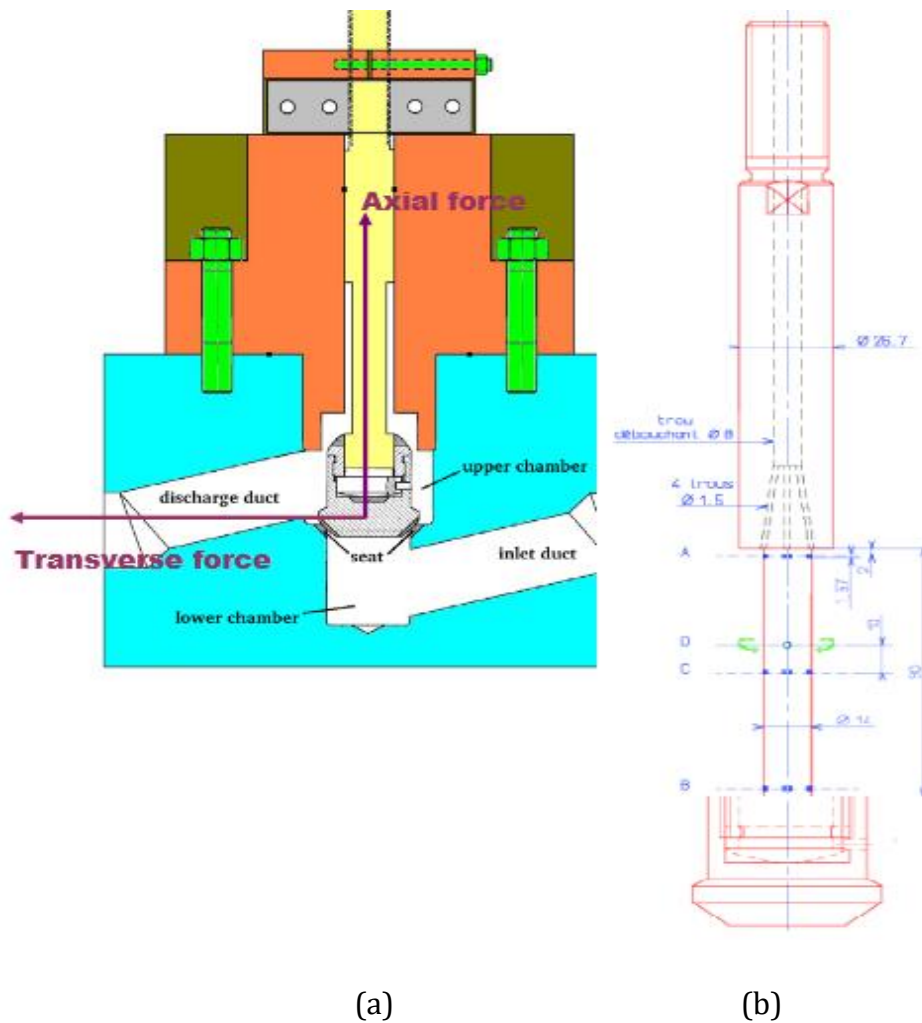


Figure 2.1: (a) the globe valve model (b) stem and the disk sketch

In other words, before the pressure drop created by the cavitation is overcome and the flow rate is sustained, the upstream pressure has to be increased and by so doing, transverse forces increase. For 16mm in figure 2.2 (e), cavitation increases with the increase in  $\Delta P$  from the viewpoint of  $\Delta P$ . From the viewpoint of  $Q^2$  as seen in figure 2.2 (f), cavitation has no effect on the transverse force as the additional pressure drop due to cavitation reduces the stem pressure drop and thus, the transverse force. They further concluded that cavitation does not cause any big change in the transverse force and whichever point of view ( $Q^2$  or  $\Delta P$ ) as the influence depends on VOP (valve opening position). They also provided numerical results for the hydraulic surface for both transverse and axial forces, which they compared with their experimental data. Their numerical and experimental results show good agreement, except for the 6mm VOP where CFD results show a 30% less agreement when compared with experiment.

However, determining how the local flow parameters of the valve changes at different sections from inlet to outlet under different flow conditions has not been considered in their research.

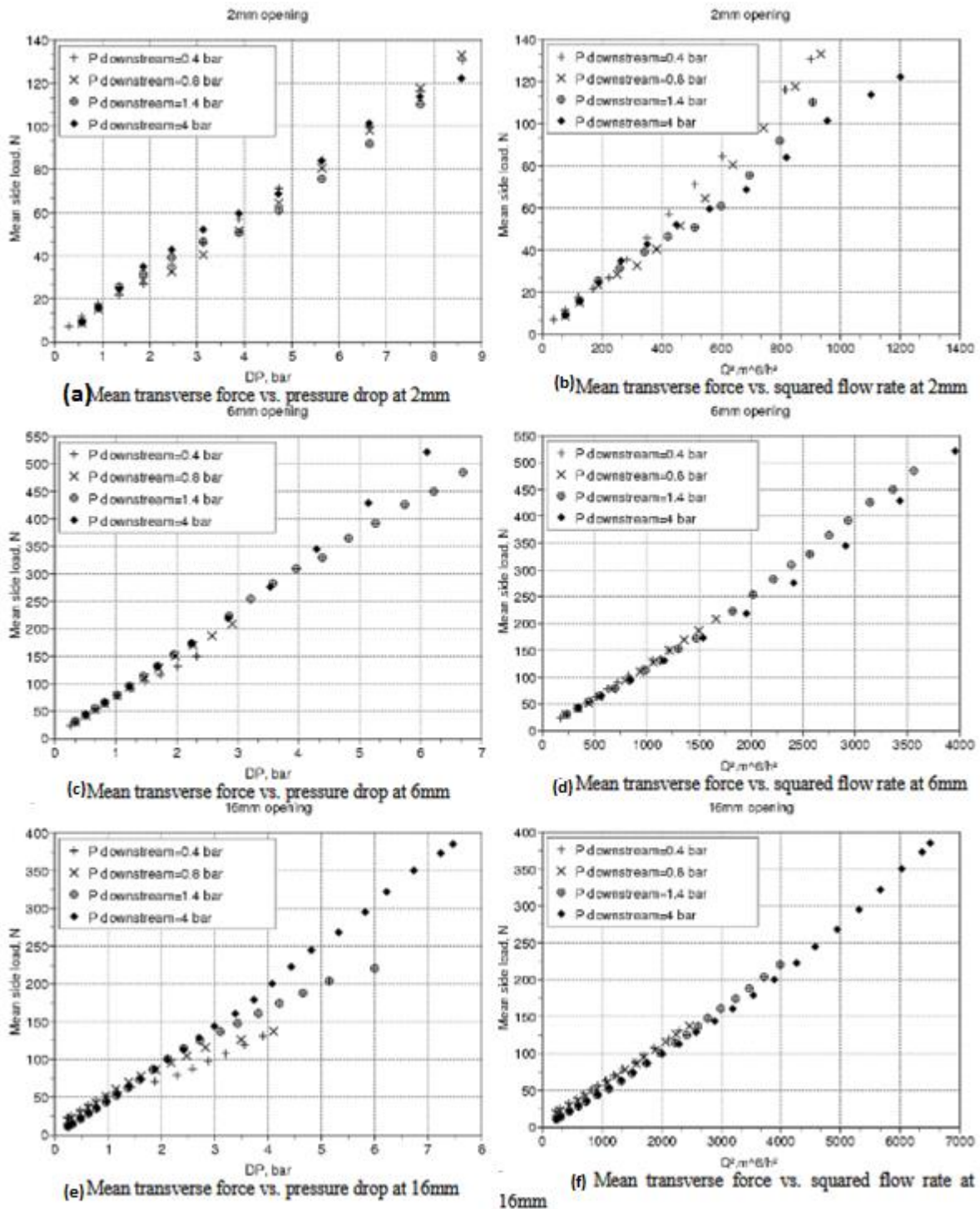


Figure 2.2: Mean side load against mean transvers force pressure drop for the different VOPs

A. Taimoor et al [45] carried out detailed CFD based investigations on a globe valve having a trim with a complex geometry. The capacity results using the CFD have been carried out and then compared with the data from experimental analysis. They revealed that there is decrease in the water pressure as it exits a row of the trim due to its surface area reduction. Furthermore, there was also an increase in the flow velocity between the rows of the cylinder [45, 46].

Capacity results also suggested that Trim Cv values were dependent on only the position of the valve opening, and independent on the differential pressure across the valve. Meaning that the trim Cv decreases as the valve opening position also decreases, as a function of the reduced area where the flow occur.

They also developed a novel predictor expression for the capacity of the trim that can be used in such process in the trim design.

In their result, the control valve was tested to evaluate the trim capacity. They used numerical modelling to justify their mesh sizing that predicted the valve trim capacity. They also used results from CFD in validating their experimental test results. The results in table 2.1 shows clearly regarding the good agreement between the CFD and experimental results of the found trim capacity.

Table 2.1 Their CFD result validation

Valve opening position (VOP) %	$\Delta P$ (kPa)	Difference between Experimental and CFD based $Cv_{Trim}$ (%)
100	341	5.06
60	370	0.88
10	375	0.33

To obtain this result, they used K- $\epsilon$  turbulence model, which showed on average, a 7% inaccuracy in predicting the valve capacity as compared SST K $\omega$  model [45].

Also in their capacity testing of the trim result, they showed the different variation in the in the flow velocity and the differential pressure within the trim disk and across the whole valve with just 10% opening. Figure 2.3 shows the flow variation from their experiment within the trim for both the static pressure and flow velocity.

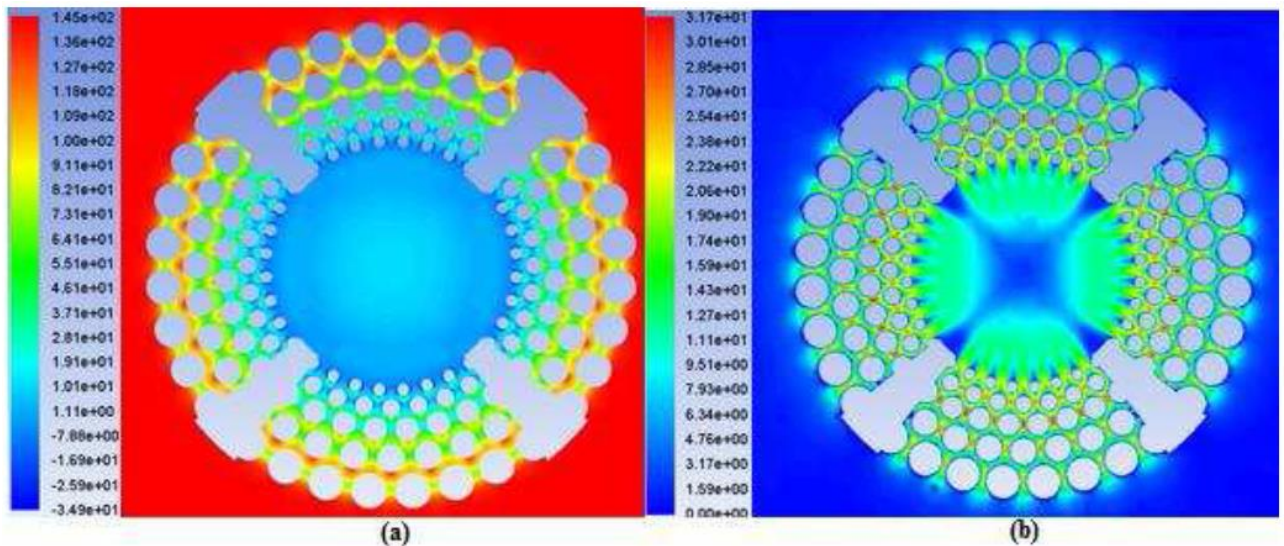


Figure 2.3: Variations of flow variables within the trim at 1,000kPa differential pressure and 10% valve opening position (a) Static Pressure (b) Flow Velocity [15]

In figure 2.3(a), pressure drops within the trim can be seen from row to row. As the water flows between two columns, pressure drops because there is reduction in the area. As water flows from one row and enters the other, pressure then again increases due to an area increase that is available for the water to flow. Therefore, creating pressure drops as the flow continue within the valve trim, instead of just a single pressure drop across the valve. In Figure 2.3(b), there is increase in the flow velocity between the columns within a row, where there is lesser area available for the flow to occur which then results in the formation of jets. As the fluid (water) exits one row and entering another, and as the area from one row to the other increases, velocity reduces so as for continuity equation to be satisfied.

While they also quantified the trim capacity, they showed in figure 2.4, the capacity testing result of the trim for different pressures across the valve.

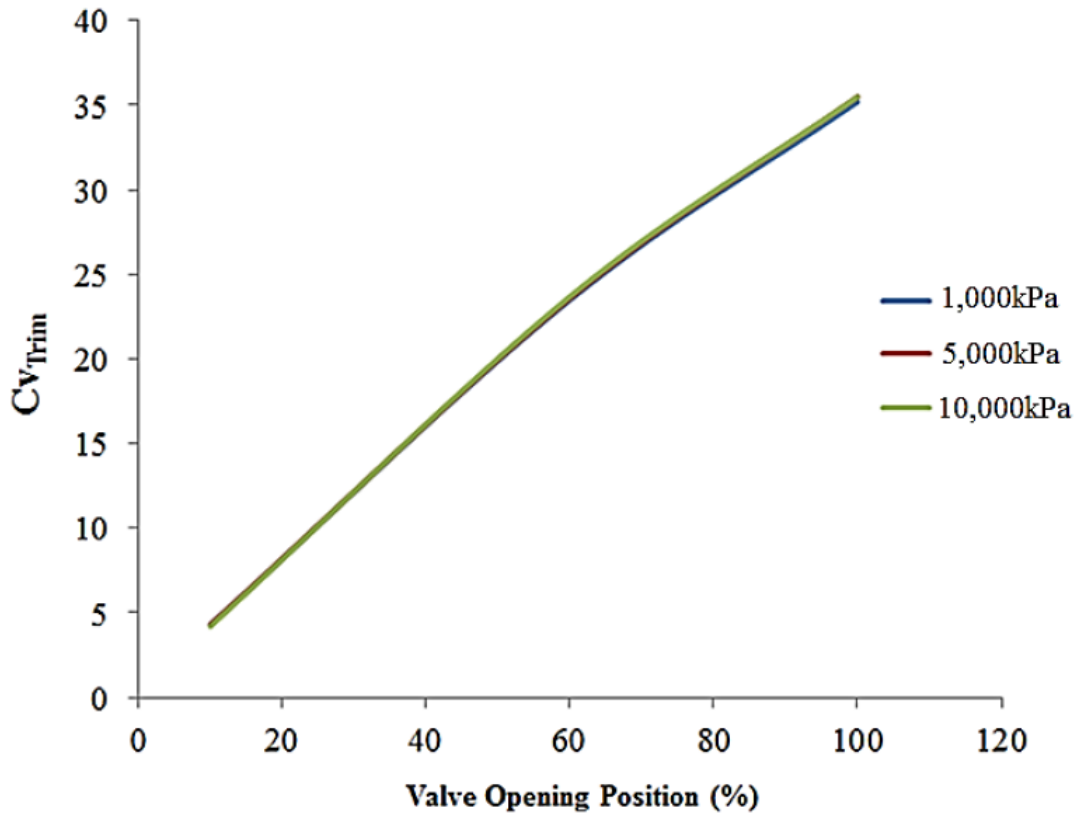


Figure 2.4: Variations in Cv Trim of the trim at various valve opening positions and differential pressures [45]

Two important features were derived from this graph.

- As there is decrease in the valve opening position, there is also decrease in the Cv of the trim vice versa. This is because smaller area becomes available for flow to occur, resulting in the decrease in the capacity of the valve.
- The trim Cv becomes almost the same for different flow condition (for differential pressure) for the same position of the valve opening.

In Taimoor et al [45] study, simulation was carried out in all of the disk's four flow paths. Similar simulation would be done on just a single flow path to see if similar result can be obtained. The gap here is that CFD has been used in determining the trim Cv as experimental procedure using intrusive sensors, when done accurately can give a better result. In addition, determining how the local flow parameters of the valve changes at different sections from inlet to outlet under different flow conditions has not been considered.

W. S. Qu et al [47] showed in their description of their valve model and CFD method that the fluid flows into the body of the valve through a 0.2m pipe as can be seen from figure

2.5(a) which shows the valve schematic they used. The fluid is then forced to jet towards the centre by the trim (perforated cylinder structure) as seen in figure 2.5 (b).

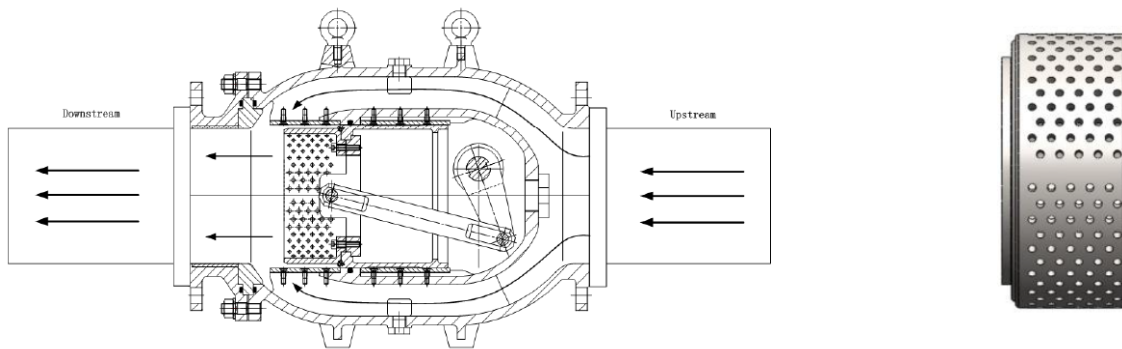


Figure 2.5(a): Valve schematic [47]

Figure 2.5(b): the cage structure model [47]

In their results, they simulated cavitation for both steady and unsteady flow for the valve. They obtained the pressure drop ( $\Delta P$ ), and compared with that of experimental data and then analysed the flow pattern for five different valve opening conditions. They used the simulation from steady flow result to predict cavitation development in an unsteady flow.

For their experimental validation, they developed a hydraulic test system. Figure 2.6 shows the setup of their test rig.

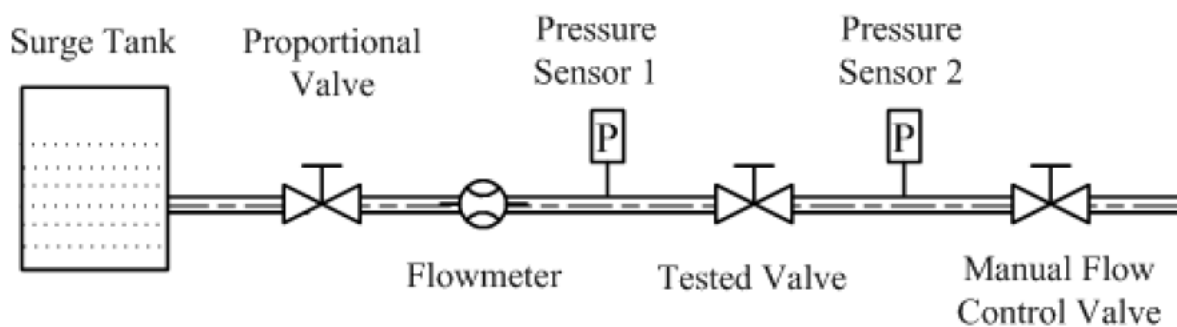


Figure 2.6; test system setup [47]

Figure 2.7 shows the resistance coefficient result between the numerical and experimental methods. The figure showed how well both results agree, with the exception at 20% opening where errors might have occurred due to the flow pattern, which was complex at a small flow rate.

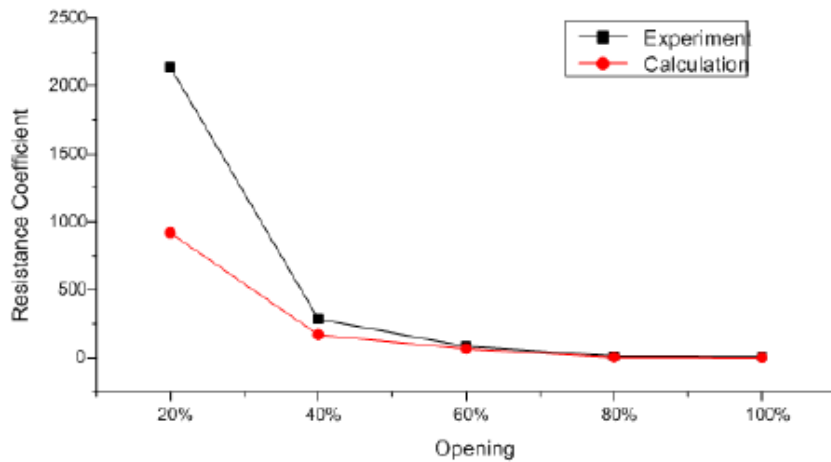


Figure 2.7: Resistance coefficient result [47]

Control valves often at least, have one reduced flow area region somewhere in-between valve body inlet and outlet. One distinctive reduced flow area region is near or at the orifice, which is defined by the proximate of the valve trim and/or valve seat. Hence, fluid flow through the control valve commonly experiences some sort of pressure drop or loss in pressure as flow travels through the reduced orifice area.

However, the use of intrusive sensors were not used in obtaining their experimental data. Fisher [48] explained that in a system, according to some aspects, an acoustic emitting sensor is used in detecting cavitation presence inside and/or nearby a flow control device, such as the control valve, by sensing its acoustic signals. This acoustic sensor is an electronic sensor arranged in such a way that it senses acoustic energy that is traveling through the solid material. In some different arrangements, the electronic sensor would include a capacitive acoustic emission sensor, a piezoceramic or other piezoelectric acoustic emission sensor, a laser interferometer acoustic emission sensor, and/or other similar types of electronic acoustic emission sensors. This sensor is preferably placed on a control valve outer surface. A processor also operates together with the acoustic emission sensor. This processor is designed to receive the acoustic information from the acoustic sensor and process that information in order to identify and/or monitor cavitation occurring in the control valve.

Butterfly valves are commonly used in water and industrial pipeline systems that have large diameter because of its simple, lightweight structure and how rapid its manipulation is. Sometimes in these sorts of valves, cavitation can occur, which will then

result in its usual vibrations, noise and the rapid deterioration of the trim of the valve, leading to further breakdown of operation of the valve. Bo-Suk Y et al [17] agreed that cavitation monitoring is of important economic interest, which is of high importance to the industry. They detected cavitation occurring in butterfly valves using support vector machine using vibration signals in which they proposed a conditioning monitoring scheme, which would detect the cavitation in the butterfly valve using an evaluation of statistical feature and an SVM (support vector machine). They extracted vibration signal stationary features from the statistical moment. These reorganized vector coupled with the SVM can then be used to distinguish between the untested and untrained data class. This method of classification validity is examined by the various signals that have been acquired from the butterfly valves with the success rate of the classification compared with that of the neural network SOFM (self-organizing feature map). They mounted two accelerometer to measure the vibration signal at various valve opening between 20 and 60%, measuring seventy times with five minutes for each condition.

However, Bo-Suk Y et al [17] did not use the comparison for real-time implementation that would lead to the probable development of a condition diagnostic and monitoring automated valve system.

As valve cavitation effect becomes devastating, it becomes very crucial to choose the correct valve where the characteristics of the valve are needed whereby one operating range side depends on incipient cavitation determination. Osterman et al [49] characterized the incipient of cavitation in an axial valve by visualization method, using high-speed camera and by hydrophone sensors. For comparison purpose, the pressure oscillations occurring inside the pipeline was measured concurrently using the hydrophone with the operating pressure effect studied for two different valve openings. For each of the incipient cavitation operating point, their corresponding points were then measured for the cavitation that are developed and the ones that has no cavitation, which is based on a constant-portion of the volumetric flow rate changes relating to the volumetric flow of the incipient cavitation. Both the signals from the hydrophone and that from visualization were then compared.

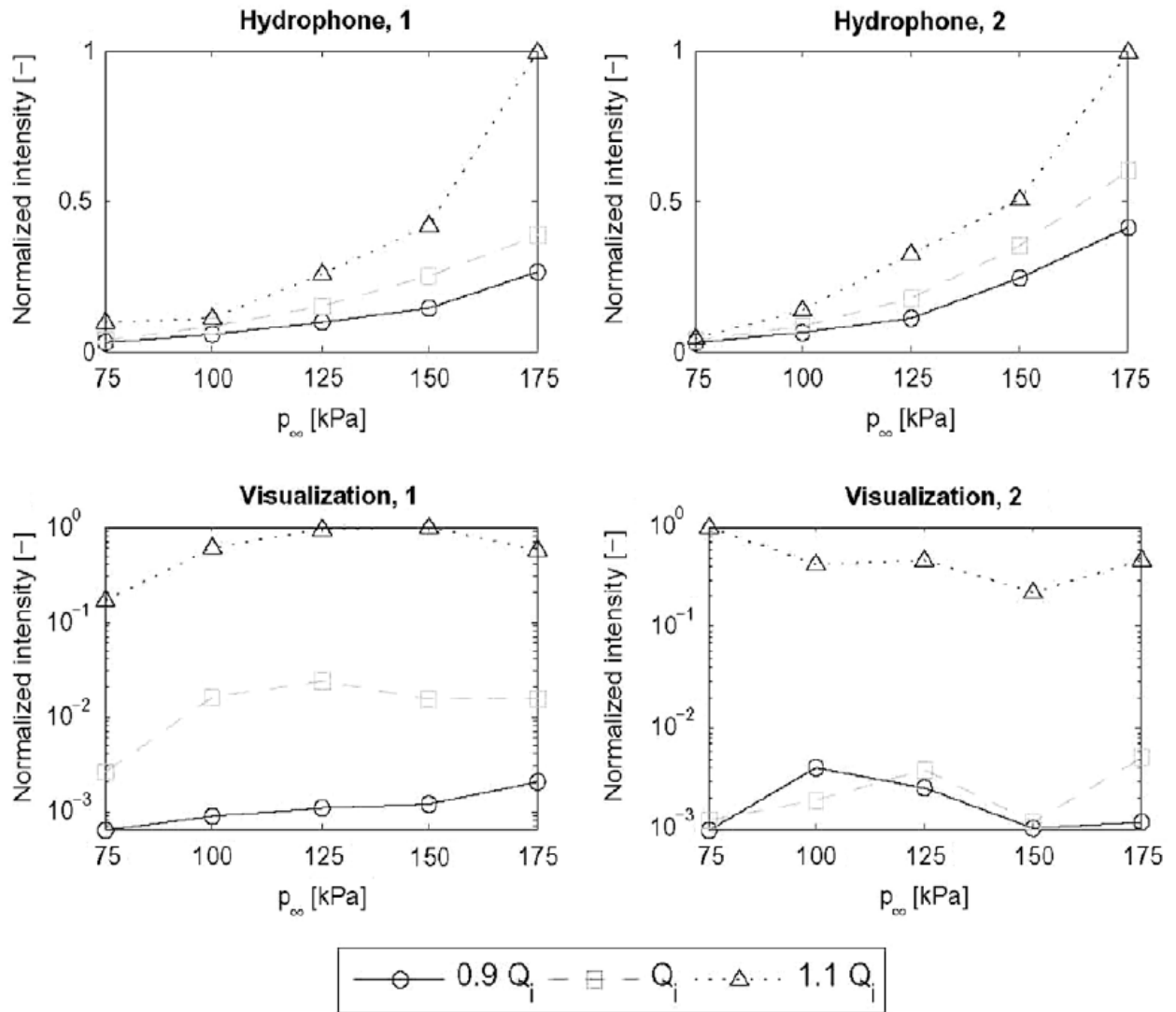


Figure 2.8: Normalized intensity for hydrophone and visualization signals for both valve openings (left-1: fully open, right-2: half-open). [49]

In their result, the comparison between visualization data and hydrophone spectrum analysis results makes it so obvious that the later does not show so much difference in the signals recorded at their various operating pressures.

For the data obtained from the hydrophone, increase seen in the signal intensity is attributed to the high value of operating pressure. At higher pressure, cavitation fluctuations are very powerful.

In contrast, visualization method shows that for either non-cavitating or cavitating flows, the intensity of signal regardless of the pressure at which it is operating fits a certain range. There is so much variation in the intensity values which makes it an encouraging

fact so much so that the logarithmic scale was used, which again points to the visualization method great sensitivity as compared to the hydrophone methods.

Nonetheless, if visualization method results for both incipient cavitation and that of non-cavitating conditions, for both valve openings were compared, they would be rather different. It was also estimated that at the first instance, incipient of cavitation was a little more extensive when compared to the second case, where it was set a little closer to the state of non-cavitation which was due to the subjective operating point determination for incipient of cavitation. Another likely reason could be the spontaneous nature of cavitation where recording the sequences much longer might give a better result.

To investigate further the visualization method accuracy, comparing with the hydrophone measurements in determining the incipient of cavitation, the intensity of the signal was plotted against the rate of flow for both methods as seen in figure 2.8. Just one case of 125 kPa operating pressure was presented for both of the valve openings. Other cases results are comparable. It can therefore be seen that the change in a gradient is significantly higher in a visualization case than in a hydrophone measurements case. Figure 2.9 shows the intensity for both the visualization and hydrophone normalized signals as a function of their flow rate for both valve openings.

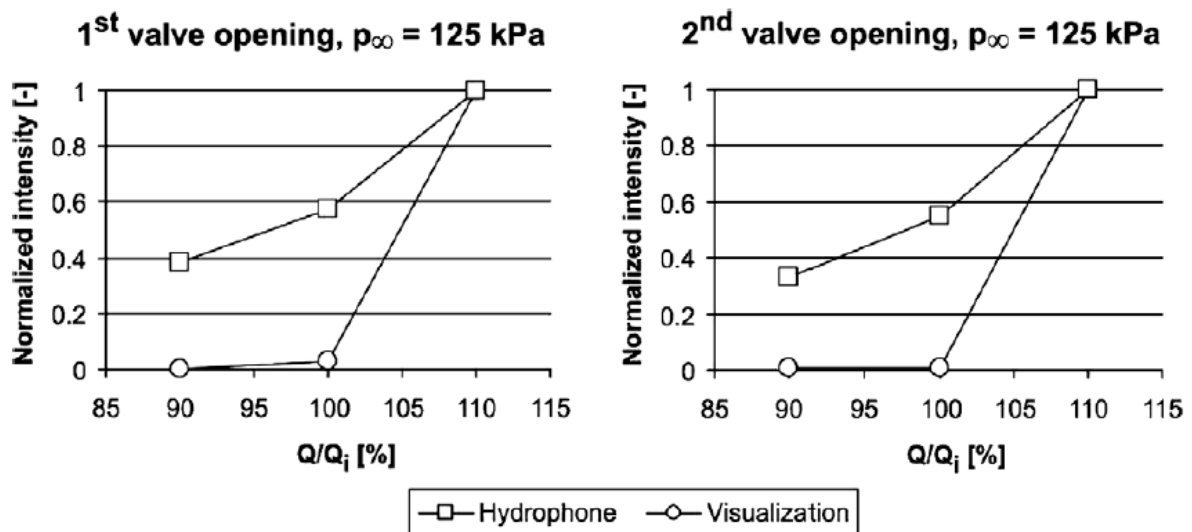


Figure 2.9; Normalized intensity for hydrophone and visualization signals as a function of flow rate for both valve openings (left-1: fully open, right-2: half-open). [49]

By using the method of visualization, the conditions for the cavitation bubbles first occurrence can be accurately and easily predicted.

The key drawback is the experimental set up preparation of the observation window.

In follow up to what Osterman et al [49] has done in their research, A. Masjedian Jazi et al [50] studied the cavitation development in the globe valve using also two different method which are the acoustic measurement and the characteristics diagram of the valve which showed a general acceptable level of accuracy in their result.

The Acoustic Emission Device detects high vibration induced frequency signals that were related to bubbles collapse under the phenomenon of cavitation. After analyzing these signals, gainful information can be acquired to know more about cavitation in the valve as is seen in figure 2.10. Figure 2.10 depicts that even when they had a low percentage of opening (less than 12%), high vibration frequency signals can be distinguished. It shows that there is production of acoustic signals as a result of the bubble collapse that induces high level of vibration frequency in this range. However, when there is higher percentage opening, those vibrations that were associated with cavitation occurrence cannot be detected.

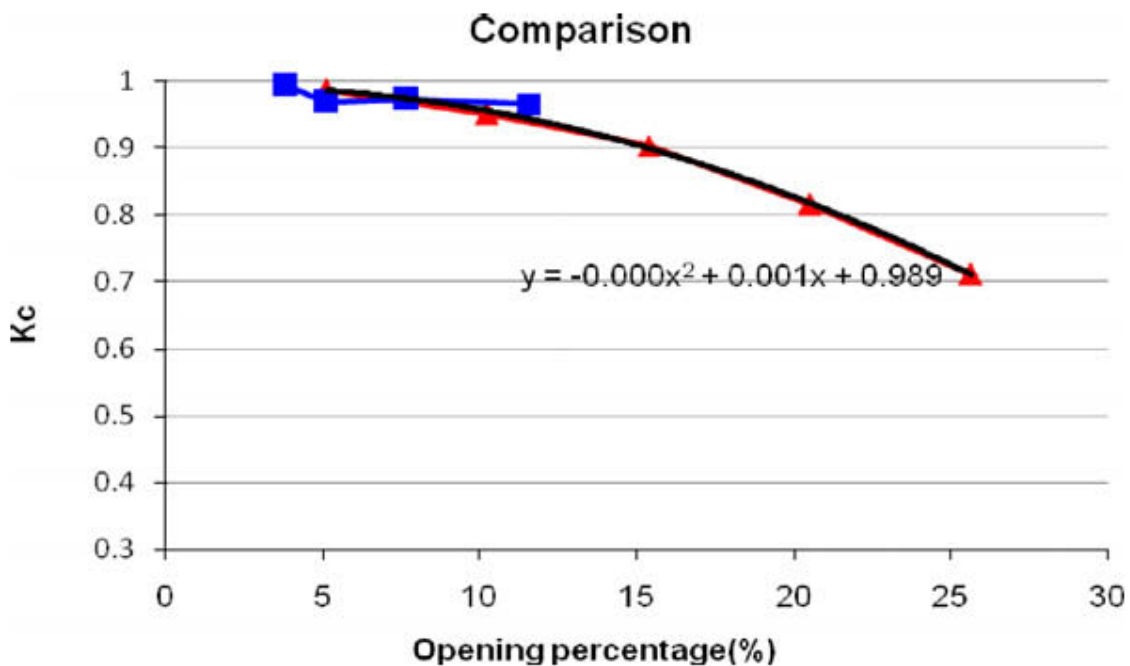


Figure 2.10: Comparison of two methods of detecting cavitation [50]

The key findings of this study suggests that the phenomenon of cavitation that are undesired can, in general, be ascribed as a function of upstream pressure, downstream pressure and flow geometry. Another key discovery of their study is that for certain valve

opening range, the point of initiation at which, in a valve, there is occurrence of cavitation can be detected and also controlled.

J Green et al [51] carried out research on CFD predictions validation by the use of process flow data obtained using an industrial control valve. They used flow test data from experiment so as to validate their CFD simulations in a control valve with complex trim. They then used both experiment and simulation data to calculate the  $C_v$  of the trim and to test the CFD software ability to be able to provide design tools for these sort of trims.

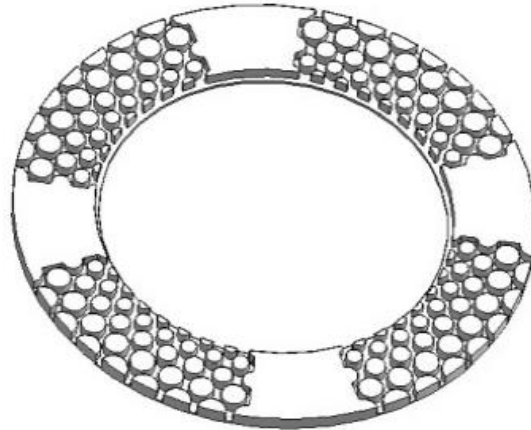


Figure 2.11: X-Stream Trim Disc.

Figure 2.11 shows the trim disc, of which 60% of these disk stacks make up the valve trim. The trims' other 40% is composed of a multiple hole trim with single cage.

They developed CFD simulation for the X stream in ensuring that the value calculated for the trim capacity is very accurate compared with the experiments. The methodology used for the CFD includes disk with single flow path creation within the software that can then be discretized using parameters of edge mesh so as to make sure that the final volume mesh density produced should be optimum to carry out accurate simulations. Boundary conditions were provided for the walls (pressure outlet, mass flow inlet), inlet and outlet, which corresponds to the actual flow conditions.

They carried out five different simulations. The first four of the simulations uses two different mass flow rates at the inlet, each with adapted and original meshes, while the fifth simulation uses a geometry that was modified with its outlet and extended so as to have a better representation of the true valve trim features as shown in figure 2.12.

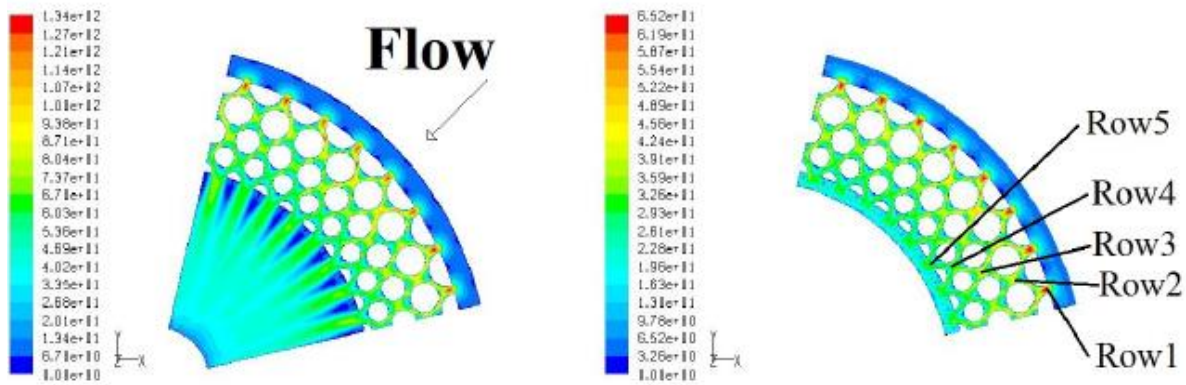


Figure 2.12; (a) Velocity Contours (m/s) for Modified Geometry (left) (b) Original Geometry (right).

Figures 2.12(a) and (b) shows the results of the velocity contours, with the direction of flow as seen on figure 2.12(a), for the valve flow through different geometries of the valve trim. As seen from the figure 2.12, peak velocities clearly occurs at the smaller cross sectional areas i.e. between each cylinders row and also at the transverse gaps between adjacent cylinder rows. More so, each cylinder row has a zone both directly behind and ahead, which has a minimal flow velocity.

Figure 2.12(a) also clearly shows the outlet zone fluid jets, which pretty much stays quite detached from each other, rather than merging quickly into a single flow. As seen from figure 2.12(b), the outlet zone does not show any of these jets. It is due to the wall proximity immediately after when the fluid has left the valve trim itself, which then forces all of the jets to merge and then flow to the outlet.

Figures 2.13(a) and (b) shows both the original and modified geometries pressure contours. On an overall view for both, there is similarity between the nature of the contour plots. The difference in their local values can be ascribed to the values of the various boundary condition used. In the modified geometry used for this simulation, the flow rate was increased so as to cover a wider flow rate values range. More so, features of flow significantly differ at only the outflow region since because in the original geometry, there is a seeming pressure buildup against the “inner” wall. While there is also this pressure buildup at the modified geometry, it is far less noticeable.

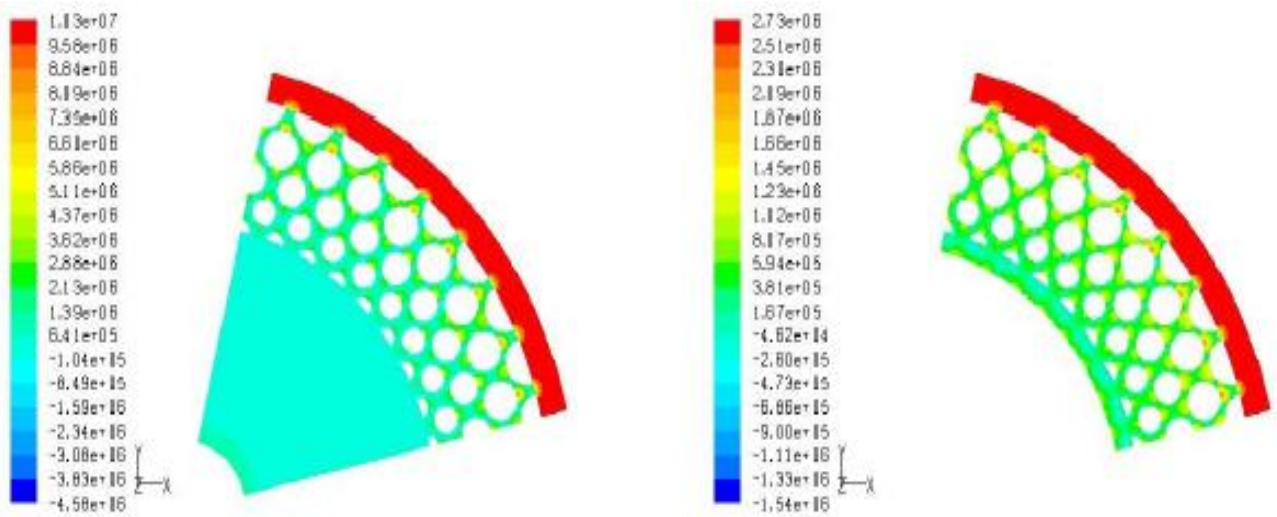


Figure 2.13 (a) Static Pressure Contours (Pa) for Modified Geometry (left) (b) Original Geometry (right).

Table 2.2 shows calculated valve capacities from the result obtained using the CFD simulation.

Table 2.2 Capacities calculated from CFD simulation results

	Flow 1	Flow 1	Flow 2	Flow 2	Mod Geom
Mesh	Original	Adapt	Original	Adapt	Original
Mass flow rate (Kg/s)	0.5	0.5	1.5	1.5	3
Inlet Pressure Pa	3.30E+05	3.23E+05	2.82E+06	2.78E+06	1.04E+07
Cv (1 path)	1.147	1.159	1.177	1.186	1.227

The results in table 2.2 shows an agreement between the five simulations for the trim capacity value. The changes that has been described previously only had a minor impact on the capacity value of the flow. It is seen that when the mesh is changed, the flow capacity increases by 0.75% and 1% for the higher and lower flow rates respectively. More so, when the flow rates are changed, the flow capacity increases by 2.28% for the adapted mesh and 2.54% for the original mesh. Finally, changing the geometry would ensure an increase in the flow capacity by a 6.52% margin.

The detection of onset cavitation can be achieved using sensors such as probes (capacitance, conductance, etc.) in determining the flow properties. A look at some of these probes would be discussed in the next section.

The conductivity probe operation principle is based on the changes in the electrical conductivity of the multi-phase flow and for the probe sensors to respond to conductivity variations of the local electrical flow characteristics when exposed to the dispersed and continuous phases. If the probe tip remains inside of the bubble, the electrical conductivity being measured will be low [9, 51].

The electrical conductivity probes are used widely in measuring the characteristics of flow of the various multiphase pipelines bubbly flows [52]. Rediniotis [53] showed that dual-sensor probe can be used in measuring the time average of the speed, the interfacial area, and the dispersed phase concentration in the water-air multiphase flows with sufficient accuracy. However, the dual-sensor probes, due to their nature, can obtain only the volume fraction and axial bubble velocity. Hence, using dual-sensor probe in measuring the dispersed phase properties in multiphase flow is not recommended as it only estimates the void fraction and velocity of the axial bubble.

Zhao et al [54] have developed an instrument with dual-sensor probe in measuring the oil volume fraction and the velocity profile in a vertical pipe of an 80mm diameter in oil-water bubbly multiphase flow. Their work reported that the superficial velocities of water were in the 0.276m/s to 0.417m/s range, superficial velocities for oil in the 0.025m/s to 0.083m/s range and the oil volume fraction mean values were in the 0.047 to 0.205 range. They reported that the oil droplet axial velocity profile had a shape of “power law” that was compared to their previous work. Their comparison found a very similar shape to that of the distribution of air velocity observed previously in water-air bubbly flow for same flow conditions.

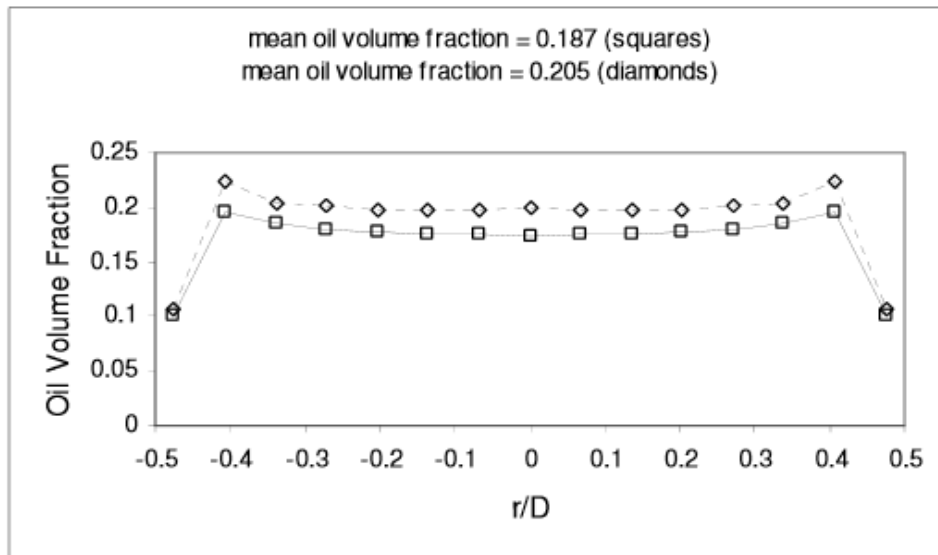


Figure 2.14: Oil volume fraction distribution [51]

Duquesne et al [55] used a dual sensor probe to carry out experimental research in a vertical pipe for water-oil dispersed flow. The pipe had a 3.8m length and 0.04m inner diameter. The main work of their research was to measure oil volume fraction, local oil interfacial area Concentration, Sauter mean diameter of oil drops and interfacial oil droplets velocity. Their experiment showed that there was variation in the water flow rates between 0.12 - 0.89m/s and 0.024 - 0.198m/s for that of oil flow rates. The effect of the probe sampling frequency on the local volume fraction at the three radial locations across half of the diameter of the test section can be seen in figure 2.15. As seen in figure 2.15,  $\frac{r}{R}$  is the ratio between the radial locations of the sensor from the centre of the test section and  $f_s$  denotes the sampling frequency.

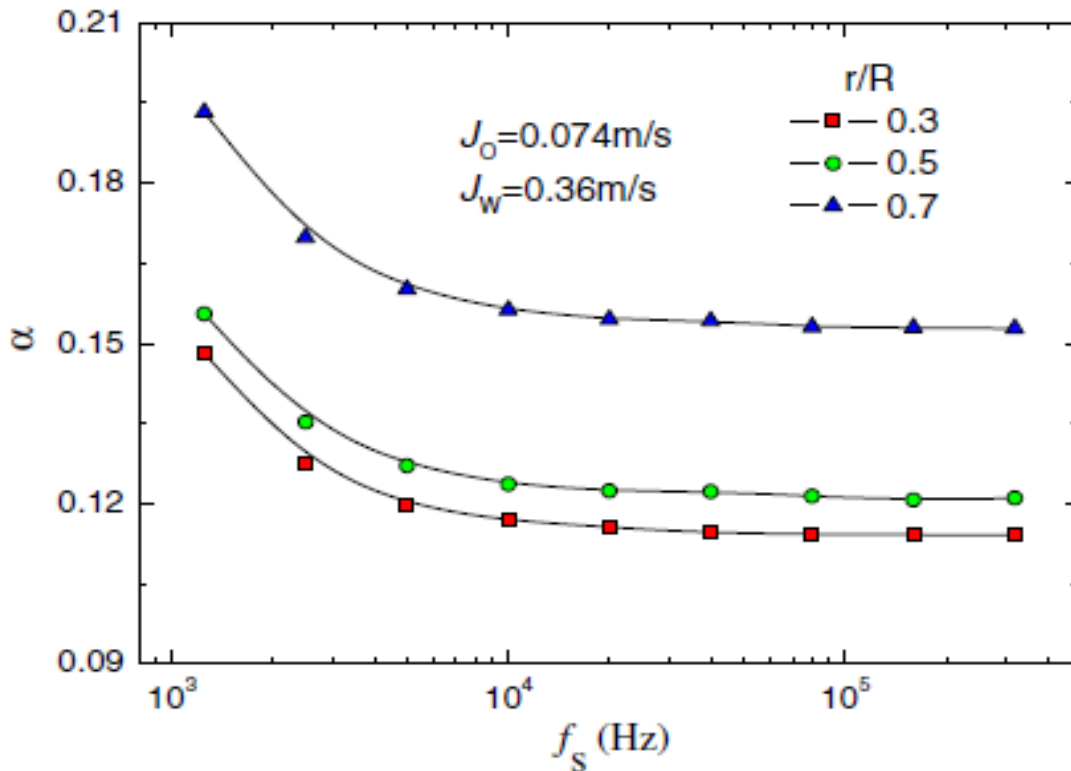


Figure 2.15: Effect of sampling frequency of on conductivity probe [55]

### 2.3 MULTI-HOLE PRESSURE PROBES

Pressure measurements are usually very vital in fluid dynamics applications. From the right measurements of pressure, other parameters such as velocity, flow angle, moments and aerodynamic forces can be determined. Pressure is usually measured from the force that is acting on a unit area. Most pressure measuring devices indicates the differential pressure, which is in relation to the pressure at atmosphere, called the gauge pressure. This measured pressure may be negative or positive with regards to the atmospheric pressure with the negative gauge pressure referred to as vacuum [56].

Depending on the application, multi-hole pressure probe can consists of three, five, seven, etc. internal probes. Each of the holes communicates with the pressure measuring devices.

Of recent, more researches have been concerned with the behaviour of flows going to domains. Though qualitative observation of flows can be obtained quite easily, a well detailed study for the 3D characteristics of flow demands a more accurate and precise flow parameters measurements at various positions around the flow domain model. For

this reason, it has become very important in considering means to improve the instrumentation of flow measurements techniques that can provide not just data that have an acceptable quality, but be quite capable of operating rapidly [57].

Generally, there are two different flow types where measurements are likely to be required.

- The attached boundary layer where there are large flow direction changes, which are not only confined and are parallel to the domain surface planes, but where the normal distance from the domain surface needs to be known at a higher accuracy degree.
- Separated flow measurements such as vortices where large flow direction changes could occur in any of the domain plane, but where measurements to a lesser accuracy degree for the first flow type are normally acceptable.

The MHP probe is a measurement technology that has been proven to resolve the 3D velocity vectors in fields of steady flow [58, 59, 60, 61]. Until very recently, the pressure in midfield could not be measured. But today, decades after the development of refined measurement methods such as the LDV (Laser-Doppler Velocimetry), HWA (Hot-Wire Anemometry) and PIV (Particle-Image Velocimetry), the Pitot-static tube principles has been called upon for the in-field static pressure measurement. This can be achieved now using MHP that has been calibrated properly. In fact, the MHP are one of the few probes, if any, that can provide the local value of all three-velocity components, both total and static pressure. MHP are based on the simple fact that the variation of static pressure occur over any solid surface that have been immersed in flow, from the maximum value equal to the stagnation pressure, to the minimum values in the order of the base pressure in the wake of the body. Pressure measurement at distinct points over the probe body can give all the required information on the components of the velocity and the in-field pressures. Careful calibration here is required. Several tips of the probe head shapes have been used for these measurements, which include hemispherical, conical, cylindrical or spherical surfaces, etc. At the point where flow information is required, these probes needs to be inserted at those specific points as the MHP provides point measurements. Since the probes are inserted into the flow fields, they are known to provide flow interference.

Hot-Wire Anemometry, Laser-Doppler Velocimetry and Particle-Image Velocimetry are some of the tools used for similar measurements. LDV and HWA, are point instruments, whereas the PIV can gather information along a plane that cuts across the velocity field being considered. Point measurements require traversing along the interested domain in mapping out the velocity field. Of all the methods listed above, the HWA is the most susceptible to flow particulates and can be damaged easily if not properly handled, making them not suitable for industrial applications. PIV and LDV require optical access to the measurement points, which can be a limitation to the rig being used in the experiment, as well as the range of the working media. As said earlier, the MHP are tools that can be reliable and robust, appropriate for many industrial applications that do not need access optically to the measurement points and work in fluids that are opaque, that could carry some particulates.

MHP calibration is a significant element and the calibrations of the MHP do not have to be repeated, unless there is damage caused to the probe tip. The number of holes on the head of the probe enables the probe to return the angle of incidence within a preferred accuracy. The more the number of holes, the more accurate the probe becomes in detecting the flow direction at larger incidence angles. Pitot-static tubes has an incidence angle limit of less than  $10^\circ$ , the fivehole pressure probes to  $55^\circ$  and seven-hole probes to  $75^\circ$ . For more than  $75^\circ$  angle of incidence, a twelve hole probe or more is needed.

The number of the holes on the probe is not related directly to the number of sensors. For example, one needs only two sensors in measuring the static and total pressure, or just a differential pressure sensor.

In many structural designs, the MHP consists of a metallic tube, with one small tube that is connected to the probe tip port. If the probe is properly aligned with the stream of flow, the disturbance that is being induced by the probe to the flow is negligible as both the velocity and pressure returns to their upstream value. By allowing the static ring pressure taps to interconnect with the interior chamber, this averaging process can be carried out successfully.

The most commonly used multihole pressure probe is the fivehole probe. Discussions of probe interference with the flow inside the valve using the fivehole probe and their applications will be presented in subsequent chapters.

### 2.3.1 PRESSURE PROBE CALIBRATION

The calibration method for this type of probe establishes the relationship that would exist between the pressure being measured and the actual velocity flow vector. This Multi-hole pressure probe are normally calibrated in the flow field where the static pressure, temperature, velocity direction and magnitude are established. Up to 3000 various probe orientation can be used when calibrating the MHP with regards to the direction of flow. At every orientation, the static and total pressure, the port pressure of the free stream are recorded with regards to the velocity components in order to generate the set of calibration data [62, 63].

The techniques for the calibration are the non-nulling and the nulling methods, with the most preferred being the non-nulling method. In this non-nulling method, the probe is placed in a flow that is known, while varying the probes yaw and the pitch angles over a matrix of angles. At each and every location in this matrix, the probes takes the measurements for the flow magnitude and direction by making use of the pressure sensors connected to each tapings on the probe [52, 60, 64]. Each of this pressure is a function of the velocity to be obtained. The fluid flow parameters and other quantities to be obtained from the calibration are dependent on the coefficients (equations 2.1 to 2.6) which are non-dimensional and are used in the probe calibration [60, 64].

$$\bar{P} = \frac{P_L + P_C + P_R}{3} \dots\dots\dots 2.1$$

$$D = P_L - \bar{P} \dots\dots\dots 2.2$$

$$CP_\alpha = \frac{P_T - P_C}{D} \dots\dots\dots 2.3$$

$$CP_\beta = \frac{P_R - P_L}{D} \dots\dots\dots 2.4$$

$$CP_{total} = \frac{P_R - P_{total}}{D} \dots\dots\dots 2.5$$

$$CP_{static} = \frac{\bar{P} - P_{stat}}{D} \dots\dots\dots 2.6$$

Where  $\bar{P}$  is the average pressure,  $P_L$  is the left port pressure,  $P_R$  is the right port pressure,  $P_C$  is the center port pressure,  $P_B$  is the bottom port pressure,  $P_T$  is the top port pressure,  $D$  is known as the denominator,  $CP_\alpha$  is the pitch angle coefficient,  $CP_\beta$  yaw angle coefficient,  $CP_{total}$  is the total pressure coefficient,  $P_{total}$  is the fluid total pressure,  $P_{stat}$  is the fluid static pressure and  $CP_{static}$  static pressure coefficient.

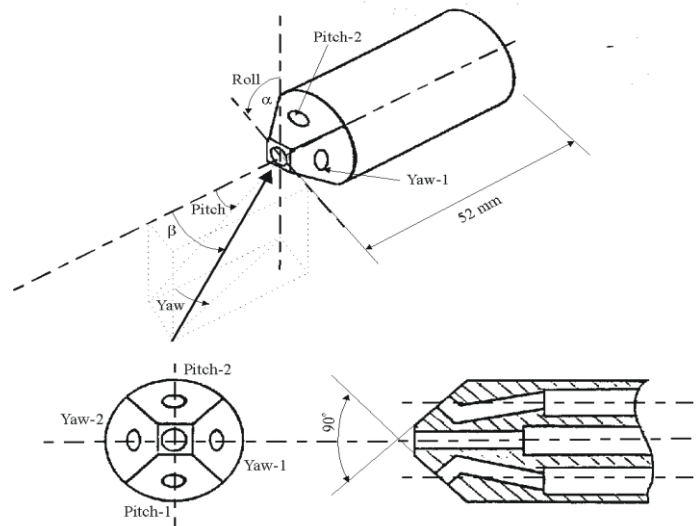


Figure 2.16: Schematic representation of a five-hole probe [64]

Many researchers have developed various ways of calibrating a certain number of multi-hole probes for varying applications for the main purpose of increasing their accuracy and improving their measurements. Some of this calibration technique would be discussed.

N. Sitaram et al [65] presented that concerning the normal  $45^\circ$  chamfer angle,  $30^\circ$  chamfer can be more desirable from more recent study for measuring flows that are unsteady. They then investigated to find the optimum angle of chamfer on a 5-hole probe. The probe has a 9.6mm head diameter with a 3mm internal tube diameter with 0.15mm clearance. They varied their probe chamfer angle from  $30^\circ$  to  $60^\circ$  in  $5^\circ$  steps. For each angle of the chamfer, the five-hole probe has been calibrated from  $-30^\circ$  to  $+30^\circ$  in  $5^\circ$  interval while presented their calibration curve for each design [65]. The signal of the fluctuating pressure averaged over a 5s period to allow for steady state condition.

The probe was calibrated using a calibration tunnel, which is fixed, with the head at the calibration section center in order to minimise the effects of duct wall and boundary layer. The multi-hole probe pitch and yaw angles can change from  $\pm 30^\circ$  and from  $\pm 180^\circ$  respectively at  $1^\circ$  interval. The rotation can be done clockwise and anticlockwise. The free stream air velocity was set at 25m/s. Figure 2.17 shows the five tubes pressure measurements with a  $30^\circ$  chamfer angle, with the pitch angles plotted against the total pressure with the pressure non-dimensional.

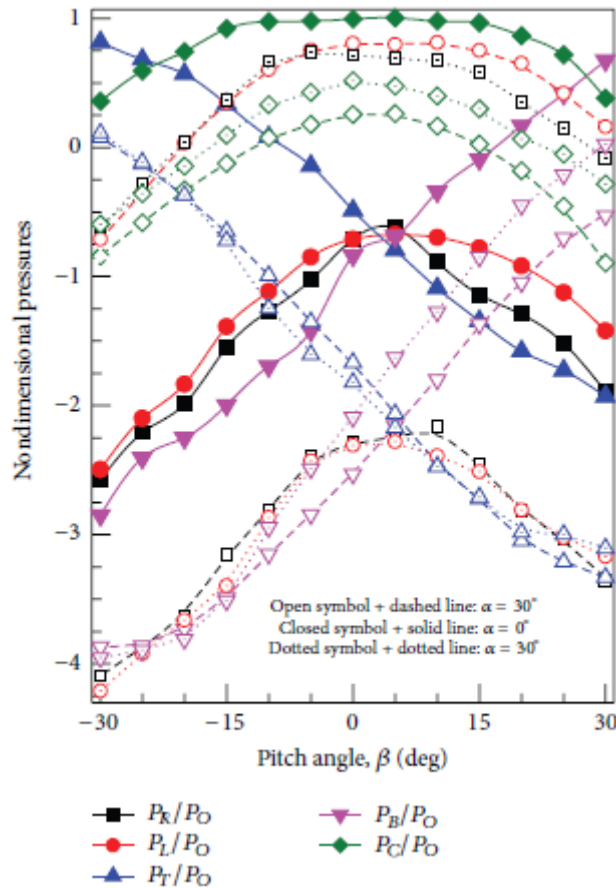


Figure 2.17: Non-dimensional probe pressures for chamfer angle of  $30^\circ$

The center, right and left holes pressure measured show a parabolic variation with the pitch angle, as expected. At pitch angle of  $-30^\circ$ , the left port pressure ( $P_L$ ) is more than that the center port pressure  $P_C$ , while  $P_L$  showed the lowest pressure value as its hole inclines to a larger flow angle. At pitch angle equal to 0,  $P_L$  and  $P_R$  (right port pressure) are almost equal at all the angles of pitch. At pitch angle equal to  $-30$  and  $30^\circ$ , the top hole pressure measurements are also nearly equal in all pitch angles with these pressures lower than its corresponding value for  $0^\circ$  pitch angle. Same goes for the bottom hole measured pressure.

As the angle of the chamfer increases, the calibration coefficient also increase as this trend was observed only for  $50^\circ$  chamfer angle.

It was concluded that the  $30^\circ$  five hole pressure probe chamfer angle has a huge range of operation, while the  $50^\circ$  five-hole pressure probe chamfer angle has a good sensitivity. The chamber wall static pressure was taken as the total pressure, as the dynamic pressure magnitude in the chamber was quite small.

R.P Akshoy et al [66] studied various algorithms in their paper and came up with a new coefficient of pressure, which overcame the limitations from other researchers in their literature review and gave fewer errors in their computation when calculating for parameters of flow. For their method, the pressure at center hole probe influence is paramount in defining other coefficients. From the fourth order regression analysis,  $r^2$  average values parameters for all of the zones for  $\alpha$  and  $\beta$  are 0.9979 and 0.9910 respectively, which are better than all the reported values for the existing methods. Their calibration was conducted in an open circuit low speed type generation facility. The probe diameter used was a 4mm diameter with a  $45^\circ$  chamfer angle. A calibration data, experimentally generated for the five-hole probe, were used in analyzing the data reduction and pressure normalization technique. Figure 2.18 depicts the five-hole probe sector map which registers for a particular yaw and pitch angles, their minimum pressures. It showed that the hole at the center pressure covers the widest pitch and yaw range compared to the other four.

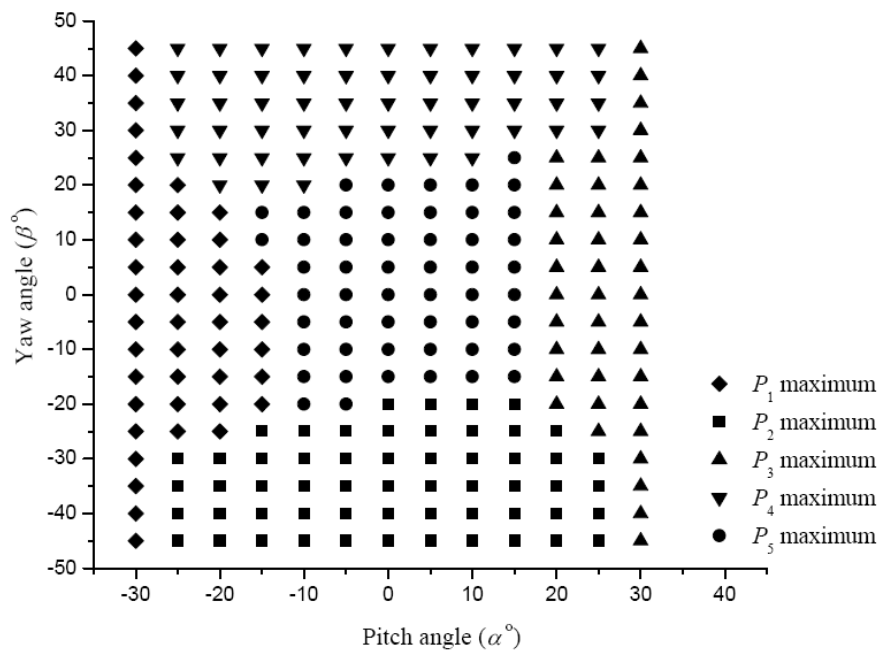


Figure 2.18: Sector map of five-hole probe [66]

At larger yaw and pitch angles however, holes 1 to 4 from the probe are more likely for the total pressure to be sensed by then making the pressure sensed by the holes (1 to 4) maximum at their corresponding locations. They then presented their overall results comparing with other methods to see the novel technique result accuracy. Table 2.3 depicts all the data reduction and pressure normalization technique combination summarized for their study.

In conclusion, the statistical analysis then recommended that the technique proposed with combined 4<sup>th</sup> order regression analysis gives a calibration result that is the best.

Table 2.3: Statistical summary of all combinations of data reduction and pressure normalization techniques

Pressure normalization techniques	Data reduction techniques	Statistical Parameters	Pitch (degree)	Yaw (degree)	Total pressure (mm of H2O)	Static pressure (mm of H2O)
Treater and Yocum (1979)	Polynomial curve-fit (4th order regression)	Uncertainty	1.2232	2.0699	0.2343	0.0824
		Standard error	0.0863	0.1460	0.0384	0.0058
		r <sup>2</sup> value	0.9957	0.9910	0.9417	0.9545
	Direct interpolation (Akima IMSL)	Uncertainty	0.4409	0.3321	0.0459	0.0116
		Standard error	0.0321	0.0234	0.0032	0.0008
Pisasale and Ahmed (2002)	Polynomial curve-fit (4th order regression)	Uncertainty	3.0493	6.2824	0.0706	0.2310
		Standard error	0.1873	0.3859	0.0043	0.0142
		r <sup>2</sup> value	0.9772	0.9476	0.8556	0.7968
	Direct interpolation (Akima IMSL)	Uncertainty	0.3198	0.1899	0.0176	0.0082
		Standard error	0.0228	0.0151	0.0011	0.0005
Gallington (1980)	Polynomial curve-fit (4th order regression)	Uncertainty	0.4026	0.6127	0.2278	0.0163
		Standard error	0.0632	0.0967	0.0374	0.0025
		r <sup>2</sup> value	0.9975	0.9907	0.9368	0.9906
	Direct interpolation (Akima IMSL)	Uncertainty	0.3133	0.0714	0.1054	0.2742
		Standard error	0.0221	0.0050	0.0074	0.0193
Proposed method (2010)	Polynomial curve-fit (4th order regression)	Uncertainty	0.3800	0.6099	0.1758	0.0199
		Standard error	0.0597	0.0962	0.0124	0.0031
		r <sup>2</sup> value	0.9979	0.9910	0.9761	0.9938
	Direct interpolation (Akima IMSL)	Uncertainty	0.2465	0.0678	0.0051	0.0020
		Standard error	0.0175	0.0048	0.0004	0.0001

Bryant et al [67] established both experimental and CFD study in measuring the 3-D velocity, static and total pressure of a gas flow of a stationary source horizontal exhaust duct by using the MHP. Their study involved two velocity and pressure measurements that are independent of the profiles across the two-exhaust duct chords with their results compared to that of the CFD results. Figure 2.19 depicts a computed profile of the obtained velocity using the multi-hole pressure probe in a 1000mm traverse spacing along the duct diametric chords that were spaced at 15°. Their study did not show any insight on a vertical duct flow and was centred only on just a single-phase flow.

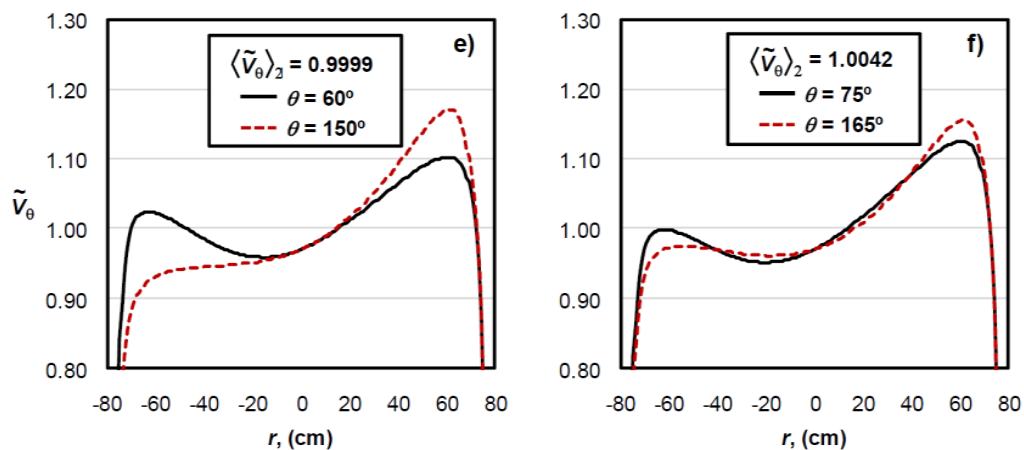


Figure 2.19: Velocities profile along diametric chords [67]

S. Kim et al [68] presented a calibration method for a five-hole pressure probe with multiple functions for diagnosing air data of a helicopter. Their work was more focused in finding the yaw, pitch, attack angle, angles of directions, static and total pressure for the helicopter. Their calibration work results showed that the five-hole pressure probe with head shaped hemispherically, gave a pressure that is evenly distributed as depicted in figure 2.20. Figure 2.20 shows the pressure surfaces for the multi-hole pressure probe result. However, their study does not give any understanding to the velocity of the travelling helicopter.

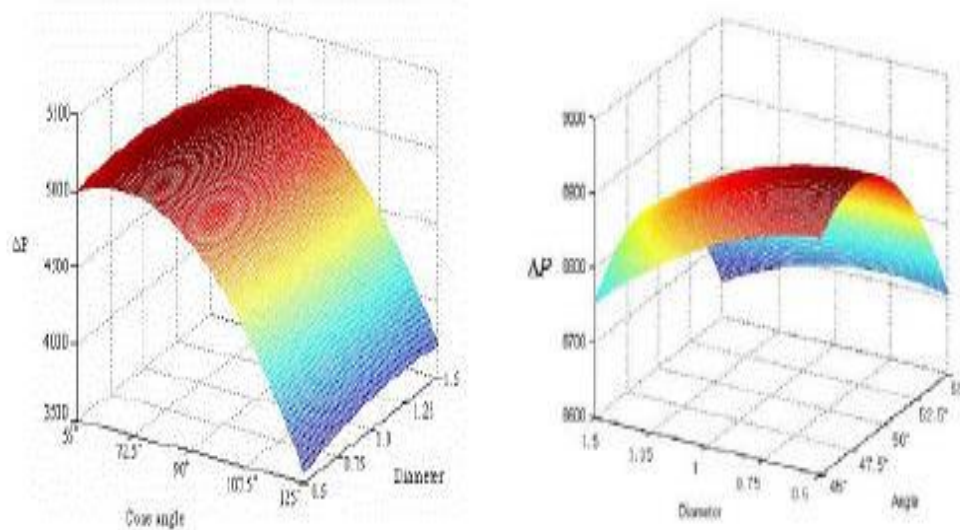


Figure 2.20: Response of surface pressures [68]

Lee et al [69] presented the calibration of a five-hole probe and data reduction applied in measuring a typical 3-D vertical flow. Their idea was to obtain the flow velocity magnitude from the measured dynamic pressure by the pressure difference between the middle hole and that of the other four holes. They also obtained the velocity direction from the pressure difference between the yaw and pitch planes side holes. The pressure probe used for this study has a diameter tube of 0.125inch with a hemisphere shaped tip. The middle probe hole is located at the hemisphere tip centre with the other four holes located symmetrically at  $30^\circ$  on the hemisphere with respect to the axes of the probe.

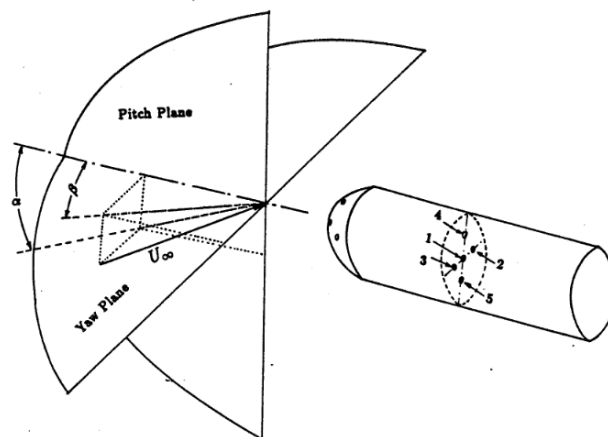


Figure 2.21: Five-hole probe schematic and velocity resolution [69]

The surface pressure coefficient sensitivity to the changes in the flow angles was derived as:

$$\frac{\partial(\Delta C_p)}{\Delta\alpha} = 8R' \cos 2\alpha \cos^2 \beta \dots\dots\dots 2.7$$

Where  $\Delta C_p$  is the change in the difference in pressure in the head of the pitch,  $R'$  is the probe radius rate of change in the axial direction.

The results of the calibration showed that no substantial change was observed within the interested range of the flow velocities (20-40m/s). Quantitative vorticity flow values were derived from the 3 velocity components vectors, static and total pressure measured data. Stream wise vorticity was gotten from the measured components of the velocity as:

$$\xi = \frac{\partial w}{\partial y} - \frac{\partial v}{\partial z} \dots\dots\dots 2.8$$

The plot for the velocity vector of a tip vortex in the flow cross plane is depicted in figure 2.22.

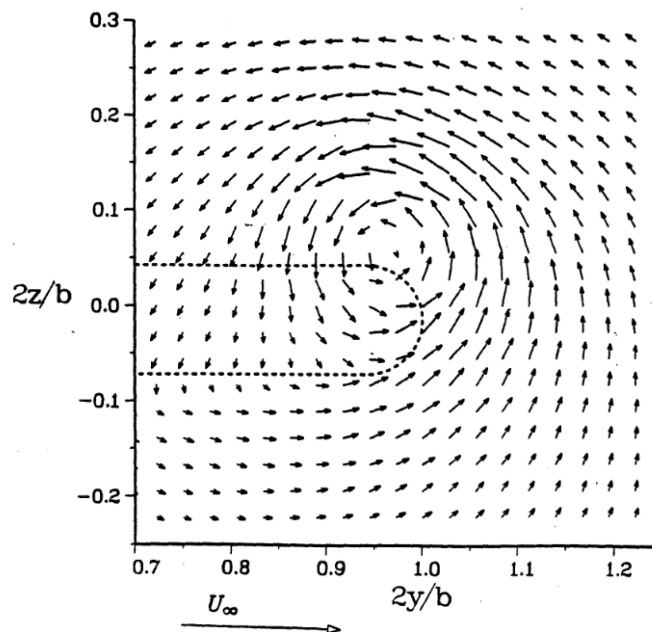


Figure 2.22: Velocity vector plot of a tip vortex in the cross plane [69]

After the calibration of these pressure probes and the determining the coefficient of calibrations, the next subsection presents how the probes are applied to various uses.

### 2.3.2 PRESSURE PROBES APPLICATION

These pressure probes are used mainly in airflow application in obtaining static and dynamic pressure heads, flow angle, velocity components, etc. in the flow domain.

Measuring turbulence at high-intensity by using a pressure probe sensors that responds fast has demonstrated to be a technique that is quite accurate and effective but unfortunately, according most literature that are available, most of these researches on pressure probe concentrates mainly on applications of higher velocity (more than 100 m/s). There are commercially available pressure probes with most of their designs meant for not just only high fluid flow velocity, but for higher bandwidth (about 10 kHz) and also for applications that are multidirectional, which increase complexity and cost drastically. Therefore, J.D Hobeck and D.J Inman [70] intended in their paper, to provide for future engineers and scientists means to developing a pressure probe sensor that can meet their specific needs. Their research focused on the designing and the analysis of a two low cost, highly sensitive pressure probes for measuring invasively in a low velocity (of less than 20 m/s) air flow that is highly turbulent. They presented their design; techniques of their calibration and modelling are discussed and experimentally validated. Table 2.5 shows all the parameters they used in their design for the pressure probe.

Table 2.4 Pressure Probe design parameters for their design

Parameter	Value	Unit(s)
Probe diameter	1.50	mm
Tip length	8.25	cm
Static port length	7.75	cm
Sensor volume	134	mm <sup>3</sup>
Pressure range	± 249	Pa
Bandwidth (uncompensated)	200	Hz
Output voltage range	± 16	mV
Sensitivity	0.064	mV/Pa

Their probe design is similar to that of the Pitot tube. They carried out both static and dynamic calibration for their probe by using hot wire probe to compare their result where the grid turbulence were simultaneously measured. The hot wire was placed at the input while the pressure probe was positioned at the outlet.

Figure 2.23 depicts the transfer function of the normalized pressure that exists between the sensor and the tip of the probe, which have been calculated using analytical technique and then compared with the transfer function measured. The results above shows a good agreement between theory and measurement results though some errors accumulated as the frequency increased.

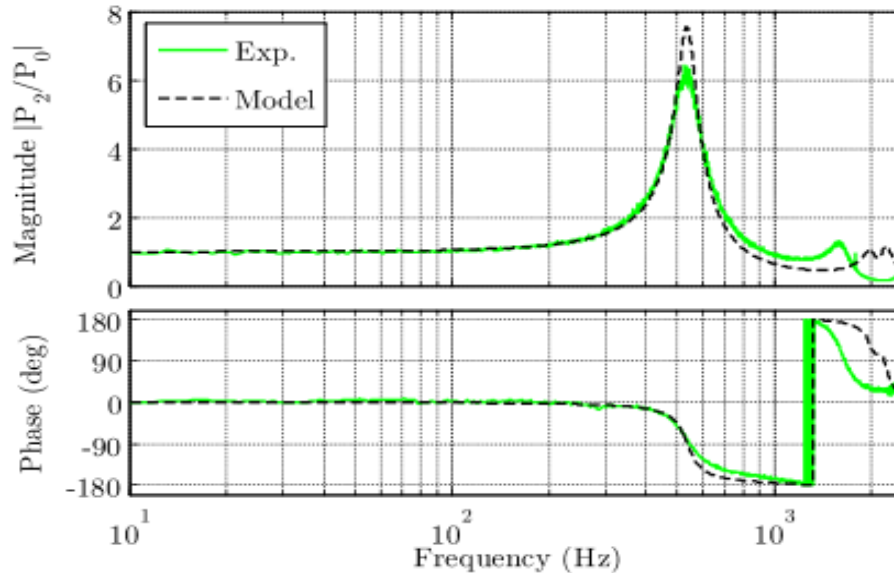


Figure 2.23; The dynamic response characteristics for the theoretical and experimental results for a pressure probe that shows the acoustic attenuation and the phase distortion between measured dynamic pressure and the sensor pressure

A.R Porro [71] designed a five-hole pressure conical probe, primarily in determining the angularity of local flow that also determine the Mach number locally. He designed the probe, which was tested using NASA facility, which was tested using SWT (supersonic wind tunnel) where pressure data were successfully acquired. These data were acquired close to the propulsion system of the compressor engine and stall. In systems of supersonic propulsion, distortion in the instantaneous dynamic flow from recent analysis, at the engine surface plane/inlet is a more reliable impending surge predictor in a compressor engine and stall as compared to the distortion in steady-state flow.

The five-hole probe has a 0.25-inch diameter, the peripheral port of the probe tip are cut back at  $30^\circ$  angle to form a cone with  $60^\circ$  included angle. The middle hole measures the pitot pressure while the other holes measure the combination of pitot and static pressure. In order for them to maximize the probe frequency response, the pressure transducers are mounted on the passages of the probe tip. The figure 2.23 shows data reduced from

the conical probe, which captured a hammer-shock that is propagating through the vicinity of the propulsion system flow field. They showed the axial effect of the propagation of the propulsion system unstart/stall transient event.

Figure 2.24 (a) shows the response of the pitch angle during the transient event. At each of the axial station, the transient at initial exceeds the  $-15^{\circ}$  transient limit but settles out the pitch angle during disturbance. Figure 2.24 (b) depicts during the unstart transient, the yaw angle response. The initial transients exceed the  $15^{\circ}$  calibration limit at the downstream axial plane. High initial yaw angle at upstream axial location is not seen. The yaw angle then remains relatively constant for the remaining transient event and have much lower magnitude than the observed angle of pitch. Figure 2.24 (c) depicts the time history of the local transient Mach number that were obtained for each of the probes.

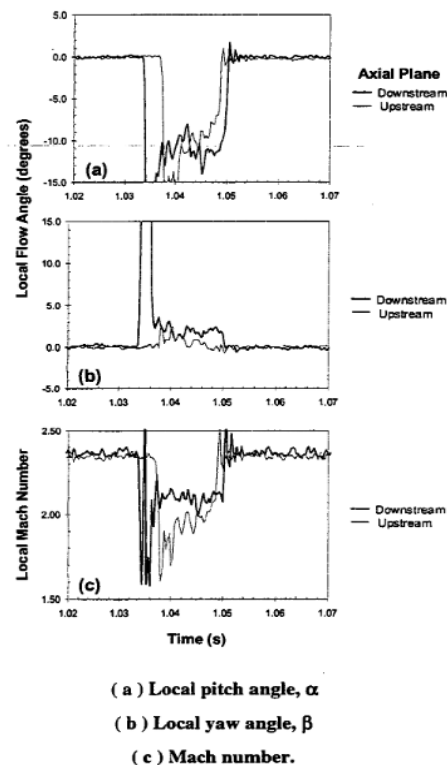
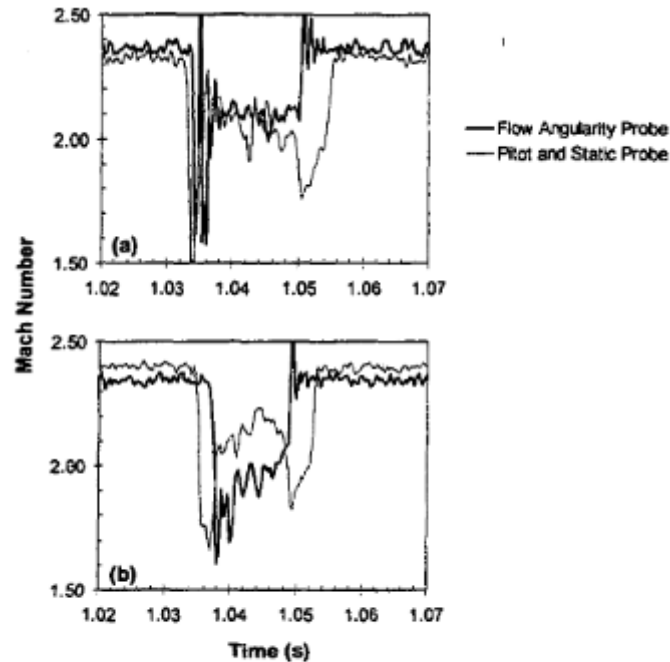


Figure 2.24: Flow angle and Mach number for transients during uneven start [71]

The effect of spatial resolution are well minimized for the probe (static and Pitot). However, one key disadvantage in using this approach is that all the pressure measurements needs to be obtained simultaneously at same location of measurements. Figure 2.24 shows the comparison between the Mach number for the pressure probe and that for the static and pitot probe at the same location. There is good agreement for the Mach number shown in figure 2.25 at their locations downstream for both techniques.

However, the data for the upstream is not that favorable though they had similar data trends.



**( a ) Downstream axial plane.**

**( b ) Upstream axial plane.**

Figure 2.25: Flow angularity pressure probe comparison and that of the pitot and static probe Mach number calculation in their flow field

In conclusion, they designed the five-hole probe in measuring fast acting transients by the installation of pressure transducers in each of the probe ports. The data from the probes were used in determining the Mach number and flow angle as the measurements from the probes did not produce the flow angle, pressures and local Mach number time histories.

Vihar et al [72] described that these multi-hole probes are used mainly in characterizing 3-D flows in complex applications. The probes provide a more accurate information that are sufficient for flow velocity measurements [72]. In their paper, the geometry of the probe influence on the flow field disturbance were presented. They accessed the parameters of the flow fields based on computing numerically, pressure and velocity fields in their model inside and around their probe. They predicted their flow field using CFD and the characteristics that links the probe head geometry and the degree of interference on flow field. Both hemispherical and conical head analyses for their static pressure, Y and Z velocity components and their results compared, have been presented.

Their work provided vital information regarding the study for the probe placement for a novel wheel arch flow mapping. Numerical flow simulation in and around the probes have also been studied. Their information presented will help the flow field characterization of the probe in future to design newer probes that will cause lesser interference [72].

The probe has a 5mm diameter with each internal probe having a 1mm diameter. The test section they used is a 230 by 230 mm cross section. The total number of mesh elements is 1.8 million. Boundary condition were velocity inlet (33.7m/s) and pressure outlet (atm) with the probe wall as smooth zero slip. The flow was turbulent which then made them to use the k-epsilon RNG model. Figure 2.26 (a) and (b) shows the conical and the hemispherical probes respectively used for their study while 2.26(c) denotes the probes designation for their pressure tapings.

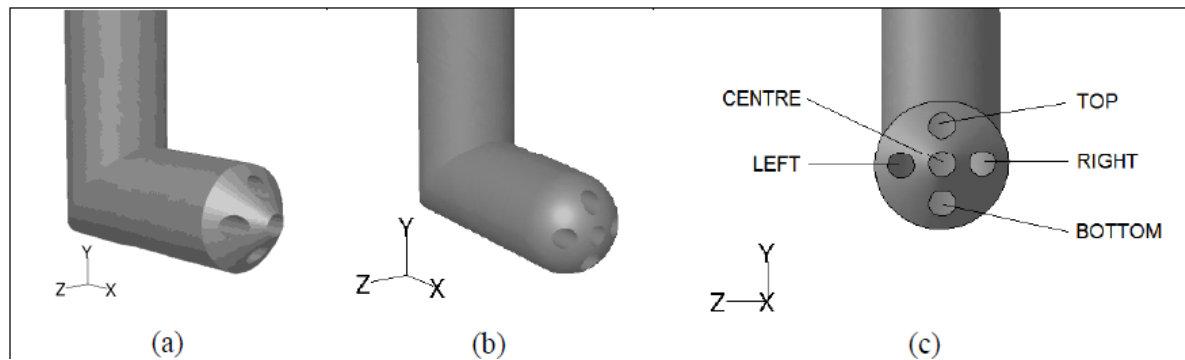


Figure 2.26: (a) Conical head probe; (b) Hemispherical head probe; (c) Pressure tap designation [72]

Figure 2.27 shows how their domain and boundary conditions are set. The probe is positioned at the centre of the flow domain with equal downstream and upstream distance. As also seen from the figure, their assigned boundary condition name were also given.

In their result, the effect of the probe have been plotted for their static pressure for both the downstream and upstream as seen in figure 2.28 (a) and (b). From the figure, it showed that the hemispherical head causes lesser obstruction in the flow field. This is so because in the upstream values in figure 2.28 (a), the gradient starts off the same but at 0.5D, the pressure rose a little for the hemispherical head when compared to the conical head. Also, the downstream static pressure (figure 2.27 b) for the hemispherical probe drops to about 15Pa at distance 3D whereas for the conical, it drop 15Pa also at distance 5D. This shows clearly that conical cause more interference than hemispherical.

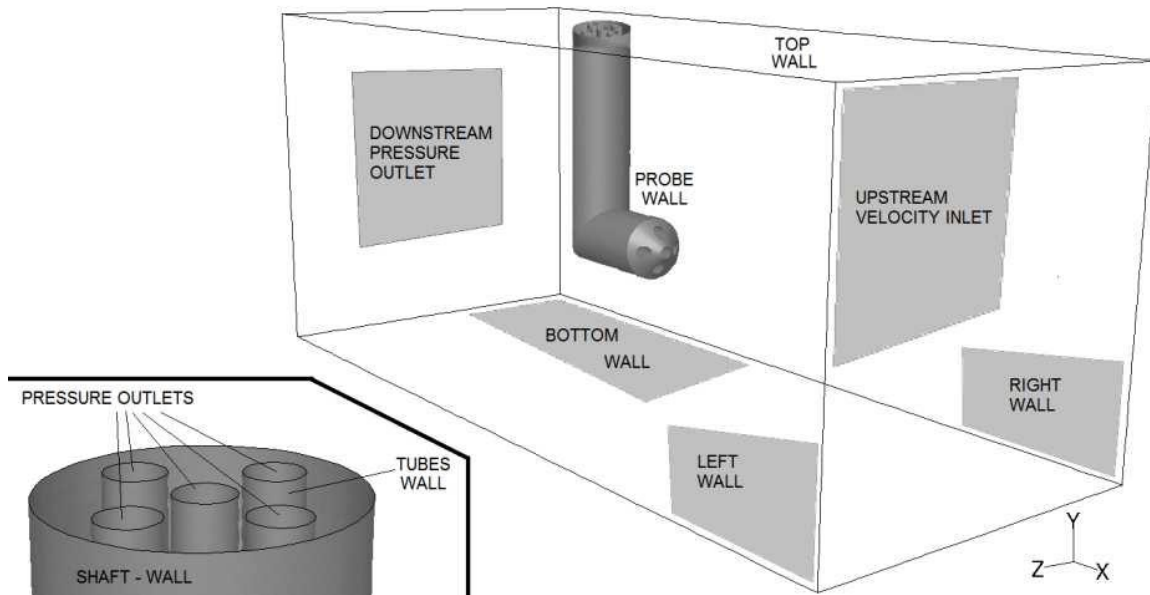


Figure 2.27: Computational domain and the boundary conditions [72]

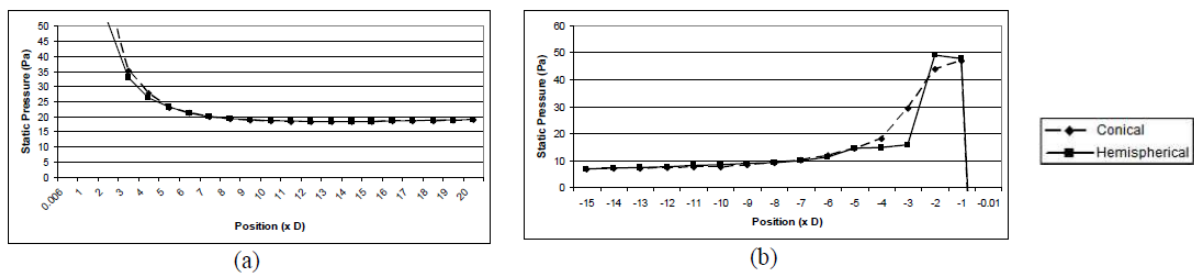


Figure 2.28: Static pressure profile along flow axis (a) upstream and (b) downstream of the probes [72]

For the velocity comparison, figure 2.29 and figure 2.30 shows the Y and Z velocity component for both the upstream and the downstream of the probes respectively. Figure 2.29 (a) depicts the Y velocity distribution along the probe upstream. The Y velocity for the hemispherical probe head falls sharply at 2D, whereas it decreases gradually as it moves upstream for the conical probe head.

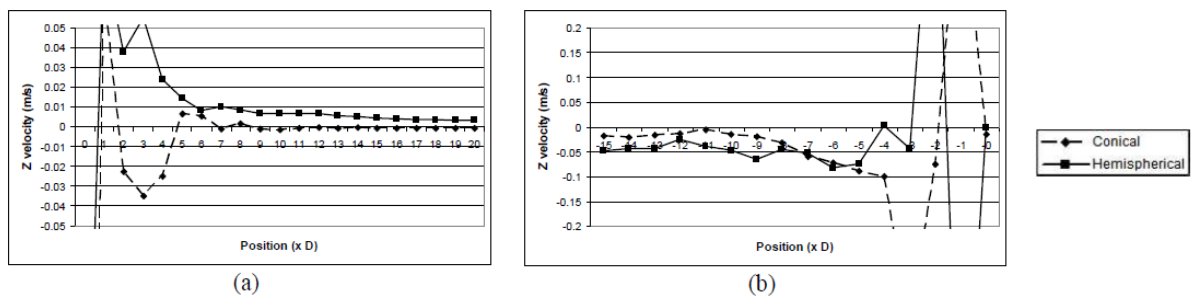


Figure 2.29: Y-velocity profile along flow axis (a) upstream and (b) downstream of the probes [72].

Figure 2.29 (b) depicts the Y velocity distribution along downstream of the probe flow axis. It shows that the hemispherical shaped probe reaches at 9D downstream, near-zero value. For the conical shape, it maintains about  $-0.05\text{m/s}$  even beyond 15D. This shows that the conical head causes more influence in the flow field when compared to the hemispherical probe.

For the Z velocity, figure 2.30 (a) and (b) depicts the probe upstream and downstream velocity respectively. Contrary to the earlier obtained result for Y velocity, the conical Z velocity drops to near-zero at 11D downstream and 7D upstream. For the hemispherical head, it drop to  $-0.04\text{m/s}$  for downstream and  $0.01\text{m/s}$  for upstream. All of these values decreases gradually as flow moves away from the probe in any of the directions, which makes the hemispherical probe not quite different from conical head in Z velocity.

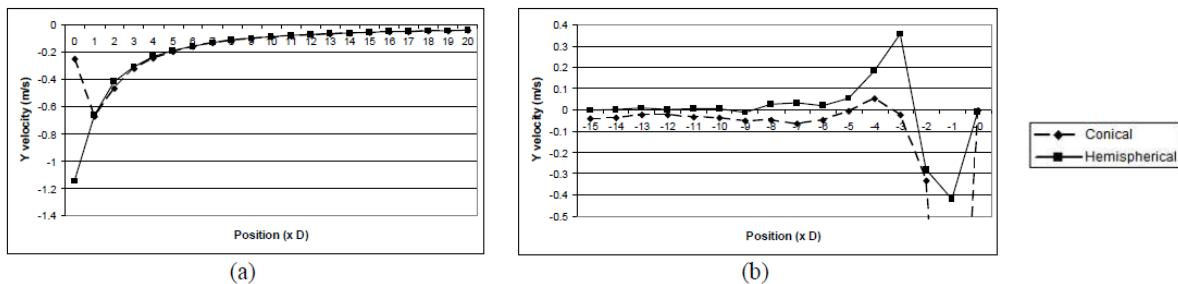


Figure 2.30: Z-velocity profile along flow axis (a) upstream and (b) downstream of the probes [72]

In conclusion, though both the transverse velocity and the static pressure are similar at the upstream for both probes, the downstream interference is significant in comparison. The average static pressure for the conical probe between 1 and 5D is 7.8% higher compared to that of the hemispherical head probe. More so, conical probe has higher Y and Z velocity. Hemispherical probe has minimal influence beyond 10D and 6D downstream and upstream respectively. Though these influences can be reduced further when the head sizes are made smaller, conical head will still have greater influence than hemispherical head.

V. Malviya et al [73] later presented an investigation of 3-D interference that multi-hole probes causes in an automotive arch wheel. Their simulation involved flow around the pressure probe which is inserted at different locations within the gap of the wheel/wheel arch. Both velocity and pressure fields along lateral and longitudinal planes was used for this analysis. A 3-D interference ellipsoid has been well-defined in order to assist for the recommendation of the probes being placed optimally and to also minimize errors that

are due to the interaction of the probes, therefore enhancing accurately, the transient flow phenomena measurement. It is worthy to note here that the probes needs to cause minimal interference for accurate results.

The probe (five-hole) is inserted on the wheel as depicted in figure 2.31.

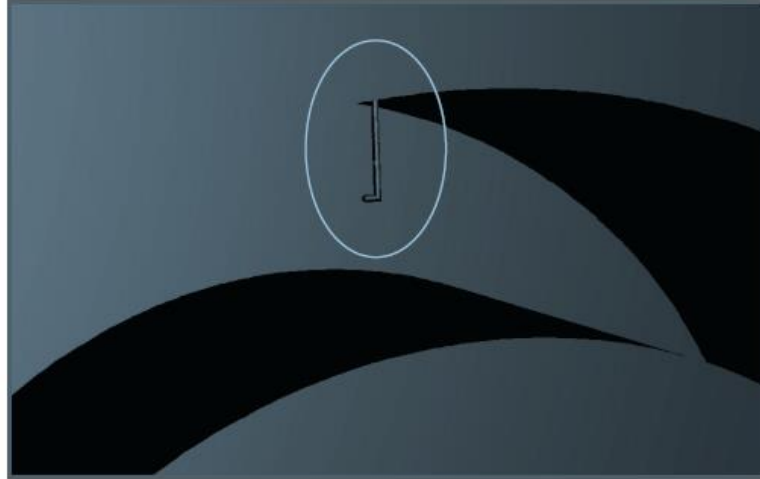


Figure 2.31: Five-hole probe location inside the automotive wheel arch [73].

Figure 2.32 shows the positions around the wheel and their direction in which the probe is been rotated which corresponds to  $0^{\circ}$ , which is the location facing travel direction and  $270^{\circ}$ , which denotes the wheel topmost location.

In order to quantify their probe influence on the wheel arch inside flow for their study, the following wheel arch configuration have been examined.

- Standard reference configuration of the wheel arch as depicted in figure 2.32 (a)
- The wheel arch with the probe at  $0^{\circ}$  as depicted in the circle in figure 2.32(b)
- The wheel arch with the probe at  $270^{\circ}$  as depicted in the circle in figure 2.32(b)

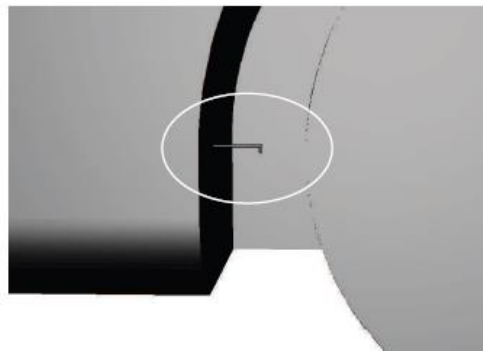
The speed of the automobile ranges from 18 to 31m/s but for this study, 30m/s has been used. Reynolds number for the vehicle is  $3.91 \times 10^6$ . The flow attack angle is maintained at  $0^{\circ}$  for both investigated configuration. Figure 2.33 shows the fivehole probe geometry that was used in their study. Conical head ( $45^{\circ}$ ) shape of 5mm outside diameter and 8.75mm head long with its details also shown in the figure 2.33 [30].

The probe effect presence on the pressure field is represented in a form that is non-dimensional using pressure coefficient ( $C_p$ ) as

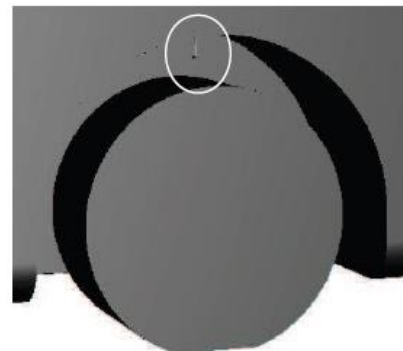
$$C_p = \frac{P - P_{\infty}}{q_{\infty}} \dots \dots \dots (2.9)$$



(a) Reference wheel arch geometry [1, 2]



(b) Probe at 0°



(c) Probe at 270°

Figure 2.32: CFD geometry of the single-axle vehicle model investigated [73].

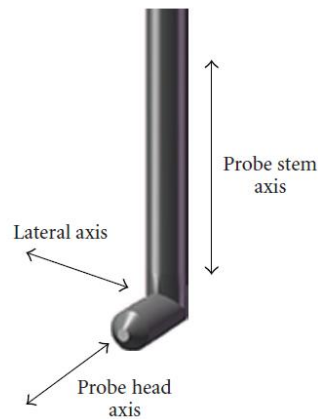


Figure 2.33: Geometry of five-hole probe [73].

Here,  $P$  denotes the local static pressure,  $P_\infty$  is the static pressure at free stream,  $q_\infty$  is the dynamic pressure at free stream. If  $U_\infty$  is regarded as the velocity at free stream, then  $q_\infty$  can be represented as

$$q_\infty = \frac{1}{2} \rho U_\infty^2 \dots \dots \dots 2.10$$

The flow domain, which they used consists of a rectangular volume of cuboid, containing the model being used is depicted in figure 2.32. It has a length of 84.67m. The inlet of the

domain is 3l upstream of the model and the outlet is 7l downstream of the model where l is the overall model length.

Both realizable k-epsilon and SST k-w were used in their research. Their CFD result was validated from experimental for the measurement of each taps of the probes. Figure 2.34 shows the comparison between the experiment and CFD values for the pressure taps.

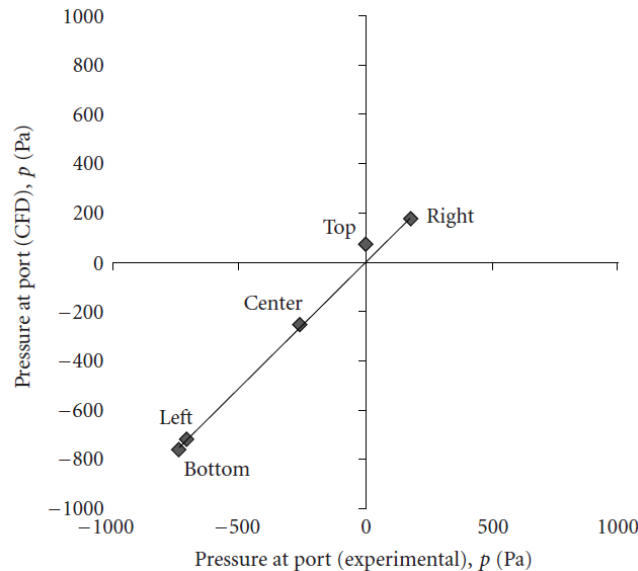


Figure 2.34: Comparison of experimental and CFD pressure values measured at the five taps (Pa) [73]

The result in figure 2.34 represents experimental at the horizontal axis and CFD simulation on the vertical axis. The huge difference observed was due to the probe orientation [73].

In their results, they concluded that the presence of the pressure probes affects the flow velocity as it modifies the field of velocity in its locality.

The probe influence in the probe stem axis front was most pronounced on the  $C_p$ . Figure 2.35 depicts  $C_p$  contours on the longitudinal plane passing through the expected axis of the probe at the  $0^\circ$  location.

It is seen that the coefficient of pressure is higher than 0.25 near the wheel surface at  $30^\circ$ . On the other hand, a low  $C_p$  value of -0.35 is formed near the lower end, just after the wheel arch.  $C_p$  also decrease upward from the location of the  $0^\circ$  where the probe would be inserted later is circled in the figure 3.35.

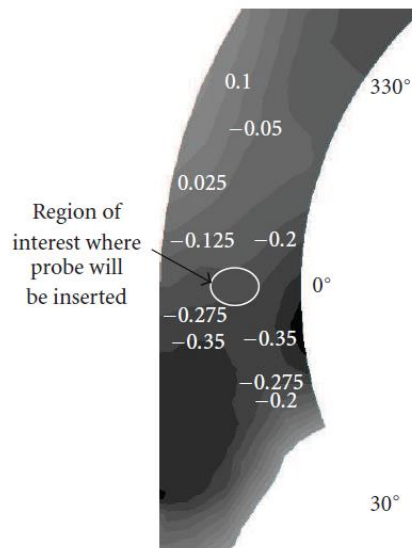


Figure 2.35: Contours of pressure coefficient ( $C_p$ ) on longitudinal (X-Y) plane at  $0^\circ$  without the probe [73].

Comparing with figure 2.35, figure 2.36 shows the  $C_p$  contour on the plane when the probe has been inserted. It is seen from figure 2.35 that  $C_p$  value goes higher than -0.25 immediately after of the tip of the probe. The  $C_p$  value is 5% higher near the region of the probe as compared to that in figure 2.36, which shows a clear probe interference.

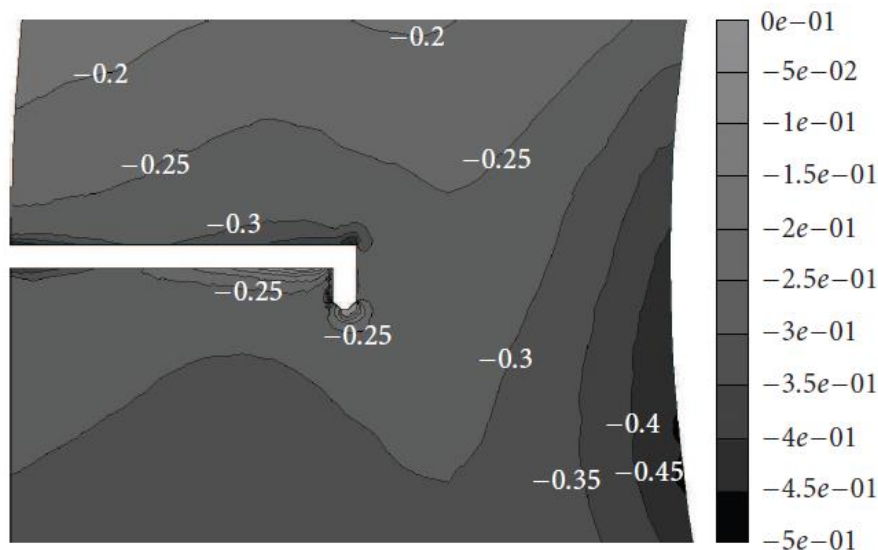


Figure 3.36: Contours of pressure coefficient ( $C_p$ ) on longitudinal (X-Y) plane with the probe at  $0^\circ$

More so, the velocity longitudinal component effect can also be seen with and without the probe. Figure 3.37 shows the longitudinal velocity contour inside the wheel arch where the probe would be placed at  $270^\circ$ . The longitudinal velocity where the probe would be place (the circle) is expected to be  $4.5\text{m/s}$ .

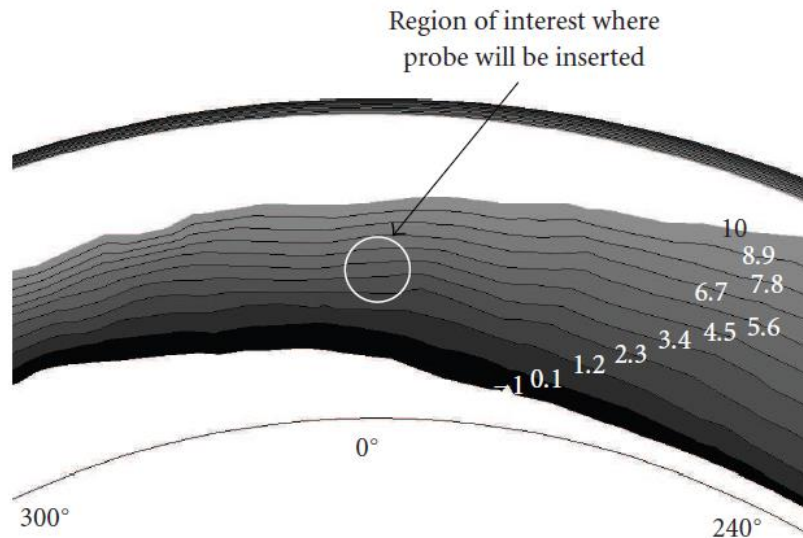


Figure 2.37: Contours of longitudinal velocity component ( $u_x$ ) at  $270^\circ$  inside wheel arch on longitudinal ( $X$ - $Y$ ) plane without the probe.

Figure 2.38 shows the longitudinal velocity contour after the probe has been placed in the marked circle as seen in the previous figure. Although the region also has a  $4.5\text{m/s}$  longitudinal velocity as expected from figure 2.38, the probe effect can be seen clearly in the region below the head of the probe. In this region, the velocity is seen to be lower than  $3.2\text{m/s}$ .

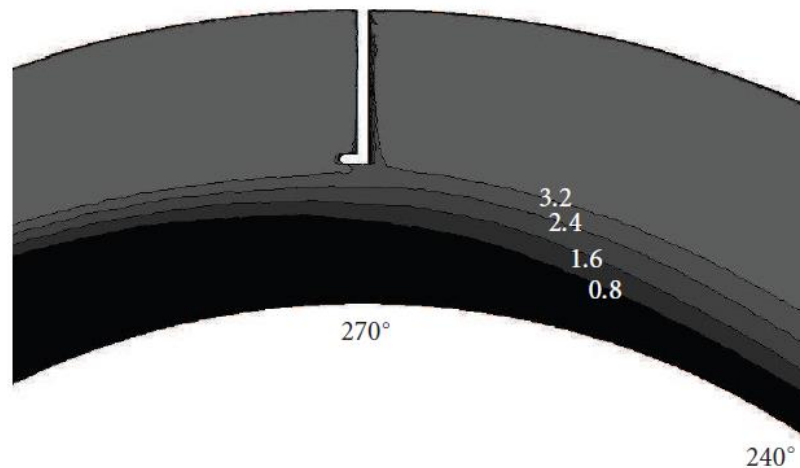


Figure 2.38: Contours of longitudinal velocity component ( $u_x$ ) inside wheel arch on longitudinal ( $X$ - $Y$ ) plane with the probe at  $270^\circ$ .

The overall probe influence can be seen on table 2.5. This interference in each of the directions can be quantified when considering the direction of the flow variable that the probe mostly influences. Table 2.5 shows a brief outline of the probe interference at both locations.

Table 2.5: Outline of influence of the probe at the investigated locations ( $d$  = probe diameter).

Probe Location	Ahead of probe	Behind probe	Below probe head	Inward	Outward
$0^{\circ}$	3.d	3.d	5.d	2.d	2.d
$270^{\circ}$	6.d	1.d	7.d	2.d	1.d

#### 2.4 EXPERIMENTAL INVESTIGATION ON CONTROL VALVE CONDITION MONITORING USING ACOUSTIC AND VIBRATION FOR FAULT DETECTION

Control valves are very important component in any control system, playing a key role in ensuring that the entire control system runs efficiently. When valve fails, it can lead to not only loss in production, but also high cost in their maintenance. One common technique in most plants for valve maintenance is based on condition monitoring of the valve so that when any form of failure occurs, they can be replaced [74]. Intan Najiha et al [74] used an acoustic emission technique in order to detect valve seat leakage early. They conducted a valve leak tightness test for internal leak to be detected despite how challenging it was. They used different statistical analysis parameters including variance, maximum frequency amplitude, and standard deviation in order to distinguish between healthy and unhealthy control valve. They developed and then tested a real time acoustic emission system of measurements. In their research, they used a 1-inch globe valve with a Cv of 14 that allows a maximum leakage rate of 34ml/min. For a healthy valve, they carried out leakage experiment on 0.5, 4, 12, 24 and 32ml/min. For the unhealthy valve, leakage rate of 41, 64 and 60ml/min was used. In their result from frequency domain analysis, they proved that the amplitudes from the acoustic emission signals increases to a higher value, exceeding the amplitude of the normal condition. The variance and standard deviation values also increased than normal. They however did not consider how different opening position on the valve affect the statistical parameters that they considered in their research.

U. Bogumil et al [75] conducted measurement and analysis of cavitation on a pressure-reducing valve. In practical terms, they performed evaluation on whether a pressure-reducing valve is under any form of cavitation in a water distribution system during operation. They collected measurements over a day period to cover both high and low demands. Noise generated by the valve, hydraulic cavitation index, the noise spectra and

acoustic cavitation index have all been used for this characterization as the four methods can provide enough information with high certainty for cavitation diagnostics. In their hydraulic measurement analysis, they observed that cavitation occurs at larger VOP (above 55%) as a result of higher flow rate, leading to higher velocities and hence, lower dynamic pressure as being depicted in figure 2.39.

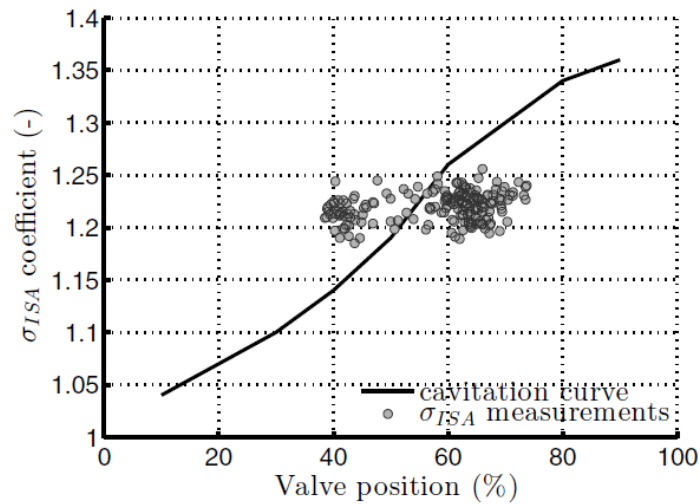


Figure 2.39: Measured coefficient of sigma against VOP and the valve calibration curve

From their analysis on the valve noise level, they deduced that the noise level being emitted by the valve fell between 103 and 105.5dB and remains reasonable constant for VOP between 40 and 75%.

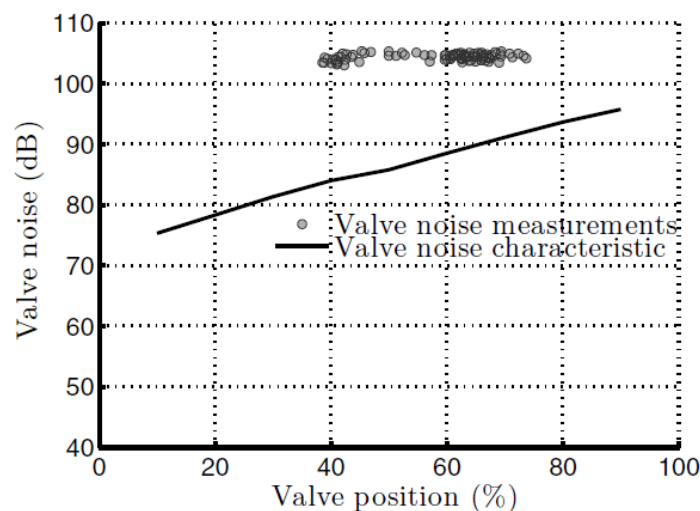


Figure 2.40: Valve noise measurements against VOP and the characteristics of the valve noise.

The measurement from the noise suggest that flashing/cavitation are the major contributors to the noise, not the turbulence, as the noise recorded is independent on the VOP since noise from turbulent flow should increase, in theory, when VOP increases.

However, they did not carry out this experiment using different flow rate.

L Zeng et al [76] studied vibration and noise in control valves that are induced by flow. They observed noise and vibration by changing continuously, the pressure ratio. They explained that different pressure fluctuations and noise under same condition could occur depending on the pressure ratio changes. In their experiment, they placed the microphone 1m outside the throat of the valve seat. For each opening, they used pressure ratio in 0.05 increment from 0.2 to 0.9 and from 0.9 to 0.2. Their result showed that the sound mutation is observed at two-pressure ratio for each of the opening, which depends on the two different pressure ratio adjustment as seen in figure 2.41.

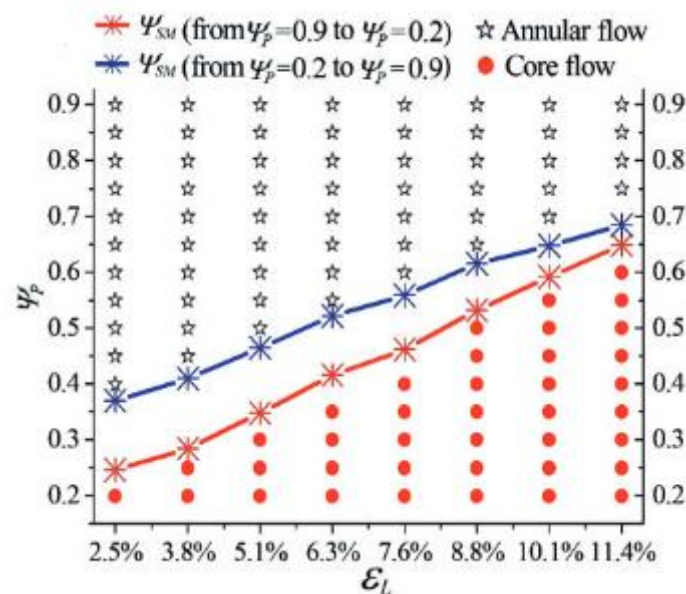


Figure 2.41: Pressure ratios and flow pattern regarding the sound mutation.

The two pressure ratio increased and their difference decreased for each of the VOP. The mutation of the sound decreases and VOP increases and then later disappears. Sound mutation changes continually, the pressure ratio at VOP of 11.4% or less.

W Kaewwaewnoi et al [77] investigated the relationship that exist between fluid leakage and acoustic emission generated by the fluid in a valve. They characterised the acoustic emission generated signals from the internal gas and liquid leakage through the valve.

They studied the influenced factors effect for the internal pressure levels, leakage rates, the valve type and size on the acoustic emission parameters. They conducted their experiment using a globe and a ball valve using different valve seat sizes (25.04, 50.8 and 76.2mm inside diameter). The leakage rate they used ranges from 1 to 6l/min at inlet pressure maintained between 100kPa to 700kPa. They found out that the AE obtained signal characteristics from the water leakage peaked over at 20-200 kHz operating frequency range. The compressed air leakage frequency gave a peak amplitude of 150 KHz resonant frequency as seen in figure 2.42. These results have been plotted in relation to the power spectrum density.

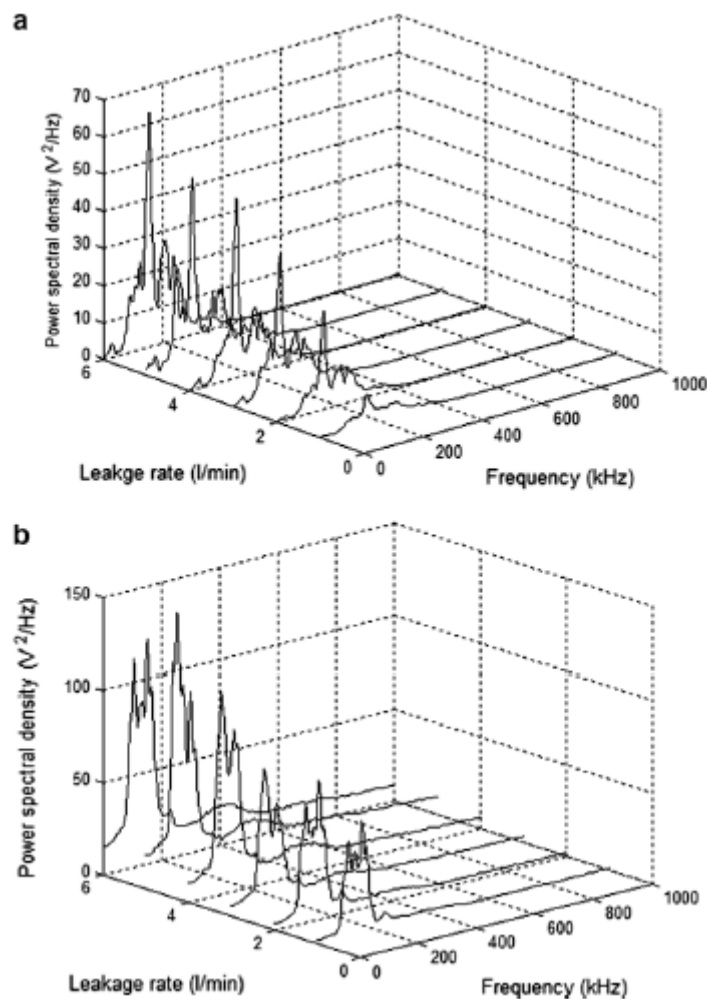


Figure 2.42 AE valve leakage signal characteristics for the 25.4mm ball valve in frequency domain at the change of leakage rate. (a) Compressed air leakage and (b) fresh water leakage.

They again, compared the effects of the type of valve on the acoustic signal generated. They showed that the acoustic signal RMS value for the globe valve was more than that of the ball valve as seen in figure 2.43 for various leakage rate and inlet pressure. They suggested that these differences might be due to the Cv generated by the globe valve which was lower than the ball valve.

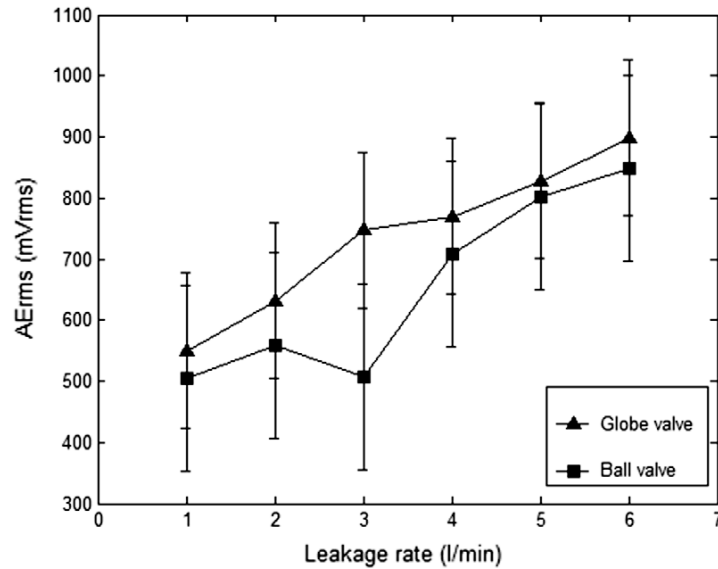


Figure 2.43: Valve type effect on acoustic emission RMS value

They concluded that the sound power theoretically derived was in good correlation with the signal power. In addition, the parameters extracted during the valve leakage for water can be used in qualitatively predicting actual leakage rate.

They however did not show how these signals vary with the leakages for the different valve opening positions.

Acoustic emission can be defined as the transient generated elastic waves as a result of rapid energy release from localised source within a material under stress.

Published literature, mostly presented in this chapter has suggested that many studies have carried out analysis using numerical method on the local flow behaviour within the control valve. A methodical investigation into how these flow parameters vary at different valve sections as the effects of flow field parameter features changes with the characteristics of the valve is yet to be quantified. In those studies, only qualitative analysis have been conducted where the effects of the flow paths geometrical features have been investigated. For this present study, systematic numerical and experimental

investigations have been conducted in quantifying the effects of flow behavioural features on the valve. For this purpose, several techniques using both intrusive and non-intrusive methods have been developed to characterise flow behaviours for when the valve is healthy and when fault has occurred and their results compared. For effective comparison purposes, several local and global flow features have been obtained.

The MHP, vibration and acoustic techniques have been chosen for this research

## 2.5 RESEARCH OBJECTIVES

The research objectives developed for this research are outlined as follows based on the literature review.

- To investigate the effect of the different probe lengths and heights on the control valve flow characteristics under single-phase condition from inlet to outlet using the Multihole probe (MHP).
- Development of flow measurement indicators in establishing flow behaviours and detecting fault under Single-phase flow condition inside a control valve using the Multihole probe (MHP).
- Development of a vibration indicator in establishing fault in a control valve under single-phase condition.
- Development of a vibration indicator in establishing fault in a control valve under Multi phase condition.
- Development of an acoustic indicator in establishing fault in a control valve under single-phase condition.
- Development of an acoustic indicator in establishing fault in a control valve under Multi phase condition.

## 2.6 LITERATURE SUMMARY

Literature reviews have been presented for diagnosing flow inside the control valve using various tools, with these tools also used as indicators in detecting faults and the effect they have on the valve performance, clearly highlighting knowledge based gaps in this research. The MHP for flow diagnostics and vibration and acoustic techniques for conditioning monitoring have been presented. All of these researches have their limitations as analysis on these flow parameters on the control valve under various conditions have been conducted. Furthermore, better and comprehensive understanding

on the flow structure within the control valve under various flow and operating condition, linking global with local flow characteristics were also presented. This chapter has showed different numerical and experimental methods in establishing the valve behaviour and predicting fault inception and development inside the valve. Some of these methods presented includes using CFD, pressure probes, acoustics and vibration techniques.

## CHAPTER THREE

### 3.0 NUMERICAL AND EXPERIMENTAL DESIGN METHODOLOGY

---

*In order for the main aim selected for this research to be properly investigated, both numerical and experimental set up have been properly designed to achieve maximum output. The numerical setup has been used for experimental validation under steady state condition until fully developed flow have been achieved. Detailed solver settings and boundary conditions is also given in this section under single phase condition*

*On the experimental setup, information on the design of the test rig including the equipment used such as the pressure sensors, microphone, flowmeter (air and water), fivehole pressure probes and the data acquisition system have been presented. It describes the procedure for the measurement system of flow diagnostics. It also provides description on the calibration procedures of all the measurement systems, their specifications and the techniques used. Finally, uncertainty and repeatability analyses have also been included.*

### 3.1 INTRODUCTION TO CFD

CFD (Computational fluid dynamics) is a technique used for system analysis in many application that include flow fields, heat transfer and other phenomena based on computer based simulation due to their complexity.

CFD simulations can help provide, in a system, more data samples. The cost it takes to carry out an experiment, which would include the variable cost involved, like hiring for the facility that would be used or even the lab technician going to carry out the experiment, is proportional to the amount of tested data points and configurations. Furthermore, using CFD codes at no extra cost, can be used in producing extremely large volumes of result, and makes such research studies quite cheap to carry out such as to optimise an equipment performance [78], if the right settings such as the solver, boundary conditions, etc. are correctly and accurately inputted and the results from CFD validated.

#### 3.1.1 WORKING OF CFD CODES

There are three very distinct techniques for numerical solutions. They are the spectra method, finite element and finite difference method. Finite volume method, which is a method of special finite difference, is common for CFD codes. Its numerical algorithm includes the integration of equations that governs fluid flow over the control volume of the flow domain, discretising or converting these resulting integral equations by an iterative method, into an algebraic solution system.

CFD codes makes use of numerical algorithms in solving the problems of fluid flow. To achieve the set aims, all of CFD packages provide a sophisticated user interface where problem parameters can be inputted with the corresponding result examined. Hence, the CFD codes comprises of three main elements.

- Pre – Processor
- Solver
- Post – Processor

The pre-processing stage consists of a user, inputting the flow problem to the CFD program to get a solution. The user defines the model geometry that needs solutions

called the computational domain. The geometry is then divided into a smaller numbers of non-overlapping regions of an appropriate size. This process is called meshing. Selecting the chemical or physical phenomena where modelling would take place, defining the properties of the fluid and making specification on the suitable boundary conditions at the cell, which corresponds with or touch the domain boundary, all included at the stage of pre – processing [79].

The solver comprises of the setting up of the numerical model chosen and then the solutions monitoring or computation. The following include the setting up of a numerical model.

- Setting up of the suitable model, which include the turbulence, energy, multiphase, etc.
- Determining what property of material would be used whether it is solid, fluid, mixture, etc.
- Inputting the condition, which the material will operate on.
- Inputting the boundary conditions.
- Suggesting the solver settings.
- Setting the initial conditions.
- Setting up also the convergence monitor.

In computing of the solutions, the following points needs to be done.

- The conservation equations (mass, energy and momentum), which are discretized are iteratively solved. A certain number of iterations needs to be achieved before a solution converges.
- A solution converges when there is a negligible change in variable in the solution from one iteration and the next iteration. Residuals helps in providing a mechanism in monitoring this trend.
- The converged solution accuracy depends upon the setup of the problem, grid independence, grid resolution and the physical model accuracy.

Post processing shows the results of the examination/simulation obtained and the model revision based on the obtained results. They include viewing the results and extracting those wanted data, calculation of those necessary parameters needed for analysis, on the anticipated results and if not, changes should be made in terms of the boundary conditions, meshing, under relaxation factor, etc.

### 3.1.2 GEOMETRY

The CAD model of the control valve used for this project is shown in figure 3.1. The figure shows both the side and the top view of the valve. In CFD however, not all parts of the valve is required for fluid flow. Thus, merging of faces and cleaning up the geometry to obtain the best possible flow path has been carried out on the body within the valve. To avoid any computational error in the measurements, addition pipe length of 600mm each has been added at each end of the valve, and to reduce errors such as pressure obtained from every simulations as seen in figure 3.2.

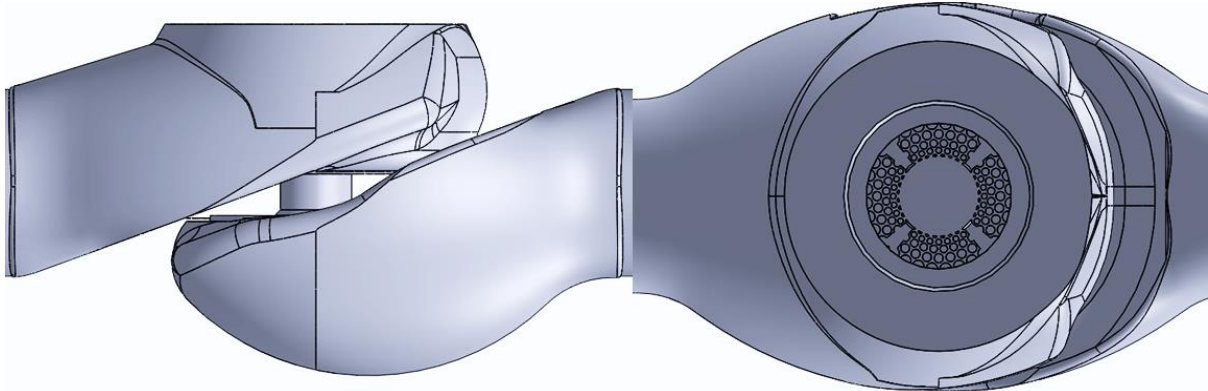


Figure 3.1: CAD model of control valve showing side and top view

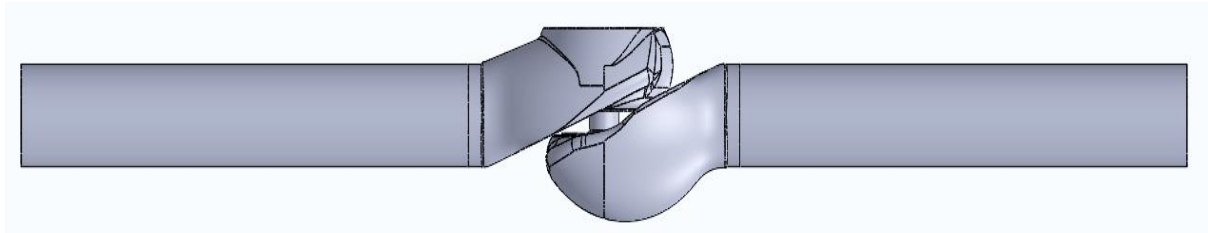


Figure 3.2: Numerical geometric model of the control valve

### 3.1.3 MESHING

Hybrid meshing concept has been used for the flow domain meshing. This simply means that two form of meshes was created in the flow domain. Hexahedral elements have been used to mesh the pipes at the inlet and outlet, whereas tetrahedral elements have been used to mesh the main valve body. Tetrahedral elements was used for the valve body due to the complex nature of its geometry, as it would allow for cell clustering on the flow domain. Hexahedral elements was used on the pipes at both the Inlet and Outlet because of:

- The simple geometry of the pipes and hence, can be able to generate a very low skewness on these pipes
- Due to lower numerical diffusion, they give a better and more accurate results

The meshing of the flow domain has been done using the given sizes:

- Minimum size of the valve body = 0.398mm
- Maximum size of the valve body = 4mm
- A constant size of 5mm was used for both pipes.

Using the above mesh sizing has been observed to give a reasonable and accurate result predicted by using the CFD solver. Therefore, the same sizing has also been used for both probes head (Conical and hemispherical). The figure 3.3 shows the meshing used for this study.

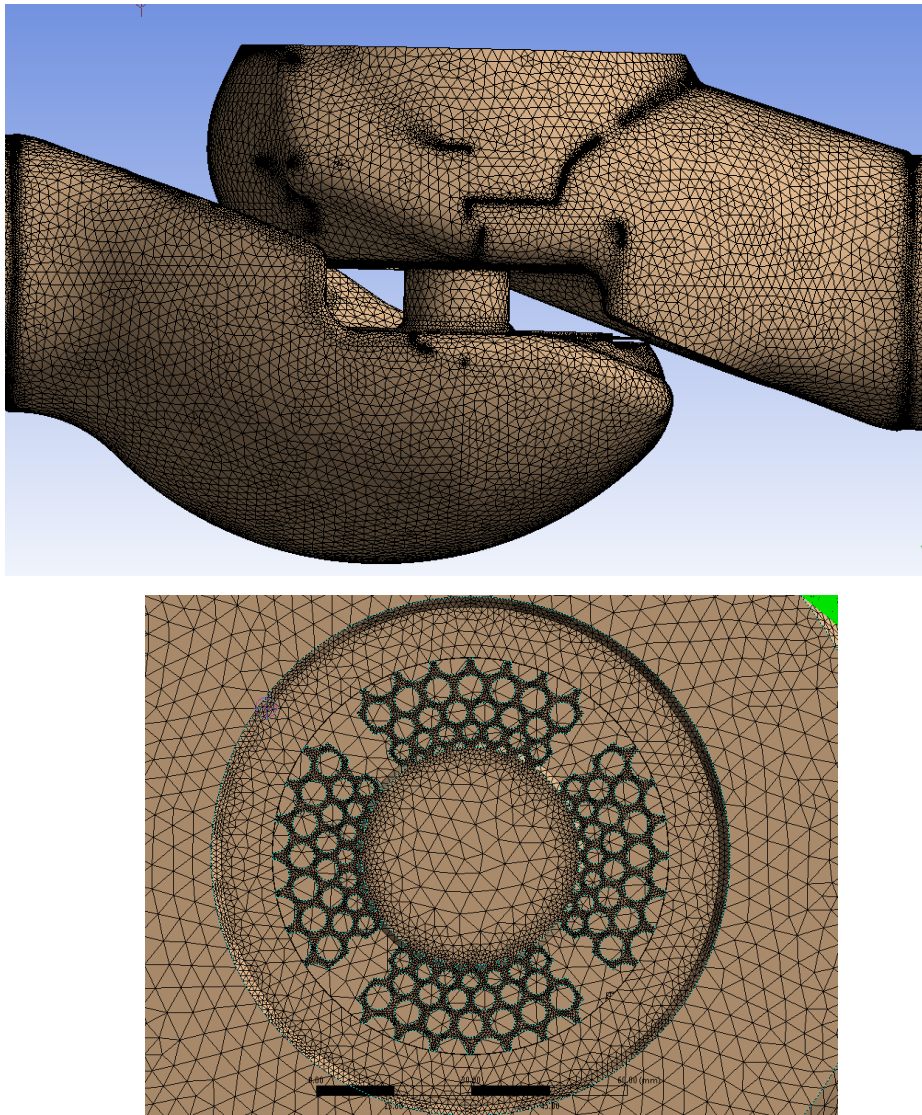


Figure 3.3: Meshing of the flow domain

### 3.1.4 SELECTION OF PHYSICAL MODELS

Since this analysis is only focused on incompressible flow (water), the solver that would be used in carrying out this analysis is the pressure-based solver. This is because the flow velocity in incompressible flow is much lower compared to the speed of sound under water ( $\sqrt{\gamma RT}$ ), making their compressibility effects negligible [79]. This reason therefore makes pressure based solver recommended for such cases. Also in this approach, the fluid density remains constant and the parameters of the primary fluid flow being solved iteratively, within the flow domain, is the pressure. However, for the analysis of compressible flow, density based solver is used.

The control valve, for this present study, has been designed in such a way that it can, at a particular valve opening position (VOP), constantly deliver a flow rate. Hence, making the flow steady, within the pipeline. This can further be supported because all the boundary condition used throughout the CFD simulation remains constant, giving rise to the steady state solver being used for this study.

Furthermore, according to the industry standards [79], it is been perceived that such types of control valves, with almost certainty, experience turbulent flows inside them making the use of turbulence modelling for accurately predicting the valve and its trims capacity. There are various types of turbulence models available to CFD package. Each turbulence model available to CFD has its disadvantages and advantages available in any CFD workbook. For flow inside the control valves, k- $\omega$  model [80] (k for turbulence kinetic energy and  $\omega$  representing the specific heat of dissipation) has proved effective in turbulence modelling within such control valves. The key reason why the k- $\omega$  model was used is its level of accuracy in modelling of high velocity gradients ( $du/dx$ ) that occurs within the trims because of the area reduction and expansion available for flow to occur. The k- $\omega$  model can be further divided into two set of equations. The Standard k- $\omega$  option and the SST (Shear-Stress Transport) option. The k- $\omega$  SST model has been preferred in this research because [79]:

- Both the transformed k- $\epsilon$  and the standard k- $\omega$  models have been multiplied by their blending function and are both combined together. This blending function for the standard k- $\omega$  model is designed to be 1 near the wall region, and this blending function is zero (0) away from these wall regions, activating the transformed k- $\epsilon$  model.

- Turbulent viscosity definition has been modified to be able to account for the turbulent shear stress transport of the flow.

The features given above makes the  $k-\omega$  SST model more accurate and reliable for wider varieties of flows such as transonic shock waves, aerofoils, flows of adverse pressure gradient, etc., when compared with just the standard  $k-\omega$  model. One other modification made in this model ( $k-\omega$  SST) is the addition of a cross-diffusion term in its  $\omega$  equation with a blending function in ensuring that its equations behave correctly in both zones (far field and near-wall) [79].

The SST  $k-\omega$  denotes two eddy-viscosity model equations because of the combination between the  $k-\omega$  and the SST (shear stress transport) equation. Combining  $k-\omega$  with SST allows the equation to be even useable under a flow with low Reynolds number and provides an accurate result at near the surface viscous-sublayer. Moreover, the SST formulation also changes its behaviour to  $k-\epsilon$  in free-stream, thereby avoiding the common  $k-\omega$  problem of being too sensitive to the turbulence inlet free-stream properties [79]. Table 3.1 shows the fluid property for this particular study.

Table 3.1: Material Properties

Material	State	Flow	Density Kg/m <sup>3</sup>	Viscosity kg/m-sec	Specific Heat J/kg-K	Thermal Conductivity W/m-K
Water	Liquid		998.2	0.001003	N/A	N/A

The table 3.2 shows a summary of the operating conditions used for the current study.

Table 3.2: Operating conditions

Parameter	Condition	Comments
Gravity	On	For accurate prediction of mass flow rate
Operating pressure	10 <sup>5</sup> Pa	Atmospheric condition
Specified Operating density	0 kg/m <sup>3</sup>	For accurate vertical flow modelling

Surface measurements has been taken on the specific trims [78] used for this research. The results shows that SLM (selective laser melting) trim roughness amplitude can go as much as 1mm. More so, from figure 3.4, it is shown that the trim surface is characterized not only by high peaks, but the surface core region can be said to be significantly rough when compared to other trims. Furthermore, a parameter called the Sdr (developed interfacial area ratio) parameter of that of the SLM surfaces is quite higher when also

compared to the EDM (electron discharge machining) trims. This parameter called the Sdr parameter is the ratio of the interfacial area where its value denotes how much percentage of the actual surface area is greater when compared to the surface area of the engineering drawing.

Within the environment of CFD, the roughness height for the XLO8 SLM trims is 8mm. This value has been used to be able to correctly validate the results of CFD using the result from the flow loop with the same flow and boundary conditions. In general however, there are geometrical imperfections common to the features of the SLM trim which are inherent and they include features like chip formation, asymmetry, reduced flow area etc. These features can occur on a large scale and can significantly affect the characteristics of flow and therefore, needed to be integrated into the CFD. Because there has never been any quantitative analysis carried out in evaluating these imperfections for this present study, an estimated value from previous experimental result has been used.

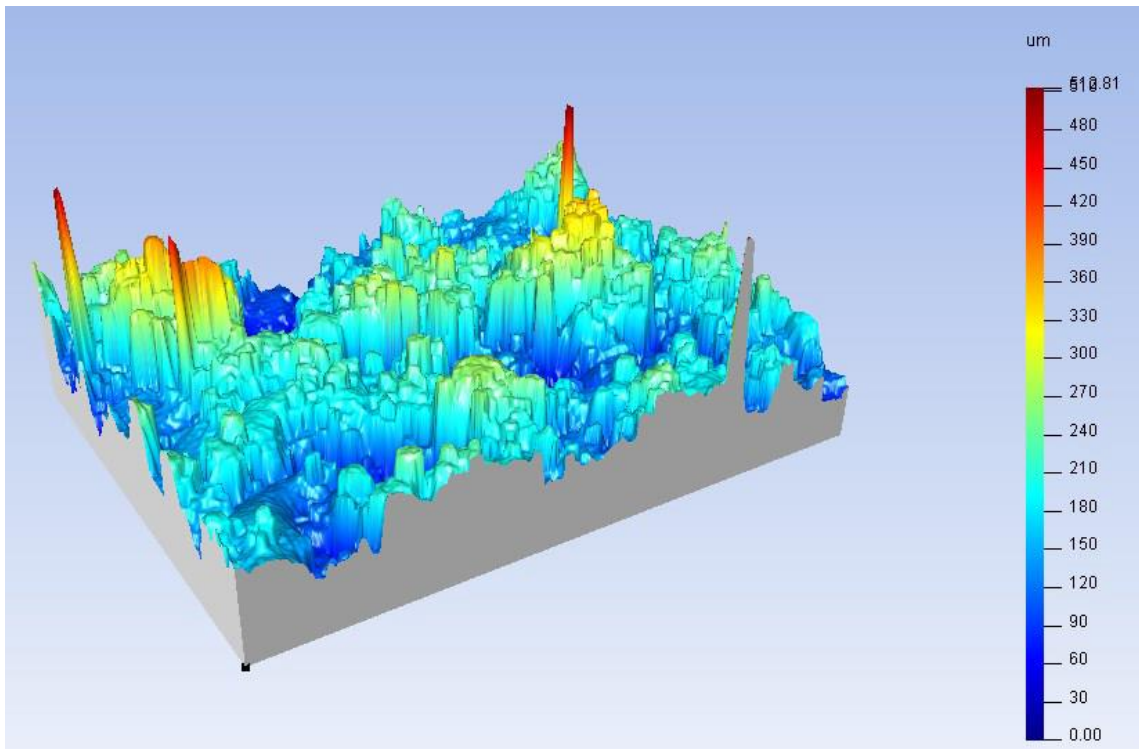


Figure 3.4: Surface finish of an experimental trim [78]

### 3.1.5 SOLVER SETTINGS

In order to predict accurately, the behaviour of the fluid flow inside the flow domain, settings on the application based solver are required. These required settings include:

- Pressure – Velocity Coupling

- Gradient
- Spatial Discretisation

Navier-Stokes equations are solved in the form of discretisation. This refers to pressure on velocity linear dependency and vice versa. Therefore, a coupling of pressure–velocity is required in predicting the pressure distribution with some level of accuracy inside the flow domain. For this study, the SIMPLE algorithm for coupling pressure–velocity has been used due to the fact that it converges the solution faster and is most times, quite accurate for flows inside and around the domain. By using SIMPLE (Semi-Implicit Method for Pressure Linked Equations) algorithm, velocity field approximation can be obtained by solving the equation of momentum. The pressure gradient term can be calculated by using the distribution of pressure from an initial guess or the preceding iteration. The equation of pressure is formulated and then solved in obtaining the new distribution of pressure. The velocities are then corrected with a new set of calculated conservative fluxes.

Gradients are required for constructing scalar values at the faces of the cell, for computing terms of secondary diffusion terms and velocity derivatives. For this study, the Green–Gauss Node–based evaluation of the gradient was used. This method reconstructs at the node, the linear function exact values from the surrounding cell–centred values on random meshes that are unstructured, by solving the problem of constrained minimization, preserving a 2<sup>nd</sup> order spatial accuracy.

The solver from CFD stores the scalars discrete values at the centres of the cell. However, face values are vital for the terms of the convection and must, from the centre values of the cell, be interpolated. This can be accomplished by using the upwind spatial discretisation scheme. When we say Upwinding, we mean that the face value is derived from the quantities at the cell upstream or the upwind relative to the normal velocity direction. For this study, second order upwind schemes were chosen for turbulent rate of dissipation, momentum, pressure, and turbulent kinetic energy. Using this second order upwind scheme leads to increase in obtained result accuracy.

### **3.1.6 CONVERGENCE CRITERIA BOUNDARY CONDITIONS**

It is often necessary for the solution to converge. When the solution converges, it indicates the stability of the solution and the flow parameters variations with respect to

the solver iterative process have been eliminated. Therefore, only a solution that is converged can be used in predicting the flow problem solution with some level of accuracy.

The convergence criterion by default for the continuity, the turbulence parameters and 3-D velocities is 0.001 in the CFD solver. This simply means that the solution would reach convergence when the change in the 3-D velocity, continuity and the turbulence parameters reaches to the fourth decimal place. However, in many real applications, this default criterion does not necessarily show that there are no more solution parameters changes because in this case, it was noticed that the solution converged quickly even though the monitored parameters have not yet reach stability. Hence, this criterion was reduced to 0.000001 as it is often advised for the convergence parameters to be monitored rather than depending on the convergence criteria at default.

For this study, mass flow rate was monitored at the inlet and outlet flow domain faces throughout the process of iteration. The solution was considered converged by the time both faces of the mass flow rate has become very stable.

The specified boundary types for the specified place in the geometry have been listed in table 3.3.

Table 3.3: System Boundary conditions

Boundary name	Boundary type
inlet	Mass flow-inlet
outlet	pressure-outlet
Trim (XL08-040)	Stationary
Trim roughness	0.008m

### 3.1.7 SCOPE OF NUMERICAL WORK

For this work, numerical studies conducted are categorised in the following:

- Validation with respect to a set of experimental data.
- Incompressible flow analysis for various lengths and height of the probe geometry.

### 3.2 EXPERIMENTAL SET UP

There are several ways in which cavitation/faults can be detected as outlined in the literature review. It can either be through visual observation, airborne acoustic and vibration measurements and using hydrophones to detect waterborne sounds. A new design technique by using a five-hole pressure probe for detecting the incipient of cavitation in the control valve would be investigated.

The control valve that has been used for this research is BV500 Globe Low Pressure Process valve from Weir control valves limited. The valve is fitted specifically with regards to this application requirement. Some of the main features of the valve include:

- Low recovery of pressure
- Low maintenance cost
- Wide process fluid variety control which makes it to last longer
- Accurate process fluid control
- Stable guiding of the cage
- High flow capacity



Figure 3.5: 4 inch BV500 Globe Control Valve [45]

The cage trim allows the valve plug to pass through, thereby causing the opening or closing of the valve. Stack of disk makes up this cage thereby forcing the fluid to pass through the little opening and hence, causing it to lose the fluid pressure.

There are different variables that are associated with the cylinder array construction.

They are

- The cylinder size
- Number of the rows which then controls the number of stages of the fluid drop in pressure
- Number of the cylinders per row

Flow tests will be conducted at five various flow conditions. They are:

1. Maximum available flow (1200LPM)
2. 1100LPM (91.6% of maximum flow)
3. 1000LPM (83.3% of the maximum available flow)
4. 900LPM (75% of the maximum available flow)
5. 800LPM (66.6% of the maximum available flow)

The different flow rates listed above are as a result of the pump setpoints, creating flow inside the loop.

For the multiphase experiments, three different airflow rates will be performed for each of the above flow rates. They are;

1. 19.8 LPM
2. 28.8 LPM
3. 38.8 LPM

Tests would be performed in non-vaporising conditions where at each flow conditions; it would be performed at 100% valve opening.

The lists of data would be recorded during the tests measurement:

- Inlet and outlet system static Pressures (in PSI)
- Inlet and outlet system Pressures from the probe measurements (in PSI) for different probe heights and positions
- Inlet and outlet velocity magnitude and components at different probe heights and positions inside the valve
- Water Inlet Temperature (T1 in K)
- Volumetric Flow Rate (Q in  $m^3/hr$ )
- Vibration signatures using accelerometer for the different flow conditions
- Acoustics signatures using a microphone for the different flow conditions

### 3.2.1 METHOD IN FINDING THE VALUES FOR C

The flow equation for a non-choked, incompressible fluids used in this case is:

$$Q = N_1 F_R F_p C_v \sqrt{\frac{\Delta P}{\rho_1/\rho_0}} \dots\dots\dots 3.1$$

Where;

Q = Volumetric flow rate in  $m^3/hr$

$N_1$  = Numerical constant depending on the units to be used.  $N_1 = 0.865$  to find  $C_v$

$F_R$  = Reynolds number factor.  $F_R$  is equal to 1 for a turbulent flow

$F_p$  = Piping geometry factor. Since no any form of fittings are attached to the piping (such as reducers, expander, etc.),  $F_p$  value equals 1 as in this case.

$C_v$  = Flow coefficient. It normally dimensionless but has a derived unit of  $\frac{2 \times 10^{-7} m^3}{s \sqrt{Pa}}$

$\Delta P$  = Differential pressure (P1-P2) between upstream and downstream pressure taps

$\rho_1/\rho_0$  = Relative density. For water flow, its value = 1

Hence, the equation 3.1 becomes:

$$C_v \left( \frac{2 \times 10^{-7} m^3}{s \sqrt{Pa}} \right) = \frac{Q}{N_1} \sqrt{\frac{\rho/\rho_0}{\Delta P}} \dots\dots\dots 3.2$$

The equation 3.2 is true, assuming that the flow is turbulent. For valves with very small  $C_v$  values, turbulent flow will exist always. If it is observed during experiments that the values of  $C_v$  are not that small as earlier mentioned and assumption for the turbulent flow are reasonable, equation 3.2 becomes therefore, the primary equation for the X-Stream valves sizing.

It is worthy to note that Equation 3.2 is only valid for:

- Newtonian fluids
- Conditions that are non-vaporizing

### 3.2.2 THE SPECIFIC TRIM USED

The name given to any particular trim denotes its features and properties the trim comes with. The particular trim that would be used for the experiment is a trim manufactured specifically by Weir valve and control company [45]:

Figure 3.6 shows the control valve trim that will be used for the experiments.

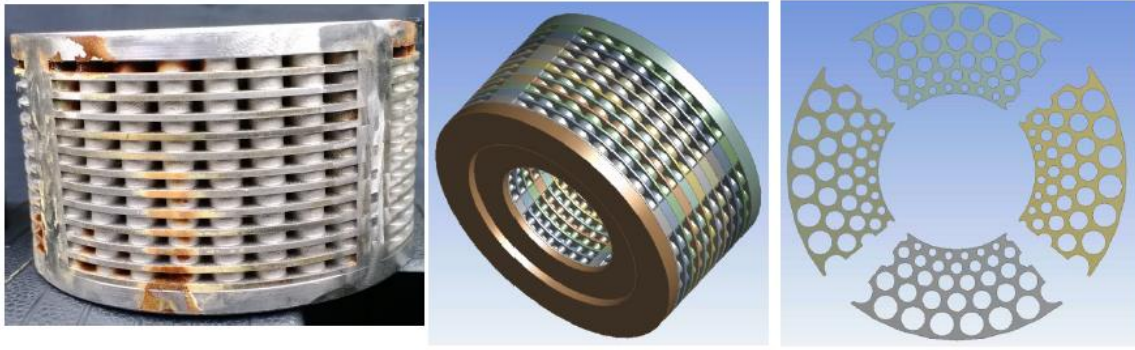


Figure 3.6: Specific control valve trim [45]

### 3.3 TEST SET UP

Figure 3.10 shows the control valve schematic and how the probe is placed inside the valve. It shows where the five-hole pressure probe would be placed.

The single phase and the multiphase experiments are performed under the same flow conditions and setup as depicted in figure 3.7. The difference in setup for the multiphase flow set up include:

- **Air injection**

The air device injection have been installed 25D upstream of the valve inlet. The device is a circular disc installed between two pipeline flanges with eight-air inlet distributed along the circular face of the disc as depicted in figure 3.8.

- **Air mass flow meter**

This has been installed to set and know what the airflow rate is, at every point in time and has been connected to the air injection line as seen in figure 3.9.

The final flow loop schematic for both single and multiphase has been presented in figure 3.10. All sensors and instruments are included in the figure.

The actual flow loop at the University of Huddersfield, used for this research is given in figure 3.11.

Using the experimental detail procedure outlined in BS EN 60534-2-4:5 [18, 78] for quantifying the control valve flow capacity, figure 3.10 and 3.11 shows the constructed flow loop used in this research. The pump used is a centrifugal pump, with a 24.1 kW shaft power at duty point, with a motor power of 37kW at the nominal speed of 2900 rpm.

The rated voltage for the motor is 3-400V at frequency of 50Hz, while that of the rated current is 65Amp. The delivery head of the pump at duty point is 54.7m and 26.2LPM flow rate. The pump stands firmly on a 2-part sand, 4 part gravel and 1 part mixture of cement. The inertia base, which is 250mm deep, is fixed to the lab floor with 4 mounts (anti-vibration), consisting of damping springs with 20mm maximum deflection at optimum load conditions, with a support of 200kg of point load, for each mount.

A flow loop has been developed for the experimental investigation. The flow loop consists of 1mx1mx1m tank that serves as a reservoir for the water. The pipe loop consists of a Polyvinyl Chloride (PVC) pipe. The pump has an impeller made of grade 14 cast iron and its housing is made of cast iron. The shaft connecting the pump and the motor is made of grade 316 steel. The pump is connected the test valve shown in figure 3.10. The valve is a 4-inch globe low-pressure valve fitted with a specialised trim used for this experiment. This valve is extensively used in various chemical processes and flow properties and undergo considerable changes during the operation. The trim used has special features that may result in considerable changes in pressure and velocities through the trim. The A351 CF8M cast has been used in the valve body manufacture. The test valve is controlled with a diaphragm that is operated pneumatically and the actuator controlled using an air supply with 4.5 bar gauge. Non-intrusive pressure transducers have been installed both at the inlet and outlet of the valve to determine the pressure difference. Other equipment used for this research are given in details in the next sub section.

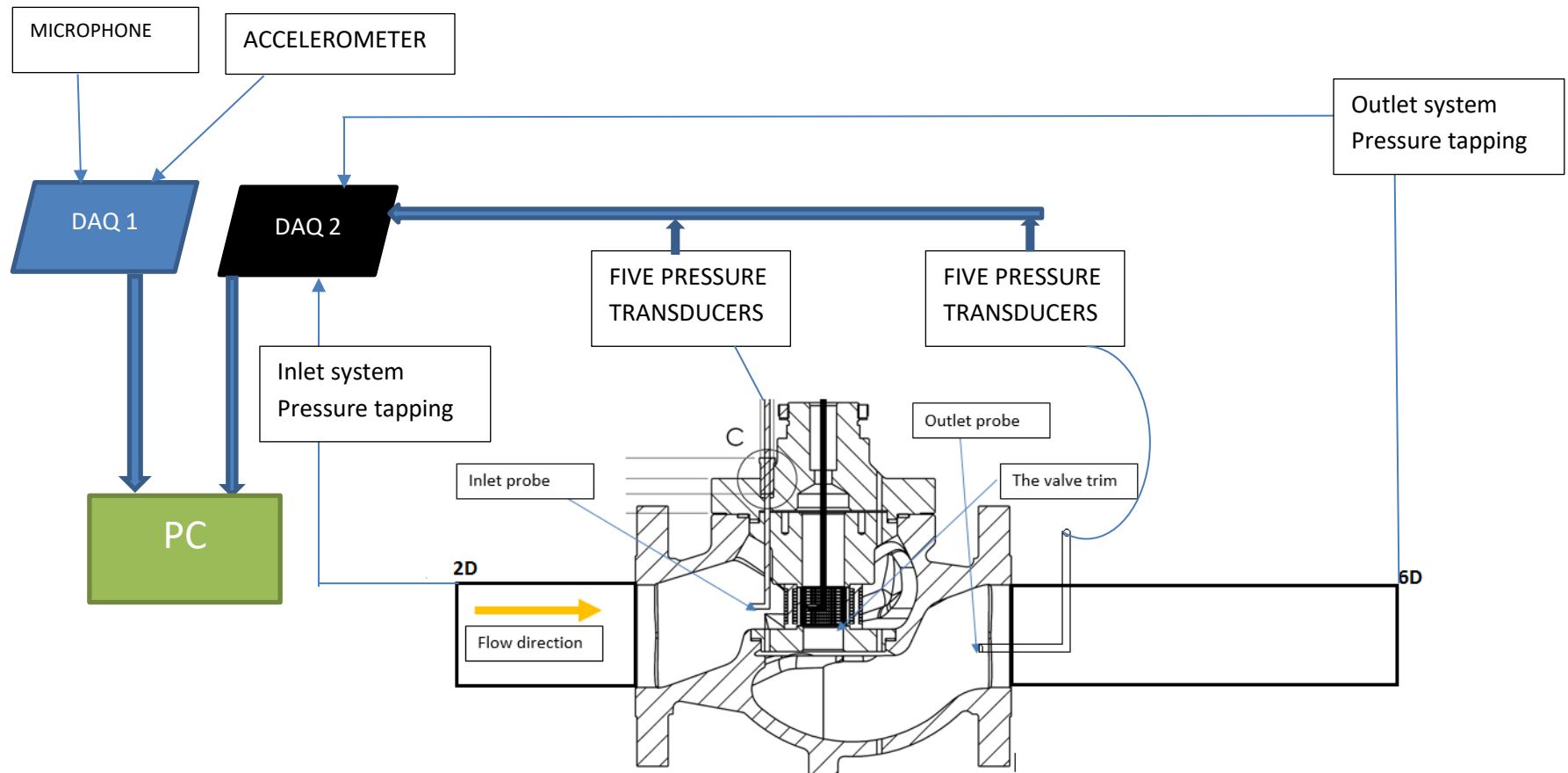


Figure 3.7: Experimental Schematic Design setup

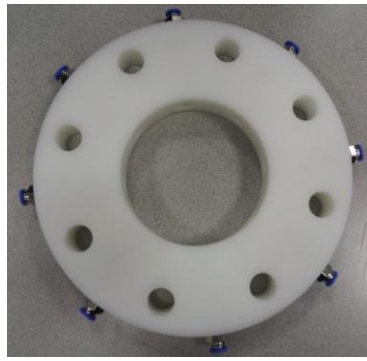


Figure 3.8: Air injection device



Figure 3.9 - Air mass flow meter (Omega FMA 1700/1800)

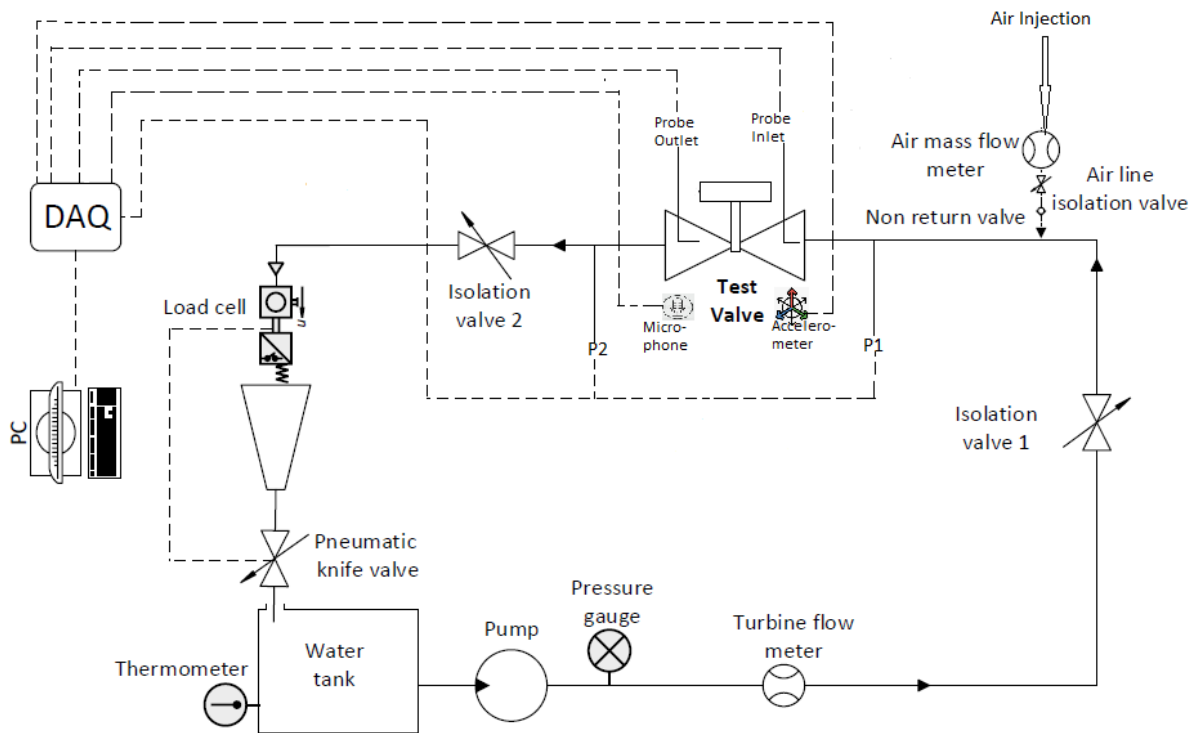


Figure 3.10 - Schematic for the Single and Multiphase flow loop design

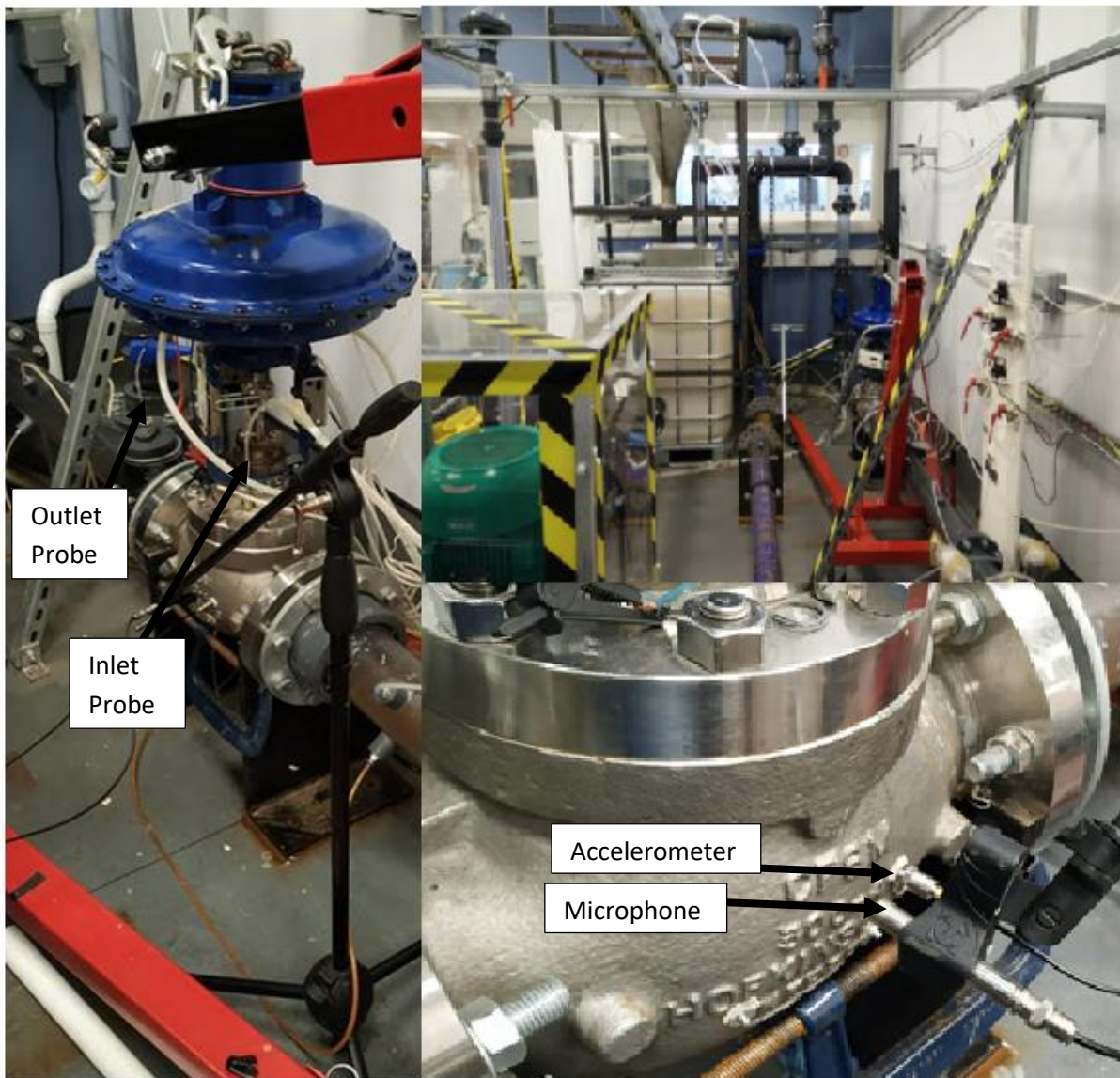


Figure 3.11: Fluid flow loop lab

### 3.4 DIFFERENT SENSORS USED FOR CONDITIONING MONITORING

The different sensors and probe design specification used for this research have been explained. The main functions for the measuring devices are to obtain physical parameters and then transform the parameters into signals that will be collected and stored by the DAQ. In monitoring the condition of the any machine, different sensors and devices can be used to measure and detect these physical parameters such as temperature, noise, acoustic, vibration, current, etc. The next section describes these sensors and devices, including the DAQs used for this study.

### 3.4.1 FIVE-HOLE PROBE DESIGN

The hemispherical probe head have been designed and has been chosen for this experiment. The probe head has a dimension of 5mm in diameter and 1.07mm of individual tapping of the probe (5). The hemispherical is a dome shape with a 2mm fillet while that of the conical head is a 45° chamfer angle. The probe design have been presented in figure 3.12.

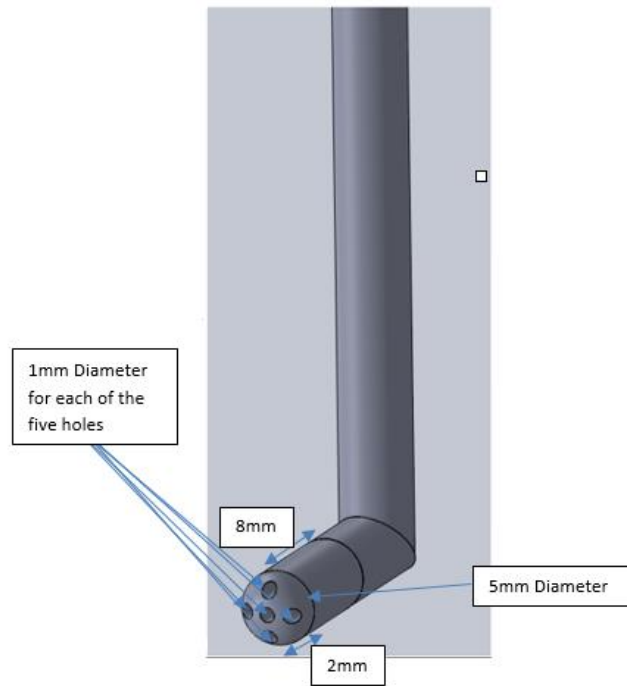


Figure 3.12: Five-hole probe

The total length of the probe head have been chosen based on the position they will be placed inside the valve.

Table 3.4: Inlet and outlet probe positions

Inlet Probe	Outlet Probe
1D	1.5D
0.8D	1.2D
0.5D	0.9D

Where D is the diameter of the valve (100mm or 10cm), in reference to the valve inlet and outlet where the probe will be positioned. Seven different heights have also been taking for both the inlet and outlet probes for the different positions.

Before any of the probes are used, they must first be calibrated using a pitot tube to ascertain the calibration set data before they can be used to measure other flow parameters from the equations already discussed in the literature review.

Calibration of these probes cannot be done inside the valve, as space inside the valve is limited. Therefore, a test section is built with transverse system that can give the yaw and pitch angle rotation during the process of calibration as seen in figure 3.13.

The main purpose for the calibrating of this probe in a flow field that is known is that when these probes are used in a flow field that is unknown, the measured pressures could be used in calculating the magnitude of the flow velocity, velocity components, flow angles, static and total pressures. For the five-hole pressure probe, its purpose is to determine experimentally, a set of the pressures data that will describe the probe response of a known flow field. For the probe application, the yaw, pitch angles, the static and total pressures, the velocity components and the 3-D velocity magnitude can be obtained for the unknown flow field from the pressure being measured and from the set of calibration data. Table 3.5 shows all the nomenclatures that would be used for the calibration that will be described in the next subsection.

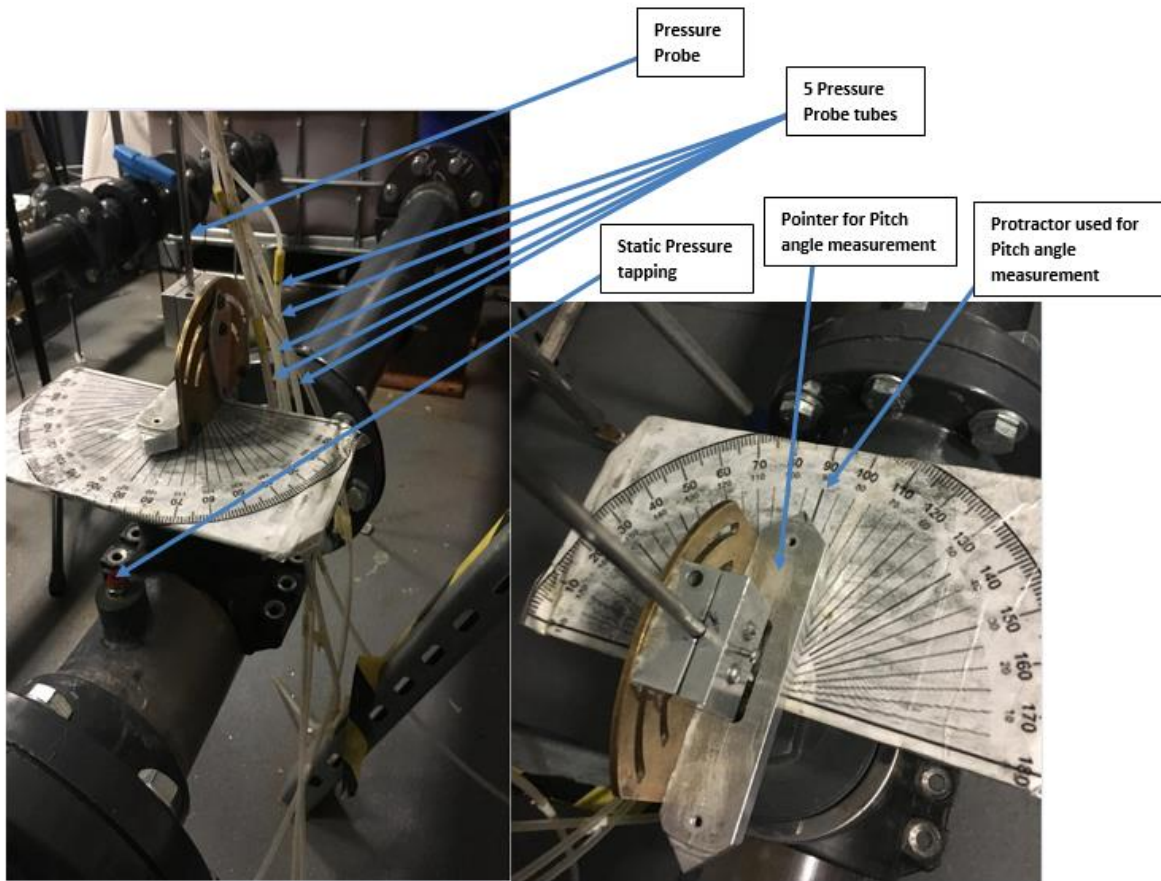
Table 3.5: Calibration nomenclature

<b>Variables</b>	<b>Parameters</b>
$\alpha$	Yaw angle
$\beta$	Pitch angle
$P_1$	Pressure measure at port #1
$P_2$	Pressure measure at port #2
$P_3$	Pressure measure at port #3
$P_4$	Pressure measure at port #4
$P_5$	Pressure measure at port #5
$CP_{total}$	Coefficient of total pressure
$CP_{static}$	Coefficient of static pressure
$CP_{\alpha}$	Coefficient of pitch angle
$CP_{\beta}$	Coefficient of yaw angle

$\bar{P}$	Average pressure
$P_{total}$	Total pressure
$P_{stat}$	Static pressure

Figure 3.13 shows the loop set up test section that would be used for the calibration. Figure 3.13 (a) shows the entire test section that was newly constructed for the calibration. The reason behind this construction was that inside the control valve was short for space, as the probe would need to be rotated during calibration. It was difficult enough to come up with the design to place these probes inside for the measurement, never mind for the calibration. Figure 3.13 (b) depicts the transverse mechanism system for the rotation of the probe.

From figure 3.13, the probe inserted into the known pipe channel has five-holes, which have each been connected to a pressure transducer. Two pressure tapings have been used for the calibration on the pipe section; they are the static and total pressure tapings to record both the total and static pressure. These values should remain constant throughout the process of calibration at a constant velocity of 2.5465m/s. This velocity has been chosen as the entire system velocity never goes above 2m/s at maximum pump flow based on the flow rig setup and configuration. The maximum velocity is that maximum centre line velocity in the velocity profile. There are other various velocity present that are below the centre line making the maximum coefficient for these velocities to be used for lower velocities. In other words, the coefficient from higher velocities can be used for predicting the flow parameters, as the coefficients used for the lower coefficient can also be used in determining the maximum flow parameters.



(a)

(b)

Figure 3.13 (a) Entire newly built test section for the calibration (b) Transverse mechanism for the calibration

The pointer is a system attached to the probe. So when the probe moves at a particular angle, so do the pointer. It can be seen that a protractor is placed below the pointer to record the probe pitch angle with regards to the flow. These angles are recorded in determining the calibration coefficients. To record the yaw angles, the probes are taken out and bent to a particular angle and then placed back inside the known flow field. Figure 3.14 shows the probe used for the calibration and for the flow measurements inside the control valve.

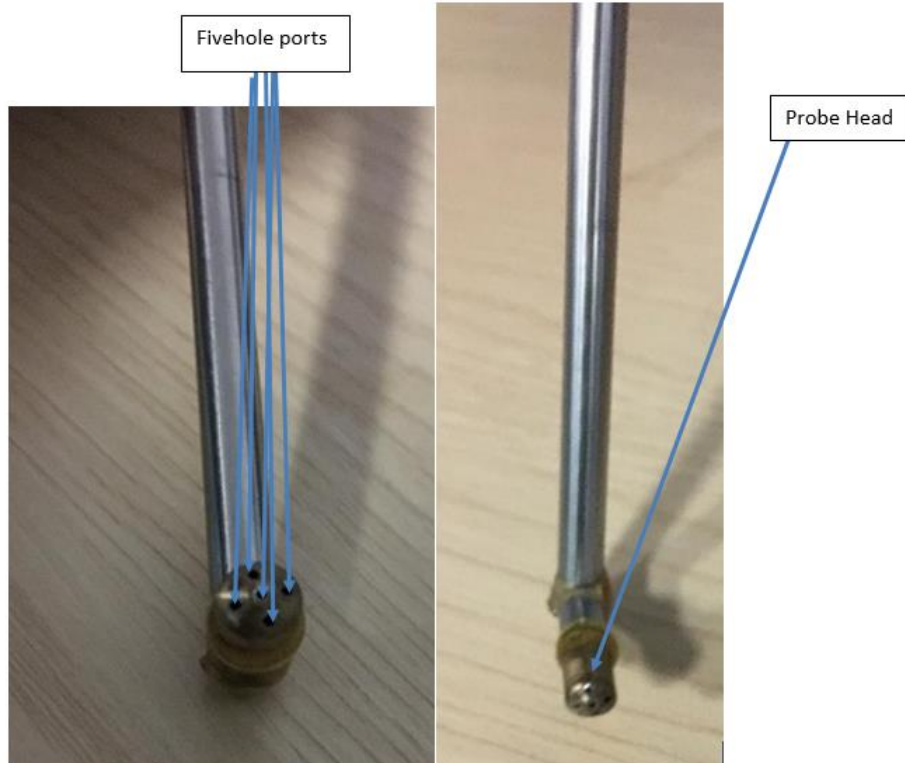


Figure 3.14: Actual MHP with hemispherical head used for the calibration

Seven pressure transducers were used during the calibration. One transducer for each of the pressure port (five in total), and two to measure both the total and static pressures inside the pipe calibration test section. All of the entire seven pressure transducers was connected to a 10Volts DC power supply.

### 3.4.2 VIBRATION SENSOR

This type of device are commonly used for machine condition monitoring, including the control valve. Figure 3.15 shows the particular accelerometer used in this study.



Figure 3.15: The piezoelectric accelerometer sensor [81]

As mentioned earlier in chapter one, faults like cavitation, in control valves can give high and abnormal vibration signatures due to the formation and collapse of bubbles. These vibrations can provide information regarding the health of the valve. As a result, such faults could be predicted and diagnosed by the monitoring of the vibration signals, which can be done using the accelerometer. For this research, the IEPE (small size and highly sensitive) model CA-YD-1182 has been used by gluing the stud on the valve body close to the valve trim. The frequency range for the accelerometer is between 0 to 15 kHz and operates at a temperature range from -40 to 120°C. APPENDIX A shows a summary of the characteristics of the accelerometer. In chapter 5, further information will be presented showing how the vibration signals have been collected and how they have been used in predicting fault occurrence.

Pressure fluctuation occur the most inside the valve trim, hence the need for the accelerometer to be placed at this location on the valve body for best possible vibration signal. Due to the sensitive nature of this sensor, PVC pipes and rubber rings have been used for the piping system in this research in order to decrease any noise interference during experimentation.

### 3.4.3 MICROPHONE (ACOUSTIC SENSOR)

Similar to vibration, noise level increases when fault such as cavitation occur inside the valve, hence, the need for a microphone in monitoring and obtaining information in regards to these faults. A free field microphone with model number CHZ-223 has been used to obtain the acoustic signatures. It comprises of two parts, the sensor itself and a preamplifier. Figure 3.16 shows the type of acoustic sensor used for experimentation.



Figure 3.16: Microphone Acoustic sensor

To obtain the best possible sound, the microphone has been placed very close to the valve body as it was noticed that when placed further away from the body, acoustic signatures was rarely obtained. The microphone diameter is 0.50inch (12.7mm), operates at a temperature between -10 and 50°C, and has sensitivity of 250 Hz 31.6mV/Pa. Summary of the technical specification for the microphone used for this study is given in APPENDIX A. Again, due to the sensitive nature of this sensor, PVC pipes and rubber rings have been used for the piping system in this research in order to decrease any noise interference during experimentation [82].

Again in chapter 6, further information has been presented showing how the acoustic signal has been collected and how it has been used in predicting fault occurrence.

#### 3.4.4 MICROPHONE PRE-AMPLIFIER

This is the second part of the microphone with model type YG-201 ICP [83]. The preamplifier helps the microphone to condition the signal from the output of the sensor. The preamplifier is depicted clearly in figure 3.17.



Figure 3.17: Microphone Preamplifier

It can operate at a temperature range between -40 and 85°C. It has a power requirement of between 2mA to 20mA with a 4mA nominal power. It has a BNC type connector and has a ½ inch (12.7mm) by 2.8 inch (70mm) dimension including the connector. Summary of the microphone preamplifier specification is given in APPENDIX A.

#### 3.4.5 PRESSURE TRANSDUCER

Both at the valve inlet and outlet, the pressure level or changes has important influence on the valve performance, together with the flow rate, hence the valve Cv. Also, the tubes from the MHP probe uses the pressure transducer to measure their respective pressure

before using the combined pressure to calculate the valve flow parameters, hence the need for the pressure transducers. The pressure are measured at the inlet, outlet and inside the valve through the inserted pressure probes for the experimental setup. Pressure transducers with same specifications have been used for this study, though all recalibrated to ensure accurate pressure readings. Impress Sensors and systems makes the pressure transducer with model number IMP-C0053-9A4-CAV-02-000. The pressure range for all the transducers are from -1 to +10 Bar G. The operating temperature is  $-20$  to  $+80^{\circ}\text{C}$  with accuracy  $< \pm 0.25^{\circ}\text{C}$ , with DC supply output voltage of 0.5 to 4.5V. These pressure transducers have been chosen according to the predicted pressure value estimates expected from the experimental setup. Figure 3.18 depicts the pressure transducer used for this research work. Also, summary of the pressure transducer technical specification is given in APPENDIX A. Of the 12 pressure transducers, one was positioned 2D upstream of the valve, one 6D downstream of the valve, 5 for each of the pressure probe (one probe at the inlet and the other at the outlet, both inside the valve at various positions).

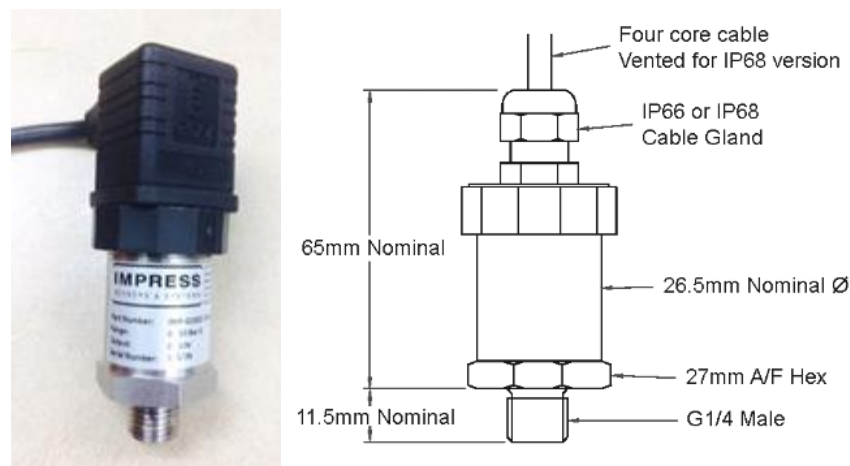


Figure 3.18: Pressure transducer (IMP pressure transmitter)

### 3.4.6 WATER FLOW METER

The rate at which the fluid flow or being pushed by the pump to any desired point is known as the pump capacity. In general, this fluid flow rate can be measured either in LPM (liters per minutes), GPM (Gallons per minutes) or  $m^3/sec$  (meters per second). According to researches, flow rate in is an influential factor to detecting faults, especially cavitation/flashing, hence the need for the monitoring of the flow rate on the test section of the control valves during experimentation. For this study however, the OMEGA-WE-

SDC pulse emitter water turbine flow meter has been used. Figure 3.19 depicts the 4 inch WE-SDC series water flow meter.

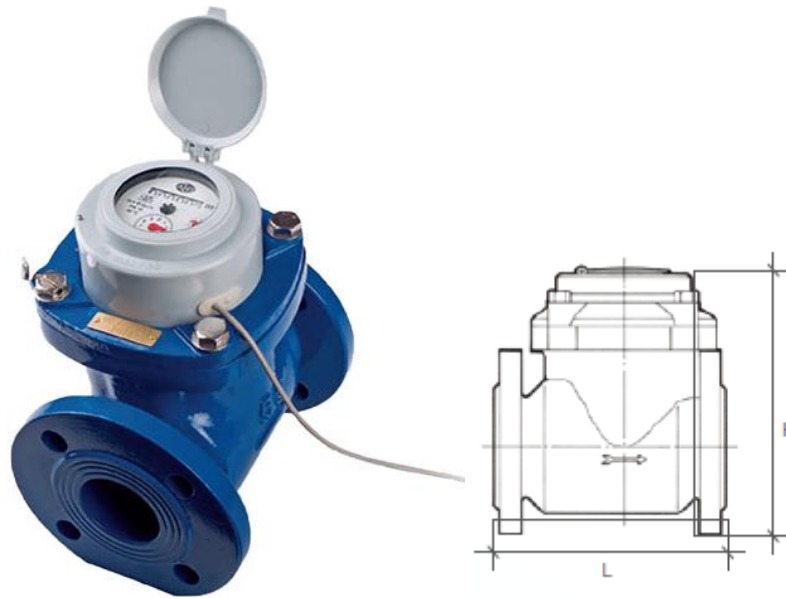


Figure 3.19: OMEGA-WE-SDC pulse emitter water turbine flow meter

The flow meter is designed in ensuring minimum head-loss at high flow-rate. The OMEGA-WE-SDC has a super-dry dial type meter with a 360° rotating clockwork. Summary details of the technical specification for the turbine flow meter is given in APPENDIX A. The flow meter has been installed 10D upstream of the control valve for accurate measurements. This particular flow meter also functions through a direct reading from a digital screen.

### 3.4.7 AIR FLOW METER

This research also makes use of an air flow meter. This type of flow meter is a mass flow type meter of the FMA 1700/1800 series, manufactured by OMEGA Engineering INC as seen in figure 3.20.



Figure 3.20: FMA 1700/1800 OMEGA air flow meter series

This mass flow meter measures the how much of air is injected into the control valve. It works in an ambient temperature of 0 to 50°C with a transducer power of 12 VDC. The technical specification for the air mass flow meter is given in APPENDIX A.

### 3.4.8 THERMOMETER

A dual channel k type temperature thermocouple thermometer has been used for the purpose of this experiment. This thermometer is depicted in figure 3.21. This has been used in measuring the water temperature both at the inlet and outlet of the valve, for single and multiphase flow condition, hence determining the water density in the calculation of the valve Cv from the water temperature table properties.



Figure 3.21: Thermometer

It consists of the temperature sensor itself (type K) and the LCD screen to display the measured temperature.

### 3.4.9 POWER SUPPLY

For this research, the rapid dual rail DC regulated power supply has been used as depicted in figure 3.22.



Figure 3.22: Rapid Power supply unit

The Rapid PSU has been used to power all the pressure transducers. The NI DAQ also used the PSU as ground for the device for the purpose of controlling the power to the DAQ within predictable limits. The input power supply voltage is 230 volts AC with supply frequency of 0-to 15V DC. A summary of the power supply unit specifications is given in APPENDIX A.

### 3.4.10 DATA ACQUISITION SYSTEM

Two data acquisition system have been used for this research, a national instrument DAQ for all the pressure transducers and Global sensor technology (GST) DAQ for the acoustic and vibration sensors.

#### 3.4.10.1 The YE6232 16 channel DAQ from GST

The aim of using this type of DAQ is to record and collect signals from the acoustic and vibration sensors. This DAQ displays the different signals on the PC via an inbuilt oscilloscope either on a curve plot or in form of actual signal values where they can be saved for further analysis. This type of DAQ is the voltage/Integrated electronic piezo electric (IWPE) with 16 channels, made by a Sinocera. This DAQ is depicted in figure 3.23.



Figure 3.23: YE6232 16 channel DAQ from GST

It captures the voltage signal from the sensors and converts to digital signal. The technical specifications can be seen in APPENDIX A. The accelerometer and the microphone are connected using coaxial BNC cable while the DAQ is connected using a USB port to the PC. The sampling frequency used by the DAQ was set at 96 KHz and the data collected for a sampling time of 30 seconds. The collected data are stored on the PC, which are later analysed in both time, and frequency domain using various statistical features with the aid of MATLAB codes in order to determine the valve characteristics and performance.

#### 3.4.10.2 USB X Series from NI

The NI USB series is a DAQ that has been used in collecting the pressure transducers signals during experiment. Different analogue input channels have been configured for each of the transducers. The NI DAQ record and stores the voltage signal coming from the different transducers. Figure 3.24 depicts the NI USB X series DAQ used for this research. After all the AI pressure ports have been configured using volts as the scaled units with signal input range of 4.5 max and 0.5V min, the acquisition mode was set at N samples. 200 samples is obtained per 7.5 seconds at sampling rate of 1.5 KHz.



Figure 3.24: NI USB X series DAQ.

The specification details for the NI DAQ have been given in APPENDIX A. All the settings have been done through the DAQ assistance, with the aid of LabVIEW code. The code has been designed in such a way that the data stores in an excel sheet for all the pressure reading on different columns after each reading.

The next subsection explains the calibration procedures that have been adopted for this research thesis.

## 3.5 SENSORS AND INSTRUMENTS CALIBRATION

### 3.5.1 FIVE HOLE PROBE CALIBRATION

#### 3.5.1.1 INTRODUCTION

Five-hole probes are flow instruments that measure fluid pressure along the tip of the probe. When the probe is calibrated properly, the information on the three components of the fluid velocity can be obtained, as well as the dynamic and static pressure. The design for a modern MHP flow velocity flow measurements is based on Pitot tube principle. Minute errors in the probe tip machining and the pressure taps location introduce errors in the measurement that only calibration can eliminate. The calibration of the probe requires the insertion of the probe into a uniform flow field that is known, traversing it along yaw and pitch angles and then measuring the corresponding pressures from each tap. Calibration procedures used for this research is described in section 3.5.1.2.

### 3.5.1.2 CALIBRATION PROCEDURES

For any instrument, including the MHP, the calibration requires the exposure to series of combination of parameter values that will require the data to be read, stored and preparation of mathematical operation before the instrument can be used as a measuring device [84]. The parameters that is expected to be obtained after the calibration include flow magnitude and direction, total and static pressure at the measurement point. All of these obtained quantities are functions of measured pressure from all of the pressure taps on the probe tips. The numbering of the pressure taps for the fivehole prove is given in figure 3.25.

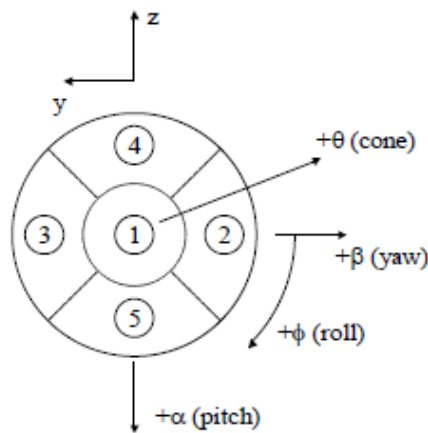


Figure 3.25: Five-hole pressure probe tapping numbering [84]

The probe orientation with respect to the oncoming stream has been defined by two angles for this calibration. They are the yaw and pitch angles ( $\beta$  and  $\alpha$ ) respectively. The collected data from the calibration are discrete data. When the instrument is used as a tool for measurement, the measured quantities fall within the discrete calibration data. Figure 3.26 shows how the probe orientation angles have been defined with regards to the free stream velocity where  $\beta$  and  $\alpha$  are the yaw and pitch angles respectively.

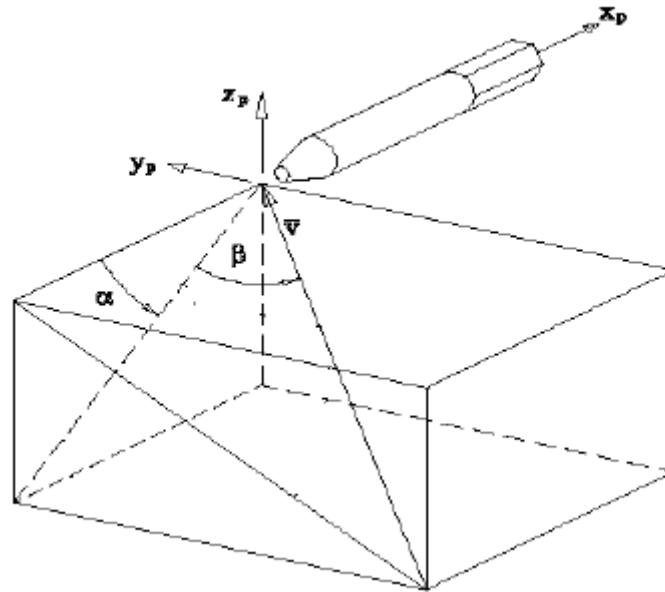


Figure 3.26: Angles defining the orientation of a probe with respect to the free stream Velocity [84]

The basic parameters for the calibration are the angles that defines the probe orientation. The calibration procedure is as follows:

- At the constant velocity of 2.55m/s, the pressure from the five taps from the probe are recorded for the different calibration  $\beta$  and  $\alpha$  angles (+15 to – 15 for both  $\beta$  and  $\alpha$ ). The static and total pressure are also recorded.
- The data for each of the different combination for  $\beta$  and  $\alpha$  are recorded for the calibrated probe.
- The measured pressure from the five-hole probe, which is given in voltage are then converted to pressure (Pascal).
- The local velocity vector at the measurement point is characterized fully by the four chosen variable, the total pressure coefficient, static pressure coefficient, yaw angle and pitch angle.
- These quantities are determined as functions of the two non-dimensional pressure coefficients formed by the measured pressure  $b_\alpha$  and  $b_\beta$ .
- Based on the numbering in figure 3.10, the following coefficients have been defined in terms of each pressure measured from each hole.

First coefficient to be calculated is what is called pseudo-dynamic pressure,  $q$ . It is defined as;

$$q = P_1 - \frac{P_2 + P_3 + P_4 + P_5}{4} \dots\dots\dots 3.3$$

Coefficient q has no physical significance but it will be shown later as it will be used to relate measured pressure to the different parameters.

- Next is to calculate the coefficient of pitch ( $CP_\alpha$ ) and yaw ( $CP_\beta$ ), coefficient of total pressure ( $CP_{total}$ ) and static pressure ( $CP_{stat}$ ) which are all defined as:

$$CP_\alpha = \frac{P_2 + P_4 - P_3 - P_5}{2q} \dots\dots\dots 3.4$$

$$CP_\beta = \frac{P_2 + P_5 - P_3 - P_4}{2q} \dots\dots\dots 3.5$$

$$CP_{total} = \frac{P_1 - P_{total}}{q} \dots\dots\dots 3.6$$

$$CP_{stat} = \frac{q}{P_{total} - P_{stat}} \dots\dots\dots 3.7$$

For each combination of  $\beta$  and  $\alpha$ , the respective port pressure,  $P_1$  to  $P_5$  are measured and recorded.

The calibration surfaces for the total, static, pitch and yaw coefficient values are shown in figure 3:27, 3.28, 3.29 and 3.30 respectively with all figures drawn on same scale.

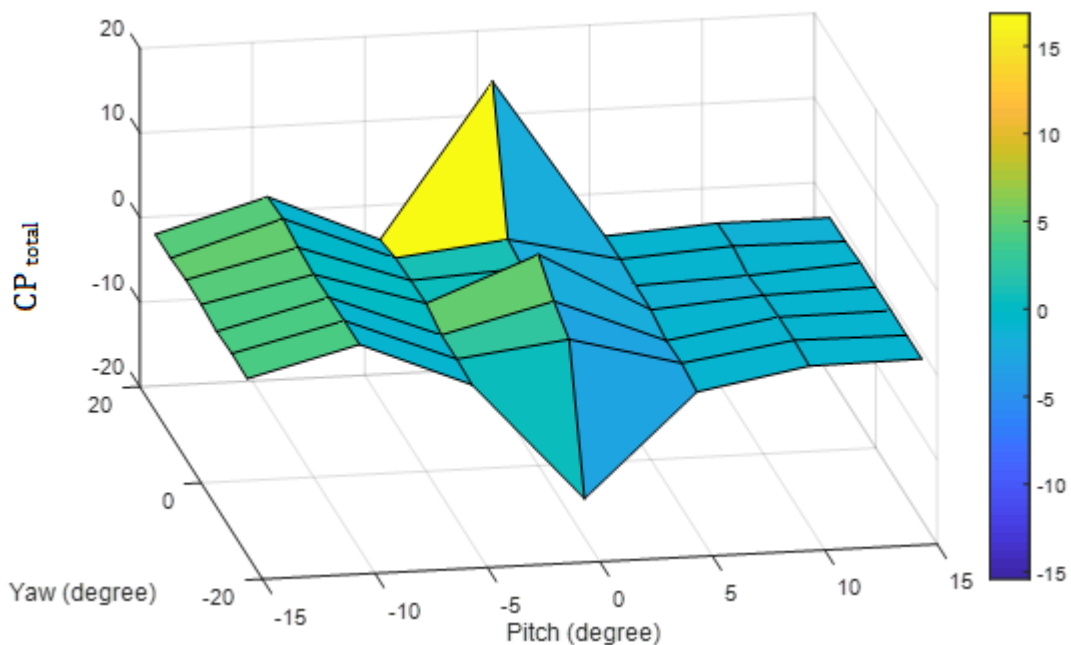


Figure 3.27: Calibration surface for  $CP_{total}$

Figure 3.27 represent a look up table where  $\beta$  and  $\alpha$  can be found in terms of values of  $CP_{total}$ . The figure enables the visualization of the function in terms of their surface. It can be seen that almost constant except for 0 degree pitch angles where variation of the  $CP_{total}$  can be notices across the yaw angles. It is seen that the maximum coefficient on the surface plot is around 15.

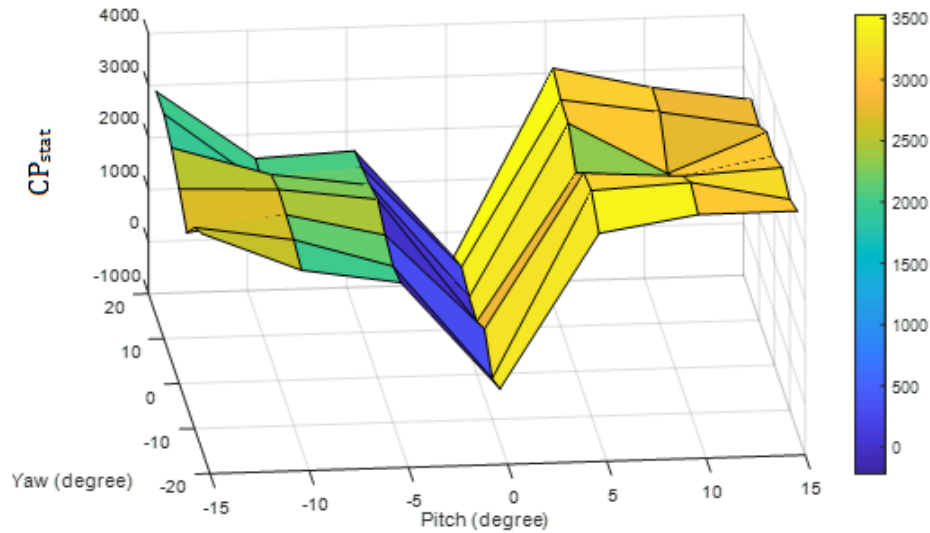


Figure 3.28: Calibration surface for  $CP_{static}$

Figure 3.28 shows the variation of  $CP_{stat}$  for the pitch and yaw angles.  $CP_{stat}$  Increases from 0 as the pitch angles increases in magnitude. This shows a representation for what the  $CP_{stat}$  value should be for a certain pitch and yaw angle.

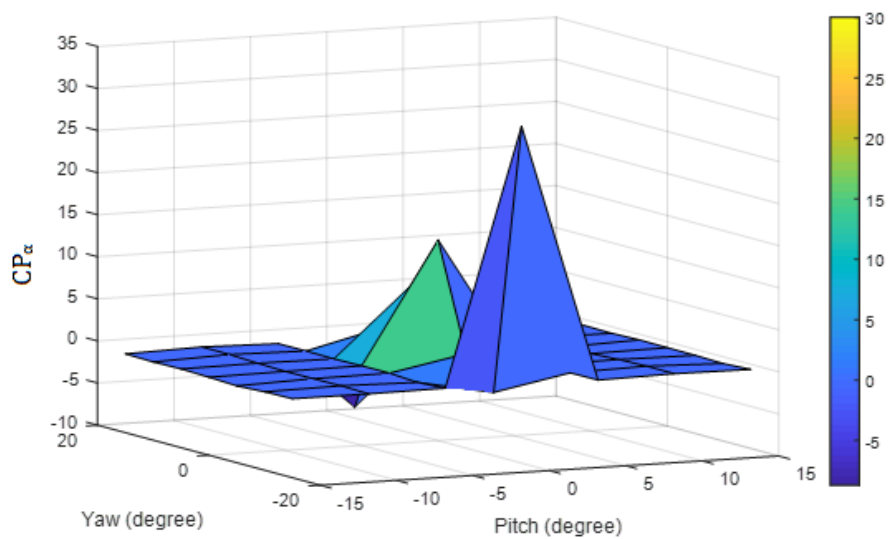


Figure 3.29: Calibration surface for  $CP_{\alpha}$

Figure 3.29 depicts the calibration surface for surface for  $CP_\alpha$  for pitch and yaw at  $\pm 15^\circ$ .

Since the yaw angle setting has been fixed for the probe calibration, the surface plots can be fitted between the values of yaw  $\beta$  as well as between the values of pitch with a constant flow velocity. The pitch and the yaw angles corresponds to the coefficients that balances the probe. The pitch  $CP_\alpha$  value can be seen to be nearly the same for the different pitch angle except for 0 degree where it varies across the different yaw angles. The maximum  $CP_\beta$  can be seen to be around 30.

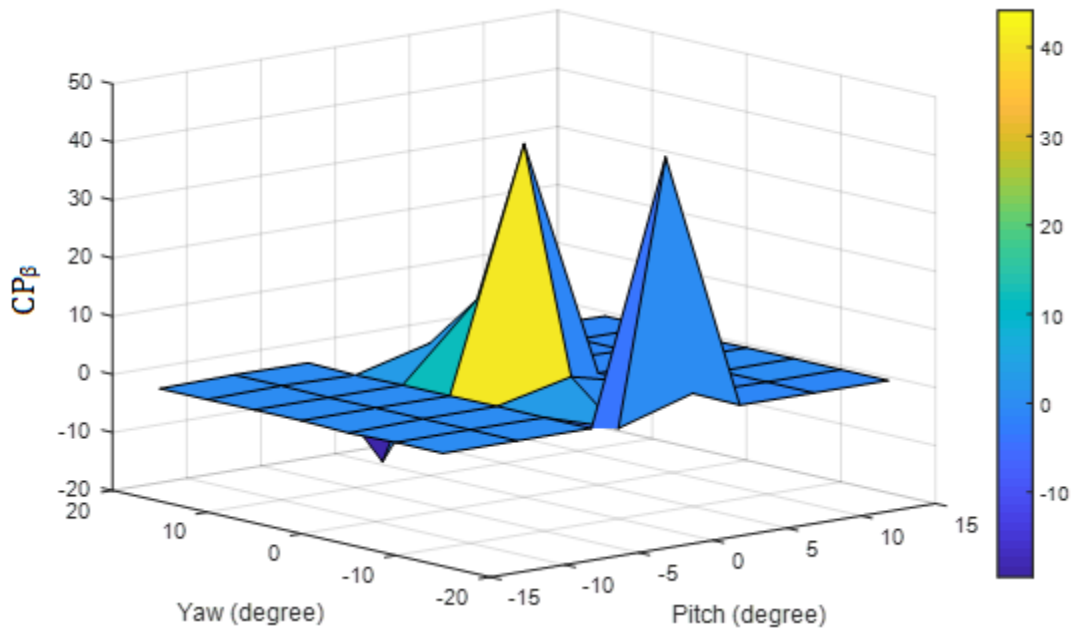


Figure 3.30: Calibration surface for  $CP_\beta$

The corresponding calibration surface for pitch and yaw values are shown in figures 3.29 and 3.30. All figures are drawn to the same scale and for the sake of clarity, only surface of pitch and yaw responses are shown.

The figure depicted in figure 3.30 is the calibration surface for surface for  $CP_\beta$  for pitch and yaw between  $\pm 15^\circ$ .

Since the pitch and the yaw angles setting were also fixed for the probe calibration, the surface plots can be fitted again, between the values of pitch and yaw at the same constant flow velocity. The pitch  $CP_\beta$  value can be seen to be nearly the same for the different pitch

except for 0 degree where it varies across the different yaw angles. The maximum  $CP_\beta$  can be seen to be around 40.

**3.5.1.3 DATA REDUCTION PROCEDURE**

After the calibration of the probe, the MHP can then be used for flow condition determination in a flow field that is unknown.  $CP_\alpha$  and  $CP_\beta$  are calculated from the recorded ports pressure. A sixth order regression formula was used for the compilation of the result. Equation 3.8 [85] describes how the polynomial was formed using  $CP_\alpha$  and  $CP_\beta$ :

$$f(x_1, x_2) = a_0 + \sum_{n_1=1}^2 a_{n_1} x_{n_1} + \sum_{n_1=1}^2 \sum_{n_2=n_1}^2 a_{n_1 n_1} x_{n_1} x_{n_2} \dots \dots \dots 3.8$$

Where f can be any of the dependent variable  $\beta, \alpha, CP_{total}, CP_{static}$  and  $a_0$  to  $a_n$  are the least square polynomial coefficients. For equation 3.8 [85],  $x_1$  represents  $CP_\alpha$  and  $x_2$  represents  $CP_\beta$ . There are 28 coefficients for the 6<sup>th</sup> order polynomial equation and the statistical properties (e.g.  $R^2$ ) have been calculated using, what is called the LINEST command.

The angles  $\beta, \alpha$  and the pressure coefficients  $CP_{total}, CP_{stat}$  are given directly by the interpolation. The static and total pressures can be calculated using the non-dimensional coefficients of pressure,  $CP_{total}$  and  $CP_{stat}$ :

$$Total\ pressure, P_{total} = p_1 - CP_{total} \cdot q \dots \dots \dots 3.9(a)$$

$$Static\ pressure, P_{stat} = p_t - \frac{q}{CP_{stat}} \dots \dots \dots 3.9(b)$$

Because the calibration has been carried out under low speed, the velocity magnitude is calculated using the equation 3.10.

$$U = \sqrt{\frac{2(P_{total} - P_{stat})}{\rho}} \dots \dots \dots 3.10$$

The Cartesian components of the velocity are calculated using the equations 3.11 (a), (b) and (c):



- Calibration pipe (D1 and D2) as seen in figure 3.32
- Power supply for the pressure transducer
- National instrument (DAQ)
- LabVIEW software



Figure 3.32: Calibration pipe

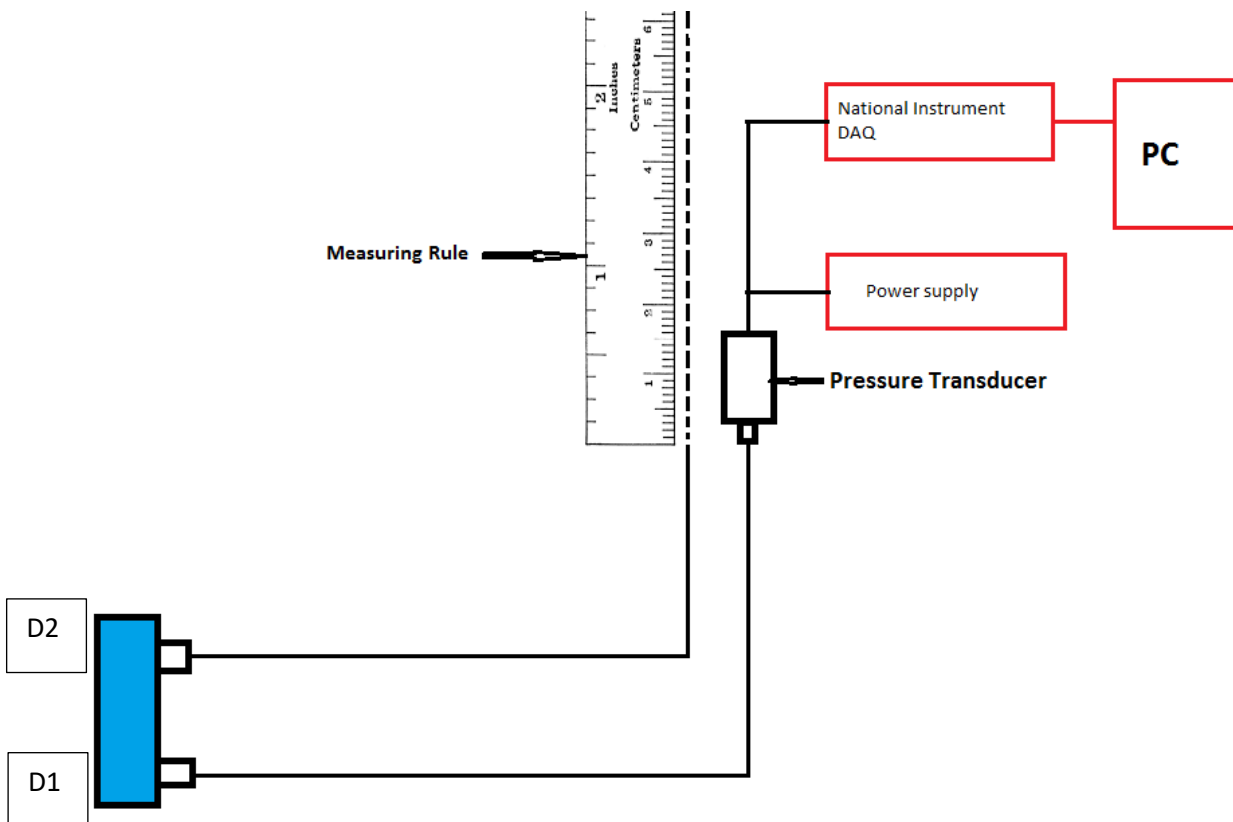


Figure 3.33: Schematic for calibrating the pressure calibration procedure

The calibration procedure is as follows:

- The calibration pipe is filled with water to allow water to come out from both D1 and D2.
- Fix the calibration pipe in a vertical position for water to be able to flow out from both D1 and D2.
- The bottom stud is connected to the pressure transducer while the top stud is connected to the atmosphere.
- The pressure transducer is placed on the wall at a specific height (base height) while a measuring tape is attached to the wall close to the pressure transducer.
- The 0 meter marking start from the base of the pressure transducer where a hose connected to the other stud is connected to. The height is increased incrementally by 1cm until 10 cm, and then 10cm increment to 90cm and finally 20cm increment to 150cm.
- For each of the heights, the LabVIEW program stores the corresponding voltage.
- The differential pressure is then calculated using  $p = \rho gh$  where  $\rho$  is the water density (998kg/m<sup>3</sup>) and  $g$  is the acceleration due to gravity (9.8m/s) for the different heights.
- The curve data is then created between the measured voltage (V) and the differential pressure (in Pa but converted to bar).

The curve data is presented in figure 3.34 for one of the calibrated pressure transducer. The equation is given as

$$y = 2.8227x - 2.5046$$

Where y is the pressure in bar and x is the measured pressure transducer voltage in Volts.

$$P = 2.8227V - 2.5046$$

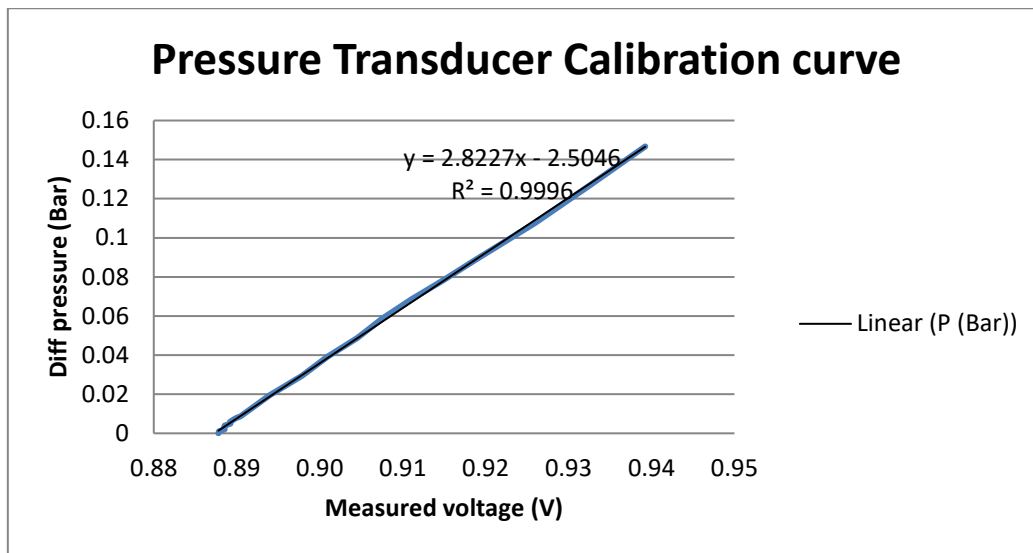


Figure 3.34: Curve data for the calibrated pressure transducer

The rest of the transducers used have been calibrated in the same manner and their different calibration equations obtained.

### 3.5.3 MICROPHONE AND ACCELEROMETER

Since it was difficult for this calibrations to be done at the university based on the non-availability of the equipment to be used, the calibration has however been carried out by the manufacture. The charts curve and qualification certificate has been presented in APPENDIX D with regards to this thesis.

### 3.5.3 FLOW METER

Details of the calibration of the using a hopper at the flow loop lab is given in this section. In order to complete the calibration process, the following equipment and devices was used.

- Hopper
- PLC (programmable logic controller)
- Load cell
- Solenoid valve
- Knife valve

The hopper is placed above the tank/reservoir where all the different closed loop in the fluid lab connects to the tank that supplies water to each loop. An electrically controlled

pneumatic knife valve is connected at the bottom of the hopper. This valve fills and drains the hopper when it reaches a prescribed set point.

In terms of the measurements, the load cell connected to the hopper measures the hoppers and the collected water gross weight. Once the hopper attains the desired set point, the knife valve actuates electronically. For the setup to be actuated, the knife valve needs to be pressurised at around 4bar by the use of the pressure regulator available in the lab. The knife valve is connected to a solenoid valve for electronic triggering. Once the desired set point is attained and the PLC registers it, the output will then be set at 0 in controlling the solenoid valve to drain the water in the hopper.

The calibration procedures is given in APPENDIX H.

### **3.6 UNCERTAINTY AND REPEATABILITY ANALYSIS**

#### **3.6.1 UNCERTAINTY ANALYSIS**

In the field of engineering, the word “error” or sometimes referred to as uncertainty does not necessary mean blunder or mistake when used in describing an aspect of measurements, though it can sometimes be. Errors in measurements signifies the inevitable uncertainty that attends all form of measurements. In this sense, it cannot be avoided, though it can be ensured that it remains as small as reasonably possible and it is a reliable estimate of how small these values can be [86].

The first step of this analysis in any process is by identifying what physical quantity is being measured. These physical quantities are being measured directly by using the different measurements sensor types. In addition, during this step of carrying out the uncertainty analysis, it is very key in describing the setup for the experiment, the sensor devices technical specifications and all other equipment being utilised for the experiment [86]. Furthermore, the measurements processes used in obtaining data from the test setup needs to be explained in clear terms. All of this information can then be properly utilised in identifying any error in the measurement processes before any uncertainty calculations. For this study, the uncertainty measurement calculations have been calculated by carrying out SD (standard deviation) of the measured data by using the equation in 3.12.

$$\sigma_x = \sqrt{\sum_{k=1}^n \frac{(x_k - \bar{x})^2}{n}} \dots\dots\dots 3.12$$

Where n denotes the number of signals for each data,  $x_k$  stand for the signal value for each data, and  $\bar{x}$  is the signal mean value.

The uncertainty in the mean value of each of the sensor signal can be calculated using the following equation:

$$S_{\bar{x}} = \frac{\sigma_x}{\sqrt{n}} \dots\dots\dots 3.13$$

Where  $\sigma_x$  is the standard deviation and n is the number of signal in the data.

Equation 3.12 and 3.13 can be used in calculating the uncertainty value for each of the different sensors used in this research based on the numerous data that have been acquired from these sensors experimentally on the control valve.

Table 3.6 gives a summary of the mean uncertainty values for the sensors used in this research.

Table 3.6: Mean uncertainty value for all the sensors

	Mean uncertainty values	Units
Vibration Sensor	0.0005	m/s <sup>2</sup>
Acoustic Sensor	3.415	Pa
Right 2 Transducer	0.041	kPa
Left 2 Transducer	0.029	kPa
Left Transducer	0.042	kPa
Bottom Transducer	0.044	kPa
Right Transducer	0.029	kPa
Top Transducer	0.029	kPa
Centre Transducer	0.049	kPa
Centre 2 Transducer	0.030	kPa
Bottom 2 Transducer	0.040	kPa
Inlet system pressure Transducer	0.035	kPa
Top 2 Transducer	0.036	kPa
Outlet system pressure Transducer	0.039	kPa

### 3.6.2 REPEATABILITY ANALYSIS

This assesses whether a device can be able to measure the same physical quantity with the same conditions multiple times using the same device and be able to achieve same results [87]. It determines how close together, in any experiment, the repeated values are. If the repeats are close together, then it is said that the measurement has a high repeatability. Repeatability can change throughout an experiment as it expresses the closeness of the results obtained by analysing the same condition in multiple of times.

For this repeatability analysis, two sample data for the same instrument have been collect at different days apart. The process for analysing the repeatability given by Deziel [88] have been used. Results have been collected for 60% VOP, for position 3 and height 7. The results have been obtained for different flow rates (800, 900, 1000, 1100 and 1200LPM).

Table 3.7 shows the obtained values for the repeatability of the different sensors used. When these values are 0, it means that there is no difference or variation among the repeatability results. So the closer to 0, the better the accuracy of the repeatability.

Table 3.7: Repeatability values at different flow rates for all the different sensors

Sensors	800LPM	900LPM	1000LPM	1100LPM	1200LPM
Accelerometer	0.158206	0.055989	0.043842	0.014571	0.124608
Microphone	0.000796	0.010039	0.070618	0.173458	0.06383
Right 2 pressure transducer	0.001672	0.001479	0.000547	0.000442	0.002512
Left 2 pressure transducer	0.000414	0.000922	5.66E-05	0.001087	0.002154
Left 1 pressure transducer	0.001121	0.000867	0.000838	0.001007	0.001168
Bottom 1 pressure transducer	0.001011	0.001389	0.001752	0.002221	0.002856
Right 1 pressure transducer	0.003581	0.003613	0.003565	0.003687	0.003588
Top 1 pressure transducer	0.00097	0.001042	0.001178	0.001441	0.001673
Center 1 pressure transducer	0.004454	0.004639	0.004476	0.00495	0.005007
Center 2 pressure transducer	0.002117	0.001976	0.003552	0.005176	0.006881
Bottom 2 pressure transducer	0.002797	0.002785	0.003311	0.002978	0.002612

Inlet pressure transducer	0.004763	0.004608	0.005112	0.005235	0.004795
Top 2 pressure transducer	0.003209	0.002531	0.001831	0.001725	0.001864
Outlet pressure transducer	0.000968	0.000874	0.000934	0.000576	0.000309

### 3.7 RISK ASSESSMENT OF THE RESEARCH

The risk assessment for this research has been carried out and the details are given in APPENDIX B.

### 3.8 SUMMARY

After the explanation of how the pressure probe, flow meter and the pressure transducers have all been calibrated, their specification, numerical and experimental set up and specifications for all the equipment used in this research, detailed outcome of the investigation using the pressure probes have been provided in the next chapter. Chapter four discusses the analysis of the flow behaviour inside the control valve based on single-phase condition at different operating and flow conditions where the probes have been placed at various positions inside the valve.

## CHAPTER FOUR

### 4.0 INTERNAL FLOW CHARACTERISTICS INSIDE THE CONTROL VALVE USING A FIVE-HOLE PRESSURE PROBE FOR SINGLE PHASE CONDITION

---

*The influence of MHP and flow condition on the internal flow characteristics inside the control valve for single-phase condition have been presented. Establishments are made to see how certain parameters such as, static pressure, velocity magnitude, pressure ratio, pressure coefficient, etc. are affected by changes in the flow and operating conditions. Furthermore, this chapter also shows how the flow coefficient ( $C_v$ ) and  $K$  value changes for the different probe positions and heights as pressure drop varies from inlet to outlet of the valve. Finally, global and local flow parameters between a healthy and faulty valve have been established and compared under different flow and operating conditions.*

## 4.1 INTRODUCTION

Most of the industrial control valves used are the globe valves because of their body shape. Within the valve body, the stem moves up and down in strokes by the valve actuator and by so doing, closes and opens the gap between the valve seat and the plug. The valve trims are machined and designed to modulate and "shape" the flow in accordance to a specific characteristic. For the entirety of this chapter, the five-hole pressure probe has been applied in determining the flow parameters for various flow condition inside a complex valve geometry. The internal flow structure inside the complex valve geometry from inlet to outlet of the valve will be determined by using the five-hole pressure probe in single-phase condition. This section would include both numerical and experimental analysis. For the numerical analysis, the valve model will be validated with experimental results. The chosen type of probe head will be compared numerically with a different head in order to see what head causes lesser flow interference. Finally, the results from the valve validating the increase in surface area velocity at different section with increase in the flow rate with regards to one of the selected experimental data have been presented. For the experimental analysis, investigations into the effect of flow conditions to the different flow parameters and how these changes affect the valve performance when fault occur inside the valve is also presented. To achieve this objective, the loop has been ran with varying flow rates and the valve operated at different VOP for single-phase condition.

## 4.2 NUMERICAL ANALYSIS

### 4.2.1 MESH INDEPENDENCE TEST

Mesh independence test has been conducted where the pressure at the inlet and mass flow rate at the outlet are being measured. The mass flow rate remained constant while pressure values kept changing. As the max face size kept increasing, so did the nodes and the mesh elements with the pressure values of 9.5%, 2.9%, 1.8% difference was observed. The 1.8% difference was finally used with about 4.5 million mesh elements. The level and concentration of mesh elements refinement around the valve body usually have a significant impact on the flow values accuracy. Therefore, the mesh quality was controlled in such a way that, on the valve flow field vicinity, there were smaller mesh

sizes around the domain in capturing accurately, the boundary phenomena and to provide results that are more concrete.

#### 4.2.1 MODEL VALIDATION

Before analysis are made as to how the design of five-hole pressure probe used in this research have been applied in measuring the parameters listed in chapter three, the numerical model of the valve first need to be validated. Figure 4.1 shows the variation in  $\Delta P$  as the flow rate changes.

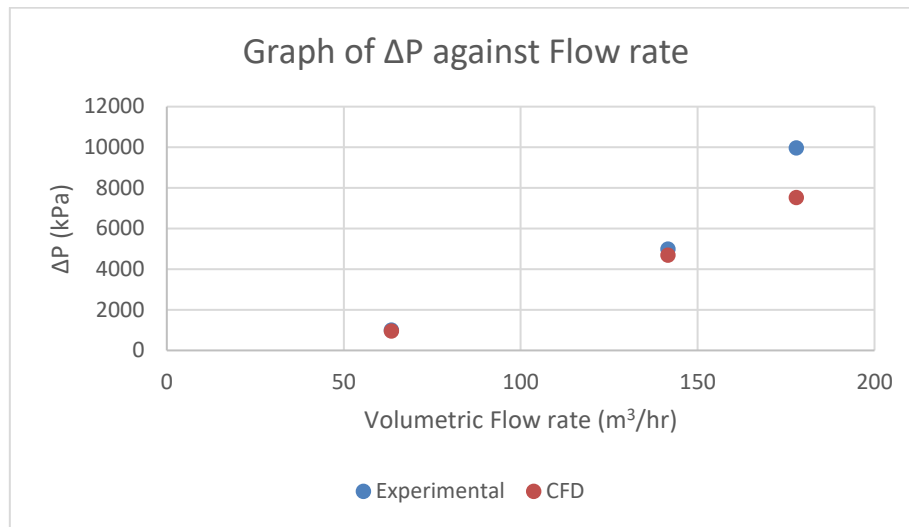


Figure 4.1: Comparison of the pressure difference (  $\Delta P$  ) between CFD and experimental results

As depicted in figure 4.1, the general picture of the graph draws to a conclusion that as the mass flow rate increases, the pressure drop also increases and the agreement between the obtained results goes further apart. Figure 4.1 shows that as the inlet pressure difference rises, so does the mass flow rate and the pressure difference also increases. At a mass flow of  $63.47\text{m}^3/\text{hr}$ , the percentage difference between the experimental and CFD was 3.5% and then increases to about 5.9% when the flow rate rises to  $141.55\text{ m}^3/\text{hr}$ . At 100 bar inlet pressure, the percentage difference rose to a very high percent of 24.5% as the flow rate reaches  $177.84\text{m}^3/\text{hr}$ .

#### 4.2.3 PROBE HEADS COMPARISON

For this section, the control valve geometry results will be analysed for both pressure and velocity flow fields with the same boundary conditions. For the remaining simulations to

be carried out, the maximum flow rate in the flow loop will be used as the inlet boundary condition (1500LPM) and with pressure outlet at 0 bar gauge pressure (atmospheric pressure). For the sake of this research, the reference points where velocity and pressure values are obtained, as seen in figure 4.2, 4.3, 4.4 and 4.5, are selected points made inside the valve geometry flow domain. The same points have been compared when there is no probe (reference measurements) and when there is probe (conical or hemispherical probe) inside the valve.

Figure 4.2 shows the pressure comparison between the conical and hemispherical heads placed at same position inside the valve against when there is no probe inside the valve (reference).

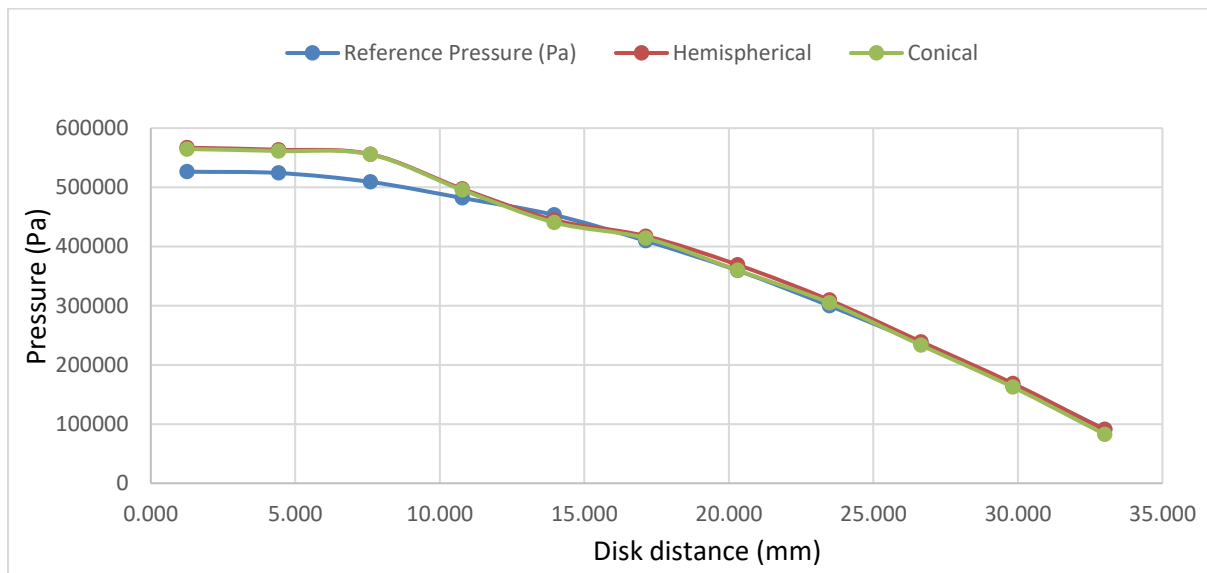


Figure 4.2: Pressure comparison between Conical head and Hemispherical head geometry

As obtained from the result, conical head had a pressure difference of 3.9% across the flow inside the trim while that of hemispherical head had 3.2% when compared to the reference pressure. This indicates, as the result are quite close in comparison that the hemispherical head has the lesser interference with its lower difference margin.

More so, hemispherical head had a better valve wall shear stress margin as its interference is quite lower, compared to conical though conical causes a bit better interference in the inlet valve pressure.

This has shown that hemispherical head is better in terms of pressure interference inside the trim.

More so, comparing the pressure values of both conical and hemispherical heads, it can be seen that the hemispherical measurements are quite close to that of the reference values when compared with conical for the global pressure distribution. Figure 4.3 shows the global comparison between both heads to the reference geometry measurements at different points from the inlet of the valve to the outlet.

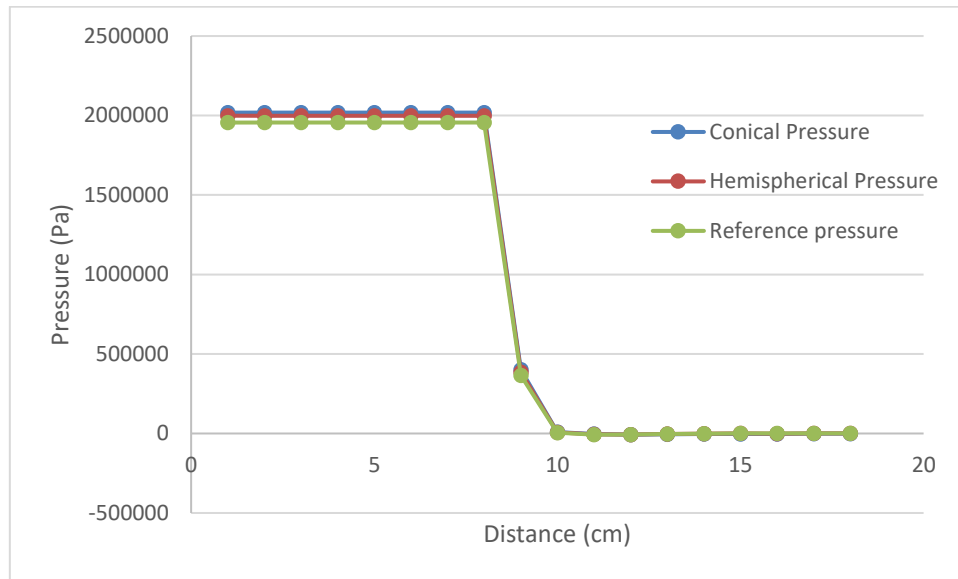


Figure 4.3: Global pressure distribution comparison between conical head and hemispherical head geometry

For the velocity analysis, figure 4.4 shows the comparison between the best geometry for the various probe heads positions (conical and hemispherical).

As observed from the results, conical head had a velocity across the flow inside the trim, almost same as the hemispherical head. This indicates, as the result are quite close in comparison, that the conical head causes slightly lesser interference.

Furthermore, the global parameter measurement of velocity also confirms that the conical head also shows a slightly better velocity results to that of the hemispherical when compared using the reference measurements with an average percentage of 8.5%.

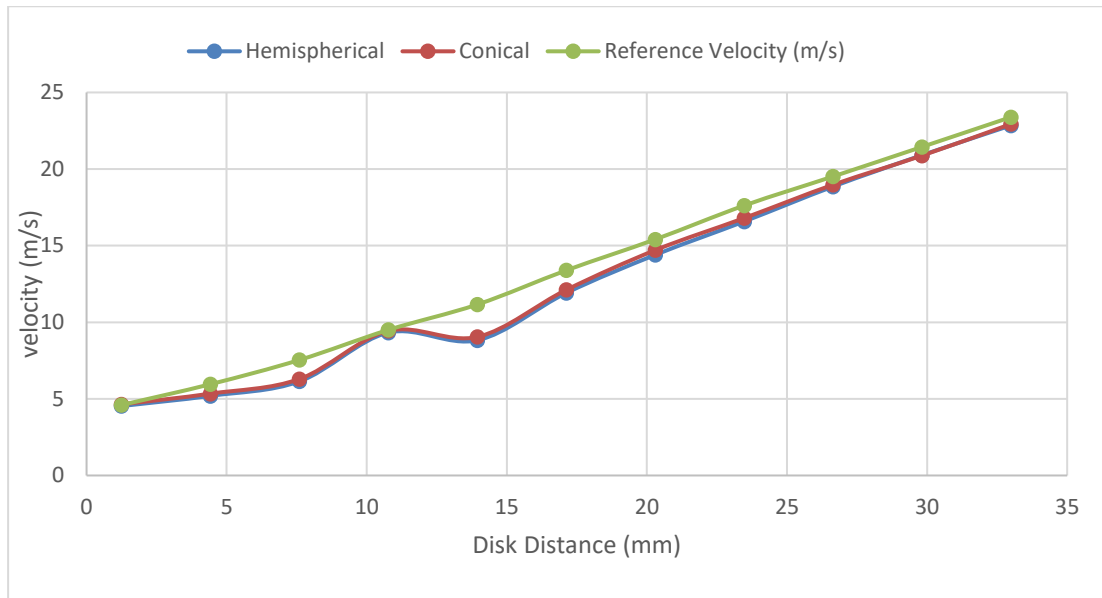


Figure 4.4: Velocity comparison between conical head and hemispherical head geometry

Figure 4.5 shows the velocity profile of the valve for both hemispherical head and conical head compared from inlet to outlet of the valve with the reference velocity.

It is clear from figures 4.4 and 4.5 for velocity that the conical head causes the lesser interference. However, it is worth mentioning that the multihole probes are pressure probe sensor.

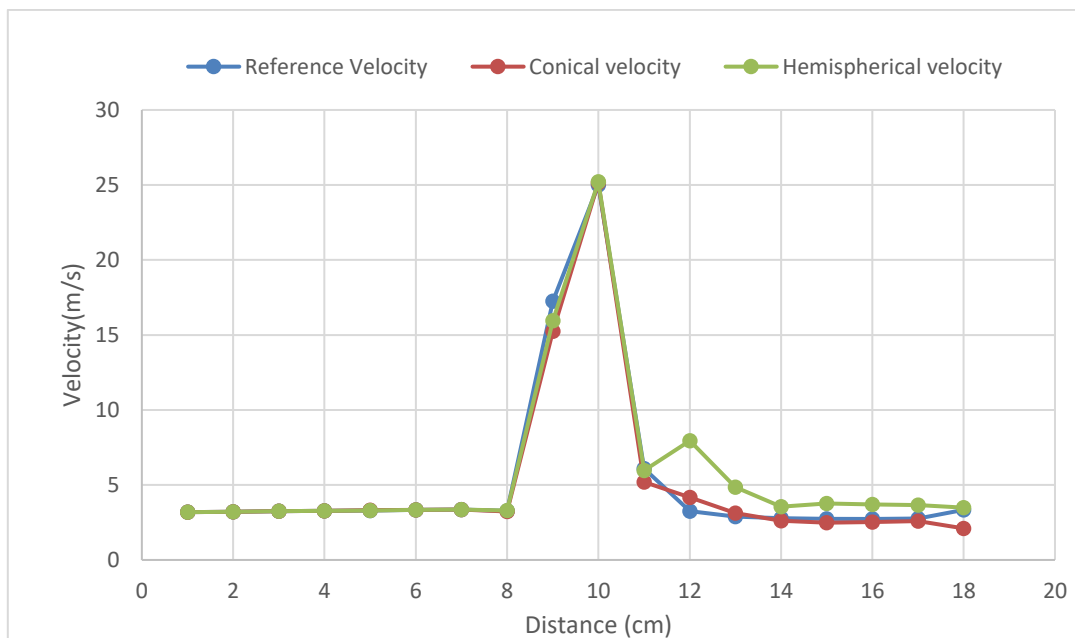


Figure 4.5: Global velocity profile of the valve between Conical head and Hemispherical head geometry

These results have shown that overall, the hemispherical head causes the lesser interference with flow inside the control valve as the pressure measured from these probes are used in determining other parameters. This has however made the decision possible in the design and manufacture of the hemispherical probe that has been used for this research. The next section discusses how this probe has been applied, where they have placed inside the valve and under what conditions data have been collected and analysed.

### 4.3 EXPERIMENTAL ANALYSIS

Before actually using the probe into real life application on the control valve, the probe have been calibrated according to the steps provided in the previous chapter (chapter three). After calibration, a 6<sup>th</sup> order calibration coefficients for pitch angle, yaw angle, static and total pressure have been obtained. In order to ensure that the calibration has given the correct and accurate coefficients, some selected pitch and yaw angles have been chosen in order to validate these results. Figure 4.6 and 4.7 depicts the angle validation plot for pitch and yaw angles respectively with an  $\pm 10\%$  angle difference range.

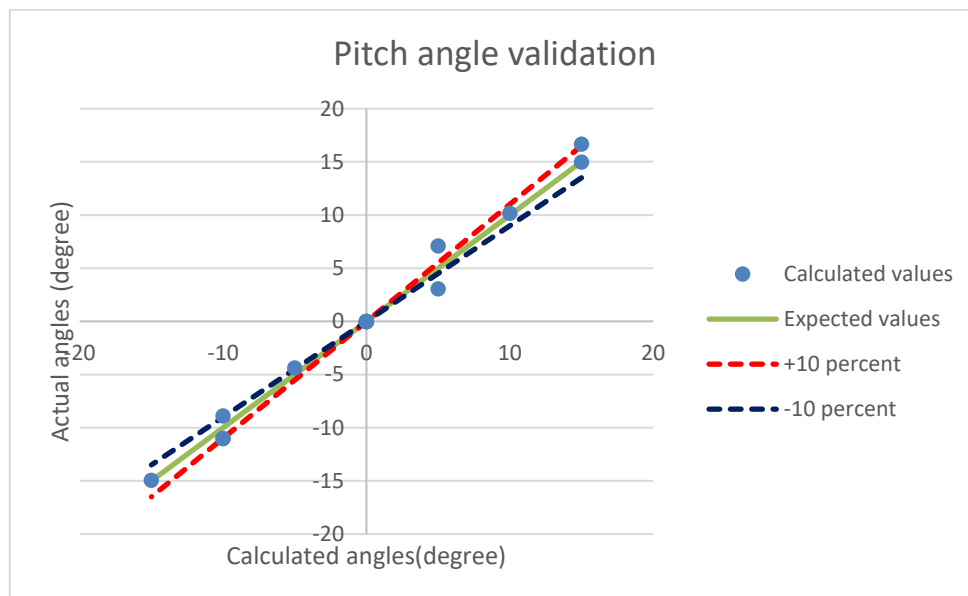


Figure 4.6: Pitch angle validation from five-hole pressure probe

It can be seen from figure 4.6 that nearly all of the calculated pitch angle values appear at the boundary or fall between the  $\pm 10\%$  ranges except for two values that just appear outside this range. The green solid line is the best-fit linear curve. This line denotes the expected angle values. Both values outside this range were noticed on  $+5^\circ$  degree for

different yaw angles. The reason might be that the tip of the probe were not exactly at  $+5^\circ$  as it should have been, hence the reason for the variation. This can be expected, as the range chosen is quite small.

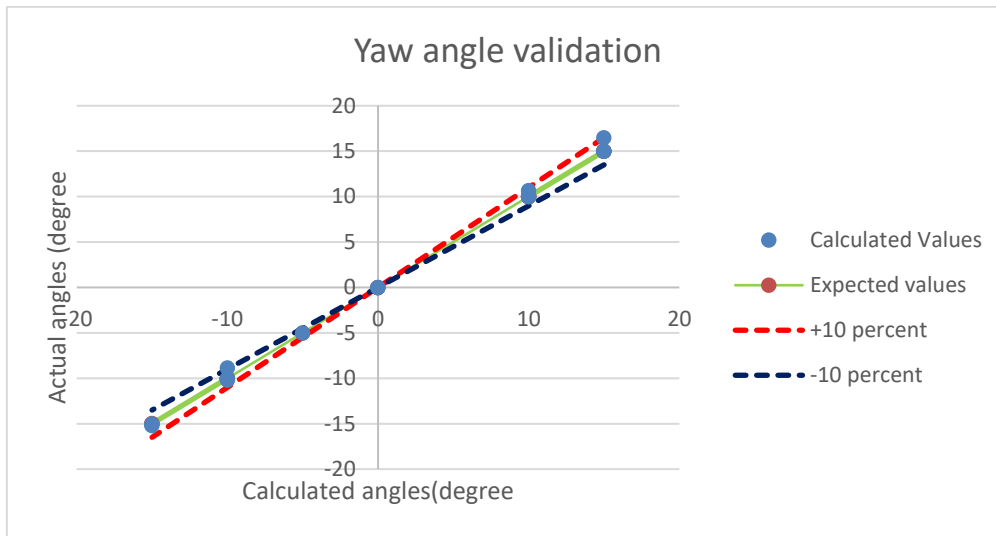


Figure 4.7: Yaw angle validation from five-hole pressure probe

On the contrary, of what was seen in figure 4.6, figure 4.7 shows that all of the calculated pitch values fall between or appear at the boundary of the  $\pm 10\%$  range. The green solid line again, denotes the best-fit linear curve. This line denotes the expected yaw angle values. All the yaw angles fall between the ranges for their respective pitch values.

After the five-hole pressure probe validation, their respective calibration coefficients can now be used to determine flow parameters in an unknown field. For all the experimental research, as we would see in this chapter and subsequent chapter (five and six), each data have been collected using the following conditions.

- For the inlet and outlet probes, three probe lengths have been designed and applied for data collection. These lengths are in reference to the inlet and outlet of the valve. The lengths used for the inlet probe are 0.5, 0.8 and 1D with reference to the valve input, while the lengths for the outlet probe are 0.9, 1.2 and 1.5D with reference to the valve outlet. It is worth mentioning here that D is the valve diameter and it is 100mm (10cm).
- For each of the six different probes (3 for the inlet and 3 for the outlet), data have also been collected for seven different heights across the valve area where flow

occurs. The total flow area at the inlet is 6cm (making a height measuring distance of 1cm increment) and at the outlet, it is 7cm (at about 1.17cm increment for each height).

- Each measurement data will be collected for different VOPs (valve opening position) namely at 10, 20, 40 60 and 80% and all for 5 different flow rates resulting from different pump set points.
- Finally, two of these measurement scenarios (acoustic and vibration), data will be collected for both single and multiphase condition, while the pressure probe is used for only single phase condition. For the multiphase condition, three different air injection flow rates have been used for each probe length and heights, and VOPs under various flow rates.
- For chapter 5 and 6, vibration and acoustic respective data for all these conditions listed above have also been collected.

#### 4.3.1 EXPERIMENTAL SINGLEPHASE INVESTIGATION ON THE CONTROL VALVE

Control valves are normally installed in pipelines in order for the process parameters that corresponds to the fluid flow to be controlled. In this section, instead, process parameters will be studied inside the control valve under single-phase condition. These parameters have been measured with the aid of five-hole pressure probes. As mentioned earlier, the probes have been placed at different positions inside the valve, before and after the valve trim, measuring local flow parameters at the inlet and outlet of the valve. For this research, flow path before the trim is considered inlet and flow after the trim is the outlet. Figure 4.8 shows the valve cross-section defining the inlet space and the outlet space.

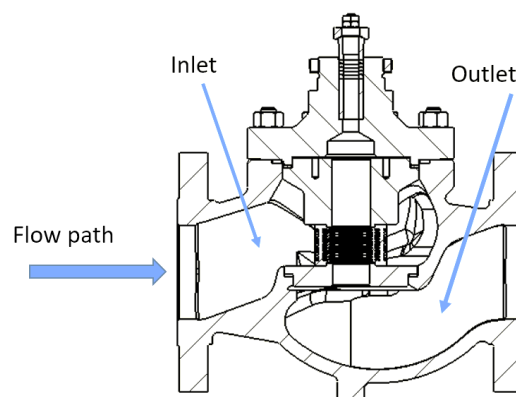


Figure 4.8: Control valve cross-section showing with inlet and outlet flow area

The test valve is connected to a centrifugal pump with the valve operated pneumatically by an actuator and fitted with a diaphragm. The actuator has a maximum air supply gauge of 4.5bar with a non-intrusive pressure measurement of 2D and 6D away from the valve to determine the inlet and outlet pressure respectively. The pressure probes are placed intrusively for local flow parameter measurements at 0.5D, 0.8D and 1D for local inlet flow measurements and 0.9D, 1.2D and 1.5D for local outlet flow measurements. Since the design of inserting the probe allows for placing the probe one at a time at the inlet and outlet for flow measurements, the inlet and outlet probes have therefore been grouped together for the purpose simplicity. They are 0.5D inlet and 0.9D outlet, 0.8D inlet and 1.2D outlet, 1D inlet and 1.5D outlet respectively. The valve has a diameter of 10cm (D). Because of the complex nature of the inside valve geometry, the flow area where flow parameters are measured with the probe at the inlet and at the outlet are 6cm and 7cm respectively from top to bottom. Seven different heights flow parameter measurements across the flow area, both at the inlets and at outlets have also been conducted. The pressure transducers used for this single phase measurements have all been presented in section 3.4.5, with their calibration equations converting from voltage (volts) to pressure (Bar). The experimental procedures for single-phase measurements using the pressure probes and other pressure transducers have been summarised using various steps as depicted in figure 4.9.

The first step is recording the water temperature before and after the valve in order to determine the density of water for flow calculation. The next procedure is to set the VOP to 80% and operate the pump at maximum set point (1200LPM). Then after the flow loop is ran at these settings while the pressure reading from the pressure probes (inlet and outlet), pressure from 2D and 6D (valve inlet and outlet) and flow rate Q are all recorded at least twice. The average values for valve pressure drop, local sectional pressure drop are used in calculating the valve flow capacity and local sectional valve flow capacity based on equation 3.2. The entire procedure is the performed for 60, 40, 20 and 10% VOPs, apart from the first step. The entire procedure is performed again for 1100LPM, 1000LPM, 900LPM and 800LPM respectively. Before going into the probe parameter measurements and analysis, the valve performance needs to be ascertained as a baseline by determining the pressure drop for different flow conditions. This analysis will be

depicted for each of the seven height as it will show similar values and trends, showing that probe inside the valve has little or no effect of the overall valve performance.

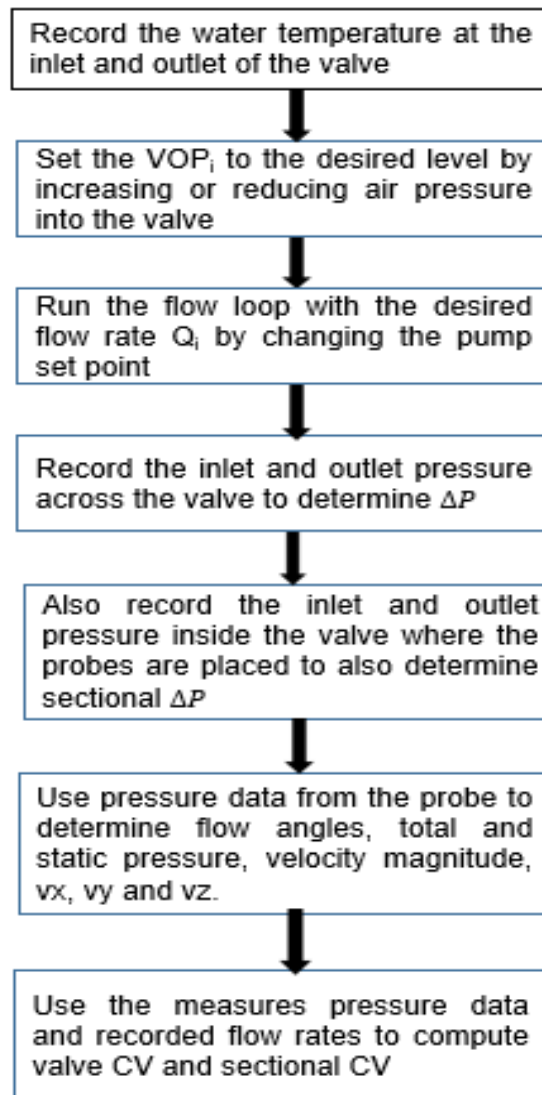


Figure 4.9: Single-phase experimental procedure flow chart

Figure 4.10 depicts all the different locations where pressure measurements from the valve have been conducted at different flow and operating conditions.

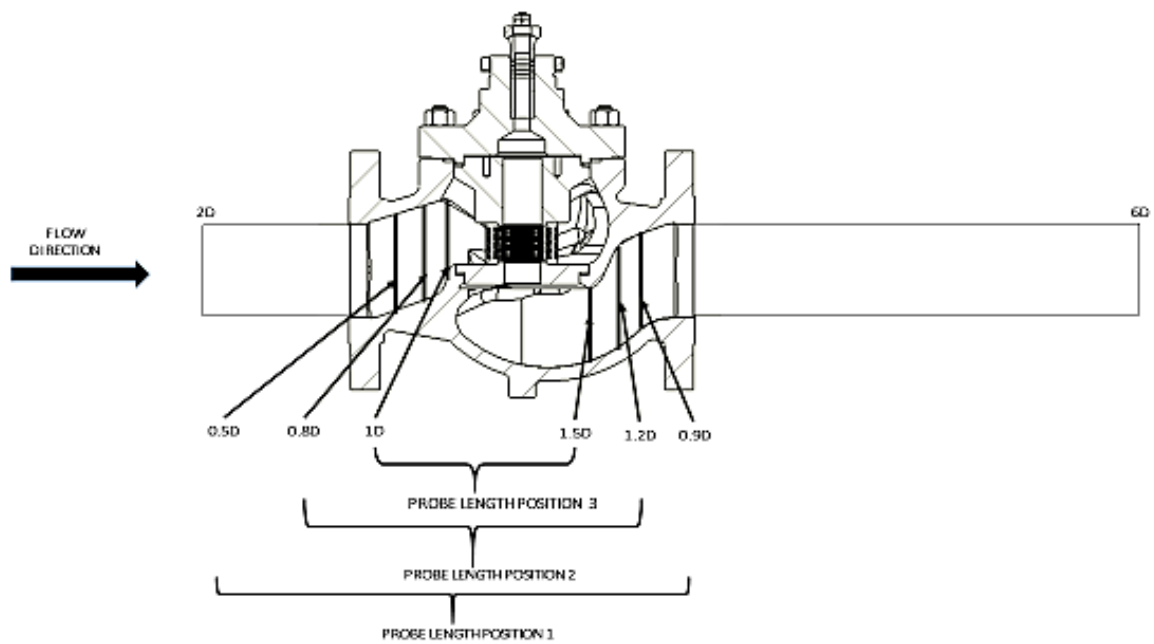


Figure 4.10: Pressure locations taken from the valve experimentation.

#### 4.3.1.1 EFFECTS OF DIFFERENT OPERATING CONDITIONS ON THE GLOBAL VALVE CHARACTERISTICS

One key parameter that measures the characteristics and the sizing (measure of energy amount being dissipated in the valve) of a valve is the valve flow coefficient,  $C_v$ . The  $C_v$  is a function of the flow rate and pressure drop with the specific gravity as 1 because of the fluid used in this research is water as given in equation 1.4. Figure 4.11 shows the pressure drop ( $\Delta P$ ) at various flow rates for the different VOPs. Differential pressure, regardless of how quickly the valve recovery characteristic can be, is vital in detecting any form of fault, whether flashing or cavitation. The distance between both points of measurements is 1160mm.

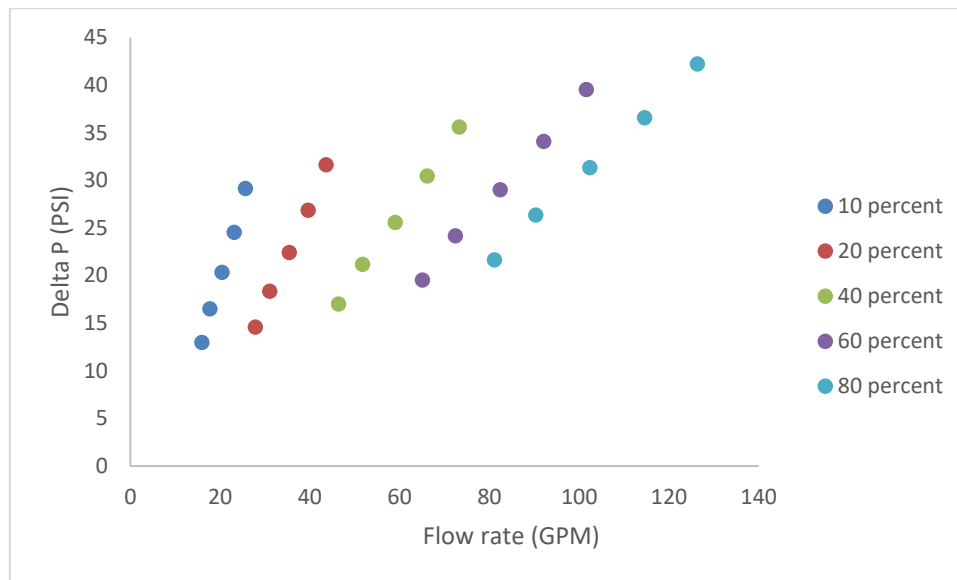


Figure 4.11: Pressure drop variations for different VOPs and for various flow rates.

As seen from figure 4.11, the pressure drop increases as the flow rate increases as they have a near linear relationship. This increase can be seen across all the VOPs. The inlet pressure increase due to the kinetic energy imparted by the pump impeller is converted into potential energy in the form of static pressure. This causes an increase in inlet pressure of the valve as the speed of the impeller increases. At the valve outlet, the pressure remains nearly constant close to the atmospheric pressure after flow passes through the valve trim that modulates the flow, therefore causing an increase in the pressure drop as flow increases across the different VOPs. Across the VOPs, pressure drop is seen to increase as passage flow area increases (VOP) from the figure 4.11. This is because as flow area increases, there is lesser flow restriction causing pressure increase as the flow rate  $Q$  increases, causing pressure drop to then increase.

Figure 4.12 shows the various  $C_v$  of the valve calculated from the pressure drop for the different VOPs at various flow rates.

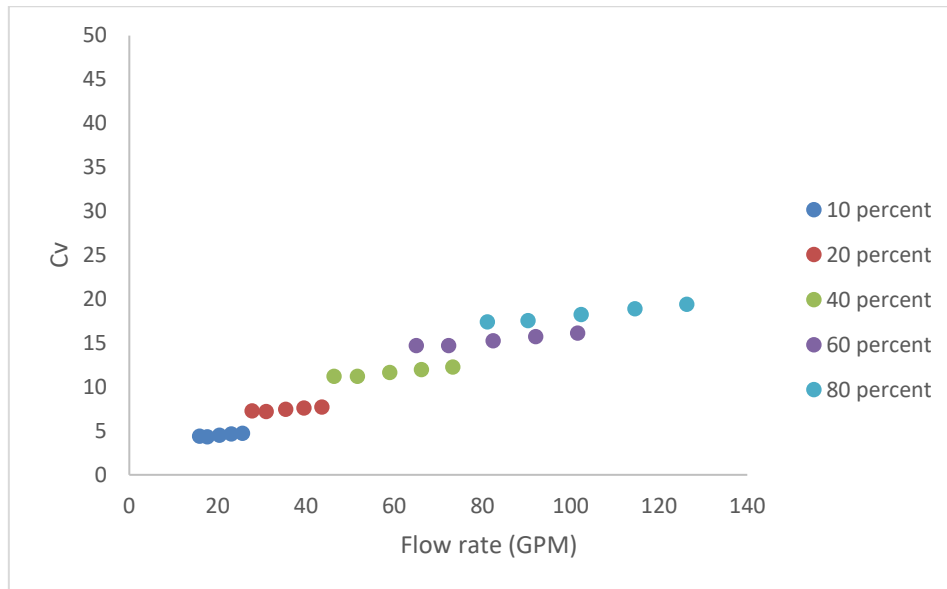


Figure 4.12: Valve Cv variations for different VOPs and for various flow rates.

It can be seen that the Cv of the valve remains same at different flow rate for a particular valve opening position. This fact has been established by [89, 90, 91, 92 and 93] that the Cv of a valve is independent of the process condition as seen in figure 4.12, that irrespective of the flowrates, the Cv remains the same (almost). A single curve in representing the Cv is presented in figure 4.13. Most researches present this single curve for the valve Cv, which corresponds to the maximum allowable flow rate in this research, by averaging the flow rate values to get a single Cv value for the different VOPs.

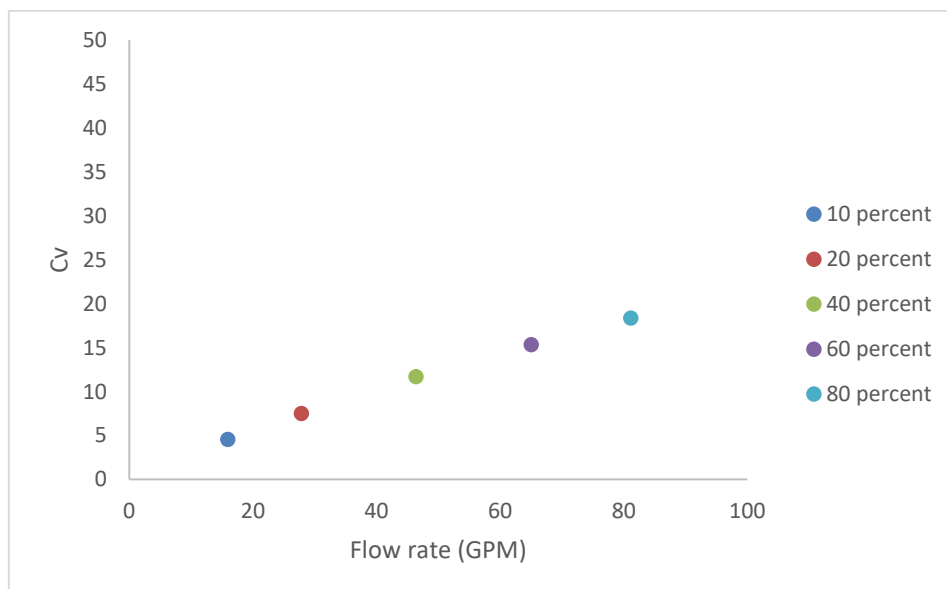


Figure 4.13: Valve Cv variation for different VOPs.

It can be seen from figure 4.13 that the valve  $C_v$  increases as the VOP increases. The  $C_v$  increases from 4.53 to 7.47 as the VOP increases from 10 to 20 %, representing a 39.3% increase. When the valve is opened further from 20 to 40%,  $C_v$  increases from 7.47 to 11.68, representing a 36% increase. Further VOP increase to 60 and 80% increases the valve flow capacity to 19.8 and 24.92, representing an increment of 23.8 and 16.4% respectively. This increase in valve  $C_v$  concerning the different opening positions is seen to be linear which confirms that the particular trim used in this research is a linear trim.

After global analysis have been conducted for the valve to see the variations of pressure values ( $\Delta P$ ) and  $C_v$  on the different flow rates, local flow analysis inside the valve have therefore been conducted to also see these variations and to better understand how flow behave under such conditions. The next subsection presents all of the analysis for the different probe positions (lengths and heights) carried out in this research.

#### **4.3.1.2 PROBE LENGTH POSITION 1 (0.5D INLET AND 0.9D OUTLET)**

In this position, the probe at the inlet is placed at 0.5D away from the valve inlet and 0.9D away from the valve outlet. These probes placed at their specific location inside the valve will measure the pressure from the different holes, which would be converted to other flow parameters like velocity magnitude, static and total pressure using calibration coefficients obtained from the pressure probe calibration. The next subsection describes the effect of static pressure drop for various flowrates at different VOPs.

##### **4.3.1.2.1 FLOW RATES EFFECTS ON LOCAL PRESSURE DROP AT DIFFERENT VOPs**

After global pressure analysis of the valve for different flow rates at 2D and 6D, local analysis using the probe for this particular position for pressure have been discussed and analysed. For this analysis, pressure drops for this position have been carried out for the different heights and various flow rates and different VOPs. Though the probe are used for velocity measurements through the pressure, the probe has also been used to determine the pressure parameters due to the complex geometry and 3D flow experienced with the valve.

From figure 4.14, similar trend can be seen for all the heights positions where the change in pressure increases as flow rate increases for all the various probe height positions. Again, the valve inlet pressure increases due to the kinetic energy impacted by the pump impeller as it is converted into potential energy in the form of pressure as the full pump

pressures exists over that of the valve. When the VOP increases or decreases, it causes the system pressure to change. These trends continues before flow goes inside the trim. This trend would be seen for any probe lengths and heights, before the valve trim. For the same set points, flow rates can be seen to depend on the VOPs as their pressure increases, so do the flow rates. The maximum flow rate for this research has been set to 1200LPM. For height 1 in figure 4.14, it can be seen that change in increases from 12.4 to 16.2 PSI as flow rate increase from 16 to 18.9GPM for 10% opening. This represent an increase of 23.8% as the flow rate increase at 15.4%.  $\Delta P$  further increases to 20.4, 25 and 30.2 PSI with an increase rate of 20.3, 18.7 and 17% at flow rate of 21.08, 23.58 and 36.19GPM representing an increase of 11.7, 12.3 and 9.6% respectively.

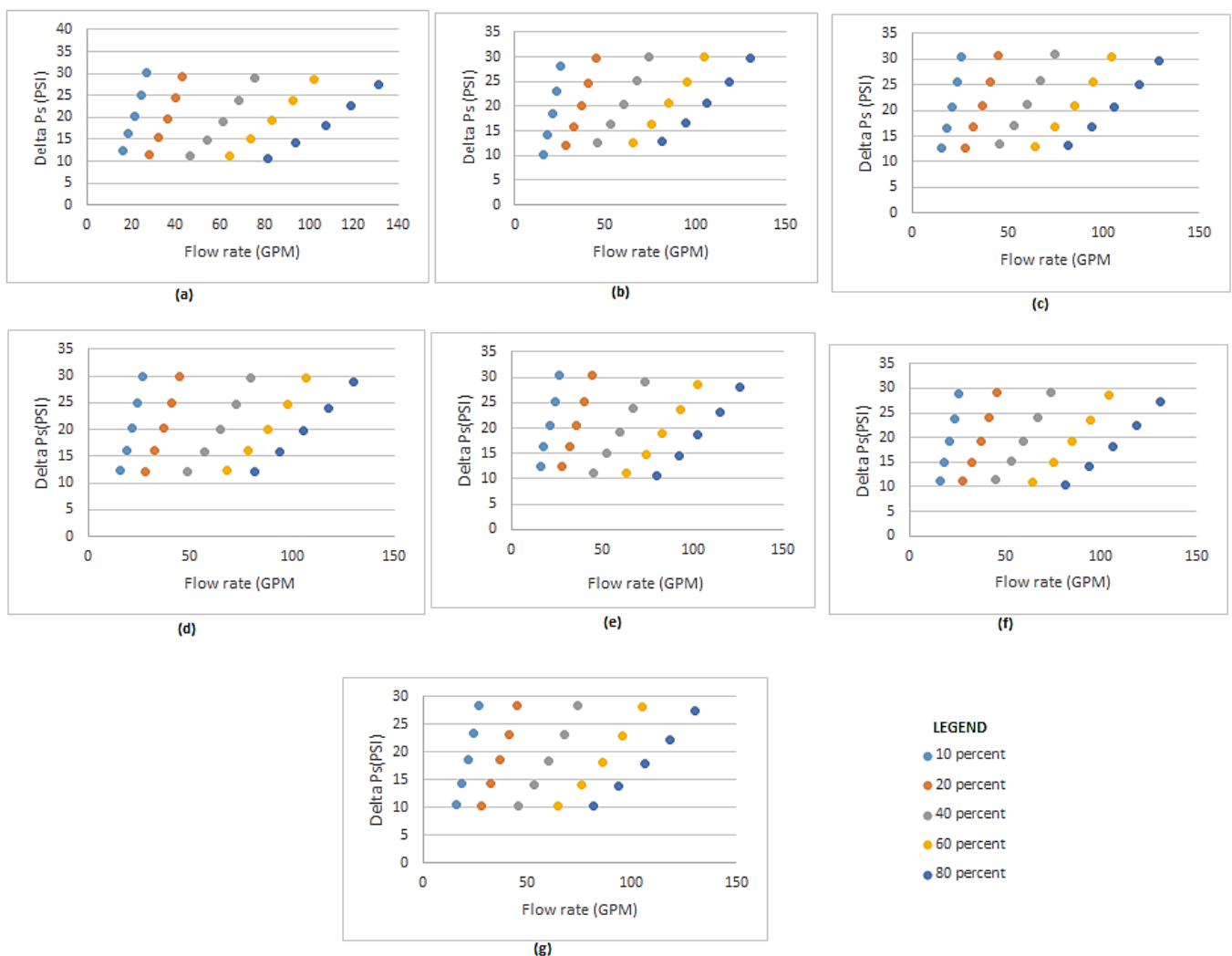


Figure 4.14: Local pressure variation for different flow rates and VOPs for the different height positions (a) Height 1 (b) Height 2 (c) Height 3 (d) Height 4 (e) Height 4 (f) Height 6 (g) Height 7

As VOP increase from 10% to 20, 40, 60 and 80% VOP, for same pump set point, flow rates begins to increase. This causes  $\Delta P$  to increase slightly as the VOP increases as explained for 10% VOP, as seen from figure 4.41(a).

For height 2 through to height 7, flow rates stays nearly the same, as similar valve operating and flow condition have been used. However,  $\Delta P$  slightly vary across the different valve heights as the inlet pressure vary because the flow in the valve system is a pressure driven flow. As the probe position goes from height 1 to height 7, the section of the probe body, which is inside the valve increases, which causes more interference to the flow. This is evident from the pressure and velocity variation from height 1 through to 7. Ideally,  $\Delta P$  should increase from height 1 through to height 3 (maximum pressure point), then starts to decrease before reaching height 7. For higher VOPs (40, 60 and 80%), height 2  $\Delta P$  decreases from height 1 before it then increases all through to height 3, unlike for lower VOPs (10 and 20%) where  $\Delta P$  starts to increase until it attains the maximum pressure at height 3. After height 3,  $\Delta P$  begins to decrease. However, as the length of the probe begins to appear more as the height increases, a similar trend can be seen where  $\Delta P$  becomes inconsistent, all through to height 7. One thing is certain though,  $\Delta P$  is maximum at height 3. At average flow rates of 16GPM (800LPM pump set point), for 10% VOP,  $\Delta P$  decreases from height 1(12.36 PSI) to height 2 (10.3), representing a decrease of 16.9%. From height 2 to height 3,  $\Delta P$  increased slightly by 23.1% and then decrease again by 3.1% from height 3 to 4.  $\Delta P$  increases slightly by 2.6% from height 4 to 5. It then increases slightly by nearly 11.8% to height 6 before decreasing slightly again by 4.3% at height 7.  $\Delta P$ . For average flow rate of 18.4GPM (900LPM pump set point), again for 10%VOP, same trend as that for 16GPM is followed. From 16.2 PSI at height 1,  $\Delta P$  is increased by 12.8% to 14.15 PSI for height 2. From height 2 to height 3,  $\Delta P$  increases slightly by 16.6% to 16.5PSI. It decreases slightly again by 2.7% from height 3 to 4.  $\Delta P$  further increases by 1.9% from height 4 to 5. It then decrease from height 5 to 6, from 16.3 to 15 PSI by 8.6% and decreases slightly to 14.47 PSI by 3.3% at height 7. For average flow rate of 22GPM (1000LPM pump set points), same trend for  $\Delta P$  is followed where it decreases from height 1 (20.37PSI) to height 2, increases at height 3, decrease at height 4, increases again from height 4 to 5, decreases from 5 to 6 and then decreases further from height 6 to 7 at 1.9, 0.6, 1.6, 1.6, 1.3 and 0.3% respectively. Same trend is again repeated for average flow rate of 24GPM (1100LPM pump set point) from height 1 for  $\Delta P$

of 23.3PSI, through to height 7 at 9.8, 12.8, 2.2, 1.5, 6.6 and 2.55% respectively. Finally, for 10% VOP at 27GPM average flow rate, same trend again is from height 1 to 7 at 6.7, 8.3, 1.8, 1.1, 4.1 and 1.77% respectively.

Again for height 2, 20, 40, 60 and 80% VOP follow similar trend as that of 10% where  $\Delta P$  increases from height 1 to 2, increase slightly from height 2 to 3, decreases from height 3 to 4. Further increases from height 4 to 5, decreases from height 5 to 6 and then decreases slightly from height 6 to 7. This trend cuts across all the average flow rates for these VOPs. For average flow rate of 28GPM, following the said trend from 11.9PSI,  $\Delta P$  percentage from height 1 to height 7 are 2.9, 7.1, 4.6, 2.7, 11.7 and 5.7% respectively. At 32.2GPM average flow rates, the percentage difference from height 1 through to 7, following same trend are 2.1, 5.9, 4, 2.2, 8.1 and 5% respectively. At 37GPM average flow rate, 1.9, 4.5, 3.5, 1.8, 6.2 and 3.2% respectively has been observed for  $\Delta P$  values from height 1 to 7. At 41GPM flow,  $\Delta P$  differential difference observed from height 1 to 7 are 1.7, 3.2, 2.7, 1.4, 4.9 and 3% respectively. And finally for 45GPM at 20% VOP, 1.4, 2.9, 2.5, 1.6, 4.2 and 2.7% were also observed.

Again for 40, 60 and 80%, the following trend ensues.  $\Delta P$  increases from height 1 to height 2, slightly increases again from height 2 to height 3 where max pressure of delta P is attained, then decrease from height 3 to 4 and again from height 4 to 5.  $\Delta P$  then increases slightly from height 5 to 6 before finally decreasing slightly from height 6 to 7. From the above analysis, it has again been seen that regardless of the VOP,  $\Delta P$  remains nearly the same as the flow rate increases across height 1 to 7. [89, 90, 91, 92 and 93] have already established this phenomenon, ensuring that the  $C_v$  remains constant.

The next section attempts to prove this fact using the MHP, where the derivation of the local sectional  $C_v$  for this position is established.

#### **4.3.1.2.2 ESTABLISHING THE SECTIONAL $C_v$ CHANGES FOR DIFFERENT VOPs USING THE MHP AT POSITION 1**

The parameter that measures the characteristics and measures the amount of energy dissipated in the valve is the valve  $C_v$  (flow coefficient). Again, the  $C_v$  is a function of both  $\Delta P$  (in PSI) and the flow rate (in GPM) with the specific gravity of one (1) as the fluid used is water as again given in equation 1.4. For this position of the MHP, the static pressure have been measured across the seven heights. The static pressure drop have been

averaged, across the seven heights, with  $P_{av static}$  obtained in order to calculate the Cv. At the inlet, the distance between the global inlet point (2D from the valve inlet) and the probe position is 250mm and that of the global outlet point (6D from the valve outlet) is 690mm, creating a 220mm distance between both probes. This position, again, would have a reduced pressure drop as the distance between P1 and P2 have reduced, having effect on the valve Cv. Average pressure at the inlet and outlet (to obtain  $\Delta P$ ) and flow rates have been obtained in determining the Cv values. Figure 4.15 shows the pressure drop ( $\Delta P$ ) for the different VOPs at various flow rates.

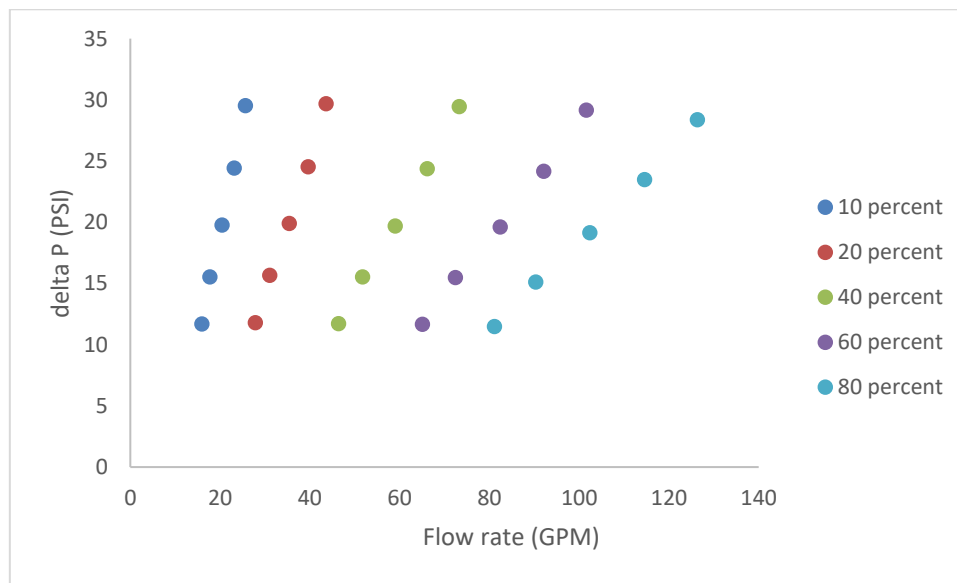


Figure 4.15: Pressure drop variations for different VOPs and for various flow rates

As seen from figure 4.15, again the pressure drop increases as the flow rate increases as they have a near linear relationship. These increases can be seen across all the VOPs. The inlet pressure increase is due to the kinetic energy imparted by the pump impeller, which is converted into potential energy in the form of static pressure. This causes an increase in inlet pressure of the valve as the speed of the impeller increases. At the valve outlet, the pressure remains nearly constant close to the atmospheric pressure after flow passes through the valve trim that modulates the flow, thereby causing an increase in the pressure drop as the flow increases across the different VOPs. Across the VOPs, pressure drop is seen to increase marginally as passage flow area (VOP) increases from the figure 4.15. This is because as flow area increases, there is lesser flow restriction causing pressure drop to increase as the flow rate  $Q$  increases.

Figure 4.16 shows the various Cv of the valve calculated from the pressure drop for the different VOPs at various flow rates.

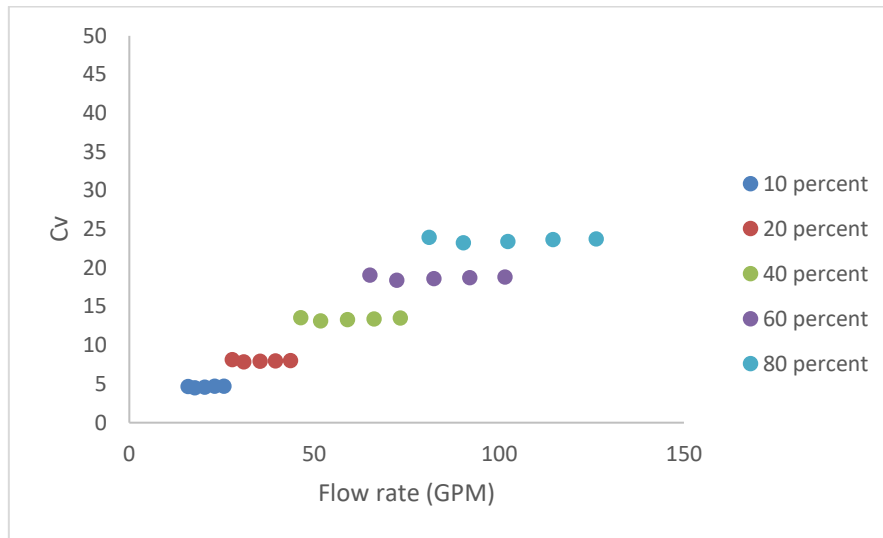


Figure 4.16: Valve Cv variations for different VOPs at various flow rates

It can be seen that the Cv of the valve remains same at different flow rate for a particular valve opening position. This fact again has been established by references given for global pressure measurement in section 4.3.1.1 that the Cv of a valve is independent of the process condition as seen in figure 4.16 and that irrespective of the flowrates, the Cv remains the same (almost). A single curve representing the Cv is again presented in figure 4.17 corresponding to the maximum allowable flow rate, by averaging the flow rate values and pressure to get a single Cv value for the different VOPs.

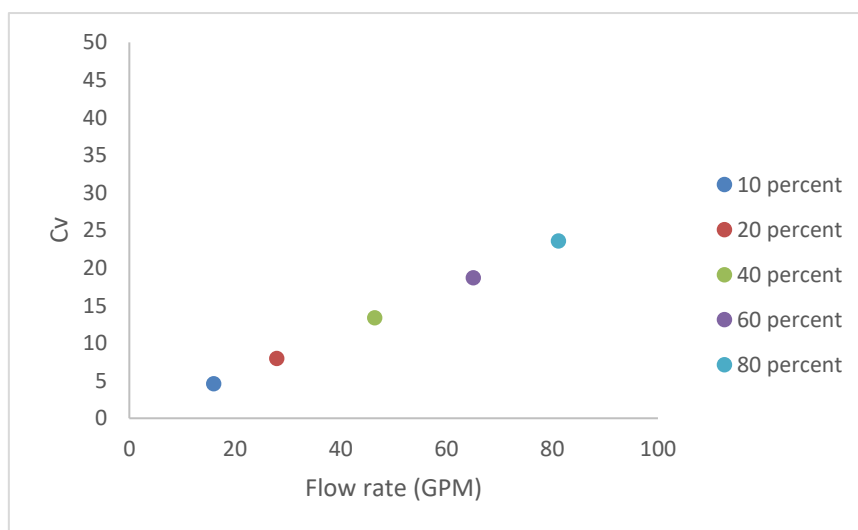


Figure 4.17: Valve Cv variation for different VOPs for position 1

It can be seen from figure 4.17 that the valve  $C_v$  increases as the VOP increases. The  $C_v$  increases from 4.63 to 7.98 as the VOP increases from 10 to 20 % with a percentage increase of 42%. When the valve is opened further from 20 to 40%,  $C_v$  increases from 7.98 to 13.38, increasing at 40.4%. Further VOP increase from 40 to 60% and 60 and 80% increases the valve flow capacity to 19.8 and 24.92, representing a 28.6 and 20.7% respectively. This increase in valve  $C_v$  concerning the different opening positions is again, seen to be linear which confirms that the particular trim used in this research is a linear trim.

For position 1 (0.5D to 0.9D), the  $C_v$  slightly increases compared to  $C_v$  calculated using the IEC BS EN standard 60534 (2D and 6D). This is because of the reduction in pressure drop and due to  $C_v$  being inversely proportional to the square of pressure drop.  $C_v$  would increase further as the distance of the probe positions decreases from the valve inlet and outlet.

The next subsection analysed the velocity profile across the different heights position at different flow rates and VOPs.

#### **4.3.1.2.3 ESTABLISHING THE VELOCITY PROFILE CHANGES FOR DIFFERENT VOPs USING THE MHP**

By considering the different sections where the probe have been placed inside the valve in the investigating areas, at different heights, the VOPs used in developing the velocity profile are 10, 20, 40, 60 and 80% have been examined. Due to the complex geometry inside the valve, it has reduced the area where the probes are placed to 60mm and 70mm at the inlet and outlet respectively. The MHP has been used to measure the local velocity for seven heights at each section/position.

Before plotting the velocity profile for the different VOPs, the average velocity using CFD have been plotted for the section where the different probes have been placed. Figure 4.18 shows that the average velocity increases as flow rate increases.

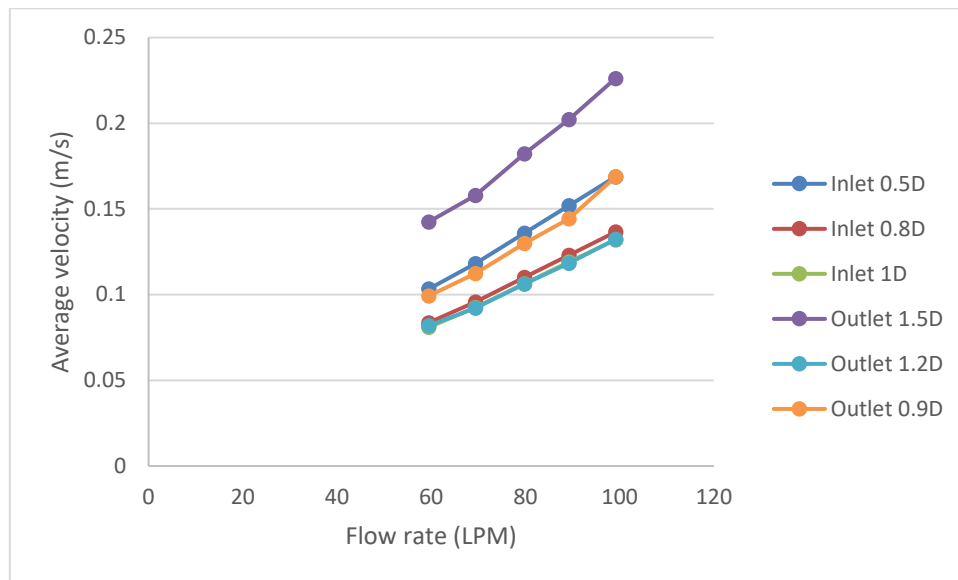


Figure 4.18: Average velocity increase validation for the different probe measurement positions for different flow rates

However, local velocity profile has been analysed for the different sections across seven heights for position 1, 2 and 3.

Starting with position 1, velocity magnitude across seven heights for the different flow rates have been analysed. Figure 4.19 depicts the velocity profile for the different pump set points at various VOPs at the inlet (0.5D).

The flow cross sectional area at this position (0.5D) is  $0.0103m^2$ . Figure 4.19 depicts the velocity profile for several flow rates at the different VOPs. The area for the different section where the probe has been placed has been calculated.

Atypical type profile have been obtained for the different VOPs at the various flow rates. The reason for this atypical profile for the different VOPs and flow rates is because of the amount of probe body causing interference inside the valve. The more the probe is inside the valve, the more the interference it causes, which in turn affects the flow parameters, including the obtained velocity. In addition, atypical profile seen for the different flow rates is relative for the different VOPs. For higher VOPs, the velocity profile becomes closer to the ideal profile for a turbulent flow. Figure 4.19 depicts the velocity profile for several flow rates at the different VOPs.

For 800LPM at 10% VOP, the trend for the velocity distribution across this position has been presented. Due to the very low VOP, unsteady flow velocity distribution has been observed.

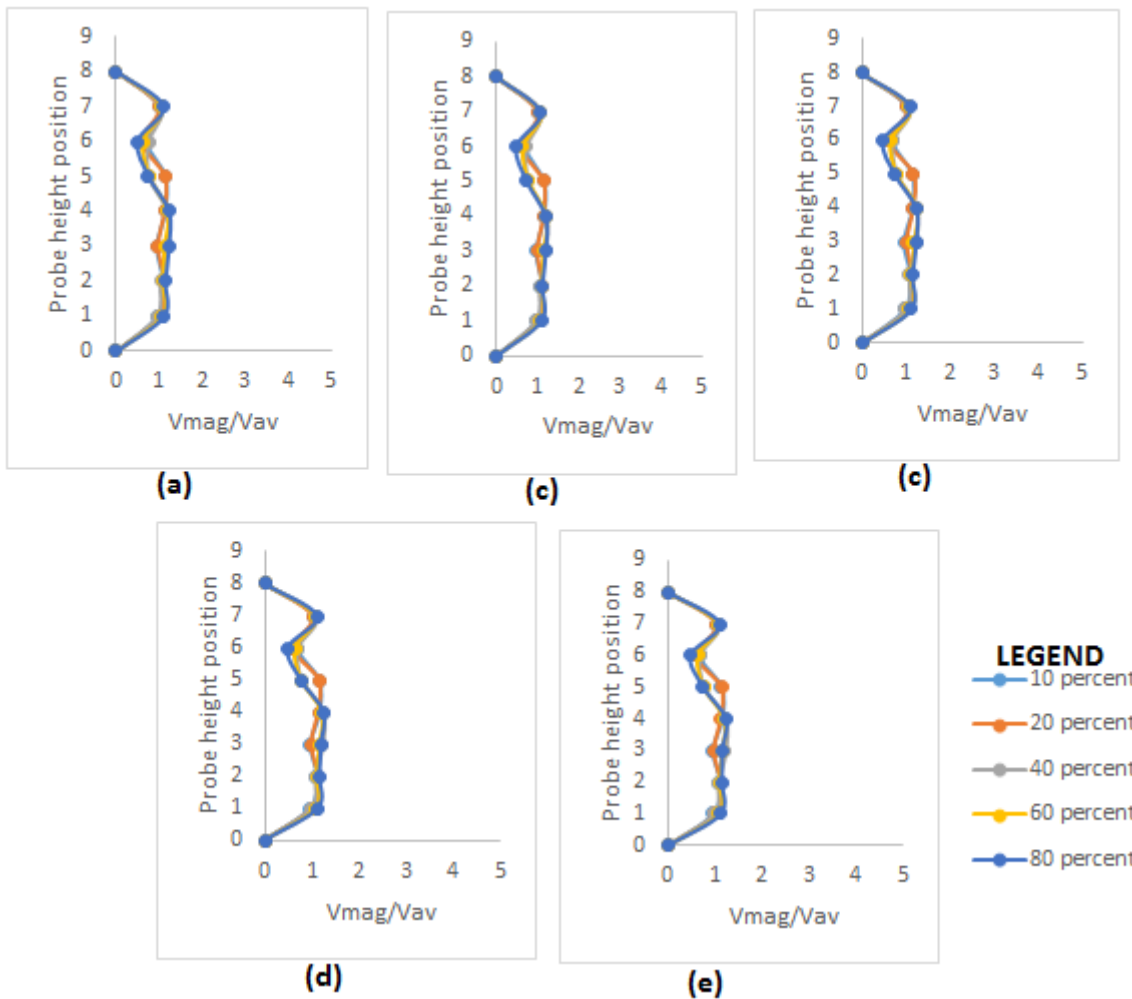


Figure 4.19: Velocity profile for the across the different heights at the probe inlet position (0.5D) for the different VOPs (a) 800LPM (b) 900 LPM (c) 1000 LPM (d) 1100 LPM (e) 1200 LPM

$V_{av}$  for the velocity at every probe positions have been calculated using equation 4.1.

$$V_{av} = \frac{A_1V_1+A_2V_2+A_3V_3+A_4V_4+A_5V_5+A_6V_6+A_7V_7}{A_1+A_2+A_3+A_4+A_5+A_6+A_7} \dots\dots\dots 4.1$$

Local velocity coefficient  $(\frac{V_{mag}}{V_{av}})$  vary from probe height 1 to height 7 where measurements has been taken. Local velocity coefficient increases from height 1 to 2, decrease from 2 to 3, increase at height 4, increase slightly again at height 5, decrease at

height 6 and finally increasing again slightly for height 7. At 0.97 velocity coefficient, following the said trend explained above, the velocity coefficient increases at 11.4% at height 2 from height 1, decreases by 14% at height 3, increases again at the rate of 16% for height 4. For height 5, velocity coefficient increases slightly by 0.2% and then drops at the rate of 38% from height 5 to 6. From height 6 to 7, velocity coefficient further increases slightly at 29%. Maximum velocity coefficient value obtained for this particular VOP is 1.15 and was seen at height 5. A decreasing velocity coefficient trend is seen for the different height positions across the VOPs. This means that as the VOP increases, the velocity coefficient decreases. For 20, 40, 60 and 80% VOPs, across the different probe heights, velocity coefficients have been seen to vary as flow rates changes. Ideally, as the flow rate increases, velocity should increase, as flow area (VOP) remains constant. However, due to the complex flow experienced because of the complex geometry and the probe calibration uncertainties, the local velocity measured has been observed to decrease slightly across the seven heights and the VOPs as flow rate increases.

As the flow rate is increased to 900 from 800LPM, velocity coefficients is seen to decrease. Velocity coefficients percentage decrease from height through to height 7 are 0.3, 0.2, 0.8, 0.2, 0.15, 0.1 and 0.2% respectively for 900LPM at 10% VOP. For 20% VOP, velocity coefficient decrease at the rate of 0.04, 1.6, 1.1, 0.3, 0.3, 0.2 and 0.06% respectively for the different probe heights. For 40% VOP, 0.9, 0.5, 0.2, 0.5, 0.6, 0.4 and 0.8% decrease have been observed from 800 to 900LPM for height 1 to height 7 respectively. At 60% VOP, percentage drop from 800 to 900LPM are 1, 0.1, 0.7, 0.03, 0.3, 1.8 and 0.3% respectively. Finally, for 80%, 0.8, 0.2, 0.08, 0.04, 0.1, 1.3 and 0.004% decrease from 800 to 900LPM from height 1 to height 7 respectively.

As the flow rate is increased from 900 from 1000LPM, velocity coefficient is seen to decrease slightly. Velocity coefficient percentage decrease are 0.04, 0.006, 0.6, 0.2, 0.4, 0.06 and 0.6% respectively for 10% VOP. For 20, 40, 60 and 80% VOP, velocity coefficient follows similar trend as seen for 10% VOP.

As the flow rate is increased from 1000 from 1100LPM, velocity coefficient is seen to decrease slightly. Velocity coefficient percentage decrease are 1.3, 0.5, 0.08, 0.1, 0.7, 1.3, and 2.7% respectively for 10% VOP. Again for 20, 40, 60 and 80% VOP, velocity coefficient follows similar trend as seen is 10% VOP from height 1 to height 7 respectively.

As the flow rate is increased from 1100 from 1200LPM, velocity coefficient is seen to slightly decrease again. Velocity coefficient percentage decrease are 0.1, 0.5, 0.8, 0.4, 0.47, 0.97 and 1.5% respectively for 10% VOP. For 20, 40, 60 and 80% VOP, velocity coefficient follows similar trend as seen is 10% VOP from height 1 to height 7 respectively.

For outlet velocity profile, same equation has been used (equation 4.1). Same trend as seen for inlet analysis for this position. For 800LP at 10% VOP, the trend for the velocity distribution across this position has been presented. Local velocity coefficient ( $\frac{v_{mag}}{v_{av}}$ ) vary from probe height 1 to height 7 where measurements have been taken.

Local velocity coefficient increases from height 1 to 2, decrease from 2 to 3, increase at height 4, decrease slightly again at height 5, decrease at height 6 and finally increasing again slightly for height 7. At 0.71 velocity coefficient, following the said trend explained, the velocity coefficient increases at 37.1% at height 2 from height 1, decreases by 46.9% at height 3, increases again at the rate of 30% for height 4. For height 5, velocity coefficient increases slightly by 0.8% and then drops at the rate of 13.7% from height 5 to 6. From height 6 to 7, velocity coefficient further increase slight at 9.9%. Maximum velocity coefficient value obtained for this particular VOP is 1.11 and was again seen at height 5. For 20, 40, 60 and 80% VOP, velocity coefficient follows similar trend as seen is 10% VOP.

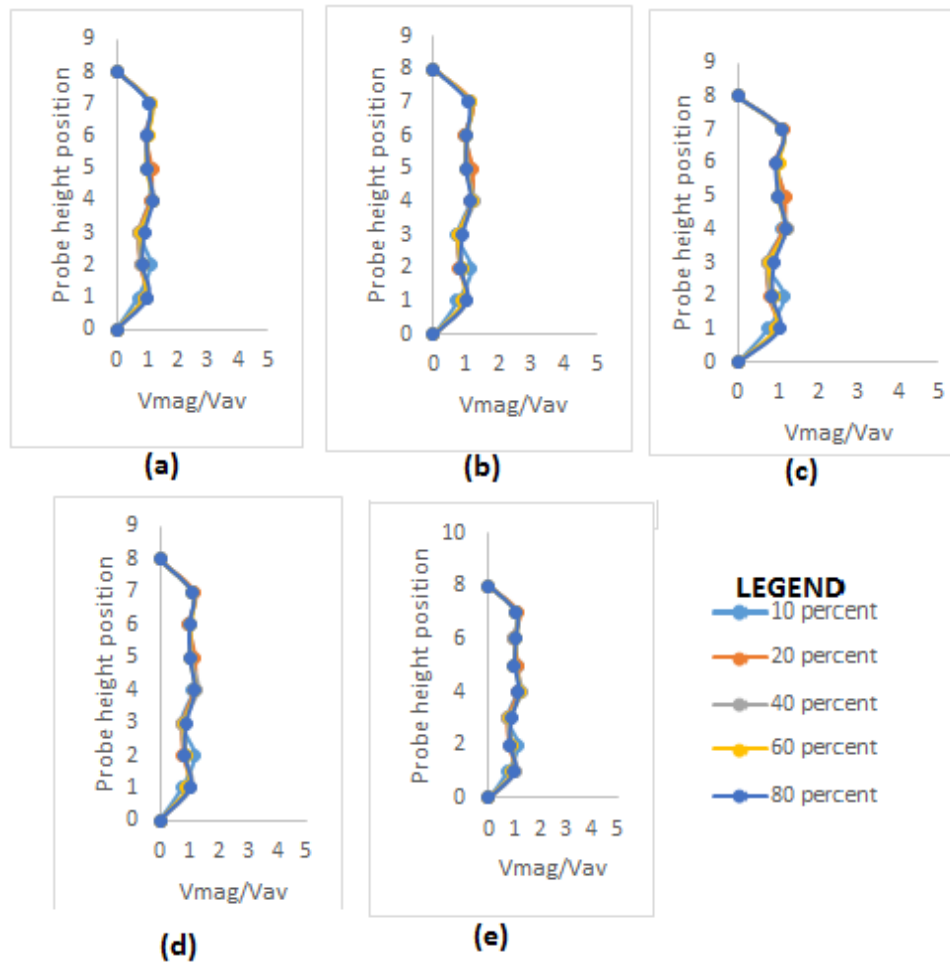


Figure 4.20: Velocity profile for the across the different heights at the probe outlet position (0.9D) for the different VOPs(a) 800LPM (b) 900 LPM (c) 1000 LPM (d) 1100 LPM (e) 1200 LPM

As the flow rate is increased from 800 to 900 LPM, velocity coefficient is seen to decrease. Velocity coefficient percentage decrease are 0.3, 0.8, 5.6, 0.5, 1.4, 0.04, and 1% respectively for 900LPM at 10% VOP. 20, 40, 60 and 80% VOP, follow similar trend from height 1 to height 7 respectively.

For 1000LPM, velocity coefficient obtained are 2.1 0.08, 0.04, 0.2, 0.5, 0.4 and 0.07% at 10% VOP from 900LPM for height 1 through to height 7 respectively. Again, 20, 40, 60 and 80% VOP, follow similar trend from height 1 to height 7 respectively.

For 1100LPM, velocity again decreases due to the complex flow and geometry inside the valve across the seven heights and different VOPs. For 10% VOP, 0.4, 0.88, 1.2, 0.8, 0.01, 0.9 and 1.7% decrease from 1000 LPM, for height 1 to 7 respectively have been observed.

Again, 20, 40, 60 and 80% VOPs follow similar trend from height 1 to height 7 respectively.

Finally, at 1200 LPM, velocity coefficient decreases as flow rate increases. It is seen at 10% VOP that the velocity coefficient decreases at 1.2, 0.13, 0.6, 0.55, 0.6, 0.39 and 0.44% for probe height 1 to 7 respectively. Again, 20, 40, 60 and 80% VOP follow similar trend from height 1 to height 7 respectively for height 1 to 7 respectively.

#### **4.3.1.3 PROBE LENGTH POSITION 2 (0.8D INLET AND 1.2D OUTLET)**

For this position, the probe at the inlet is placed at 0.8D away from the valve inlet and 1.2D away from the valve outlet. These probes placed at their specific location inside the valve will measure the pressure from the different holes, which would be converted to other flow parameters like velocity magnitude, static and total pressure using calibration coefficients obtained from the pressure probe calibration. The next subsection describes the effect of static pressure drop for various flowrates at different VOPs.

##### **4.3.1.3.1 FLOW RATES EFFECTS ON LOCAL PRESSURE DROP AT DIFFERENT VOPs**

After global pressure analysis of the valve for different flow rates at 2D and 6D, and 0.5D and 0.9D (position 1), local analysis using the probe for this particular position for pressure drop have been discussed and analysed.

From figure 4.21, similar trend can be seen for all the heights positions where the change in pressure increases as flow rate increases for all the various probe height positions. Again, the valve inlet pressure increases due to the kinetic energy impacted by the pump impeller as it is converted into potential energy in the form of pressure as the full pump pressures exists over that of the valve. When the VOP increases or decreases, it causes the system pressure to change. These trends continues before flow goes inside the trim. This trend would be seen for any probe lengths and heights, before the valve trim. For the same set points, flow rates can be seen to depend on the VOPs as their pressure increases, so do the flow rates. The maximum flow rate for this research has been set to 1200LPM.

For height 1 in figure 4.21, it can be seen that differential pressure increases from 10.8 to 14.6 PSI as flow rate increase from 15.72 to 18.3GPM for 10% opening. This represent an increase of 26.1% as the flow rate increase at 14.3%.  $\Delta P$  further increases to 18.76,

23.3 and 28.7 PSI with an increase rate of 22, 19.5 and 18% respective at flow rate of 21.08, 23.58 and 36.19GPM at an increase rate of 13.03, 10.6 and 9.8% respectively.

As VOP increases from 10 to 20%, 20 to 40, 40 to 60 and 60 to 80%, for same pump set point, flow rates increases and causes  $\Delta P$  to increase. Similar trends can be seen for the remainder of the VOPs, except for the increase in flow rates and pressure drop as the VOP increases and flow area expands.

For height 2 through to height 7, flow rates stays nearly the same, as similar valve operating and flow condition have been used. However,  $\Delta P$  slightly vary across the different valve heights as the inlet pressure vary due to the fact that the flow in the valve system is a pressure driven flow.

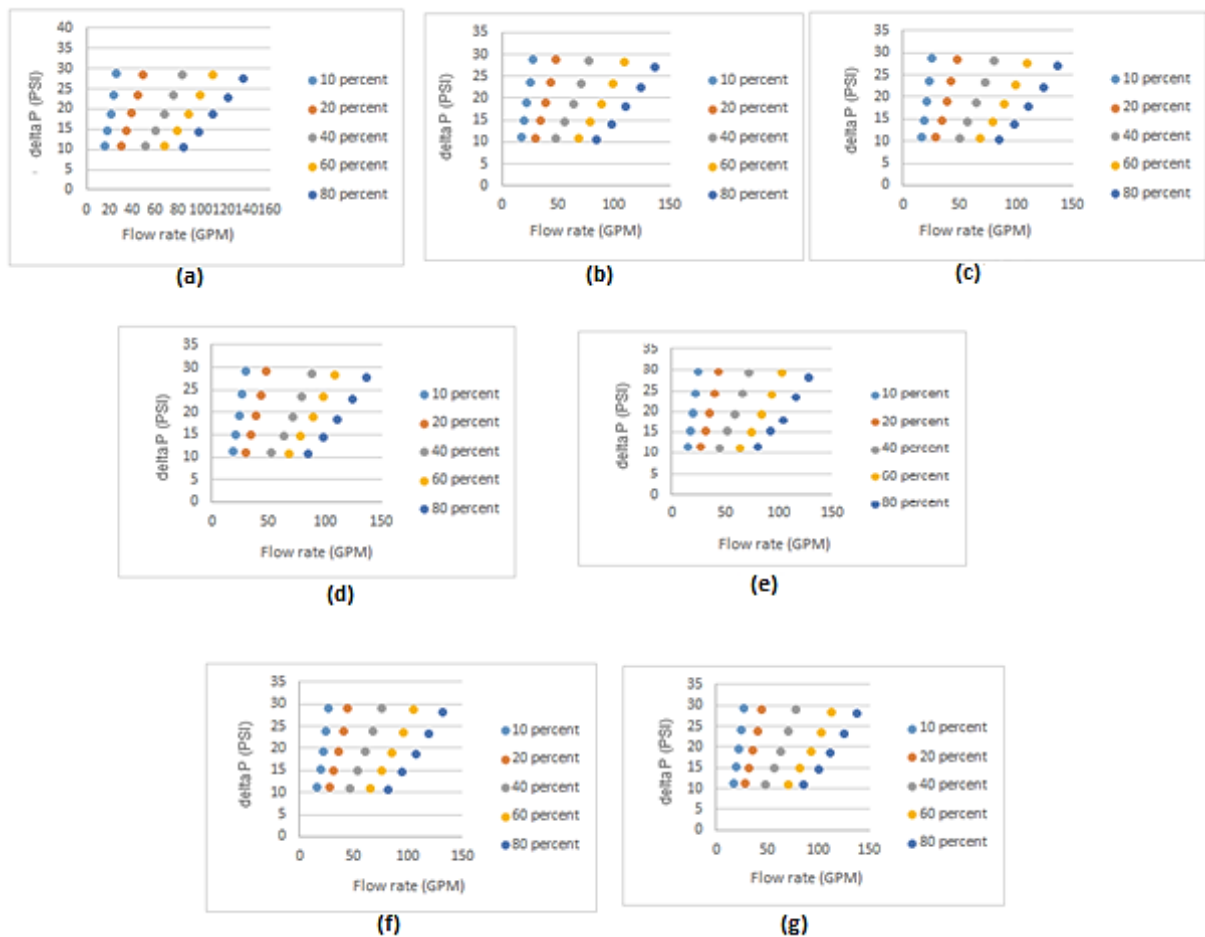


Figure 4.21: Local pressure variation for different flow rates and VOPs for the different height positions (a) Height 1 (b) Height 2 (c) Height 3 (d) Height 4 (e) Height 4 (f) Height 6 (g) Height 7

As the probe position goes from height 1 to height 7, the section of the probe body which is inside the valve increases, which causes more interference to the flow. This is evident again from the pressure and velocity variation from height 1 through to 7. Ideally,  $\Delta P$  should increase from height 1 to height 5 (maximum pressure point), then starts to decrease from height, before reaching height 7. For higher VOPs (40, 60 and 80%), height 2  $\Delta P$  decreases from height 1 before it then increases all through to height 5, unlike for lower VOPs (10 and 20%) where  $\Delta P$  starts to increase, until it attains the maximum pressure at height 5. After height 5,  $\Delta P$  begins to decrease. However, as the length of the probe begins to appear more as the height increases, a similar trend can be seen where  $\Delta P$  becomes inconsistent, all through to height 7. One thing is certain though,  $\Delta P$  is maximum height 5. At average flow rate of 16GPM (800LPM pump set point), for 10% VOP,  $\Delta P$  increases from height 1 (10.8 PSI) to height 2 (11.02), representing an increase of 2%. From height 2 to height 3,  $\Delta P$  decreased slightly by 0.6% and then increase again by 1.9% from height 3 to 4.  $\Delta P$  further increases by 2% from height 4 to 5. It then decreases by nearly 1.36% to height 6 before rising slightly by 0.2% at height 7.  $\Delta P$ , for average flow rate of 19GPM (900LPM pump set point) at 10%VOP, follows the same trend as that for 16GPM. From  $\Delta P$  of 14.6 PSI at height 1,  $\Delta P$  increases by 1.7% to 14.88 PSI for height 2. From height 2 to height 3,  $\Delta P$  decreased slightly by 0.7% to 10.95PSI. It increases slightly again by 1.9% from height 3 to 4.  $\Delta P$  further increases by 2% from height 4 to 5. It then starts to decrease from height 5 to 6, from 11.37 to 11.2 PSI by 1.36% and increases slightly to 11.23 PSI by 0.2% at height 7. For average flow rate of 22GPM (1000LPM pump set points), same trend for  $\Delta P$  is followed where it increases from height 1 (18.76PSI) to height 2, increases at height 3, increase at height 4, increases again from height 4 to 5, decreases from 5 to 6 and then decreases from height 6 to 7 at 1.9, 0.6, 1.6, 1.6, 1.3 and 0.3% respectively. Same trend is again repeated for average flow rate of 24GPM (1100LPM pump set point) from height 1 with  $\Delta P$  of 23.3PSI, through to height 7 at 1.9, 0.5, 1.3, 1.7, 1.2 and 0.2% respectively. Finally, for 10% VOP at 27GPM average flow rate, same trend again is seen from height 1 to 7 at 0.6, 0.2, 1.1, 1.5, 1.2 and 0.2% respectively.

For 20, 40, 60 and 80% VOPs, similar trend as that of 10% are observed where  $\Delta P$  increases from height 1 to 2, decrease slightly from height 2 to 3, increases from height 3 to 4. Further increases from height 4 to 5, decreases from height 5 to 6 and then

decreases slightly from height 6 to 7. This trend cuts across all the average flow rates for these VOPs. As the VOPs increases, the flow rate increases but  $\Delta P$  remains slightly the same.

From the above analysis, it has again been seen that regardless of the VOP,  $\Delta P$  remains nearly the same as the flow rate increases across height 1 to 7. [89, 90, 91, 92 and 93] again have already established this phenomenon, ensuring that the  $C_v$  remains constant.

The next section attempts to prove this fact using the MHP, where the derivation of the local sectional  $C_v$  for this particular position is established.

#### **4.3.1.3.2 ESTABLISHING THE SECTIONAL $C_v$ CHANGES FOR DIFFERENT VOPs USING THE MHP**

As mentioned earlier, the parameter that measures the characteristics and measures the amount of energy dissipated in the valve is the valve  $C_v$  (flow coefficient) which is a function of flow rate and  $\Delta P$  with a specific gravity of one (due to the fluid used being water) given in equation 1.4. For this position of the MHP, the static pressure has been measured for the different height with the average static pressure drop  $P_{av static}$  obtained for all the heights in order to calculate the  $C_v$ . At the inlet, the distance between the global inlet point (2D from the valve inlet) and the probe position is 280mm and that of the global outlet point (6D from the valve outlet) is 720mm, creating a 160mm distance between the two probes. This position, again, would have a reduced pressure drop as the distance between P1 and P2 has reduced, having a significant effect on the valve  $C_v$ . Figure 4.22 shows the pressure drop ( $\Delta P$ ) for the different VOPs at various flow rates.

As seen in the figure 4.22, the pressure drop increases as the flow rate increases for the various VOPs.  $\Delta P$  Increases because inlet pressure increases due to increase in flow rate due to the pump's impeller, while outlet pressure remains constant across the different VOPs. Across the VOPs, pressure drop is again seen to reduce marginally as the flow passage area increases from the figure.

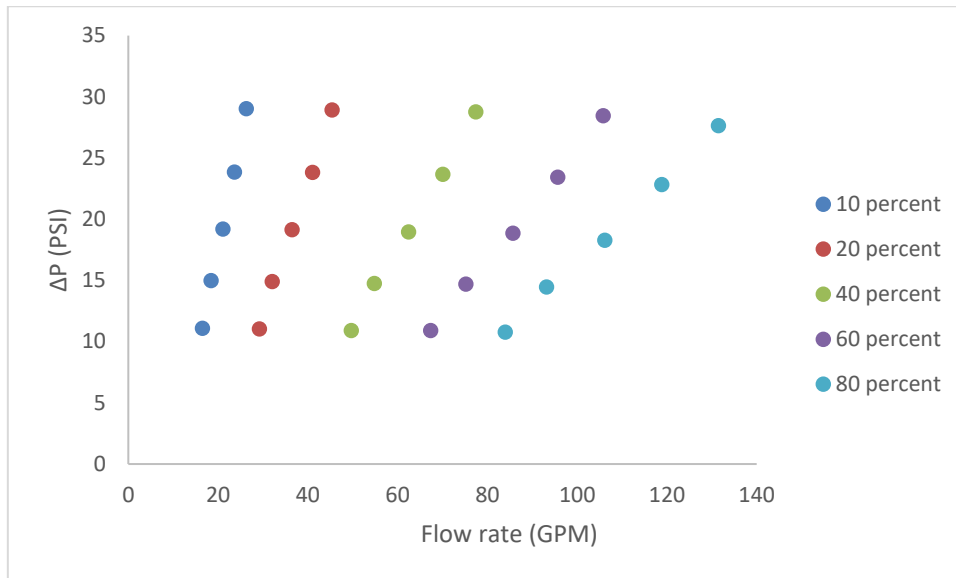


Figure 4.22: Pressure drop variation for different VOP and for various flow rates for position 2

Figure 4.23 shows the various Cv value of the valve calculated from the pressure drop for the different VOPs at various flow rates.

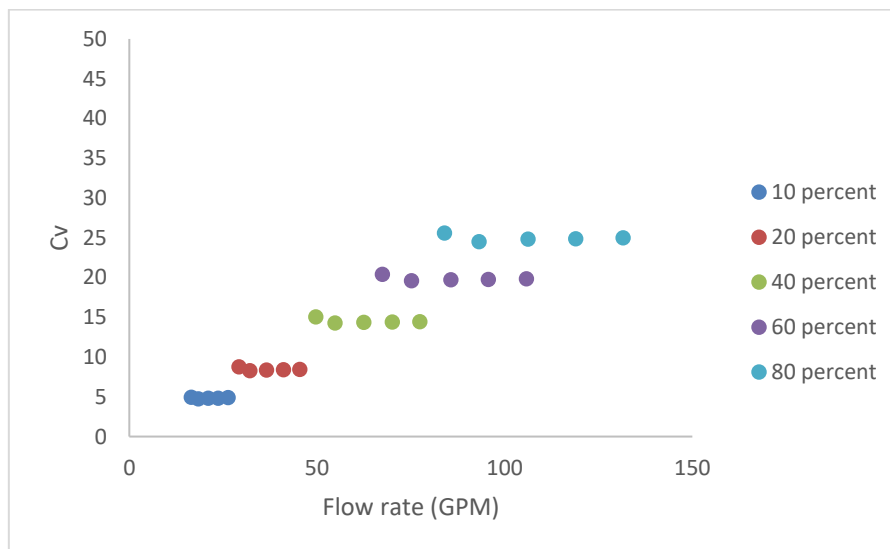


Figure 4.23: Valve Cv variation for different VOP and for various flow rates for position 2.

It is again seen that the Cv of the valve remains the same at different flow rates for a particular valve opening position. This fact has been established by [89, 90, 91, 92, and 93] that the Cv of a valve is independent of the process condition as seen in figure 4.23 that irrespective of the flowrates, the Cv remains the same (almost). At 10% VOP, Cv

remains nearly constant at 5. For 20, 40, 60 and 80% VOP, Cv on the figure remains at around 9, 15, 20 and 25 respectively. A single curve representing the Cv is depicted in figure 4.24.

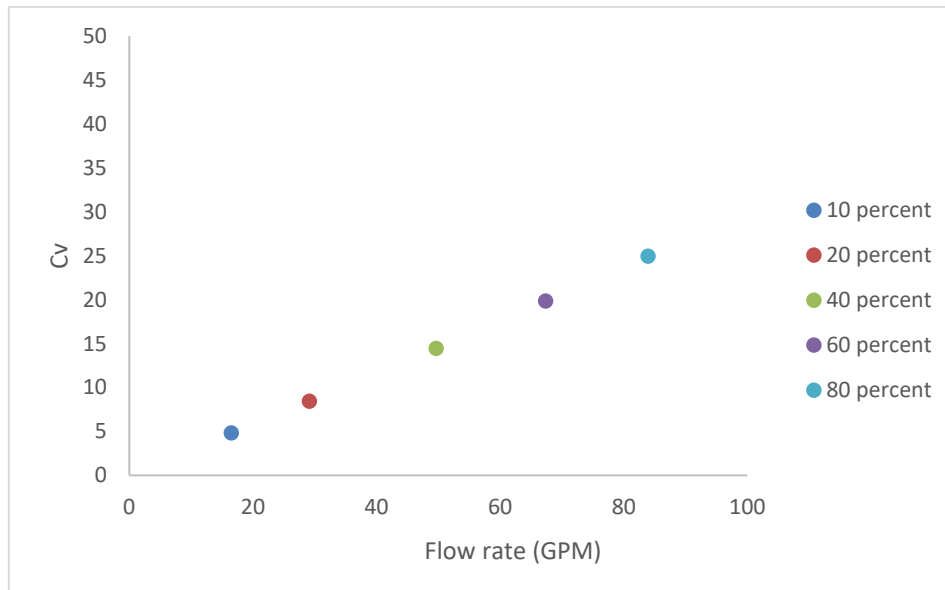


Figure 4.24: Valve Cv variation for different VOP for position 2.

It can further be seen from figure 4.24 that as the VOP increases, valve Cv increases. The Cv increases from 4.84 to 8.44 as the VOP increases from 10 to 20 %. When the VOP increases further from 20 to 40%, Cv increases from 8.44 to 14.49. Further VOP increase to 60 and 80% increases the valve flow capacity to 19.86 and 24.95 respectively. This increase in valve Cv, about the different opening positions, is seen to be linear, also confirming that the trim used in this research is a linear trim.

For position 2 (0.8d to 1.2d), the Cv slightly increases compared to Cv calculated using the IEC BS EN standard 60534 (2D and 6D) and for position 1 (0.5D to 0.9D). This is because of the reduction in pressure drop and due to Cv being inversely proportional to the square of pressure drop. Cv would increase further as the distance of the probe positions decreases from the valve inlet and outlet.

Again, the velocity profile constructed for the different flow and operation conditions, across the various heights for each section, at the inlet and outlet have been presented in the next section for this position.

#### 4.3.1.3.3 ESTABLISHING THE VELOCITY PROFILE CHANGES FOR DIFFERENT VOPs USING THE MHP

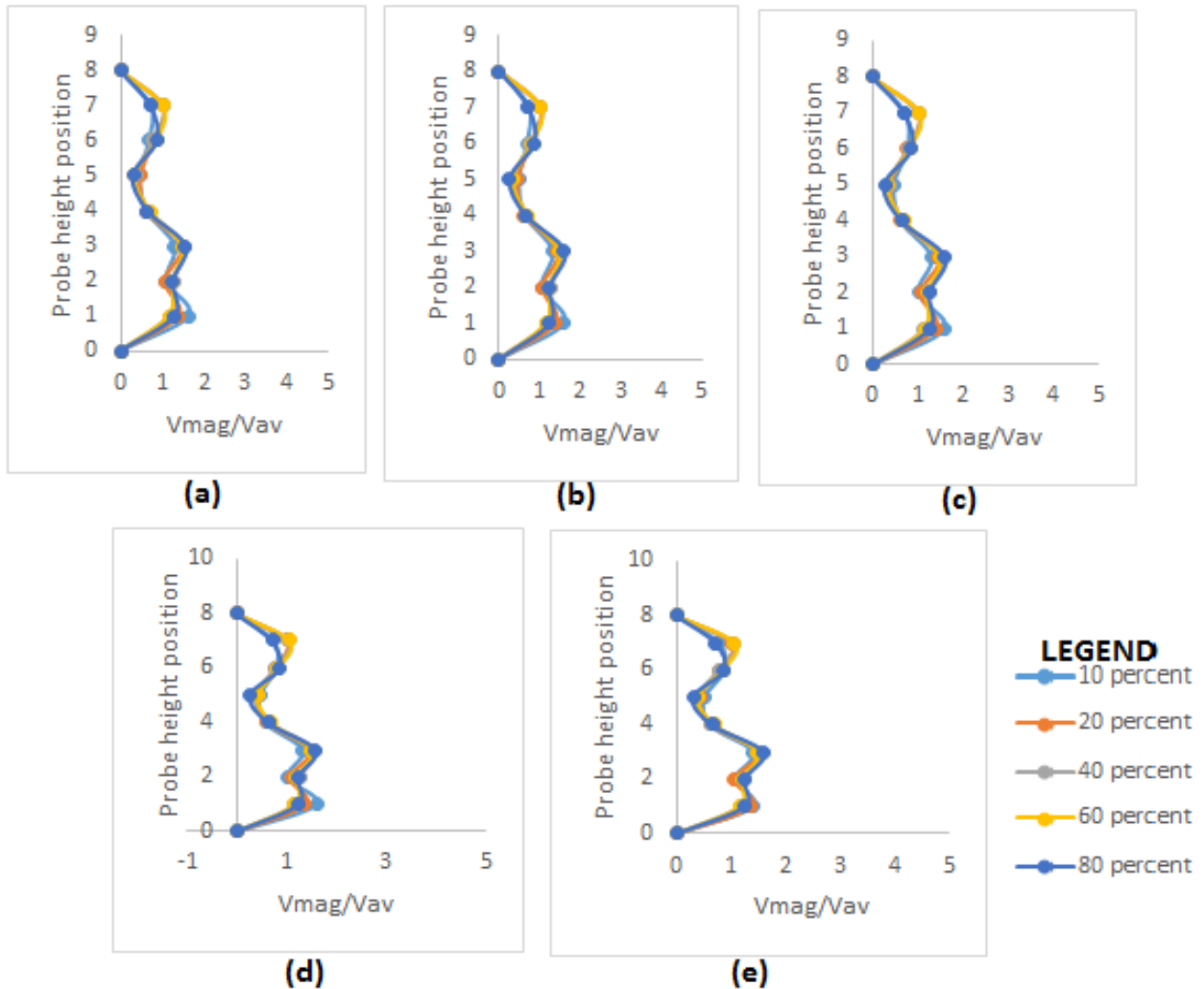


Figure 4.25: Velocity profile for the valve across the different heights at the probe inlet position (0.5D) for the different VOPs (a) 800LPM (b) 900 LPM (c) 1000 LPM (d) 1100 LPM (e) 1200 LPM

The flow cross-sectional area at this position (1D) is  $0.0136m^2$ . For each flow rate, velocity distribution has been obtained for the different VOPs. Again, atypical type profile has been obtained for the different VOP at the various flow rates. The reason for this atypical profile for the different VOPs and flow rates is again because of the amount of probe body causing interference inside the valve. The more the probe is inside the valve, the more the interference it causes, which in turn affects the flow parameters, including the obtained velocity. In addition, the atypical profile seen for the different flow rates is

relative for the different VOPs. Figure 4.25 depicts the velocity profile for several flow rates at the different VOPs and equation 4.1 has been used for calculating  $avg$ .

For 800LP at 10% VOP, the trend for the velocity distribution across this position has been given in figure 4.25. Due to the very low VOP, unsteady flow velocity distribution has been observed. Local velocity coefficient ( $\frac{V_{mag}}{V_{avg}}$ ) vary from probe height 1 to height 7 where measurements have been taken. Local velocity coefficient decreases from height 1 to 2, increase from 2 to 3, decrease at height 4, decrease slightly again at height 5, increase at height 6, and finally increasing again slightly for height 7. At 1.6 velocity coefficient, following the said trend explained above, the velocity coefficient decreases at 48.6% at height 2 from height 1, increases by 15.1% at height 3, decreases again at the rate of 51.3% for height 4. For height 5, the velocity coefficient decreases by 37.9% and then increases at the rate of 33% from height 5 to 6. From height 6 to 7, the velocity coefficient further increases slightly at 6.6%. A decreasing velocity coefficient trend is seen for the different height positions across the VOPs. This means that as the VOP increases, the velocity coefficient decreases. For 20, 40, 60 and 80% VOP, across the different probe heights, the velocity coefficient has been seen to decrease as VOP increases. Ideally, as the flow rate increases, velocity should increase, as the flow area remains constant.

As the flow rate is increased to 900 from 800LPM, the velocity coefficient is seen to decrease. Velocity coefficient percentage decrease are 1.5, 3.4, 2.5, 0.6, 6.4, 1.5 and 0.4% respectively at 10% VOP. For 20, 40, 60, and 80% VOP, across the different probe heights, the velocity coefficient has been seen to decrease as VOP increases for height 1 to 7 respectively from 800 to 900LPM.

For 1000LPM from 900LPM, velocity coefficient obtained are 0.5, 3.3, 0.8, 1.3, 1.2, 1.3 and 0.6% at 10% VOP, for height 1 through to height 7. Similar trends is also experienced for 20, 40, 60, and 80% VOPs.

For 1100LPM, velocity again decreases due to the complex flow and geometry inside the valve across the seven heights and different VOPs. For 10% VOP, 0.3, 0.99, 1.4, 9, 0.1, 2.2 and 2.4% decrease from 1000 LPM 10%, height 1 to 7 respectively have been observed. Again, similar trend is also experienced for 20, 40, 60, and 80% VOPs.

Finally, at 1200 LPM maximum flow rate, the velocity coefficient decreases as the flow rate increases. It is seen that at 10% VOP, the velocity coefficient decreases at 12.7, 3.9, 5.1, 4.4, 8, 9.5, and 5.2% respectively for probe height 1 to 7. Similar trend is also experienced for 20, 40, 60, and 80% VOPs for height 1 to 7 respectively.

Figure 4.26 depicts the velocity coefficient profile for this section across the seven-heights and different VOPs. The flow cross-sectional area at this position (1.2) is  $0.0242m^2$ . For each flow rate, velocity coefficient distributions have been obtained for the different VOPs. Again, atypical type profiles have been obtained for the different VOPs at the various flow rates. The reason for this atypical profile for the different VOPs and flow rates is as a result of the amount of probe body causing interference inside the valve. Similar profiles seen at the inlet is also experienced at the outlet.

Again, equation 4.1 has been used. Because of the very low VOP, unsteady flow velocity distribution has been observed. Again, the local velocity coefficient ( $\frac{V_{mag}}{V_{av}}$ ) varies from probe heights 1 to height 7. Local velocity coefficient decreases from height 1 to 2, increases from height 2 to 3, decreases from height 3 to 4, and decreases further from 4 to 5, increases from 5 to 6, and again from 6 to 7. For 800LP at 10% VOP, velocity coefficient from 1.39, following the said trend explained above, the velocity coefficient increases at 34.3, 9.6, 64.8, 17.1, 12.4, and 7.5% respectively.

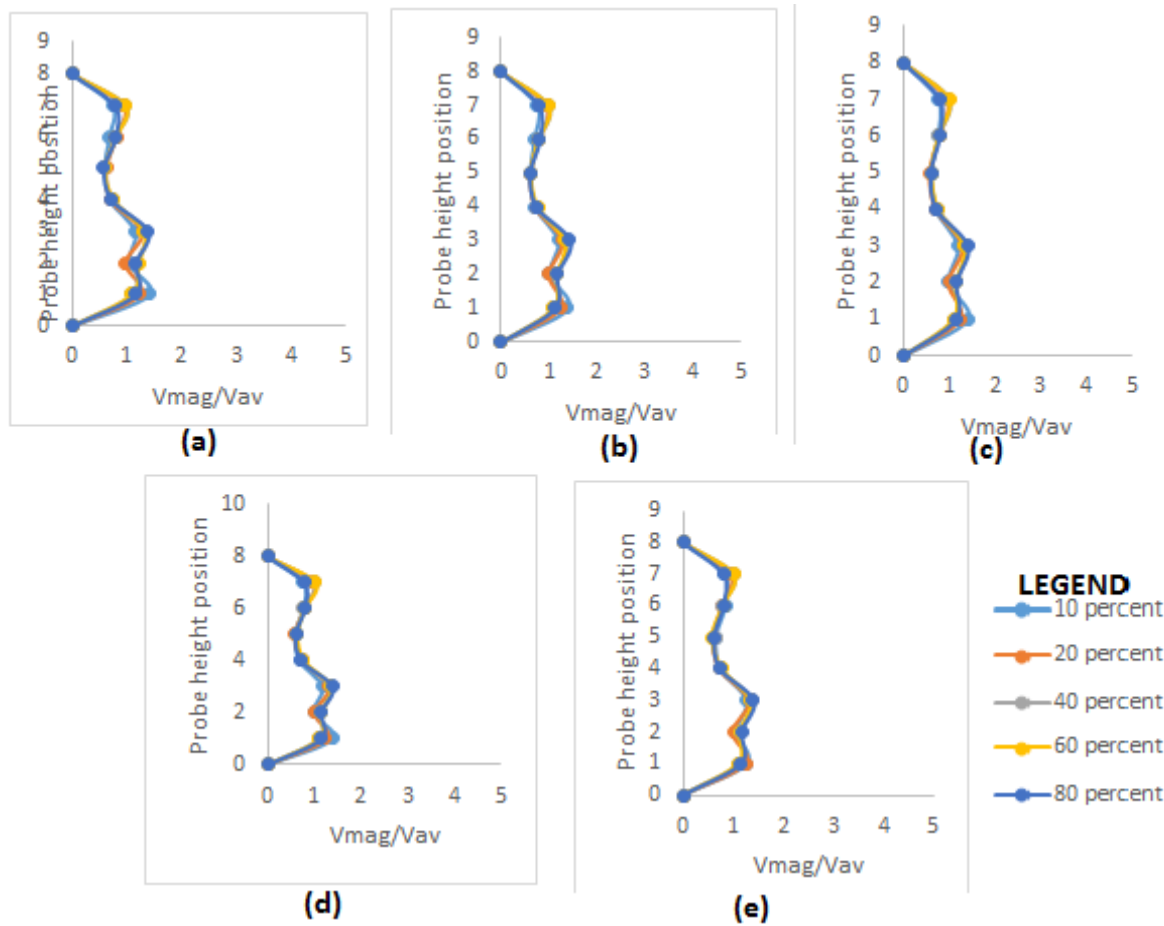


Figure 4.26: Velocity profile for the valve across the different heights at the probe outlet position (0.9D) for the different VOPs(a) 800LPM (b) 900 LPM (c) 1000 LPM (d) 1100 LPM (e) 1200 LPM

A varying velocity coefficient trend is again seen for the different height positions across the VOPs. This means that as the VOP increases, the velocity coefficient varies. For 20% 40%, 60% and 80%VOP, similar trends as 10% can be observed where the velocity coefficient decreases for height 1 and 2 and increases for height 3 to 7 respectively.

As the flow rate is increased from 800 to 900LPM, the velocity coefficient is seen to decrease.

The percentage decrease for the velocity coefficients are 0.9, 3.3, 2.5, 1.8, 1.3, and 1% respectively at 10% VOP for 900LPM. For 20, 40, 60, and 80% VOP, for height 1 to height 7, similar trend is observed.

At 1000LPM, velocity coefficients obtained are 0.16, 3.1, 0.5, 1.33, 0.3, 9.7 and 0.1% from 900LPM at 10% VOP for height 1 to height 7. For 20, 40, 60, and 80% VOP, for height 1 to height 7, similar trends are again observed.

For 1100LPM, the velocity coefficient decreases again from 1000LPM due to the complex flow and geometry inside the valve, across the seven heights and different VOPs. For 10% VOP, 0.15, 1, 0.1, 2.3, 1.6, 1.1 and 2.6% decrease for 10%, height 1 to 7 respectively have been observed. For 20, 40, 60, and 80% VOPs, for height 1 to height 7, similar trends are observed from 1000 to 1100 LPM.

Finally, at 1200 LPM, the velocity coefficient decreases as the flow rate increases. It is seen at 10% VOP that the velocity coefficient decreases at 10.3, 5.3, 5.4, 5.9, 7.7, 7.4, and 5% for probe height 1 to 7 respectively. For 20, 40, 60, and 80% VOP, for height 1 to height 7, similar trends are again observed for height 1 to 7 respectively.

#### **4.3.1.4 PROBE LENGTH POSITION 3 (1D INLET AND 1.5D OUTLET)**

For this position, the probe is placed 1D and 1.5D at the inlet and outlet respectively away from the valve. These probes placed at their specific location inside the valve will measure the pressure from the different holes, which would be converted to other flow parameters like velocity magnitude, static, and total pressure using coefficients obtained from the calibration of the pressure probe. The next subsection would describe the effect of static pressure drop at different VOPs for various flowrates.

##### **4.3.1.4.1 FLOW RATES EFFECTS ON LOCAL PRESSURE DROP AT DIFFERENT VOPs**

After pressure drop analysis of the valve for different flow rates at 2D and 6D, 0.5D and 0.9D, and 0.8 and 1.2D, local pressure drop analysis using the probe for this particular position has been discussed and analysed. From figure 4.27, again, similar trends seen for both positions in previous sections can be seen for all the heights positions where the delta pressure increases as flow rate increases for all the various probe height positions. When VOP increases or decreases, it causes the system pressure to change. These trends continue before flow goes inside the trim. For height 1 in figure 4.27, it can be seen that  $\Delta P$  increases from 10.9.8 to 13.6 PSI as flow rate increase to 19.2 from 16.4GPM for a 10% opening. This represent  $\Delta P$  increase of 28.2% as the flow rate increase at 15%.  $\Delta P$  further increases to 17.9, 22.6 and 27.7 PSI with an increased rate of 23.9, 20.6, and 18.5%

respective at flow rate of 21.9, 24.57, and 27.1GPM at an increasing rate of 12.03, 10.86 and 9.38% respectively.

At 20% VOP, for same pump set point, flow rates increases when compared to 10% VOP. This in turn, causes the  $\Delta P$  to increase as the VOP increases. This is because as the kinetic energy from the pump increases due to an increase in the VOP, potential energy in the form of the pressure would then reduce, as the total energy remains constant. This again causes pressure to increase as the VOP increases. As the flow rate increases from 16.4 to 28.1 GPM (10 to 20%),  $\Delta P$  stays nearly the same at a 3% variation from 10% VOP. Similar to 10% VOP, the flow rates increases to 32.8, 37.1, 41, and 45.1 GPM from 19.3, 21.9, 24.6, and 27.1GPM causing a  $\Delta P$  difference of 3, 2.2, 1.7, and 1.4% respectively for 20% VOP.

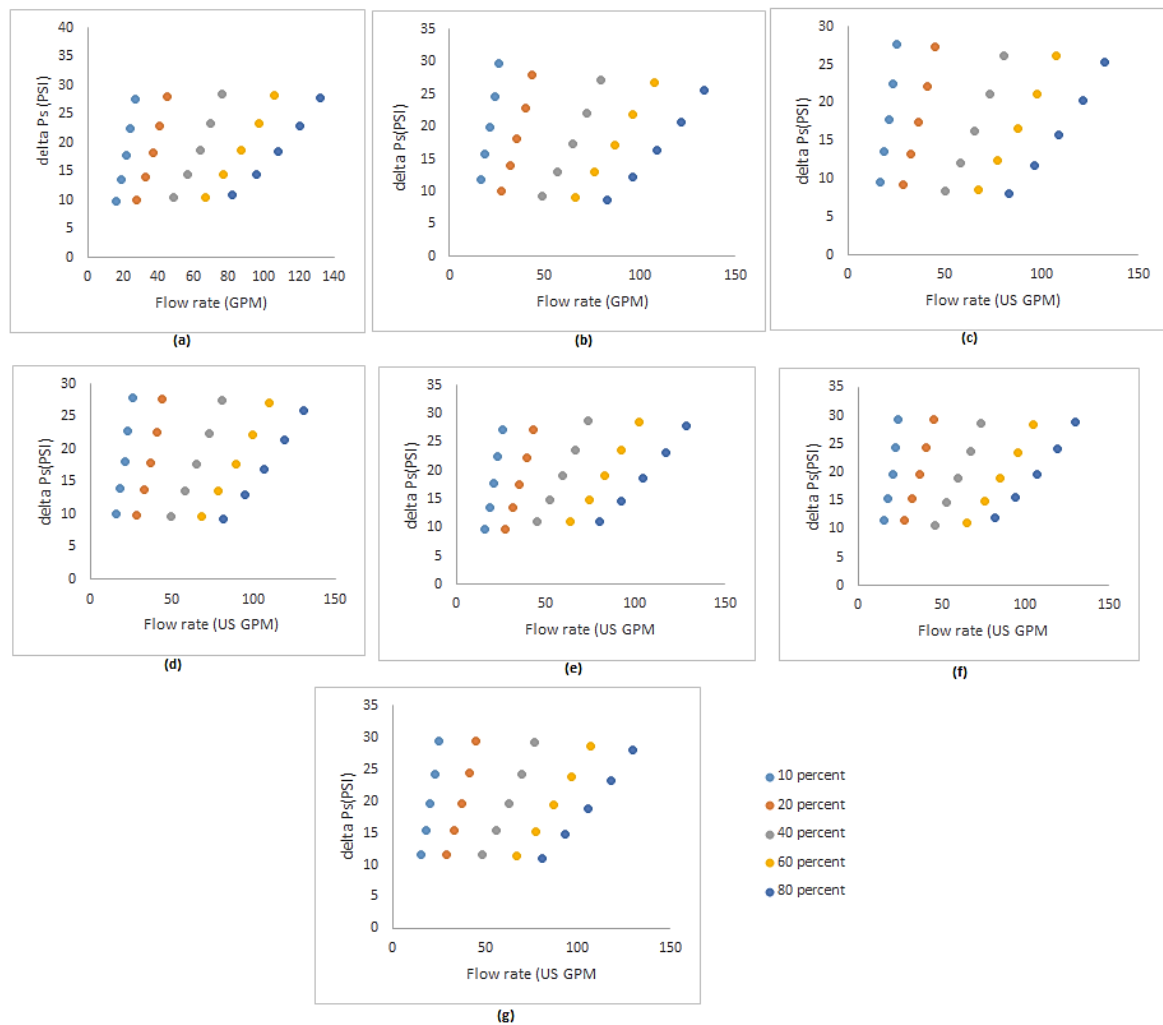


Figure 4.27: Local pressure variation for different flow rates and VOPs for the different height positions (a) Height 1 (b) Height 2 (c) Height 3 (d) Height 4 (e) Height 4 (f) Height 6 (g) Height 7 for position 3

At 40% VOP, as said earlier during 20% VOP analysis, the flow rate increases when VOP increases, and in turn, potential energy in the form of pressure decreases as  $\Delta P$  changes slightly. Same trends is also seen for 40 to 60% VOP and 60 to 80% VOPs for similar reasons.

At height 2 through to height 7, flow rates stays nearly the same, as similar valve flow and operating condition have been used. However,  $\Delta P$  slightly vary across the different valve heights as the inlet pressure varies because the flow in the valve system is a pressure-driven flow. As the probe position goes from height 1 to height 7, the section of the probe body, which is inside the valve increases, which causes more interference to the flow. This is again evident from the pressure variation from height 1 through to 7.

At average flow rates of 16.1GPM (800LPM pump set point), for 10% VOP,  $\Delta P$  increases from height 1(9.78 PSI) to height 2 (11.89), representing a 21% increase. From height 2 to height 3,  $\Delta P$  decreased by 18.8% and then increase slightly again by 3.6% from height 3 to 4.  $\Delta P$  decreases by 2.1% from height 4 to 5. It increases by nearly 18% to height 6 before decreasing slightly by 0.14% at height 7.  $\Delta P$ , for an average flow rate of 18.7GPM (900LPM pump set point), at 10%VOP, follows a similar trend as that for 16.2GPM. From  $\Delta P$  of 13.6 PSI at height 1,  $\Delta P$  increases by 15.3% to 15.7 PSI for height 2. From height 2 to height 3,  $\Delta P$  decreased slightly by 13.6% to 13.5PSI. It increases again by 2.5% from height 3 to 4.  $\Delta P$  decreases slightly by 2.3% from height 4 to 5. It then starts to increase from height 5 to 6, from 13.6 to 15.4 PSI by 13.7% and decreases slightly to 15.44 PSI by 0.19% at height 7. For an average flow rate of 21.27GPM, the same trend for  $\Delta P$  is again seen where it increases from height 1 to height 2, decreases at height 3, increase at height 4, decreases again from height 4 to 5, increases from 5 to 6 and then decreases from height 6 to 7 at 8.8, 8.3, 1.2, 1.7, 8.8 and 0.2% respectively. The same trend is repeated for an average flow rate of 23.4GPM (1100LPM pump setpoint) from height 1  $\Delta P$  of 24.6PSI, through to height 7 at 1.9, 0.5, 1.3, 1.7, 1.2, and 0.2% respectively. Finally, for an average flow rate of 25.8GPM, the same trend occurs from height 1 to 7 at 7.1, 6.7, 0.7, 2.4, 8, and 0.1% respectively.

For 20%, 40%, 60%, and 80% VOP, similar trends are observed as 10% VOP.

Again, from the above analysis, it has again been seen that regardless of the VOP,  $\Delta P$  vary slightly across height 1 to 7 as the flow rate increases.

After the pressure drop has been established for this probe position, the next section, using the MHP, derives the local sectional  $C_v$  based on these pressure drops.

#### 4.3.1.4.2 ESTABLISHING THE SECTIONAL $C_v$ CHANGES FOR DIFFERENT VOPs USING THE MHP

As mentioned in previous sections, the  $C_v$  measures the characteristics and measures the amount of energy dissipated in the valve, which is a function of flow rate and  $\Delta P$  given again in equation 1.4. For this position, the average static pressure  $P_{av static}$  have been obtained for all the heights in calculating the  $C_v$ . At the inlet, the distance between the global inlet point (2D from the valve inlet) and the probe position is 300mm and that of the global outlet point (6D from the valve outlet) is 750mm, creating a distance of 110mm between the two probes. This position, again, would have a more reduced pressure drop as the distance between P1 and P2 has reduced, which will have an effect on the valve  $C_v$ . Figure 4.28 shows the pressure drop ( $\Delta P$ ) for the different VOPs at various flow rates at this position.

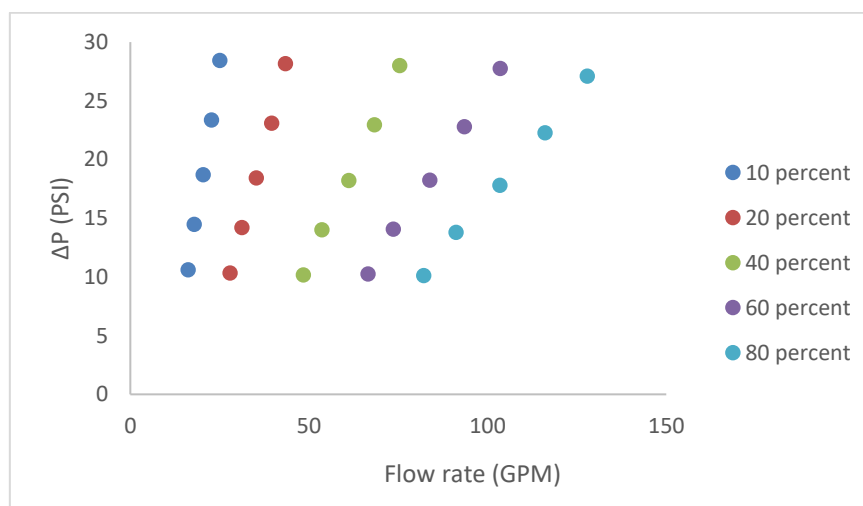


Figure 4.28: Pressure drop variation for different VOP and for various flow rates for position 3.

As seen from figure 4.28 again, the pressure drop increases as the flow rate increases for the various VOPs with the reasons already given in the previous two sections. Across the VOPs, the pressure drop is again seen to marginally reduce as the flow passage area increases from figure 4.28.

Figure 4.29 shows the various Cv value of the valve that has been calculated from the pressure drop for the different VOPs at various flow rates.

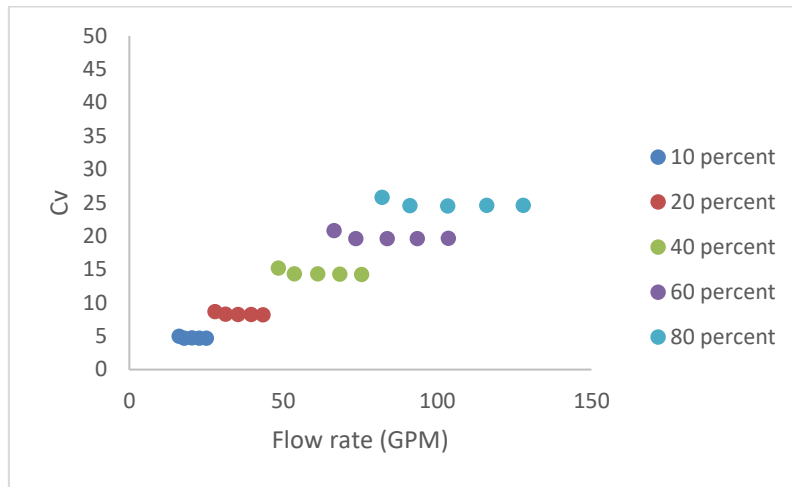


Figure 4.29: Valve Cv variation for different VOP and for various flow rates for position 3.

It is again seen that the Cv of the valve remains nearly the same at different flow rates for a particular valve opening position. This fact has already established by [107, 108, 109, 110, and 111] that the Cv of a valve is independent of the process condition as seen in figure 4.29 that irrespective of the flowrates, the Cv remains the same (almost). At 10% VOP, Cv remains nearly constant at close to 5. For 20, 40, 60, and 80% VOP, Cv remains at around 9, 14, 19, and 24 respectively. A single curve that represents the valve Cv is depicted in figure 4.30.

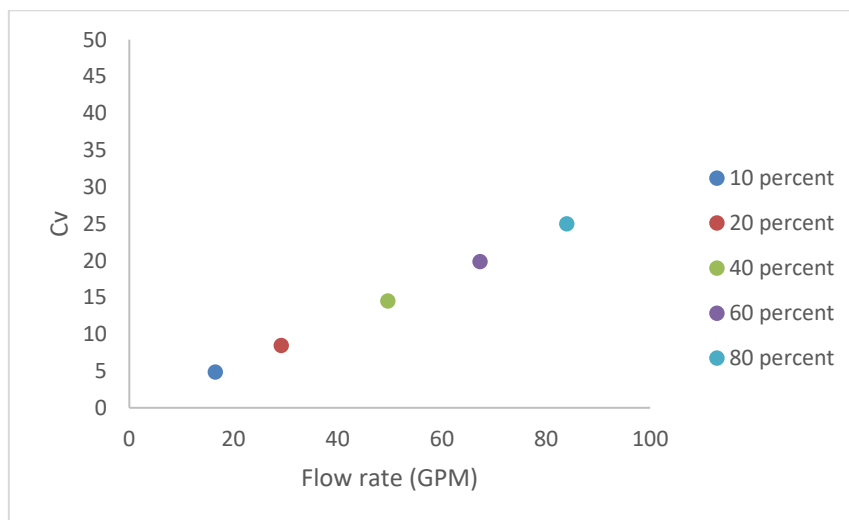


Figure 4.30: Valve Cv variation for the different VOP for position 3.

It can further be seen from figure 4.230 that as the VOP increases, valve Cv increases. The Cv increases to 8.31 from 4.75 as the VOP increases to 20 from 10 % increasing at a rate of 42%. When the VOP increases further from 20 to 40%, the valve Cv increases from 8.31 to 14.47 at a rate of 42.5%. Furthermore, when the VOP increases to 60%, the Cv increases to 19.8 at a rate of 27%, and at 80% VOP, Cv increases to 24.95 representing a 20% increase. This increase in valve Cv, about the different opening positions, is seen to be linear, also confirming again that the trim is a linear trim.

For position 3 (1d to 1.5d), the Cv slightly increased when compared to Cv calculated using the IEC BS EN standard 60534 (2D and 6D), for position 1 (0.5D to 0.9D) and for position 2 (1D to 1.5D). This is because of the reduction in pressure drop and due to Cv being inversely proportional to the square of pressure drop. Cv would increase further as the probe position distance decreases from the inlet to the outlet of the valve.

Velocity profile has again been constructed at the different flow and operation conditions, across the various heights for each section at the inlet and outlet, have been presented in the next subsection for this position 3.

#### **4.3.1.4.3 ESTABLISHING THE VELOCITY PROFILE CHANGES FOR DIFFERENT VOPs USING THE MHP**

For position 3, velocity magnitude across seven heights for the different flow rates have been analysed. Figure 4.31 depicts the velocity profile for the different pump set points at various VOPs at the inlet (1D).

The flow cross-sectional area at this position (1D) is  $0.0148m^2$ . For each flow rate, velocity distribution has been obtained for the different VOPs. Atypical type profiles have again been obtained for the different VOPs at the various flow rates. The reason for this atypical profile for the different VOPs and flow rates is because of the amount of probe body causing interference inside the valve. Again, equation 4.1 has been used in calculating the average velocity for this inlet profile at this position. Again, the different area for this section has been obtained from the geometry to be used in calculating the local flow area for the different heights.

For 800LP at 10% VOP, the trend for the velocity distribution across this position has been presented. Local velocity coefficient increases from height 1 to 2, decrease from 2

to 3, increase at height 4, increases slightly again at height 5, decreases at height 6, and finally increasing again slightly for height 7. At the 0.4 velocity coefficient, following the said trend explained above, the velocity coefficient increases at 65% at height 2 from height 1, decreases by 62% at height 3, increases again at the rate of 40.8% for height 4. For height 5, the velocity coefficient increases slightly by 2.1% and then drops at the rate of 14.5% from height 5 to 6. From height 6 to 7, the velocity coefficient further increases slightly at 0.02%. The maximum velocity coefficient value obtained for this particular VOP is 1.45 and was seen at height 5. A decreasing velocity coefficient trend is seen for the different height positions across the VOPs. This means that as the VOP increases, the velocity coefficient decreases. For 20, 40, 60, and 80% VOP, across the different probe height, the velocity coefficient has been seen to decrease across height 1 to 7 respectively as observed for 10% VOP.

As the flow rate is increased from 800 to 900LPM, the velocity coefficient ( $\frac{V_{mag}}{V_{avg}}$ ) is seen to decrease. The observed velocity coefficient percentage decrease are 2.1, 0.14, 8.8, 0.5, 2, 1.3 and 1.37% respectively for 10% VOP. Similar trends from height 1 to height 7 are also observed for 10, 20, 40, 60, and 80% VOP.

From 900 to 1000LPM, velocity coefficient obtained are 1.2, 1.5, 0.5, 0.4, 2.1, 0.3 and 1.3% at 10% VOP from 900LPM for height 1 through to height 7. Again, similar trend were observed from height 1 to height 7 is also observed for 10, 20, 40, 60, and 80% VOP.

For 1100LPM, velocity again decreases due to the complex flow and geometry inside the valve across the seven heights and different VOPs from 1000LPM. For 10% VOP, 4.1, 0.67, 4.1, 1.9, 2.1, 1.1 and 2.6% decrease from 1000 LPM 10%, height 1 to 7 respectively have been observed. 20, 40, 60, and 80% VOPs show similar trends as that of 10% VOP.

Finally, at 1200 LPM maximum flow rate, from 1100LPM, the velocity coefficient decreases as the flow rate increases. It is seen that at 10% VOP, the velocity coefficient decreases at 1.6, 1.2, 1.3, 0.9, 0.4, 0.0086, and 1% respectively for probe height 1 to 7. At 20, 40%, 60%, and 80% VOP, a similar percentage decrease have been observed from height 1 to 7.

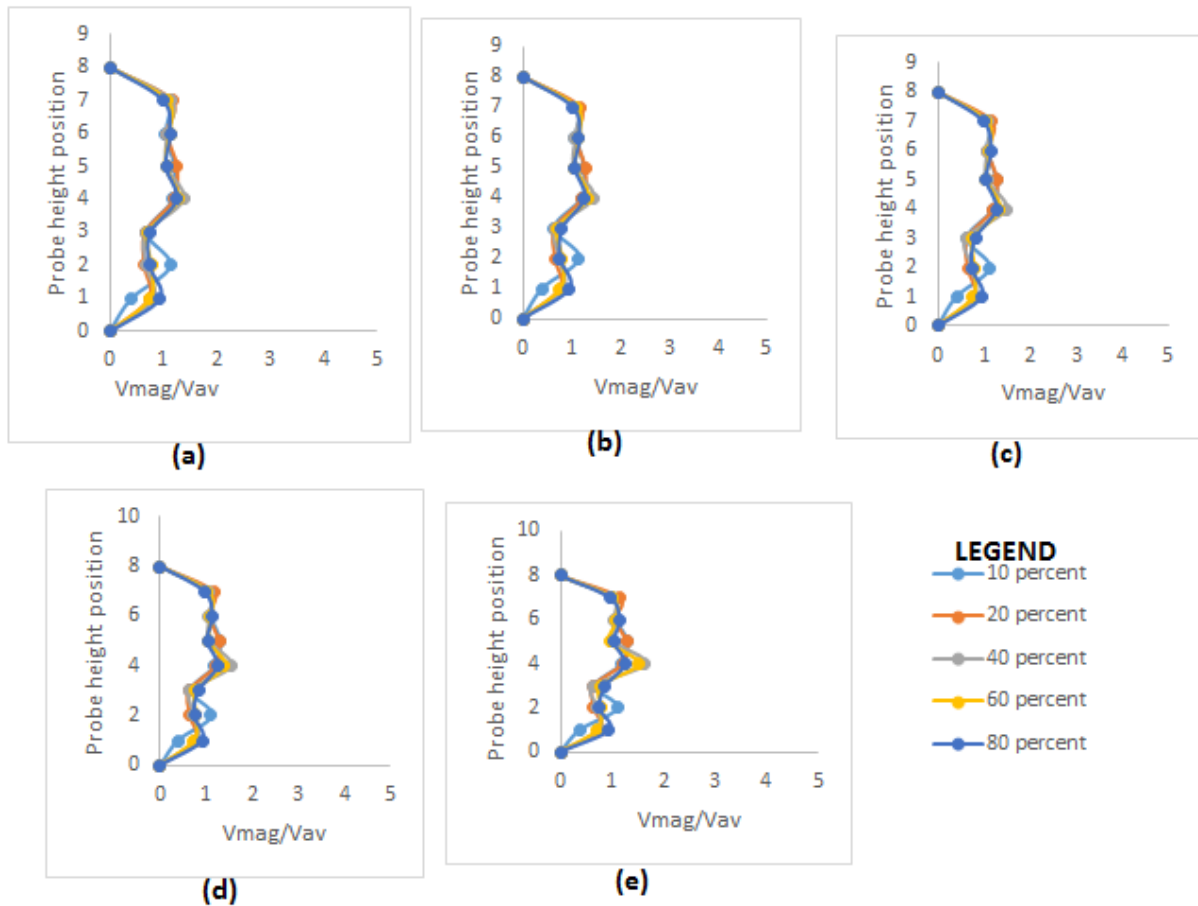


Figure 4.31: Velocity profile for the valve across the different heights at the probe inlet position (0.5D) for the different VOPs (a) 800LPM (b) 900 LPM (c) 1000 LPM (d) 1100 LPM (e) 1200 LPM for position 3

After the inlet velocity coefficient profile analysis for this position has been carried out, the outlet (1.5D) profile has been analysed. Figure 4.32 depicts the velocity coefficient profile for this section across the seven-heights and different VOPs. The flow cross-sectional area at this position (1D) is  $0.0226m^2$ . Again, the local flow rate given in equation 4.1 has been obtained in calculating the average velocity. Local velocity coefficient ( $\frac{V_{mag}}{V_{avg}}$ ) has been obtained for this section. ( $\frac{V_{mag}}{V_{avg}}$ ) increases slightly from height 1 through to height 5, decrease further at height 6 and for height 7. For 800LP at 10% VOP, the velocity coefficient from 0.93, following the said trend explained above, the velocity coefficient increases at 0.01% at height 2, increases by 8.8% at height 3, increases for height 4 at the rate of 10.9%. For height 5, the velocity coefficient increases slightly by 0.5%. It then decreases at the rate of 27.7% and 3% from height 5 to 6 and from 6 to 7 respectively. The maximum velocity coefficient obtained for this particular VOP is 1.16

and was again seen at height 5. A decreasing velocity coefficient trend is again seen for the different height positions across the VOPs. This means that as the VOP increases, the velocity coefficient decreases. Again for 20, 40, 60, and 80% VOPs, the velocity coefficient has been seen to decrease across height 1 to 7.

As the flow rate is increased from 800 to 900LPM, the velocity coefficient is seen to decrease. Percentage decrease for the velocity coefficient are 0.0012, 0.7, 0.13, 0.2, 0.02, 0.36 and 0.54% respectively at 10% VOP for 900LPM. 20%, 40%, 60% and 80% VOPs show similar trends as seen in 10% for the velocity coefficient as they decrease from probe heights 1 to 7.

At 1000LPM, velocity coefficient obtained are 0.0067, 0.44, 0.034, 0.19, 0.194, 0.198 and 0.05% from 900LPM at 10% VOP for height 1 to height 7. For 20, 40, 60 and 80% VOP decrease for height 1 to height 7 for the velocity coefficients as seen in figure 4.32.

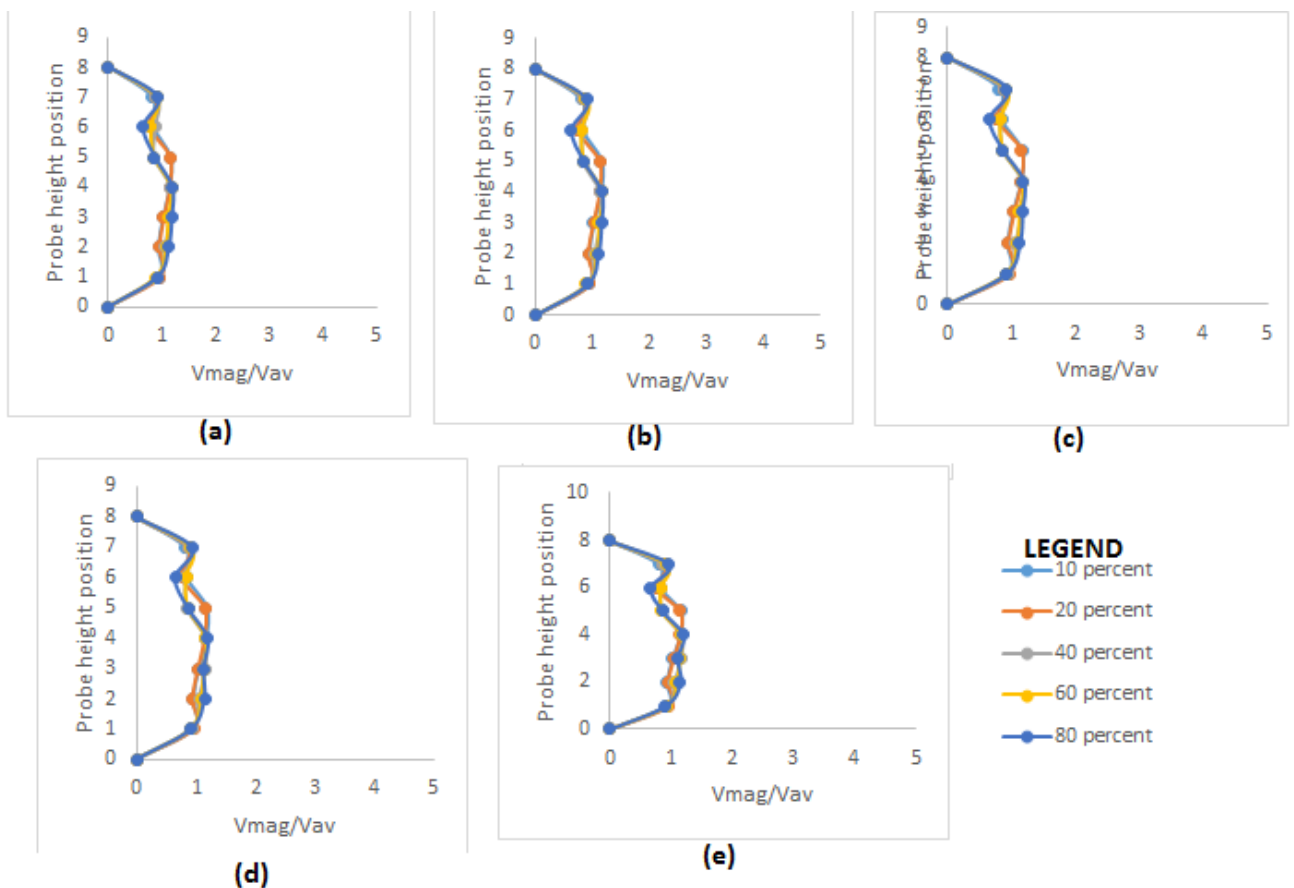


Figure 4.32: Velocity profile for the valve across the different heights at the probe outlet position (0.9D) for the different VOPs(a) 800LPM (b) 900 LPM (c) 1000 LPM (d) 1100 LPM (e) 1200 LPM for position 3

For 1100LPM, the velocity coefficient decreases again from 1000LPM due to the complex flow and geometry inside the valve, across the seven heights and different VOPs. For 10% VOP, 0.2, 0.37, 0.09, 0.1, 0.03, 0.049 and 0.19% decrease for 10%, height 1 to 7 respectively have been observed. At 20%, 40%, 60% and 80% VOP, velocity coefficients decrease for height 1 to 7 have been observed from 1000 to 1100 LPM.

Finally, for 1200 LPM water flow rate, the velocity coefficient decreases as the flow rate increases. It is seen at 10% VOP that the velocity coefficient decreases at 0.1, 0.07, 0.2, 0.27, 0.007, 0.32 and 0.55% for probe height 1 to 7 respectively. At 20, 40, 60, and 80% VOPs, decrease from height 1 to 7 for the velocity coefficients was observed.

The final subsection in this chapter investigates how the different probes positioning have considerable effects on the flow parameters and how they vary from inlet to outlet of the valve.

#### **4.3.1.5 INVESTIGATION OF THE EFFECT OF THE DIFFERENT PROBE LENGTHS POSITIONS ON FLOW PARAMETERS**

After analysis from the different probes and their specific position, their respective measurement parameters are compared in this section to see how these parameters change and by how much from the valve inlet to outlet. The parameters compared include static pressure,  $\Delta P$ , sectional  $C_v$ , pressure ratio, and pressure coefficient and how they change as flow goes from the inlet to the outlet and for the different probe positions as the flow passage area changes.

##### **4.3.1.5.1 DIFFERENT MHP LENGTHS EFFECTS ON DELTA P ( $\Delta P$ )**

Because of the different sections where the probes are placed at the inlet and outlet of the valve for the different positions studied in the previous section, the effect of these positions (positions 1, 2 and 3) cause changes in the pressure drop as the flow distance between the inlet and outlet probe changes. Comparisons of these different pressure drops have been made for different VOPs.

From figure 4.33, it has been seen that as the probe distance between the inlet and the outlet reduces, the pressure drop reduces. This is because as the distance decreases, there is less kinetic energy (in the form of pressure energy) loss as flow goes from inlet to outlet.

The more the flow distance, the more pressure energy is lost. For all VOPs, pressure drop can be seen to increase as flow rates increases.

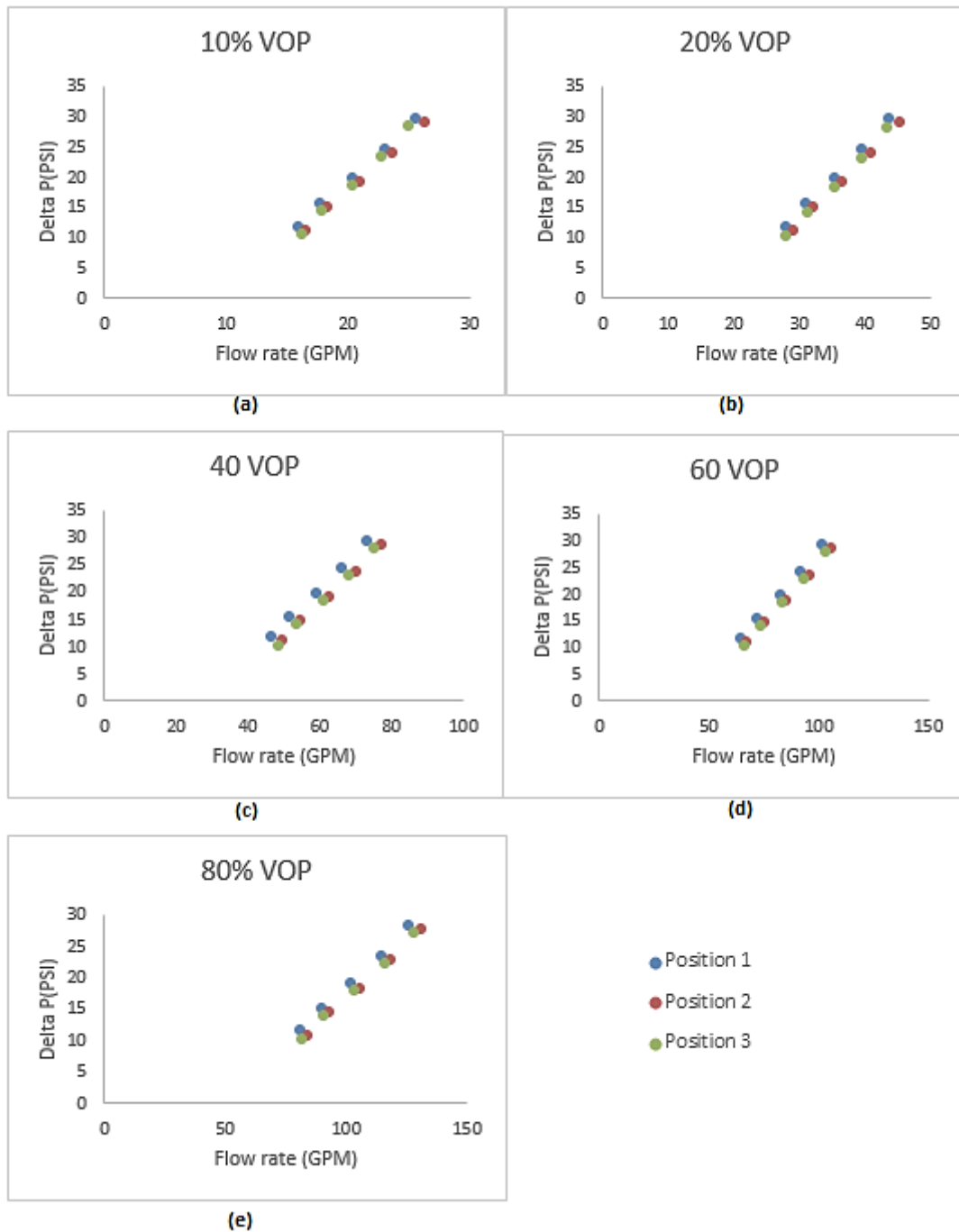


Figure 4.33: Pressure drop comparison for different flow rates and VOPs for the different probe positions (a) 10% (b) 20% (c) 40% (d) 60% (e) 80%

For 10% VOP, at the lowest flow rate,  $\Delta P$  reduces from position 1 at 11.68 PSI to position 2 at 11.11 PSI, representing a percentage reduction of 4.9% and 4.49% percentage

reduction from position 2 to 3. This reduction of  $\Delta P$  can be seen for all flow rates from position 1 to position 2 and from 2 to 3. As the flow rate increase to 17.68 GPM,  $\Delta P$  from position 1 to 2 to 3 goes from 15.5 to 14.98 to 14.48PSI, representing 3.5 and 3.38 percentage reduction respectively. As flow increases to 20.4GPM, percentage reduction difference goes from 2.75 to 2.58% as  $\Delta P$  changes from positions 1 to 2 and from positions 2 to 3 respectively. Again, for 23.1 GPM,  $\Delta P$  reduction observed are 2.3 and 2% for position 1 to 2 and from 2 to 3. Finally, at the maximum flow rate (25.6GPM) for 10% VOP, the percentage reduction difference observed was 1.6 and 2.1% respectively. It can also be seen that the percentage pressure drop decreases as the flow rate increases for all VOPs.

Again, 20, 40, 60, and 80% VOPs all follow similar trends as discussed for 10% with their respective pressure drop values and how much their values change across the different flow rates for the different probe positions. **4.3.1.5.2 DIFFERENT PROBE POSITIONS EFFECT ON THE SECTIONAL  $C_v$**

After pressure drops for the different probe position has been analysed in the previous section which in turn affect the  $C_v$ , comparisons have been established for the different probe positions and how much the  $C_v$  has changed for these positions. As the pressure drop reduces, the  $C_v$  increases, and vice versa.

Figure 4.28 shows the different probe position  $C_v$  of the valve at the different VOPs.

It has been seen previously that the  $C_v$  remains the same at different flow rates for a particular valve opening position, as the  $C_v$  is independent of the process condition. A single curve comparison for the  $C_v$  has been made as seen in figure 4.34.

It can be seen again from figure 4.34 that the valve  $C_v$  increases as the VOP increases. The  $C_v$  increases from 4.53 to 4.62 to 4.75 and to 4.84 for 10 % VOP for global, positions 1, 2 and 3, representing  $C_v$  variation increase of 1.85, 4.5, and 1.8% respectively. At 20% VOP,  $C_v$  increases from 7.47, 7.95, 8.31 and 8.4 for global, position 1, 2, and 3, representing  $C_v$  variation increase of 6.3, 5.5 and 1.6% respectively.  $C_v$  increases from 11.67 to 13.37 to 14.47 and 14.48 at 40 % VOP for global, positions 1, 2 and 3, representing 12.7, 7.6 and 0.1%  $C_v$  variation respectively. For 60% VOP,  $C_v$  values for global, position 1, position 2 and position 3 are 15.3, 18.7, 19.84 and 19.85, representing 18.1, 5.7 and 0.05%

respectively. Finally, at 80%, Cv values for global, position 1, position 2 and position 3 are 18.3, 23.6, 24.8 and 24.95, representing 22.3, 5.46 and 0.6% respectively.

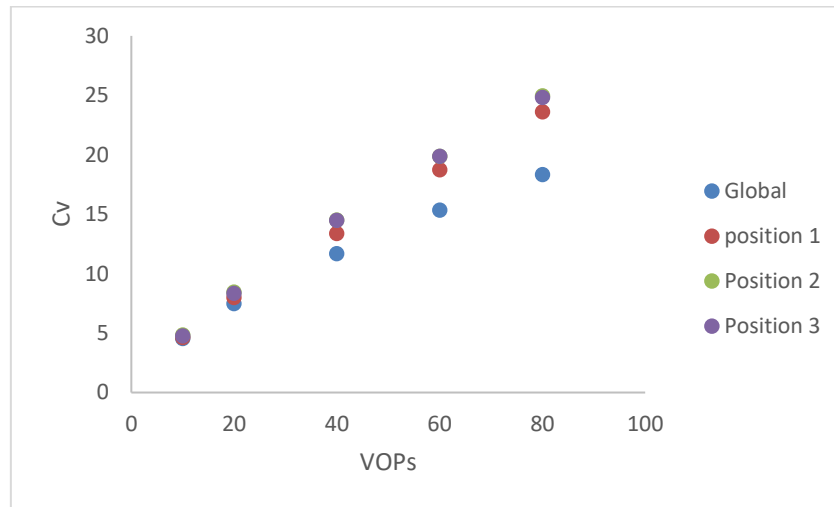


Figure 4.34: Cv comparison for different flow rates and VOPs for the different measurement positions

#### 4.3.1.5.3 DIFFERENT PROBE LENGTHS EFFECTS ON THE PRESSURE VARIATION FROM VALVE INLET TO OUTLET

As seen from figure 4.35, as the fluid flows from the inlet to outlet, the potential energy is converted to kinetic energy and in the process of conversion; energy in the form of pressure energy is lost. This causes pressure to keep reducing as the fluid flows through the different sections where the probe has been placed from inlet to outlet. Figure 4.35 shows how the static pressure decreases from 0.5D at the inlet to 0.9D at the outlet for (a) 10% (b) 20% (c) 40% (d) 60% and (e) 80% VOP.

At 10% VOP, the flow goes through the different sections from 0.5D, 0.8D, 1D, 1.5D, 1.2D, and finally at 0.9D, before exiting the valve. At 800LPM, the pressure measured are 16.43, 16.22, 16.12, 5.52, 5.11, and 4.75 PSI, creating a decreasing pressure trend, representing a 1.2, 0.6, 65, 7.2, and 7.1% respectively. As the flow rate increases, the pressure also increases across a particular probe position. For 900LPM, pressure values at the same probe positions are 20.2, 20.06, 20.003, 5.52, 5.06, and 4.7PSI, showing a reducing trend, representing 1.1, 0.26, 72.4, 7.6 and 6.9% respectively. At 1000LPM, pressure values recorded are 24.51, 24.32, 24.2, 5.52, 5.1, and 4.75 PSI, representing 0.78, 0.3, 77.2, 7.6 and 6.9% reduction respectively. At 1100LPM, again, pressure values measured are 29.2,

28.97, 28.9, 5.52, 5.1, and 4.74 PSI, representing 0.7, 0.2, 80.8, 7.4 and 7.26% reduction respectively. Finally, at 1200LPM, 34.3, 33.96, 33.96, 5.53, 4.91, and 4.73 PSI have been recorded for the different probe positions, which represents 0.87, 0, 83.7, 11.1 and 3.5% respectively. Across all the VOPs, it is seen from the figure that the pressure ratio between 1D and 1.5D drops rapidly due to the pressure drop experienced. Between the two locations is the valve trim, causing the pressure to drop that low.

Similar trends, but different values were also recorded at 20, 40, 60 and 80% VOP as seen in figure 4.35.

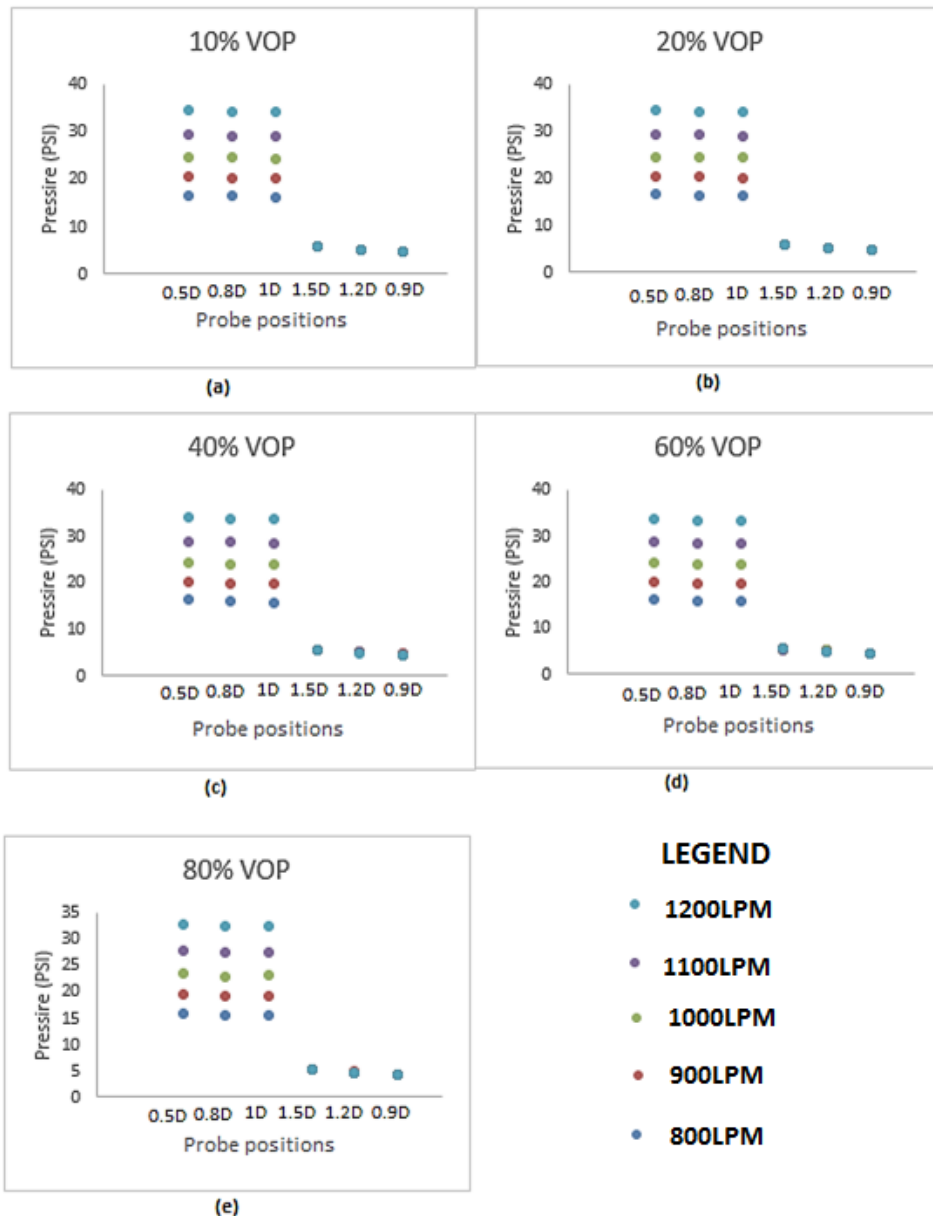


Figure 4.35: Pressure comparison for different flow rates and VOPs for the different probe positions (a) 10% (b) 20% (c) 40% (d) 60% (e) 80%

#### 4.3.1.5.4 DIFFERENT PROBE LENGTHS EFFECTS ON THE PRESSURE RATIO VARIATION FROM VALVE INLET TO OUTLET

The pressure ratio is the ratio of outlet pressure ( $P_2$ ) over inlet pressure ( $P_1$ ). This parameter has been monitored from inlet to outlet in order to ensure that the pressure ratio, at no point in time, reaches 1. When it reaches 1, no flow would occur. Figure 4.36 shows how the ratio is changing as the fluid flows from 0.5D at the inlet to 0.9D at the outlet for (a) 10% (b) 20% (c) 40% (d) 60% and (e) 80% VOP.

As already been shown how pressure decreases when water flows from inlet to outlet, the pressure ratio always stays less than 1. Since the rate at which pressure increases across the different VOPs is similar, the pressure ratio shown in figure 4.36 can be seen to have similar values at the different VOPs. Again, it is seen from the figure that the pressure ratio between 1D and 1.5D drops rapidly due to the pressure drop experienced. Between the two locations is the valve trim, again causing the pressure to drop that low.

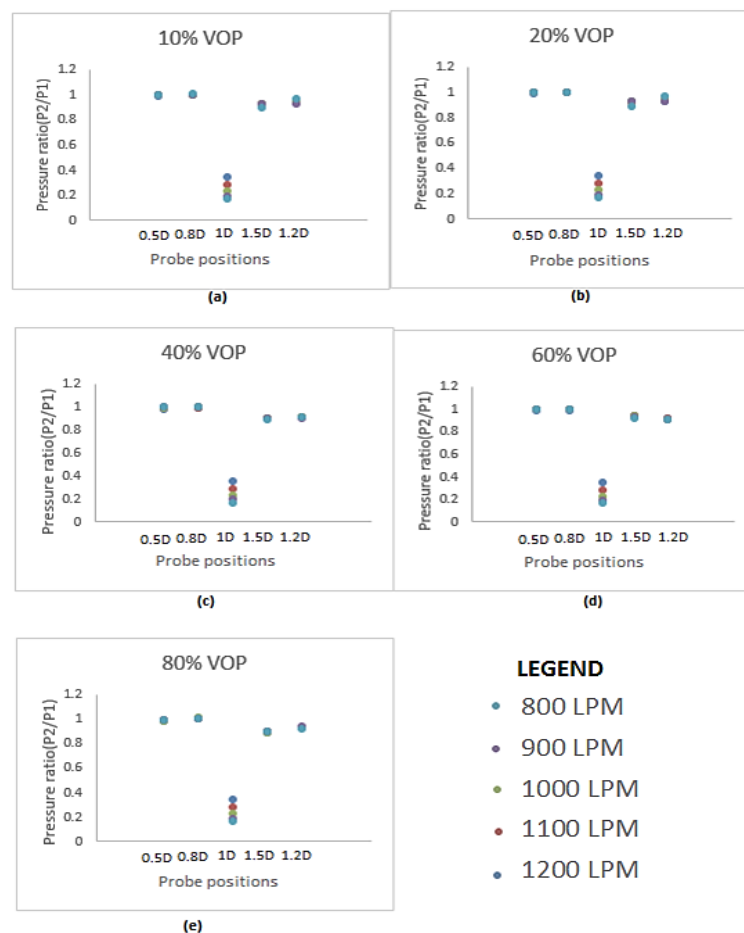


Figure 4.36: Pressure ratio comparison for different flow rates and VOPs for the different probe positions (a) 10% (b) 20% (c) 40% (d) 60% (e) 80%

#### 4.3.1.5.5 DIFFERENT PROBE LENGTHS EFFECTS ON THE PRESSURE COEFFICIENT VARIATION FROM VALVE INLET TO OUTLET

Pressure coefficients ( $C_p$ ) describes the relative pressure in the entire flow field and is non-dimensionless. Every measurement point where the probe is placed has its unique pressure coefficient. Across the valve, where the probes have been placed from inlet to outlet,  $C_p$  values have been calculated. Again, the measurement points at the inlet are (0.5D, 0.8D, and 1D) and at the outlet (1.5D, 1.2D, and 0.9D). The importance of calculating  $C_p$  (pressure drop/dynamic pressure) for the valve is to determine those critical locations inside the valve, which can be used in predicting the fluid pressure at those probe locations located inside the valve. Figure 4.37 shows the  $C_p$  variation across the valve for the different flow rates at (a) 10% (b) 20% (c) 40% (d) 60% and (e) 80% VOP.

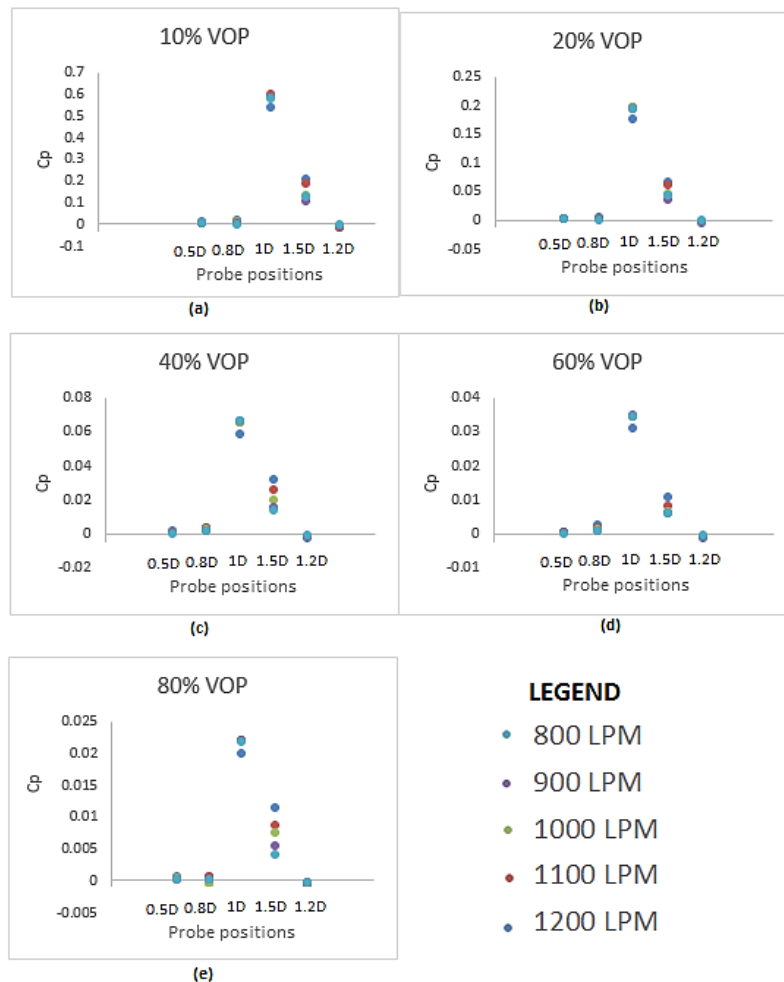


Figure 4.37:  $C_p$  comparison for different flow rates and VOPs for the different probe positions (a) 10% (b) 20% (c) 40% (d) 60% (e) 80%

This analysis is can prove very vital as the flow area at the different measurement sections changes. The flow cross-sectional area at 0.5D, 0.8D, 1D, 1.5D, 1.2D and 0.9D are 0.0103, 0.0136, 0.0148, 0.0226, 0.0242 and  $0.0153m^2$  respectively. The highest Cp values, across all the VOPs, can be seen when flow transitions from 1D to 1.5D. This is because of the huge pressure drop experienced due to the trim. Cp value increase from 0.5D to 1D and then decreases until it reaches 1.2D. This trend is the same for all VOPs as seen in figure 4.37.

At 10% VOP, Cp obtained at 0.5D, 0.8D, 1D, 1.5D and 1.2D are 0.0069, 0.0157, 0.54, 0.2 and -0.019 respectively for 800LPM, representing a 56.2, 97, 62.2 and 109% variation . Over a 100% Cp values is observed at the end of the last probe at 1.2D because of the negative Cp value at that particular point, seen for all flow rates. This negative Cp value is due to the reduced flow cross sectional area experienced at that section. As flow rate increases to 900LPM, Cp values obtained at same positions are 0.006, 0.0068, 0.596, 0.19 and -0.014, representing 10.9, 98.8, 68.6 and 107% variation. For 1000LPM, 0.0039, 0.0073, 0.587, 13.25 and -0.011 for same positions are obtained for Cp values, representing 46.6, 98.7, 77.4 and 108% variation from 0.5D to 1.2D. For 1100LPM, Cp values obtained at same positions are 0.0032, 0.0057, 0.58, 0.101 and -0.009, representing 44.4, 99, 82.5 and 109.2% variation. Finally, for 1200LPM, Cp values are 0.004, -0.0002, 0.576, 0.125 and -0.004, representing 104, 100, 78.3 and 103% variation.

The trend seen at 10% is similar for 20, 40, 60, and 80% VOPs as seen in figure 4.37.

#### **4.3.1.5.6 DIFFERENT PROBE LENGTHS EFFECTS ON THE Cv VARIATION FROM VALVE INLET TO OUTLET**

The valve performance or any of one of the valves components can be quantified by the use of the valve Cv (flow capacity) as explained in chapter 1 and the equation is given in 1.4. In equation 1.4, the pressure used for the differential pressure calculation is static pressure. This pressure applies only when the flow passage area between P1 and P2 is the same. When the static pressure has been used, negative Cv was obtained. Because of this reason, the static pressure has been converted to total pressure (total kinetic energy) by the addition of the dynamic pressure. Nowhere, to my knowledge, has the total energy been used for Cv calculation, making this novel as the flow passage area changes as water flows from inlet to outlet.

Again, because  $C_v$  remains constant as flow rate, an average single value across the various position has been obtained. Figure 4.38 depicts the  $C_v$  variations from inlet to outlet, as a function of  $Q$  and  $\Delta P$  (energy difference) for the different valve VOPs.

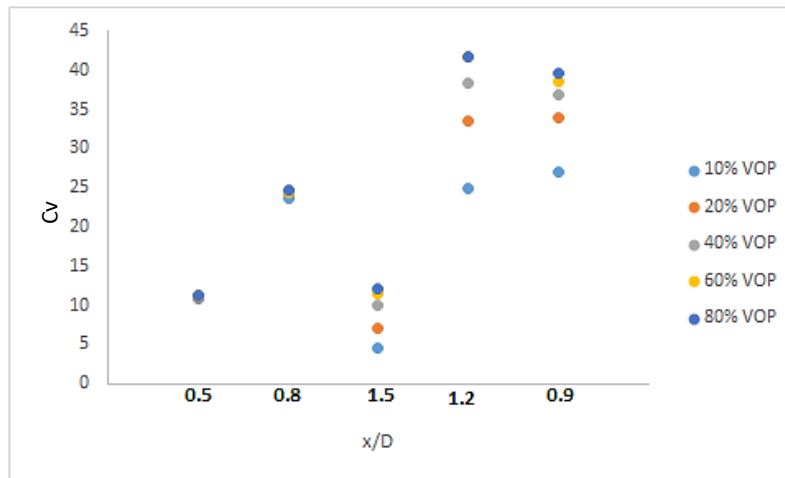


Figure 4.38:  $C_v$  comparison for different VOPs at the different probe positions

Ideally, the  $C_v$  has been seen to increase as flow changes from inlet to outlet at different positions. This is because the pressure drop keeps increasing for these positions as flow transits from inlet to outlet. The sharp drop seen at  $x/D$  of 1.5 is because of the huge pressure drop. This huge pressure drop difference was obtained at the position before and after the trim. The trim is known for causing a huge pressure drop because of the trim holes. The value at 1.5 ( $x/D$ ) can also be regarded as the trim  $C_v$  as measurements were taken just before and after the trim.  $D$  is the valve diameter, while  $x$  is the distance away from the inlet and outlet of the valve.

At 10% VOP, across the different positions seen from figure 4.38, the  $C_v$  values recorded from inlet to outlet are 10.8, 23.57, 1.54, 24.94, and 27.10 respectively. As the VOP increases for similar conditions, the  $C_v$  increases at the same positions. The percentage increase from 10% to 20% VOP observed are 2.4, 3, 36.4, 25.8, and 20.2% respectively across the different measurement positions. From 20 to 40% VOP, the percentage increase difference recorded are 0.4, 0.009, 28.4, 12.55, and 8.1% respectively across the different positions. From 40 to 60% VOP, 0.3, 0.65, 12.1, 7.8 and 4.2% respectively were observed.

At 80% VOP, from 60% VOP, the percentage difference recorded are 0.03, 0.9, 6, 0.07 and 2.75% respectively.

The total  $Cv$  for the control valve system has been calculated for the different VOPs using equation 4.2.

$$Cv_{control\ valve\ system} = \frac{1}{\sqrt{\sum_{i=1}^n \frac{1}{Cv_i^2}}} \dots\dots\dots 4.2$$

In this research,  $i=5$  as there are five different  $Cv$  across the valve system (at different positions, from inlet to outlet) that have been obtained experimentally, across different VOPs. Figure 4.39 shows the calculated total  $Cv$  of the control valve system for the different VOPs. For 10, 20, 40, 60, and 80% VOP, the total  $Cv$  obtained for the control valve system are 4.02, 5.6, 6.8, 7.3, and 7.5 respectively. As earlier explained,  $Cv$  remains nearly constant across the different flow rates but increases as VOP increases. As seen from figure 4.39, the percentage increase from 10 to 80% VOP obtained are 29, 17.5, 6.1, and 2.7% respectively across the different VOPs.

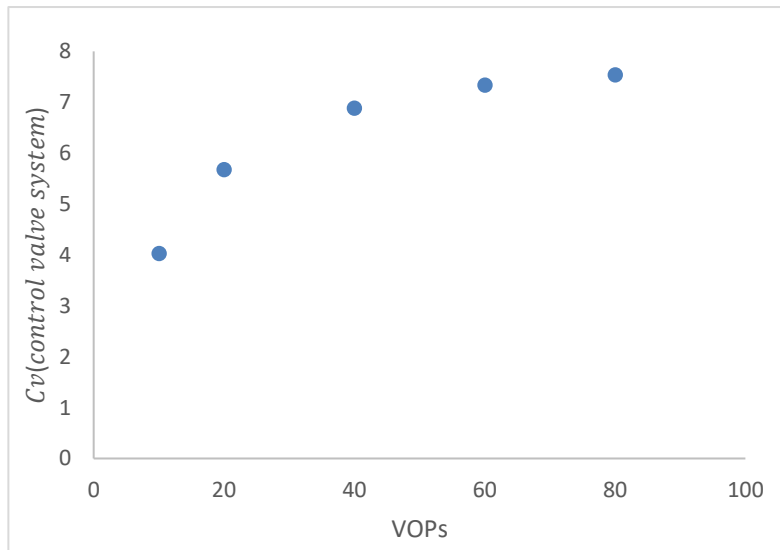


Figure 4.39: Varying  $Cv$  total for the control valve system across the different VOPs.

In order to express  $Cv_{control\ valve\ system}$  as a function of the valve opening position (VOP), regression analysis with multiple variables has been carried out on the results presented in this section. Equation 4.3 shows the predictor expression that has been obtained.

$$Cv_{control\ valve\ system} = 8.54VOP^{0.298} \dots\dots\dots 4.3$$

In checking the predictor expression validity for the data obtained in this section, equation 4.3 has been used in calculating the total Cv of the control valve system compared with data plotted in figure 4.39. It has been seen that equation 4.3 gives a percentage error of 4.8%, making the equation capable of predicting the Cv as a function of VOP with more than 96% accuracy.

**4.3.1.5.7 DIFFERENT PROBE LENGTHS EFFECTS ON THE VALVE K VALUE VARIATION FROM VALVE INLET TO OUTLET**

The valve body flow capacity has been computed for the different VOPs in the previous section. These Cv, for the different sections, have been used in calculating the k values. K is a coefficient, which depends on the valve geometry [94]. The equation for the k value is given in equation 4.4.

$$K = Cv_{valve\ body} \left( \frac{D_{seat}}{D_{valve}} \right)^2 \dots\dots\dots 4.4$$

$D_{seat}$  and  $D_{valve}$  are the diameter of the valve seat and of the valve, which are 38mm and 101.6mm respectively.

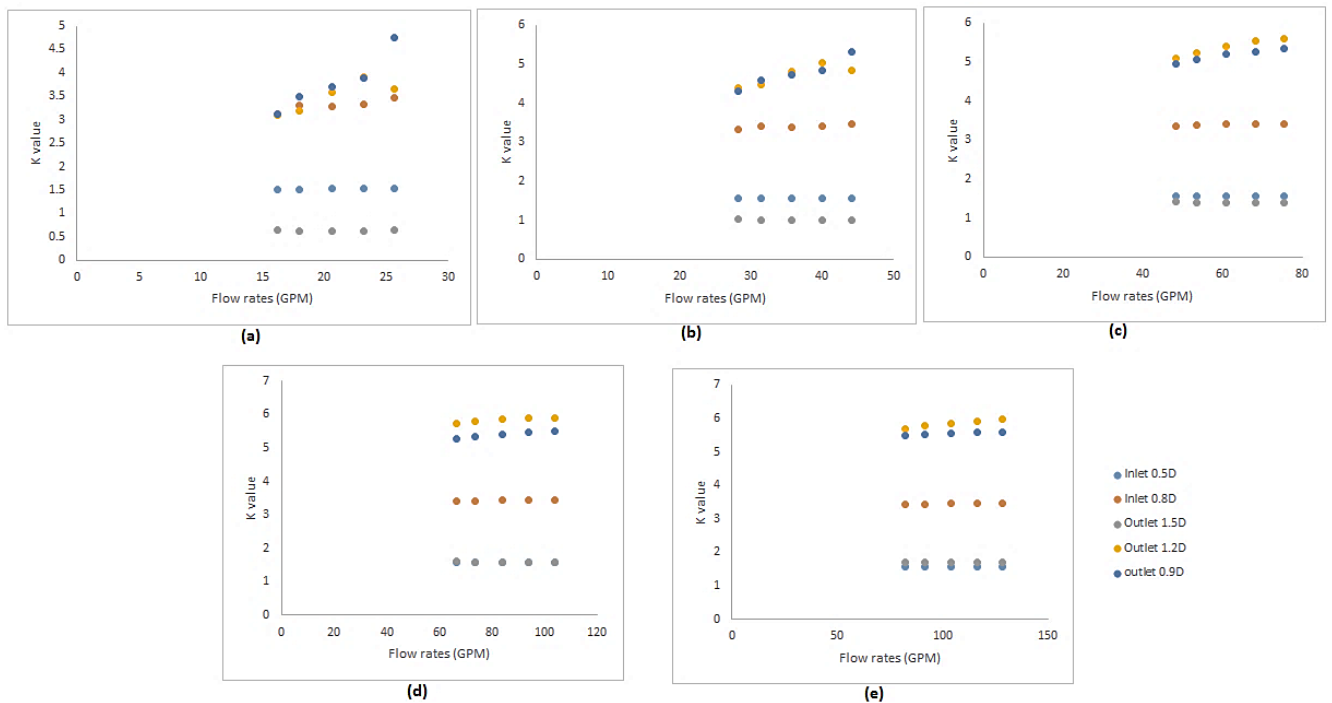


Figure 4.40: Varying K value for the different sections of the control valve body at different flow rates across the different VOPs (a) 10% (b) 20% (c) 40% (d) 60% (e) 80%.

Knowing the  $K$  values, the valve can optimally be designed in order to improve the performance. Since  $K$  is a function of the  $C_v$ , they remain constant for various flow rates but slightly change at different VOPs as seen in figure 4.41.

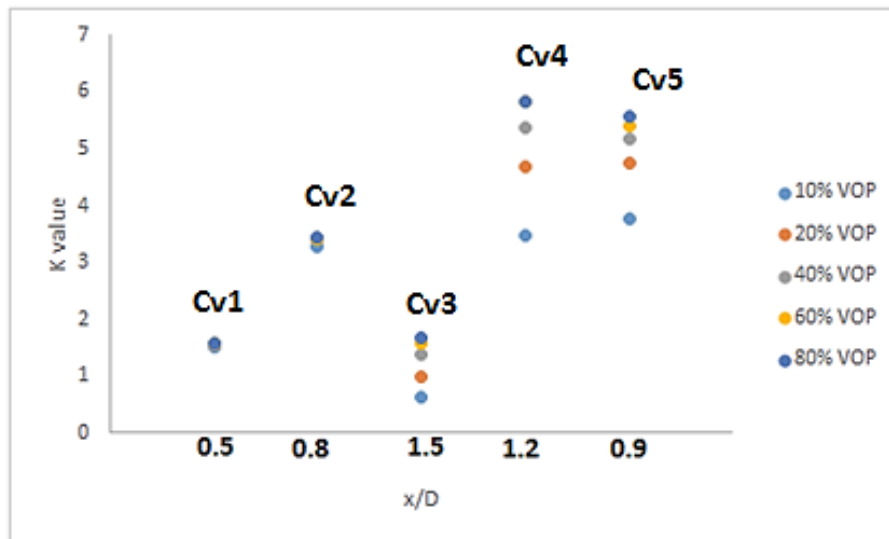


Figure 4.41: Average  $K$  value for the different sections of the control valve body across the different VOPs

The sharp drop in  $K$  values seen at  $x/D$  of 1.5 is because of the huge pressure drop, like in CV. This huge pressure drop difference has been obtained at positions before and after the trim. The trim causes higher pressure-drop because of the trim holes. The value at 1.5( $x/D$ ) can also be regarded as the  $K_{trim}$ .  $D$  is the valve diameter, while  $x$  is the distance away from the valve inlet and outlet.

At 10% VOP, across the different positions seen from figure 4.35, the  $K$  values recorded from inlet to outlet are 1.52, 3.29, 0.6, 3.4, and 3.79 respectively. As the VOP increases for similar conditions, the  $K$  value slightly increases at the same positions. The percentage increase from 10% to 20% VOP observed for  $K$  values are 2.4, 3, 36.4, 25.8, and 20.2% respectively across the different measurement positions. From 20 to 40% VOP, the percentage increase differences recorded are 0.4, 0.009, 28.4, 12.55 and 8.1% respectively across the different positions. From 40 to 60% VOP, 0.3, 0.65, 12.1, 7.8 and 4.2% respectively.

At 80% VOP, from 60% VOP, the percentage difference recorded are 0.03, 0.9, 6, 0.07 and 2.75% respectively.

### 4.3.1.5.8 DIFFERENT K VALUE EFFECT AS A FUNCTION OF REYNOLDS NUMBER FROM VALVE INLET TO OUTLET FOR DIFFERENT VOPs

Figure 4.42 shows the K value as a function of Reynolds number for the different VOPs across the different sections from inlet to outlet of the valve. Four K values (k1, k2, k3, and k4) obtained in the previous section have been plotted as a function of the Reynolds number for 0.5D inlet to 0.8D inlet (k1), 0.8D inlet to 1D inlet (k2), 1.5D outlet to 1.2D (k3) outlet and 1.2D outlet to 0.9D outlet (k4).

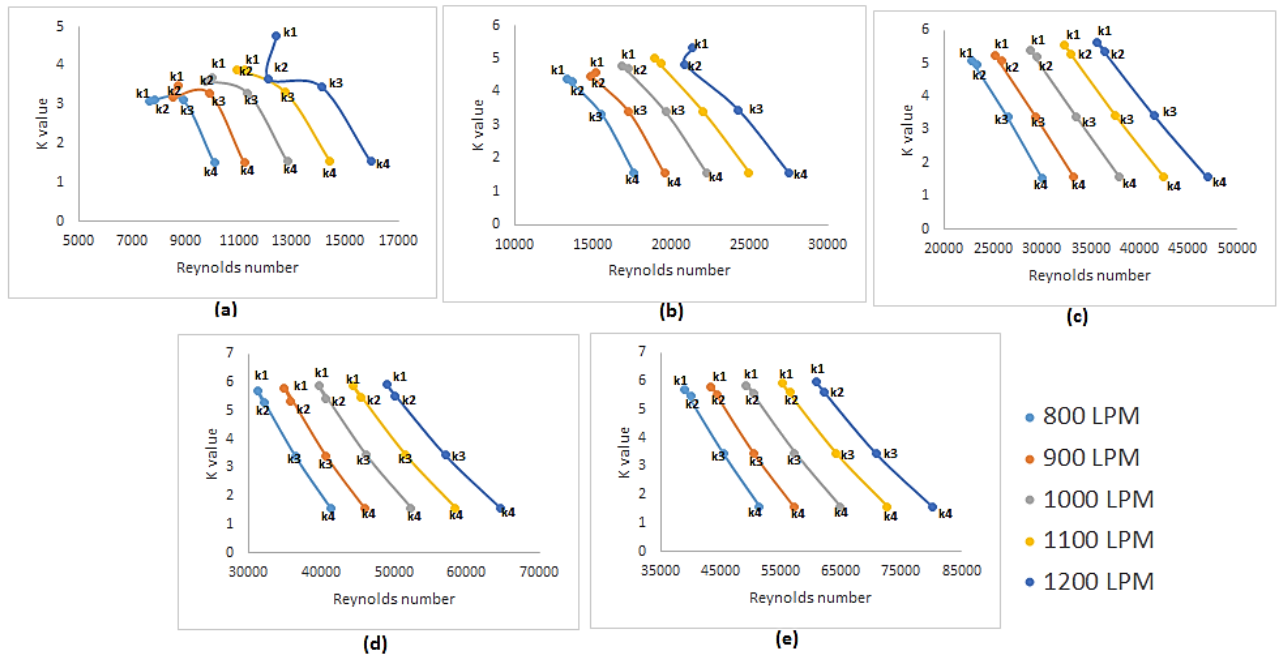


Figure 4.42: Effect of K value as a function of Reynolds number at different VOPs  
 (a) 10% VOP, (b) 20% VOP, (c) 40% VOP (d) 60% VOP (e) 80% VOP

The hydraulic diameter has been used to calculate the Reynolds number, as the different flow section is not circular. As the flow rates increases, the Reynolds number increases for the different VOPs. Again, across the different K values (k1 to k4), Reynolds number is seen to reduce as hydraulic diameter decreases for constant density and dynamic viscosity. Again, K values remain constant at same section across the different flow rates for all VOPs.

At 800LPM, 1.5, 3.1, 3.09, and 3.12 have been recorded for k1, k2, k3, and k4, Reynolds number calculated are 10098, 8918.6, 7667.4, and 7845.4 respectively for 10% VOP. K value increases as VOP increase from 10 to 20% VOP, 20 to 40%, 40 to 60%, 60 to 80% VOP as Reynolds number increases.

At 900LPM, 1.5, 3.29, 3.19, and 3.49 have been recorded for k1, k2, k3, and k4, Reynolds number calculated are 11212, 9901.7, 8512.6, and 8710.2 respectively for 10% VOP. K value increases as VOP increase causing an increase in Reynolds number. Similar trends are seen from 40 to 60%, and from 60 to 80% VOP for the 900LPM flow rate.

At 1000LPM, 1.53, 3.28, 3.59, and 3.69 have again been recorded for k1, k2, k3, and k4. Reynolds number calculated at these k values are 11212, 9901.7, 8512.6, and 8710.2 respectively for 10% VOP. From 10 to 20% , 20 to 40%, 40 to 60%, and 60 to 80% VOP, k increases as Reynolds number increases.

At 1100LPM, 1.53, 3.3, 3.9, and 3.88 have been recorded for k1, k2, k3, and k4, Reynolds number calculated are 14431, 12745, 10957 and 11211 respectively for 10% VOP. K value increases as VOP increase for 20, 40, 60, and 80% VOP as Reynolds number increases.

At 1200LPM, 1.529, 3.46, 3.66, 4.75 have been recorded for k1, k2, k3, and k4 for calculated Reynolds number of 15984, 14116, 12136 and 12418 respectively for 10% VOP. Again, K value increases as the VOP increase for 20, 40, 60, and 80% VOP as Reynolds number increases.

$$K_{control\ valve\ system} = 1.836Re^{0.00272}VOP^{0.09} \dots\dots\dots 4.5$$

Again, K value for the control valve system  $k_{control\ valve\ system}$  as a function of the Reynolds number and valve opening position (VOP), regression analysis with multiple variables have been carried out on the results presented in this section. Equation 4.5 shows the predictor expression that has been obtained.

In checking the predictor expression validity for the data obtained in this section, equation 4.5 has been used in calculating the total K value of the control valve system compared with data plotted in figure 4.39. It has been seen that equation 4.5 gives a percentage error of 2.25%, making the equation capable of predicting the K value as a function of Reynolds number and VOP with more than 97% accuracy.

The next section compares the different local and global parameters between healthy and faulty valves, and how these parameters changes for the different flow and operating conditions.

### 4.3.2 ESTABLISHING GLOBAL AND LOCAL FLOW PARAMETERS BETWEEN HEALTHY AND FAULTY VALVE CONDITION AT DIFFERENT FLOW RATES AND VOPs

In this section, different global and local flow parameters have been established and compared between a healthy valve and a faulty valve. Fault has been created inside the valve by blocking one of four flow paths. This has caused additional flow restrictions inside the valve, which affect the valve flow parameters.

#### 4.3.2.1 GLOBAL PRESSURE DROP COMPARISON

Because of the blockage of one flow path, flow rates at the same VOP changes. For the faulty valve condition, flow rates decrease when compared to a healthy valve. This then causes pressure drop to slightly increase, as there are more flow restrictions. Global pressure drop has been obtained at 2D (inlet) and 6D (outlet) for 60 and 80% VOPs.

Figure 4.43 shows the global pressure drop difference between healthy and faulty valves for 60 and 80% VOPs.

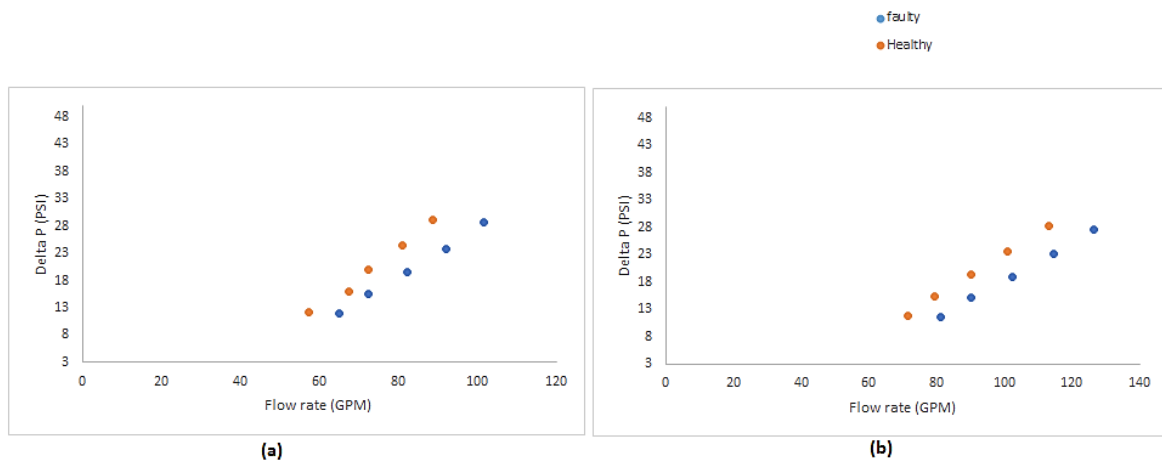


Figure 4.43 Global pressure drop comparison for the healthy and faulty valves at different flow rates for (a) 60% (b) 80% VOPs.

At 60% VOP, the faulty valve global pressure difference has been observed to increase from the healthy valve as flow rates increase due to the addition of flow restriction caused by the path blockage (fault). Flow rates, for the same condition, decrease from healthy to faulty valve. Flow rates for 60% VOP are 65, 72.3, 82.4, 92.1, and 101.6 GPM for healthy valve and decrease to 57.3, 67.5, 72.4, 80.9, and 88.8 GPM for the faulty valve respectively for the same pump set points at the rate of 11.8, 6.7, 12.1, 12.1 and 12.5% respectively.

This caused pressure drop to increase from 11.8, 15.5, 19.5, 23.8, and 28.6PSI for the healthy valve to 12.2, 15.9, 20.02, 24.4, and 29.2PSI for the faulty valve at the rate of 3.1, 2.4, 2.6, 2.2 and 1.8% respectively.

At 80% VOP, flow rates for the same condition decrease from healthy to the faulty valve. Flow rates for 80% VOP are 81, 90.3, 102.3, 114.5 and 126.3GPM for healthy valve, decreases to 71.6, 79.4, 90, 100.8 and 113.3GPM for the faulty valve respectively for same pump set points at the rate of 11.6, 12, 11.9, 11.99 and 10.3% respectively.

This caused pressure drop, again, to increase from 11.69, 15.1, 18.9, 23.08, and 27.6PSI for the healthy valve to 11.9, 15.45, 19.3, 23.6, and 28.28PSI for the faulty valve at the rate of 1.7, 2, 2.1, 2.2 and 2% respectively.

#### 4.3.2.2 GLOBAL Cv COMPARISON

As seen from the previous section, pressure difference increases from healthy to the faulty valve. This has therefore caused changes in the valve Cv, which is a function of flow rates and pressure drop as seen in equation 1.4.

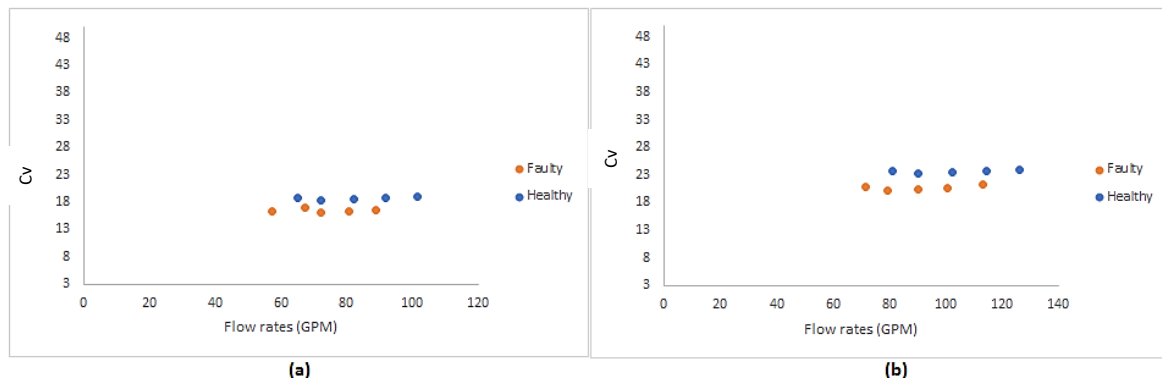


Figure 4.44: Global Cv comparison for the healthy and faulty valves at different flow rates for (a) 60% (b) 80% VOPs.

Global Cv increases from faulty to healthy valve as seen in figure 4.44 for 60 and 80% VOPs. It is also seen that across flow rates, Cv should remain nearly the same as seen from the figure. Average Cv has been obtained for the different VOPs at different flow rates. A single value has been obtained for the healthy and faulty valve across both VOPs.

Figure 4.45 shows the single value global Cv between health and faulty valve for 60 and 80% VOPs

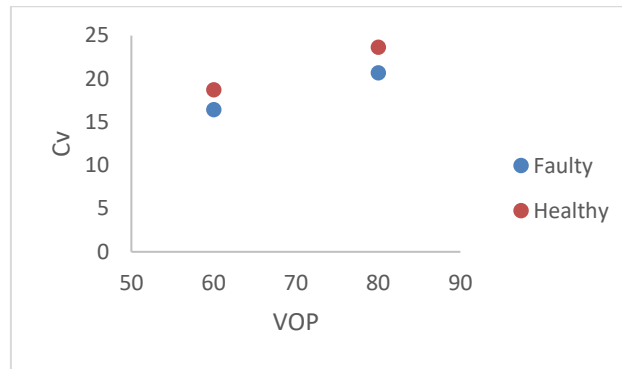


Figure 4.45: Single value global Cv comparison for the healthy and faulty valves at different flow rates for 60 and 80% VOPs.

As the Cv increases from 16.4 for faulty to 18.7 for healthy value, representing a 12.16% increase for 60% VOP. At 80% VOP, global Cv increases from 20.69 for faulty to 23.66 for the healthy value, representing a 12.53% increase.

#### 4.3.2.3 LOCAL SECTIONAL PRESSURE DROP COMPARISON

Again, because of the blockage of one flow path, flow rates at the same VOP decreases. For the faulty valve condition, flow rates decrease when compared to the healthy valve. This then causes the pressure drop to increase, as there are more flow restrictions. The local section pressure drop between inlet and outlet of the valve using the MHP, across the seven heights have been obtained. Again, compared to when the valve is a healthy valve, pressure drop has been obtained at position 3 for 60 and 80% VOPs is seen to increase for the faulty valve.

Figure 4.46 shows the local sectional pressure drop difference between healthy and faulty valve for 60 and 80% VOPs, using the MHP.

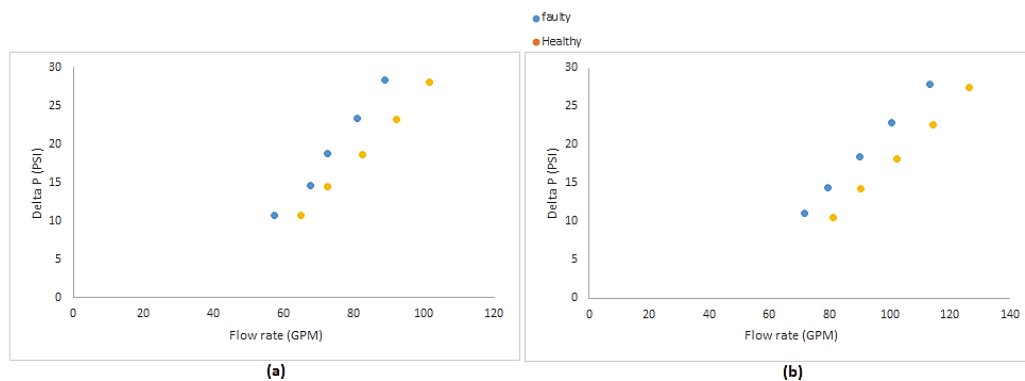


Figure 4.46: Local sectional pressure drop comparison using the MHP for the healthy and faulty valves at different flow rates for (a) 60% (b) 80% VOPs.

At 60% VOP, the faulty valve local sectional pressure drop has been observed to increase slightly from the healthy valve as flow rates increases due to the addition flow restriction caused by the path blockage (fault). Flow rates, for the same condition, decrease from healthy to faulty valve. Flow rates for 60% VOP are 65, 72.3, 82.4, 92.1, and 101.6GPM for healthy valve decreases to 57.3, 67.5, 72.4, 80.9, and 88.8GPM for the faulty valve respectively for same pump set points at the rate of 11.8, 6.7, 12.1, 12.1 and 12.5% respectively.

This has caused local sectional pressure drop for the healthy valve to increase from 10.70, 14.5, 18.65, 23.19, and 28.15PSI to 10.77, 14.57, 17.74, 23.31, and 28.34PSI for the faulty valve at the rate of 0.6, 0.4, 0.46, 0.5 and 0.68% respectively.

At 80% VOP, flow rates for the same condition, decrease from healthy to faulty valve. Flow rates for 80% VOP are 81, 90.3, 102.3, 114.5 and 126.3GPM for healthy valve, decreases to 71.6, 79.4, 90, 100.8 and 113.3GPM for faulty valve respectively for same pump set points at the rate of 11.6, 12, 11.9, 11.99 and 10.3% respectively.

This has again caused local pressure sectional drop using the MHP to again increase from 10.56, 14.2, 18.3, 22.6 and 27.47PSI for the healthy valve to 11.01, 14.39, 18.45, 22.93 and 27.83PSI for faulty the valve at the rate of 4.1, 1.2, 1.29, 1.3 and 1.29% respectively.

#### 4.3.2.4 LOCAL SECTIONAL Cv COMPARISON

As seen from the previous section, pressure difference increases from healthy to faulty valve. This has therefore caused changes in the valve Cv, which is a function of flow rates and pressure drop as seen in equation 1.4.

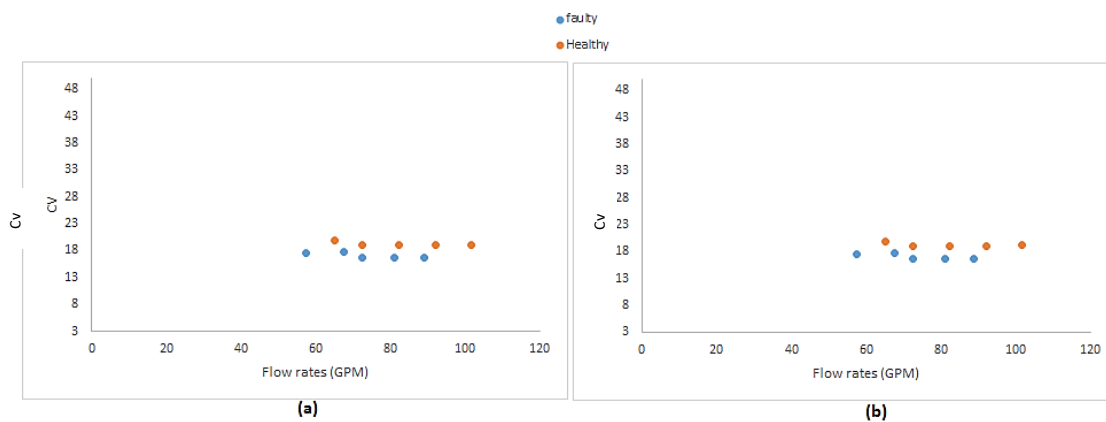


Figure 4.47: Local sectional Cv comparison for the healthy and faulty valves at different flow rates for (a) 60% (b) 80% VOPs.

Local sectional  $C_v$  increases from faulty to healthy valve as seen in figure 4.47 for 60 and 80% VOPs. It is also seen that across flow rates,  $C_v$  remains nearly the same as seen from the figure. Average  $C_v$  has been obtained for the different VOPs at different flow rates. A single value has been obtained for the healthy and faulty valves across both VOPs.

Figure 4.48 shows the single value local sectional  $C_v$  between health and faulty valve at 60 and 80% VOPs.

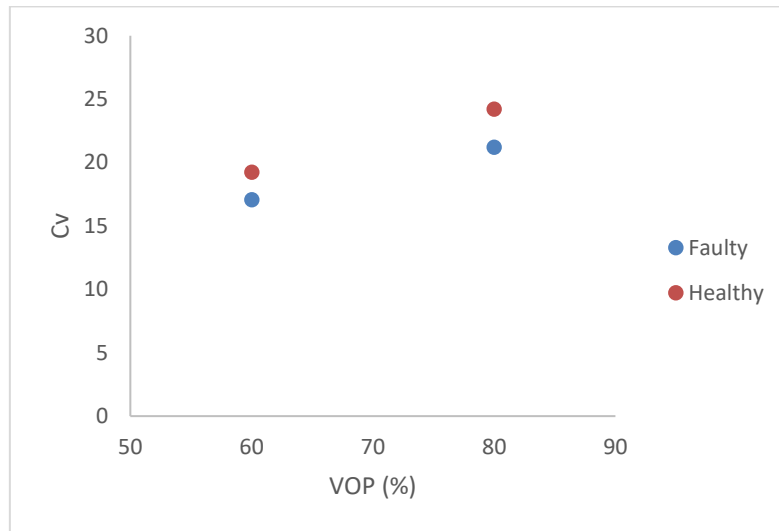


Figure 4.48: Single value Local sectional  $C_v$  comparison for healthy and the faulty valve at different flow rates for 60 and 80% VOPs

As the local  $C_v$  increases from 17.07 for faulty to 19.245 for healthy valve, representing an 11.3% increase for 60% VOP. For 80% VOP, local sectional  $C_v$  increases from 21.2 for faulty to 24.2 for healthy value, representing a 12.53% increase.

#### 4.4 SUMMARY

The MHP has been calibrated and calibration coefficients obtained. These coefficients have been used in calculating the different flow parameters. The MHP has been placed at the inlet and outlet of the valve and across seven heights at different positions. Different parameters have been obtained at these different positions. Parameters such as pressure, velocity, pressure difference,  $C_v$  have been obtained and analysed. Furthermore, comparisons for the different parameters have been made for the different positions and how much these parameters vary as flow goes from inlet to outlet of the valve.

In addition, different global and local flow parameters have been compared for healthy and faulty valve, showing how these parameters change significantly as seen for these comparisons.

The next chapter discussed the results obtained for a healthy and faulty valve from using vibration technique as a tool in analysing the flow behaviour inside the valve for single and multiphase conditions.

## CHAPTER FIVE

### 5.0 VIBRATION BEHAVIOUR OF THE CONTROL VALVE UNDER VARIOUS FLOW CONDITIONS FOR SINGLE PHASE AND MULTIPHASE FLOW

---

*This chapter establishes vibration signals for the control valves to easily identify and evaluate the valve performance when incipient faults occurs while in their early stage of development under normal operating conditions. Such faults, when detected early, can prevent the deterioration of the valve performance. Using vibration signatures behaviours from vibration sensors (accelerometer) can establish how the flow should behave under such conditions. Results obtained from both time and frequency domain in achieving a holistic understanding regarding faults detection have been analysed on the valve. Also in this chapter, different flow and operating condition effect on the valve such as various flow rates, various VOPs, air injection and probe lengths and heights have been investigated and established using several statistical features in both time and frequency domain.*

## 5.1 ADVANTAGES AND DISADVANTAGES OF USING VIBRATION TECHNIQUE

Accelerometers (vibration sensor) that are available in the market have the frequency and temperature ranges, and sensitivities that are necessary to detect when a fault occur in most control valves. In general, the accelerometer type sensors are easy to install on the valve body and can be placed easily in area where the sensitivity is high in detecting any expected fault. The various type and sizes of the accelerometer available commercially mean that selecting anyone for easy positioning would always be possible. Vibration signal analysis in both time and frequency domain can show key information about the severity of the fault inside the valves.

On the other hand, it sometimes becomes very difficult in industrial application to control vibration signatures that arise from other parts of the same equipment/machine, or other equipment/machine. This intrusive vibrations from the background may soil the signal, thereby making fault diagnostics a bit difficult and hence, the need for analysing the signal statistically.

The next subsections will analyse the vibration signatures for the different flow and operating conditions in time and frequency domain for single and multiphase conditions.

## 5.2 DEVELOPMENT OF VIBRATION INDICATOR FOR SINGLE PHASE FLOW CONDITION INSIDE A HEALTHY CONTROL VALVE

Unlike with the pressure probes where local flow parameters are being analysed, the flow parameters inside the flow field vary (sometimes slightly) for what the probe measures at different heights and lengths. Again, like the  $C_v$ , which is a global performance parameter measured from static pressure at 2D and 6D, the different pressure probe heights and lengths does not have any effect on the  $C_v$  as they remain the same as long as the flow and operating conditions are same.

### 5.2.1 TIME DOMAIN ANALYSIS

Before analysing the vibration signals for the different flow and operation conditions in this chapter, figure 5.1 and 5.2 establishes the similarity in the vibration signals for different heights of same probe length and for different probe lengths of same height respectively, when flow and operating condition are same or similar in the time domain.

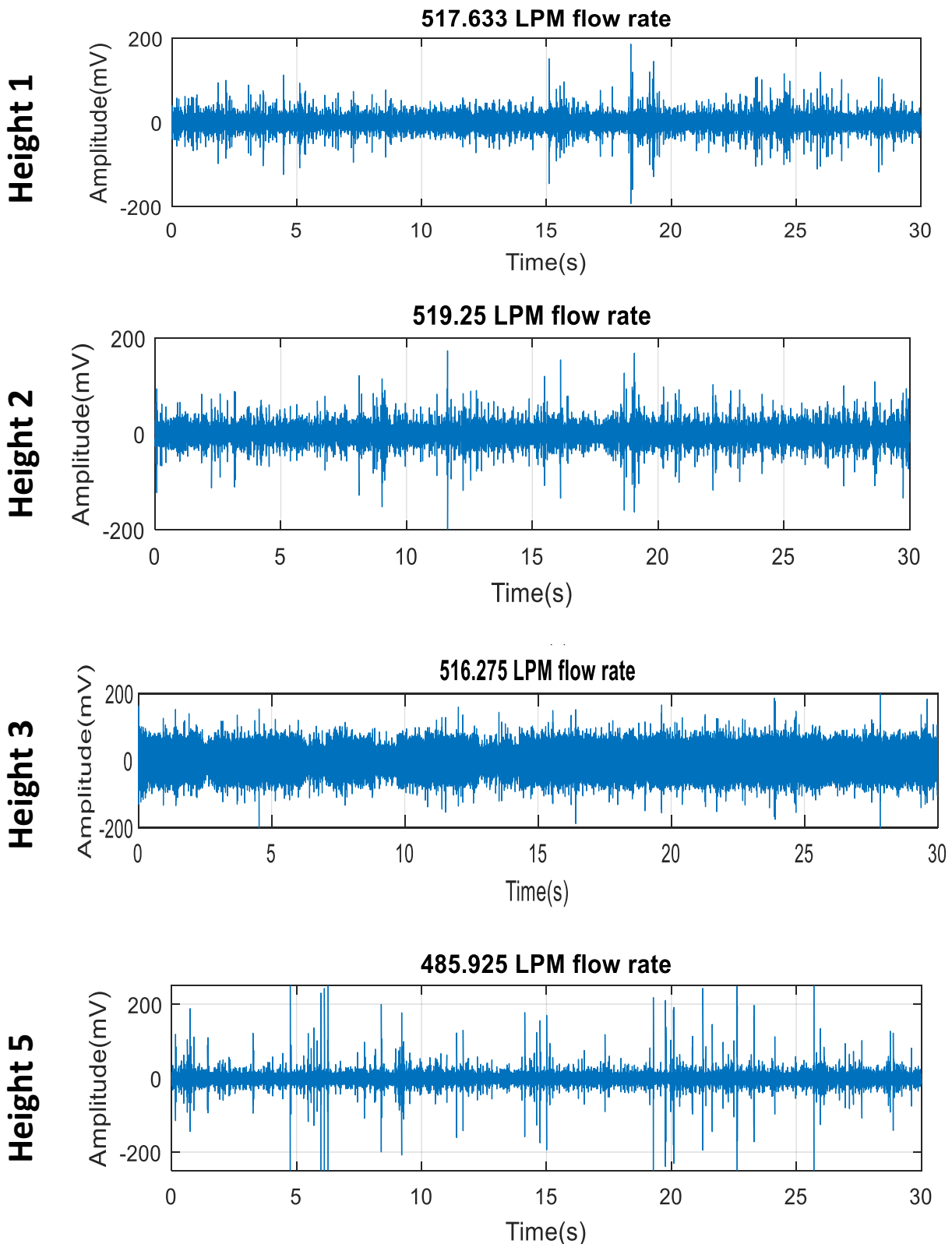


Figure 5.1: Vibration signals for various probe height for the same probe length

As said earlier, the probe inside of the valve does not affect the global vibration signatures of the control valve. It can be seen from figure 5.1 that the vibration amplitude are very similar for the different heights. This shows that the vibration features will also be similar

in time domain even with the slight difference in flow rates, which fall between 485 and 519LPM. The different flow rates have been chosen for convenience in demonstrating the vibration signal changes with flow rate changes. The flow conditions used for figure 5.1 are 80% VOP and 1200 pump set point, all for length 1. The RMS values, which signifies the strength of the vibration signals are 6.395, 6.403, 6.9 and 6mV for height 1, height 2, height 3 and height 5 respectively. Figure 5.2 depicts the similarity in the vibration signatures for the same probe height position at different lengths.

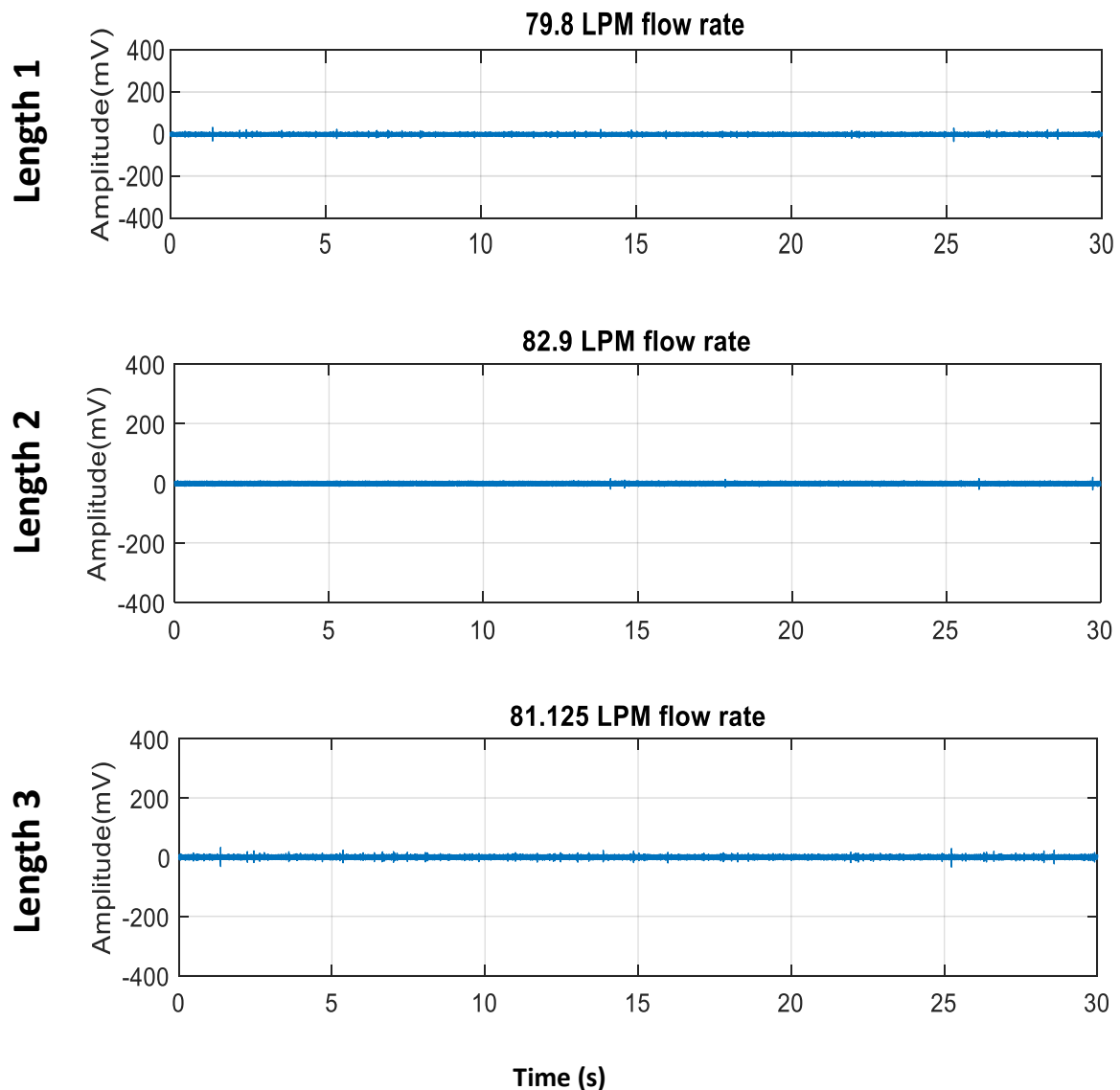


Figure 5.2: Vibration signal amplitude similarities for the same probe height and different probe lengths

Figure 5.2 depicts the similarity in the vibration signatures for same probe height position at different lengths. The vibration signal seen in figure 5.2 has been taken for

10% VOP and at 1000 LPM pump set points for the different probe lengths. The RMS values, which again signifies the strength of the vibration signals, are 2.17, 2.08 and 2.25mV for length 1, length 2 and length 3 respectively.

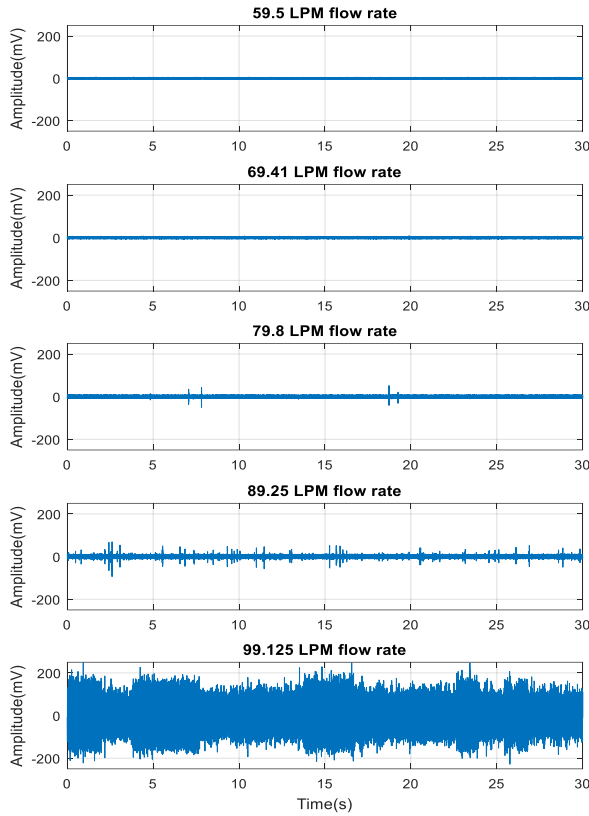
Time-domain and frequency analysis for both healthy and faulty valve would be used in determining the valve conditions. In the following section, statistical parameters such as RMS value, Peak-to-peak, standard deviation and kurtosis are analysed to identify trends of vibration signals in time domain. Five different VOPs have been used in this research at different flow rates because of different pump set points, which are 800, 900, 1000, 1100, and 1200 LPM.

### 5.2.1.1 RAW VIBRATION SIGNALS

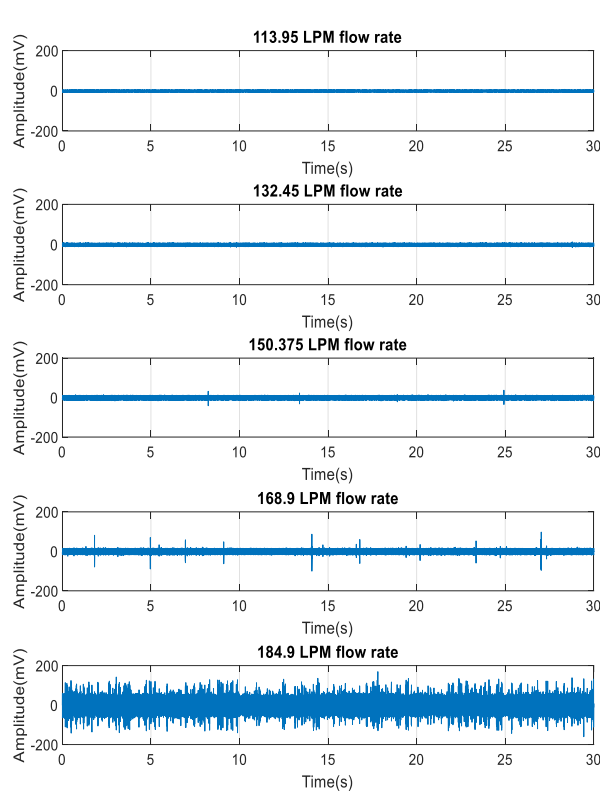
The raw vibration signals for the different flow rate for all the various VOPs have been presented in figure 5.3. The figure shows the relationship that exists between time and the vibration amplitude for various flow rates. It can be seen for all VOPs that as the flow rate increases, the amplitude of the raw vibration signal increases. The vibration signals have been taken for a 30 secs sampling time and a sampling frequency of 96 kHz. Different level of vibration can be seen in figure 5.3 with same pump setpoints used at the different VOPs, giving rise to different flow rates. The vibrations are because of flow-induced impact on the valve. Further in-depth analysis is carried out using statistical parameters to clearly understand how these changes occur and what has caused them to change.

# ESTABLISHING VIBRATION BEHAVIOUR OF THE CONTROL VALVE UNDER VARIOUS FLOW CONDITIONS

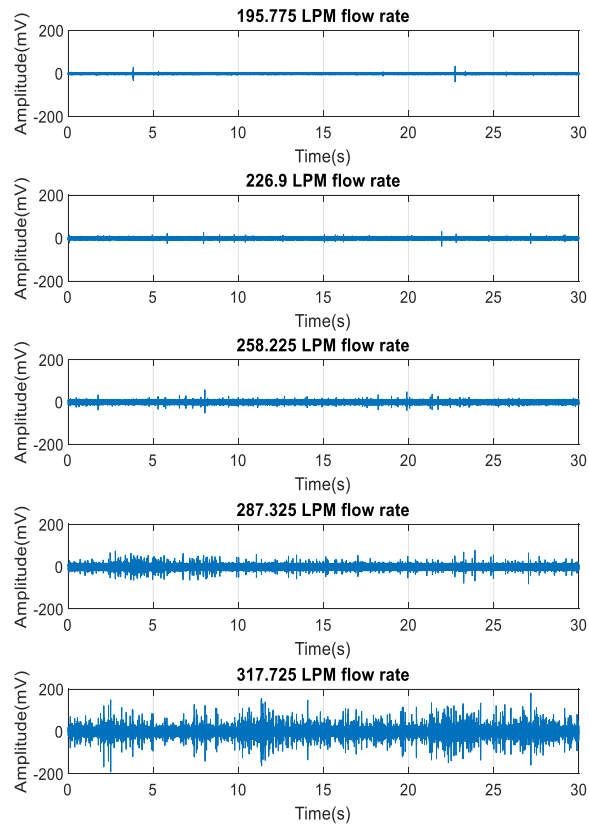
## 10% VOP



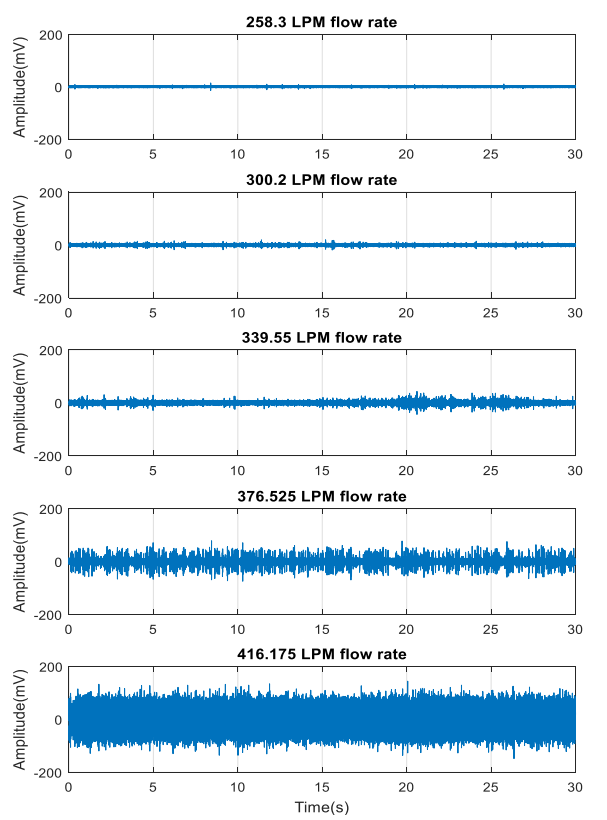
## 20% VOP



## 40% VOP



## 60% VOP



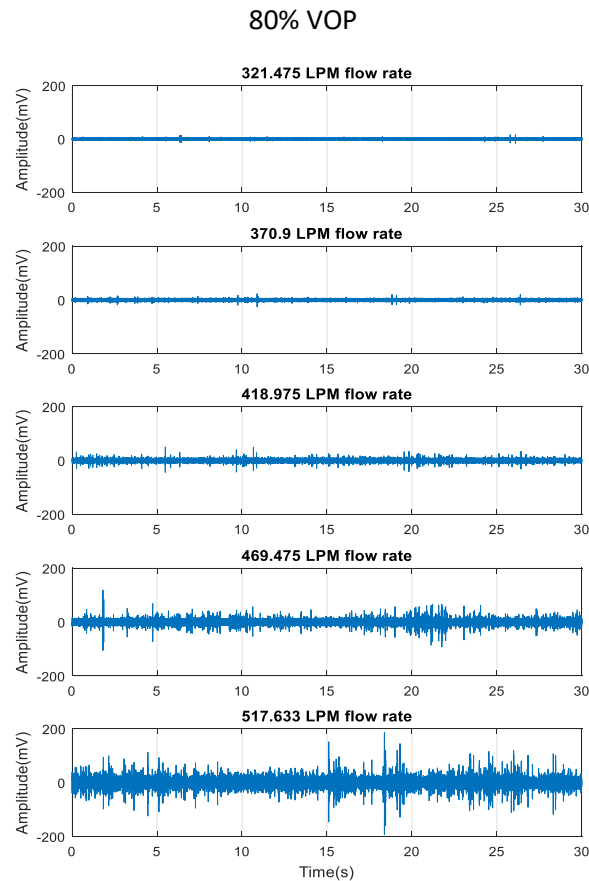


Figure 5.3: Single-phase raw vibration signals for varying flow rates at different VOPs

### 5.2.1.2 VARIOUS STATISTICAL PARAMETERS

For the vibration characteristics, a series of experiments have been performed and the data have been collected for the different flow and operating conditions explained in the previous section 5.2.1.1. For the single-phase condition, the vibration signals have been analysed in time domain. In time domain, statistical parameters such as RMS, peak-to-peak, kurtosis and Standard deviation have been analysed. These four parameters combine to give a holistic representation of the vibration data as they complement each other.

#### A. RMS Values

RMS shows the level of vibration produced at the valve, indicating the signal strength. Therefore, at any flow changes that affect the valve, the RMS of the vibration signal will change. The equation for this value has already been presented in chapter 1.

Figure 5.4 shows the RMS values variation for the various flow rates at 10, 20, 40 60 and 80% VOPs. The figure shows an increasing trend for RMS at all the different VOPs as the

flow rate increases. RMS shows the level of vibration produced at the valve, indicating the signal strength. Therefore, at any flow changes that affect the valve, the RMS of the vibration signal will change.

As VOP increases, RMS should reduce. This is because of more vibration caused due to the reduced flow area passage experienced during the experiments. The trends for RMS is to be expected because of the clear vibration amplitude increase with an increase in flow rates as shown in figure 5.3. For 10% VOP, vibration signal in mV increases by 28.1% from 1.4 as flow rate increases from 59.5 to 69.4 LPM. As flow rate increases to 79.8, 89.1 and 99.1LPM, percentage variation increase observed at these flow rates are 26.7, 26.4 and 91.8% respectively.

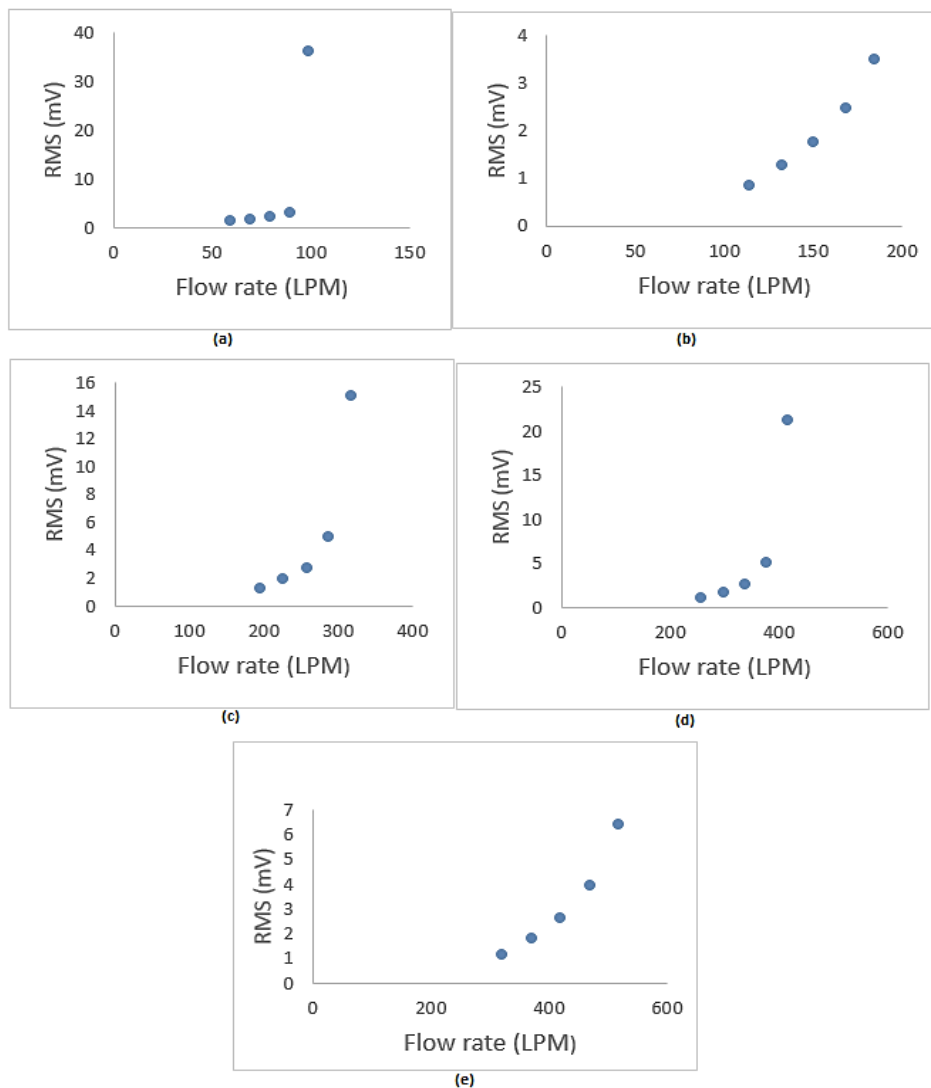


Figure 5.4: RMS variation for various flow rates at the different VOPs (a) 10% VOP (b)

20% VOP (c) 40% VOP (d) 60% VOP (e) 80% VOP

20, 40, 60 and 80% VOPs shows similar trends, as the RMS values decrease slightly as VOP increases for same flow condition.

Peak-to-Peak amplitude, standard deviation and Kurtosis were also analysed, and they all gave similar trends where their values increases as flow rates increases and for same flow rate condition, their values decrease as the VOP increases. For kurtosis [99] however, the data corresponding to 20 and 80% valve opening shows an increasing trend as the flow rate increases. However, for 60% valve opening, there is a sharp drop at the maximum flow rate. This shows that the peakedness of the signal for the maximum flow rate at 60% VOP is lower as compared to other flow rates for this VOP. The higher kurtosis values signify that more peaks are greater than  $3\sigma$  (peaks greater than 3 times RMS) [95]. The drop in kurtosis values simply means that the number of peaks present in the signal for the maximum flow rate drops, hence there is a drop in kurtosis value [95].

After time domain analysis has been carried out for single-phase condition, for a healthy valve, the next section 5.2.2 presents analysis carried out on vibration signal in frequency domain using FFT and mean frequency.

### 5.2.2 ANALYSIS IN FREQUENCY DOMAIN

As mentioned earlier, the vibration amplitude level of the signal depends on the operating and flow conditions inside the control valve. The results seen from the analysis in time domain showed that when the valve is operated under low VOP and maximum flow rate, the maximum level of vibration and noise occurs. When the control valve is working at higher VOPs and low flow rates, less vibration and noise occur. This can be attributed to several reasons; one is because of impeller blades interaction within the pump. Another reason is because of an increase in turbulent flow inside the valve. One other key reason is because of the flow passage area due to the VOPs causing an increase in the flow rate. In this research, for frequency domain analysis, FFT and mean frequency have been used. FFT plot displays the frequency components that are present in the signal. It shows how much power is present at a particular frequency. If the vibration increases, the magnitude of that particular frequency component will increase. Mean frequency is one of the most useful features in frequency domain analysis. They are used in describing the frequency content of the signal [96, 97]. It accesses the signal power distribution across the frequencies. It is an average frequency, which is the product of the signal power and the

frequency, divided by the total sum of the signal power spectrum [98]. The higher the signal amplitude, the higher the mean frequency.

### A. Fast Fourier Transform (FFT)

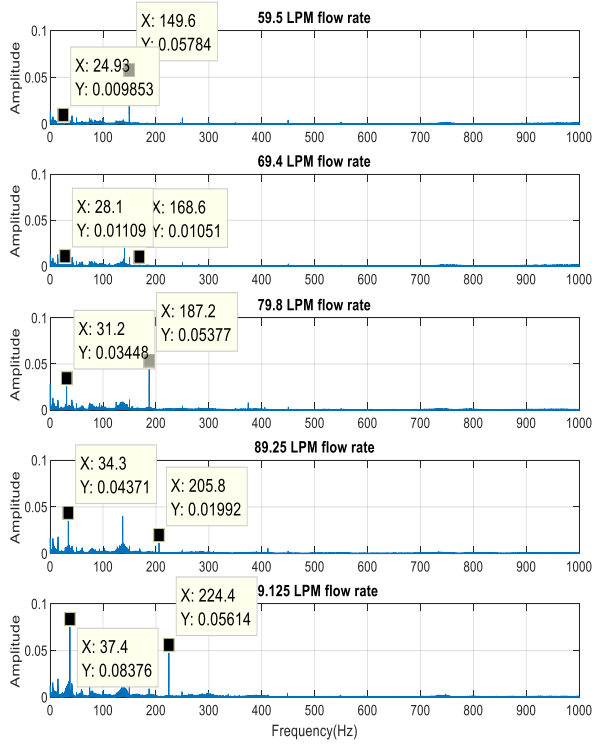
FFT has been used to see how the magnitudes of these frequency components change when the flow regime changes, and by how much they increase or decrease. Figure 5.5(a), (b), (c), (d) and (e) shows the FFT plots for the different flow rates at 10, 20, 40, 60 and 80% VOPs respectively. The signal has been sampled at 96 kHz. Figure 5.8 shows the FFT plot of the signal for 0-1 kHz.

Figure 5.5 shows a better understanding associated with the dynamics of the control valve as the vibration signals in time domain have been transformed into frequency domain using FFT. The peak amplitude can be seen distinctively in the frequency range of 0-1000 Hz. As the flow rate increases, the peak amplitude increases.

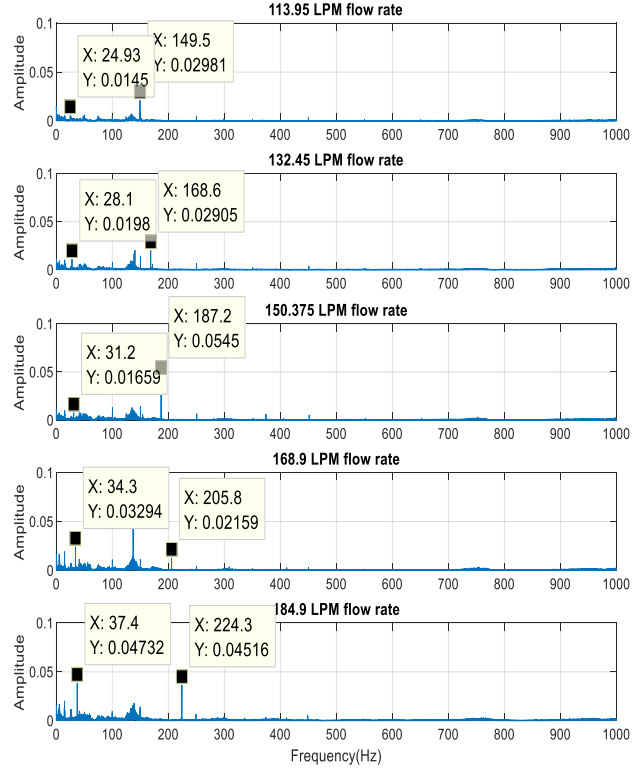
This increase is due to vibration amplitude increase as the flow rate increases. Regardless of the VOP, the amplitude peaks for the different flow rates occur at a similar frequency and at a similar pump rotation speed. They show discrete characteristic components that are present within the entire frequency spectrum causing the flow periodicities due to pump rotation speed and the blade interactions. Therefore, at every pump set point, for the different VOPs, the peaks occur at similar frequencies. Looking at the scale for all the figures in figure 5.5, it can be seen that the highest peaks observed keep on increases as the flow rate increases for the different VOPs between 20-40Hz. Again, higher peaks are seen specifically at all the VOPs for the different at 149.6, 168.6, 187.2, 205.8 and 224.4Hz respectively. This means that as the flow rates increase for the different VOPs, the frequency at which the high peaks occurs also increases. For 10% VOP, the maximum peak recorded between the 20-40Hz were 0.009, 0.01, 0.034, 0.043 and 0.083mV respectively. For 20% VOP, maximum peak recorded were 0.014, 0.019, 0.0166, 0.033 and 0.047mV respectively. At 40% VOP, maximum peak recorded are 0.012, 0.029, 0.022, 0.026 and 0.067mV respectively for the different flow rates. For 60% VOP, 0.009, 0.02, 0.0177, 0.019 and 0.037mV for the different flow rates have been observed. For 80% VOP, 0.005, 0.015, 0.023, 0.025 and 0.08 mV occurring at around 24.9 28.07, 31.17, 34.2 and 37.3 Hz respectively for all the VOPs have been observed.

ESTABLISHING VIBRATION BEHAVIOUR OF THE CONTROL VALVE UNDER VARIOUS FLOW CONDITIONS

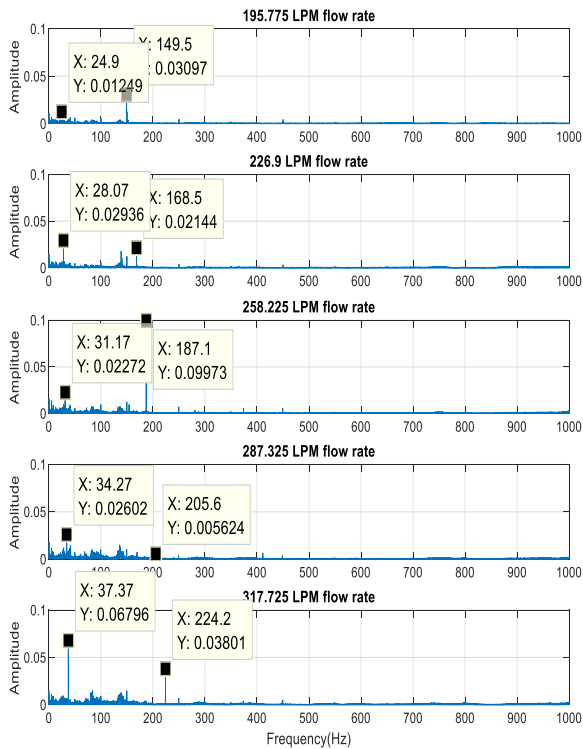
10% VOP



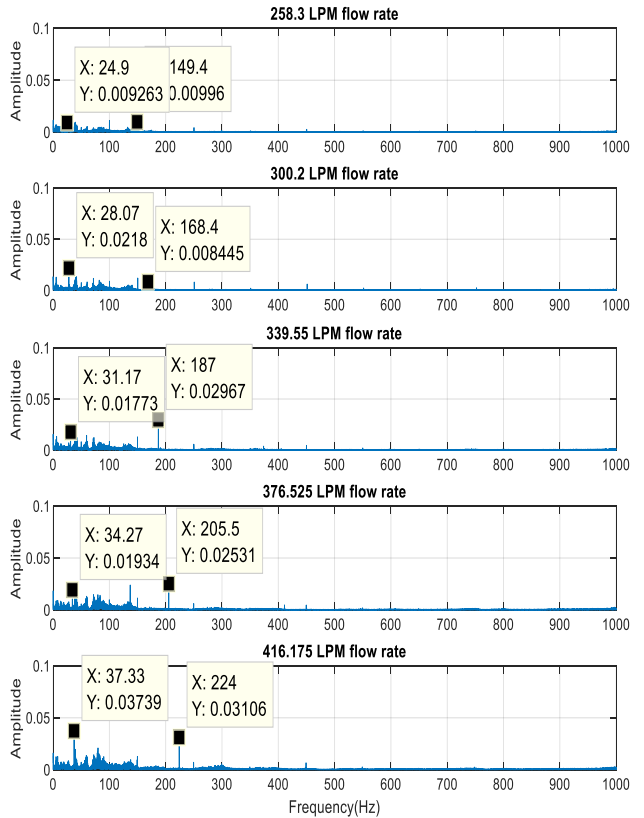
20% VOP



40% VOP



60% VOP



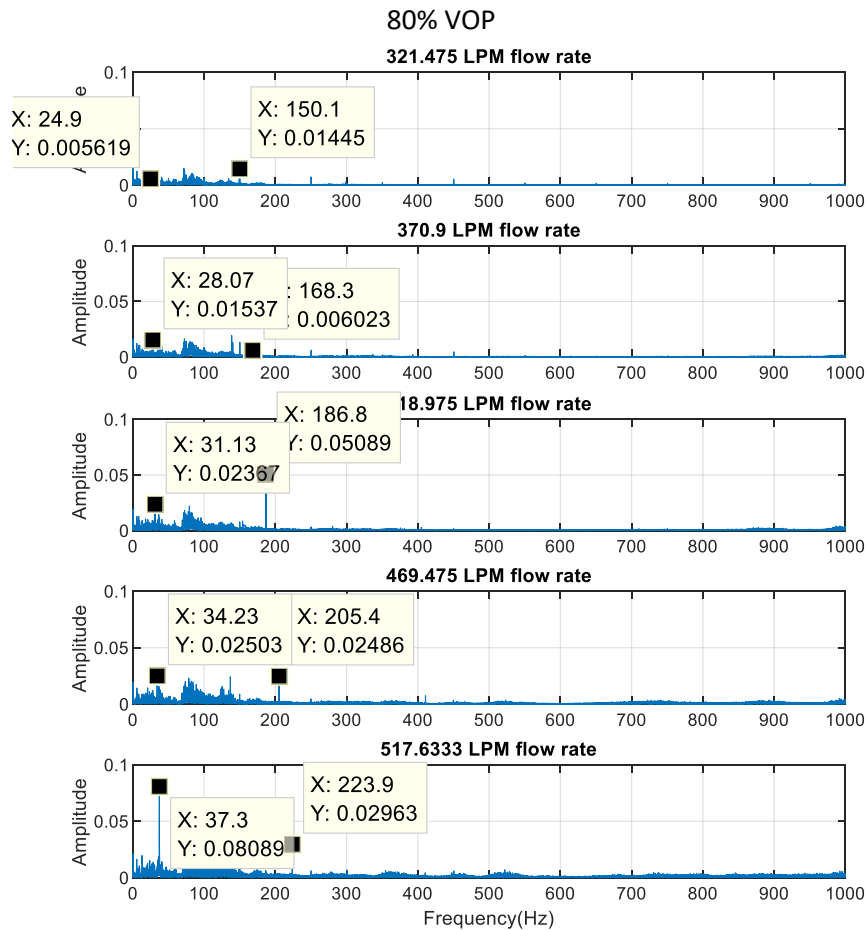


Figure 5.5. Vibration signal spectrum for the valve at different flow rates at 10%, 20%, 40%, 60% and 80% VOPs

### B. Mean Frequency

Figure 5.6 shows the mean frequency from the vibration signatures as a function of flow rate. It can be seen that at across all VOPs, mean frequency increase as flow rates increases. This is because as the flow rates increases, the signal strength increases, and in turn, have an increasing effect on the mean frequency across the entire vibration frequency spectrum. While FFT shows you what component on each frequency and how much amplitude they have, the mean frequency shows the average frequency for the signal across the frequency spectrum.

Figure 5.9 (a), (b), (c), (d) and (e) shows the mean frequency for the different flow rates at 10, 20, 40, 60 and 80% VOPs respectively.

For 10% VOP, mean frequency increases from 204.97 Hz at low flow rates to 3398.4 Hz at the maximum flow rate. Mean frequency increases at 55.5, 48.3, 47.2 and 50.1% respectively across the different flow rates.

20, 40, 60 and 80% VOPs, for similar flow conditions, mean frequency increases as the VOP increases. This is because of the increase in the valve flow area, increasing the frequency spectrum of the signal.

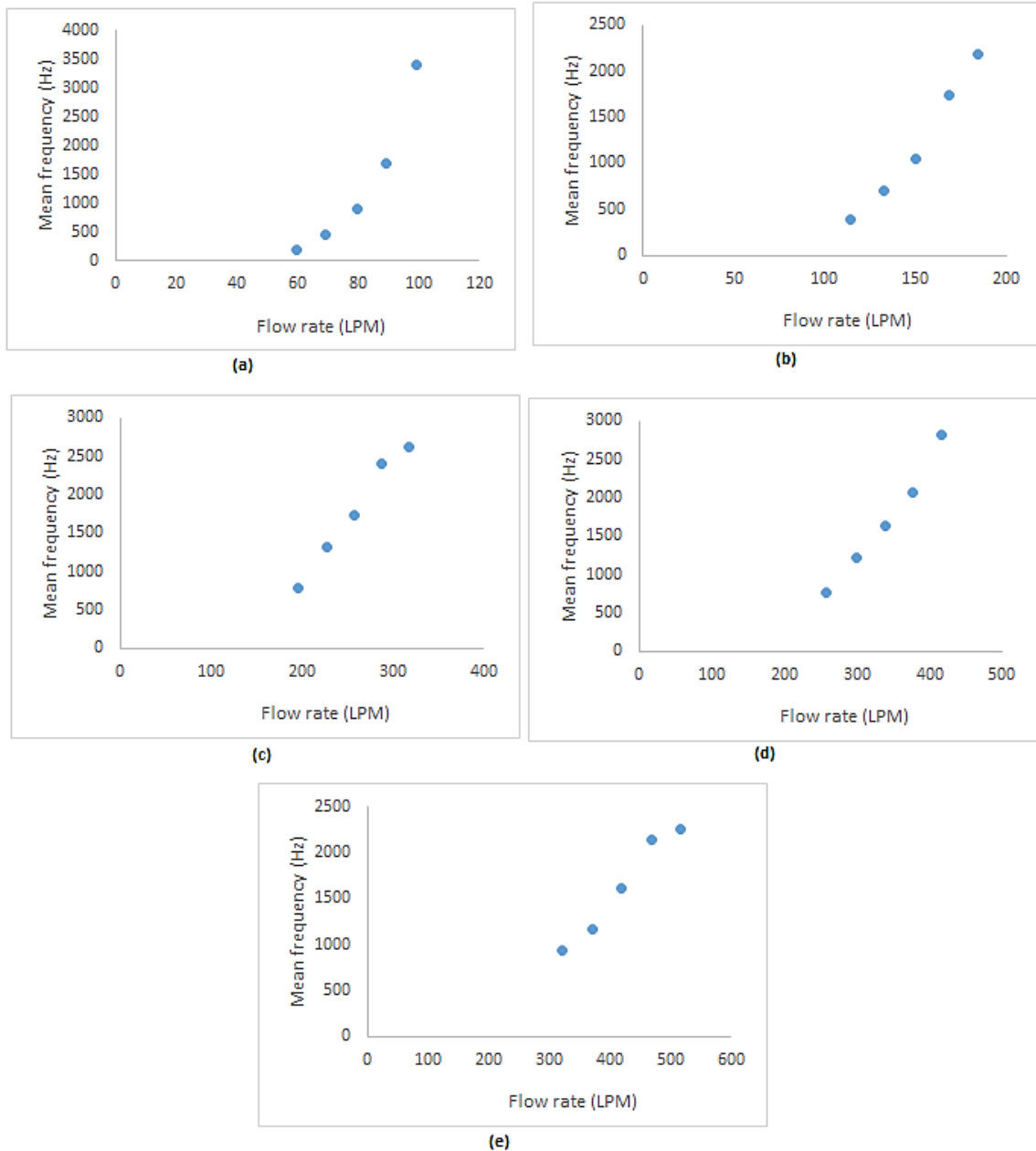


Figure 5.6. Mean frequency for the valve at different flow rates (a) 10% (b) 20% (c) 40% (d) 60% (e) 80%

### 5.3 DEVELOPMENT OF VIBRATION INDICATORS FOR MULTIPHASE FLOW CONDITION INSIDE A HEALTHY CONTROL VALVE

A wide range of operating conditions have been selected for tests in the laboratory. These conditions correspond to the actual operating conditions for this valve in real life. The test flow rates range covers the most important operating range needed for the operation of such valves. Because of the construction features present within the valve, there may be a likelihood of cavitation and flashing. To simulate this condition, airflow has been injected in the pipe loop creating multiphase flow conditions. Three different airflow rates have been used in these conditions to understand the dependence of airflow rate on the level of vibration obtained with a view to establishing the effectiveness of vibration measurement as a technique for flow regime change identification.

For the multiphase experiments, the following airflow rates have been used for each of the above water flow rates. The airflow rates of 19.8 LPM, 28.8 LPM and 38.8 LPM have been used in the present investigation. In a control valve during its operation, the valve opening may change depending on the process requirement. In the present investigation, only 60% and 80% VOPs have been analysed in frequency domain for multiphase flow tests because, at lower VOPs, gas accumulates at the valve upstream for a certain period, causing uncertainties in the measured data.

Again, for multiphase flow condition, analysis has been carried out in both time and frequency domain using the same features.

#### 5.3.1 TIME DOMAIN ANALYSIS

Figure 5.7 shows the RMS values variation respectively for the multiphase flow at different flow rates for 10, 20, 40, 60 and 80% VOPs. The trends for RMS show increasing RMS values as the flow rate increases as depicted in figure 5.7 (a), (b), (c), (d) and (e). These trends are similar to that of single-phase condition. 80% VOP generates higher RMS for lower flow rates. However, at higher flow rates, 60% VOP generates higher RMS values, when compared to 80%. 20% VOP is seen to have the lowest RMS values. Again, these values are to be expected as vibration amplitude increases with flow rate increase as shown in figure 5.7 at 19.8 LPM, 28.8 LPM and 38.8 LPM airflow rates.

The trends for RMS (Figure 5.7) for 10, 20, 40, 60 and 80% VOPs show almost linear trends, with the values increasing as flow rates increase. The vibration generated for

multiphase flow conditions is quite higher than that observed for single-phase for both 60 and 80% VOPs. The RMS of the vibration signals for single-phase (60% VOP) for the flow rates (pump set point variation) are 1, 1.6, 2.5, 5 and 21.2 mV. Comparatively, for multiphase flow conditions with the lowest airflow rate (19.8 LPM), the values jump to 7.8, 10, 14.2, 18.8 and 27.1 mV respectively for similar flow rates of water. The results have been seen to deviate from single to multiphase by 87, 84, 82, 73 and 22% respectively. This shows how the vibration signal changes due to the flow regime change from single to multiphase.

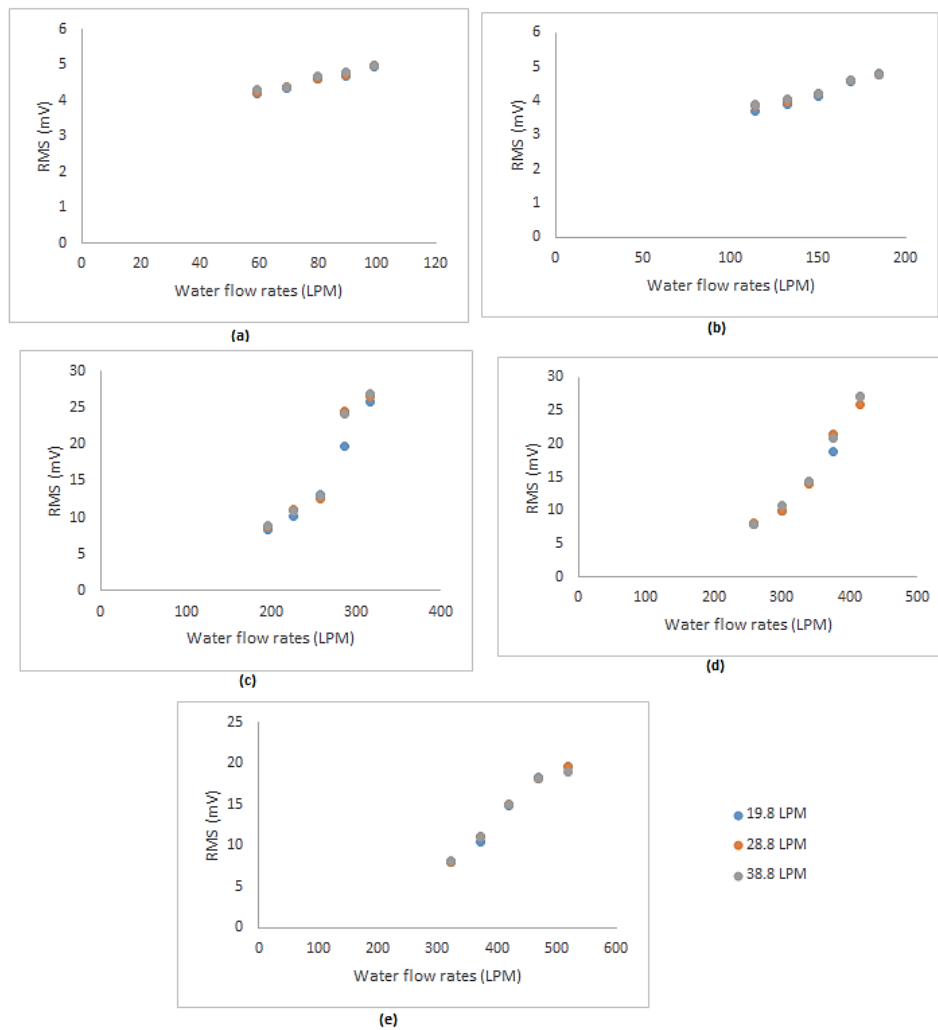


Figure 5.7. Multiphase RMS variation for the different flow rates at (a) 10% (b) 20% (c) 40% (d) 60% (e) 80% VOP

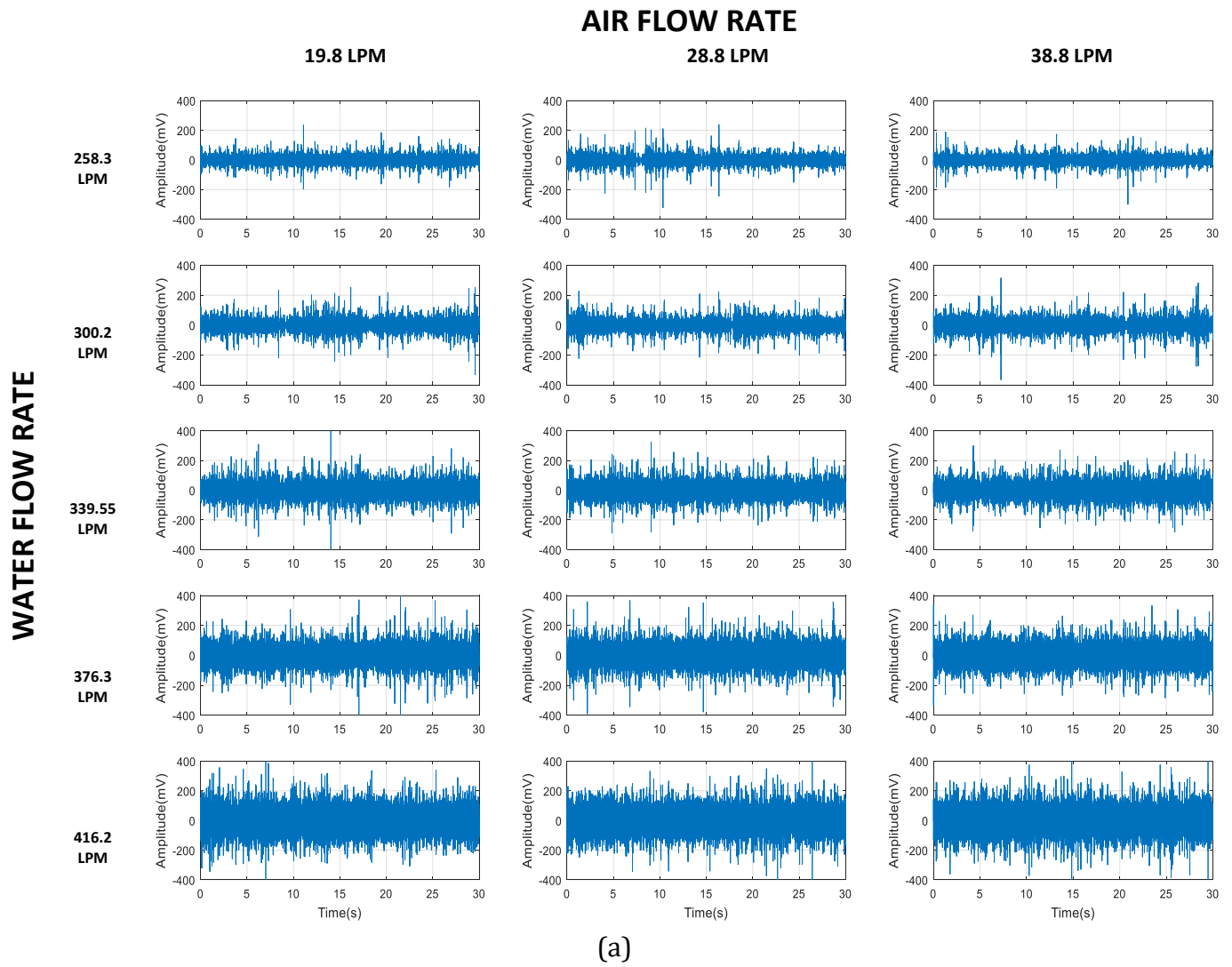
Furthermore, as the airflow rate increases from 19.8 to 28.8 LPM, the RMS values changes slightly from 7.8 to 8.2mV, representing a deviation of 4.3%, and from 28.8 to 38.8LPM, RMS deviates by nearly 2% for lowest water flow rate. At the maximum water flow rate,

from 19.8 to 28.8 LPM airflow, the RMS values deviate slightly by 4.8% and from 28.8 to 38.8LPM, RMS deviates by nearly 4.4%.

These slight RMS value increase is because of airflow rate increasing. A similar trend is observed at 80% VOP where the RMS values of the vibration signal go from 1.1, 1.76, 2.65, 3.94 and 6.4 mV to 8, 10.45, 14.9, 18.3 and 19.5 mV, from single to multiphase flow conditions, representing a deviation from single-phase of 86, 83, 82, 78 and 67% respectively. As the airflow rate then increases from 19.8.8 to 28.8 and to 38.8, the RMS values deviate by 0.3 and 0.1% respectively.

Peak to Peak, standard deviation and kurtosis have also been carried out with all three parameters showing similar trends as RMS values, except for kurtosis where for 80% VOP, kurtosis is seen to decrease with increase in flow rates. A similar trend can also be observed for 60% VOP as flow rate increases except for sharp peaks occurring for the low and higher airflows. This trend is totally opposite as that for single-phase which goes in the opposite direction. This again shows the change in the dynamic flow behaviour as flow changes from single phase to multiphase due to the extra vibration in multiphase. This is because the air volume fraction is decreasing as the water flow rate is increasing, hence the decrease in the signals peak and tail shape (heavily or light-tailed) and in the kurtosis values.

Standard deviation has not been analysed for multiphase as it has been seen that SD has the same values as RMS. This is because, for the random stationary vibration signal, the mean is equal to zero.



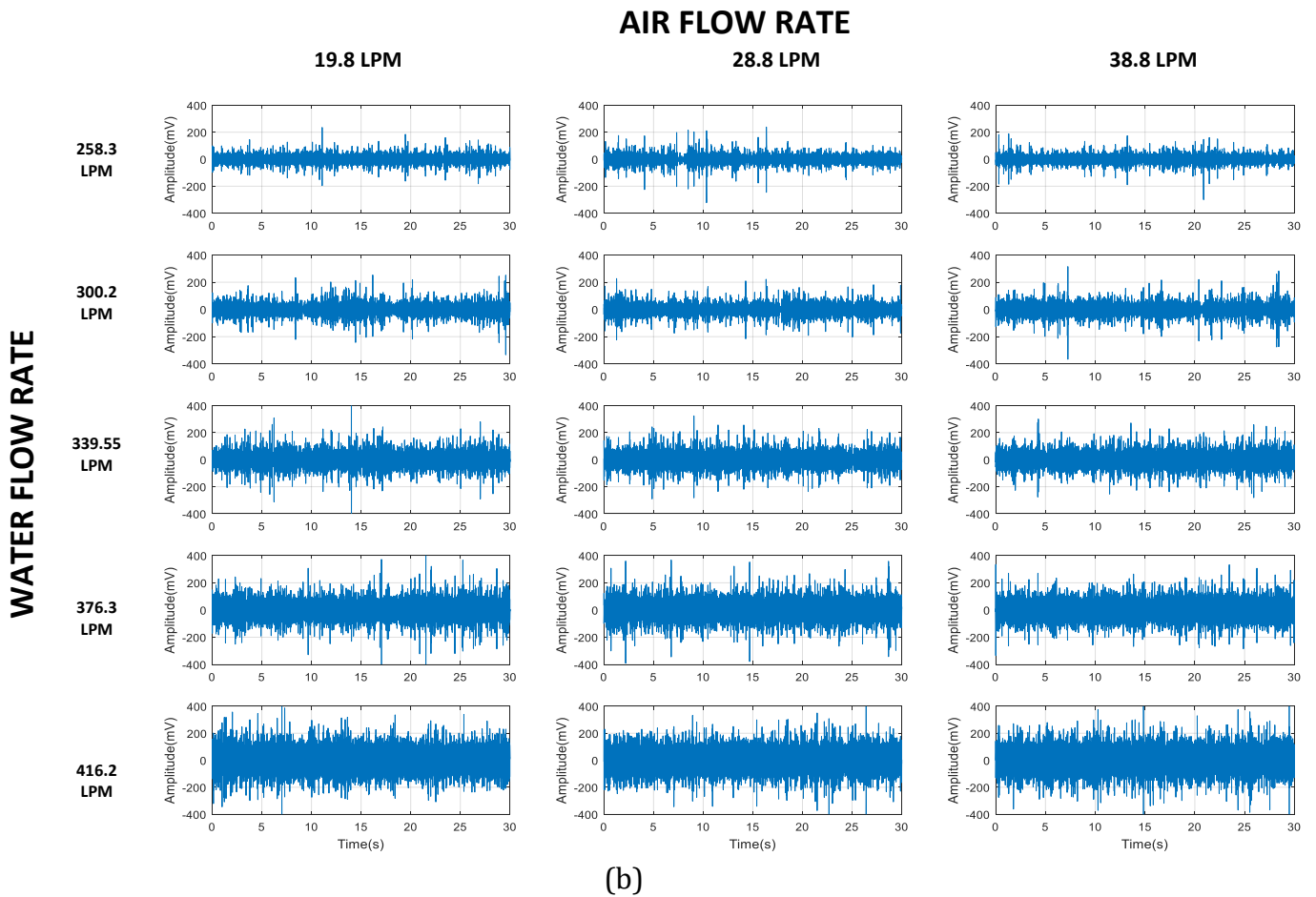
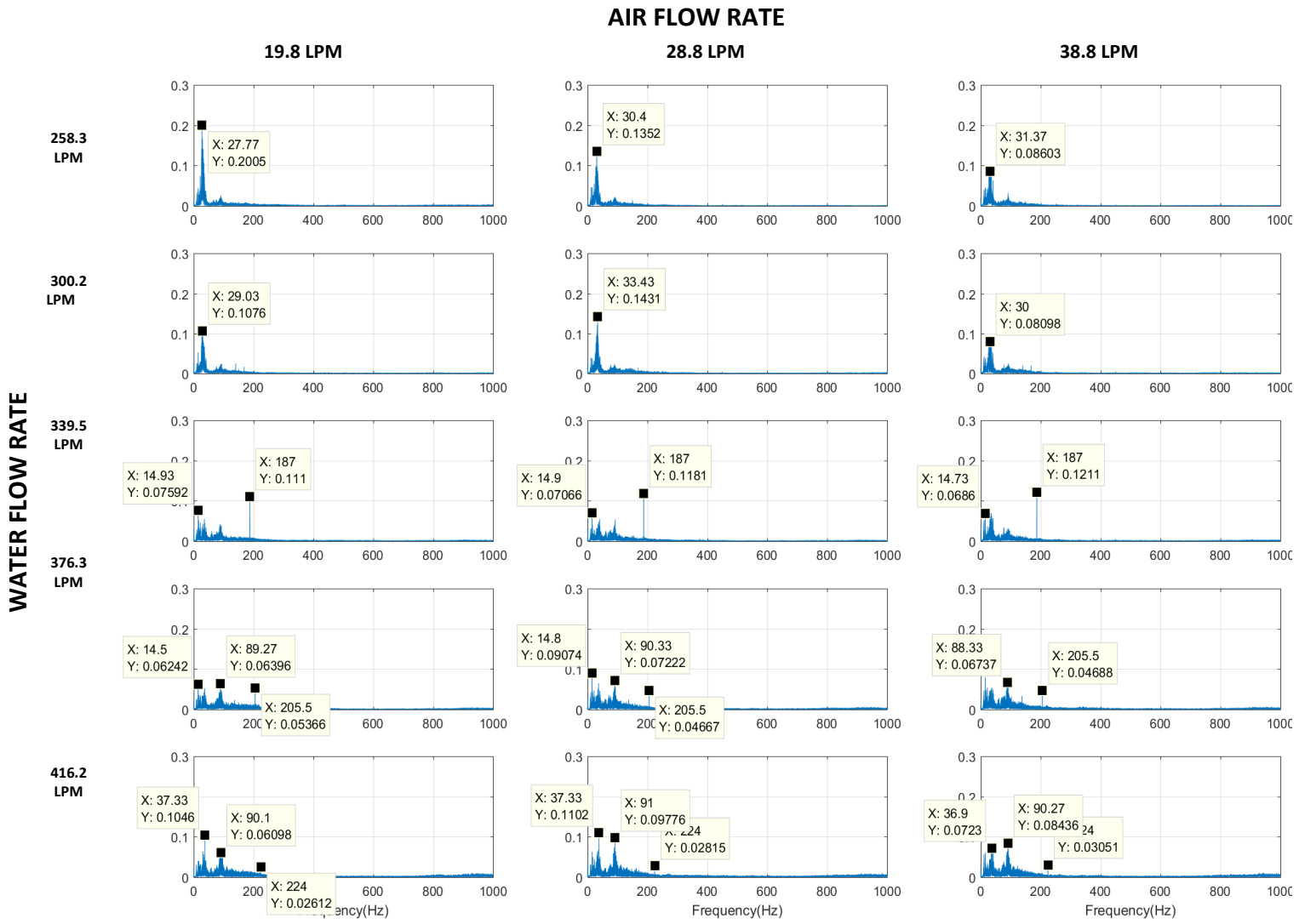


Figure 5.8. Multiphase vibration amplitude variation for the different flow rates at for water flow rate of (a) 60% (b) 80% VOP

As already mentioned, figure 5.8 (a) and (b) shows the vibration signal for the different water flow rate at 19.8, 28.8 and 38.8 LPM airflow for 60 and 80% VOP.

### 5.3.2 FREQUENCY DOMAIN ANALYSIS

Figures 5.9 (a) and (b) shows the FFT plots for various water flow rates at 60% and 80% VOPs respectively for the different airflow rates. The signal, again, has been sampled at 96 kHz. Figure 16 shows the FFT plot of the vibration signal for 0-1000Hz for 60 and 80% VOPs. The reason is that the dominant frequencies are observed within this region similar to that observed for single-phase flow conditions.



(a)



can be seen for both single and multiphase at around 40 and 150 Hz. For 80% VOP, the amplitude of the frequency components is seen to deviate for the different water flow rates by 64, 50, 63, 11 and 2.7% respectively at the 40 Hz frequency from single to multiphase (19.8 LPM airflow). For 150 Hz, the amplitude frequency components deviate by 19, 2.4, 79, 22.4 and 46% respectively. However, due to the injection of bubbles to create the multiphase condition, additional frequency component can be seen lower frequencies (between 0 to 10 Hz), where they are completely absent for single-phase.

These peaks are due to the air bubbles present in the flow. As the airflow rate increases, the peak amplitude increases because of the increase in air bubbles, which coalesce with each other or break into smaller bubbles. As a result, vibration increases. These also show how the flow behaves when transitioning from single to multiphase condition in terms of how much vibration is generated on the valve. A similar occurrence can also be seen for 60% VOP. For single and multiphase, similar peaks, but with higher amplitudes, occur at similar frequencies. For 258.3, 300.2, 339.6, 376.5 and 416.2 LPM water flow rates, frequency components occur at around to 26 and 180 Hz for both single and multiphase, with highest peaks occurring at 180 Hz. However, due to the injection of bubbles to create the multiphase condition, additional frequency component can be seen again at a lower frequency (around 15 Hz), where they are completely absent for single-phase. These components, from completely absent in single-phase to 0.2, 0.11, 0.07, 0.06 and 0.01mV for the different water flow rates. Increase in the water flow rate causes a reduction in amplitude at this frequency as seen in figure 5.9 (b). These values change as air bubble injection increases from 19.8 to 28.8 and to 38.8 LPM, causing the flow regime to change at these conditions.

Figure 5.10 shows the mean frequency for the vibration signals at multiphase conditions as a function of water and the airflow rate for 60% and 80% VOPs.

Figures 5.10 shows a clearer understanding of how much frequency exists in the signal spectrum for the multiphase flow conditions of the vibration signal by calculating the average frequencies. Figure 5.10 shows the vibration signal mean frequency at different water flow rates for (a) 60% VOP and (b) 80% VOP. Unlike single-phase, the introduction of air bubbles increases the vibration strength, thereby increasing the amount of power in the frequency spectrum, which has caused the mean frequency to increase significantly

across the spectrum for both 60 and 80% VOPs. For single-phase flow, an increasing trend was seen as the flow rate increase. For the multiphase condition, mean frequency drop slightly at higher flow rate across the different airflow rate for both VOPs.

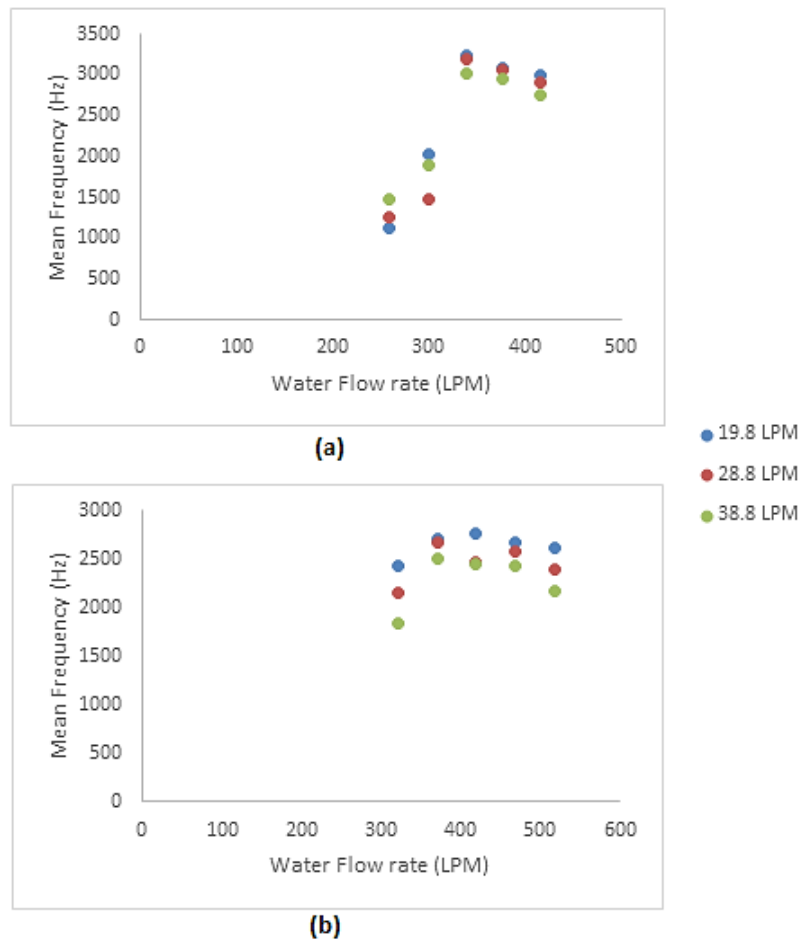


Figure 5.10: Vibration mean frequency for the valve at different flow rates for (a) 60% VOP, (b) 80% VOP.

This is because, for higher VOPs (60 and 80%), vibration strength decreases and higher flow rates for multiphase flow causes the power spectrum to decrease, making the mean frequency to decrease. For 60% VOP, across water flow rates of 258.3, 300.2, 339.6, 376.5 and 416.2 LPM, mean frequency increases from 758.2 Hz to 1136.6 Hz. This is from single phase to multiphase (19.8LPM), representing an increase in deviation of 33.3%. Across the remainder of the flow rates (300.2, 339.6, 376.5 and 416.2 LPM), the percentage variation increase observed were 40.2, 49.6, 33.3 and 5.8% respectively. From 19.8LPM to 28.8LPM, the frequency spectrum decreases, making the mean frequency to reduce. This is because of the increase in the air volume fraction (bubbles), causing the mean

frequency to reduce. It is however noticed that for the flow rate of 300.2 LPM, there is a slight increase in the mean frequency from 19.8 to 28.8LPM. This percentage decrease of about 9% can be because of one-off measurement uncertainty. For the remainder of the flow rates, the percentage increase variation are 27.8, 1.3, 1.9 and 2.8% respectively. Again, from 28.8 to 38.8LPM, mean frequency increase at lower flow (300.2 and 339.6LPM), the percentage increase observed were 17.9 and 28.7% respectively. For the remainder of the flow rates, the percentage decrease recorded were 5.6, 3.6 and 5.5% respectively.

At 80% VOP, from single to multiphase (19.8LPM), percentage increase recorded were 61.6, 57.2, 41.5, 19.7 and 14% respectively across the different flow rates. Mean frequency for 80% VOP experience a steady decrease across the different airflow rates, unlike for 60%. Mean frequency from 19.8 to 28.8 LPM for airflow rate reduces at the rate of 10.8, 1.4, 10.6, 2.8 and 8.6%. From 28.8 to 38.8 LPM, mean frequency again decreases for all water flow rates (321, 370, 418, 469 and 517 LPM) at percentage decrease variation of 14.9, 6.2, 1.1, 6.2 and 9.6% respectively.

After analysis have been carried out for single and multiphase flow for a healthy valve, the next two sections discuss the vibration characteristics for a faulty valve and comparisons made.

## **5.4 DEVELOPMENT OF VIBRATION INDICATOR FOR SINGLE PHASE FLOW CONDITION INSIDE A FAULTY CONTROL VALVE**

This section presents data analysis for a faulty valve and compares with that of a healthy valve. The control valve trim gave four flow paths as already described in chapter one. The faulty valve has been created by using a solid material to block one of the flow paths entirely. This blockage has had significant changes in the flow parameters, as would be seen in the analysis in section 5.4.1 and 5.4.2, affecting the vibration characteristics of the valve. The analysis has again be carried out in both time and frequency domain and their results compared to the healthy valve.

### **5.4.1 TIME DOMAIN ANALYSIS**

For the faulty vibration characteristics, like the healthy valve, a series of experiments have been performed and the data have been collected for the different flow and operating conditions and their results compared. For single-phase condition, the faulty

vibration signals have been analysed in time domain using statistical parameters such as RMS, peak-to-peak, kurtosis and Standard deviation. For faulty valve vibration analysis, only 60 and 80% VOPs have been analysed for different flow conditions.

Because of the blockage of one of the flow paths, vibration signal increases as the flow area reduced. This has caused more vibration as the same amount of water, passing through the entire trim for the healthy valve, also needs to pass through the same trim that has one path blocked.

The RMS values have been presented in figure 5.11, comparing both healthy and faulty vibrations signals for 60 and 80% VOPs at same pump flow rates.

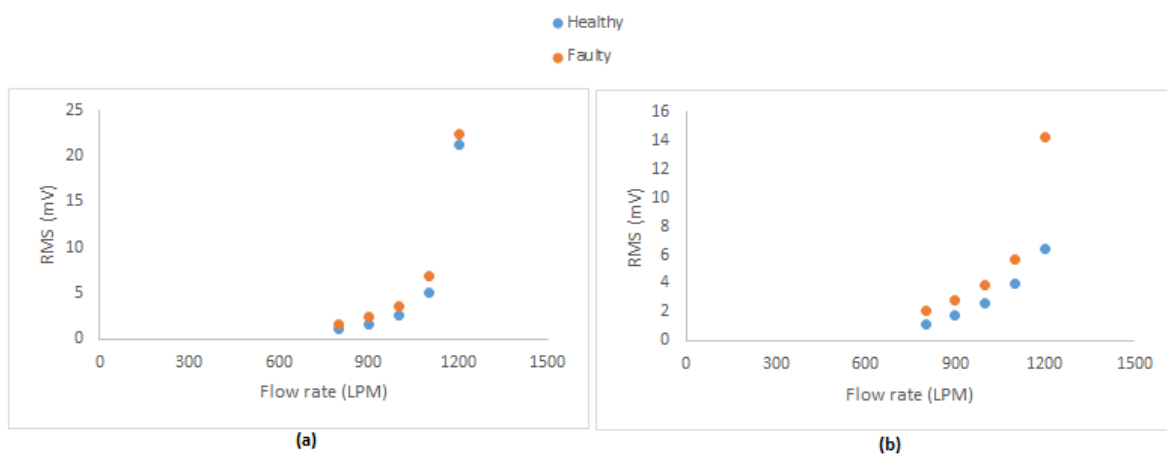


Figure 5.11: RMS value comparison between the healthy and faulty valve at different flow rates for (a) 60% VOP (b) 80% VOP

As seen in figure 5.11, the RMS value for the vibration signal increases for the faulty valve from healthy valve for the different flow and operating condition.

At 60% VOP, for healthy valve, the vibration signal observed for the RMS value are 1.02, 1.63, 2.5, 5 and 21.17mV for 800, 900, 1000, 1100, 1200LPM flow rates respectively. For faulty valve, the vibration amplitude, in the form of RMS value increases, from healthy valve condition, at 34.9, 32.9, 27.6, 27 and 5.3% for the different flow rates.

For 80% VOP, from 1.12, 1.76, 2.6, 3.9 and 6.39mV for healthy valve, RMS value increases at the rate of 44.8, 38.2, 32.2, 30.5 and 55.1% for the faulty valve.

Peak-to-Peak, standard deviation and Kurtosis comparison between the healthy and faulty vibrations signals for 60 and 80% VOPs at same flow rates have also been made. They show similar trends as seen in figure 5.11 for RMS values. Again, like for healthy valve, the SD deviation is the same as that of RMS values because the mean signal is equal to zero, already explained in the previous section of this chapter.

The next section analysed the healthy and faulty valve vibration signals and their analysis compared in frequency domain for single-phase flow.

#### **5.4.2 ANALYSIS IN FREQUENCY DOMAIN**

Again, for the faulty valve, analysis has been carried out for the same conditions as the healthy valve for the vibration signal, this time in frequency domain. When faults occur inside the valve, the frequency components changes. These changes are significant in the analysis of the vibration signal so that when the fault occur, they can be detected and acted upon. In this research, for faulty valve analysis in frequency domain, FFT and mean frequency has again been used.

##### **A. Fast Fourier Transform (FFT)**

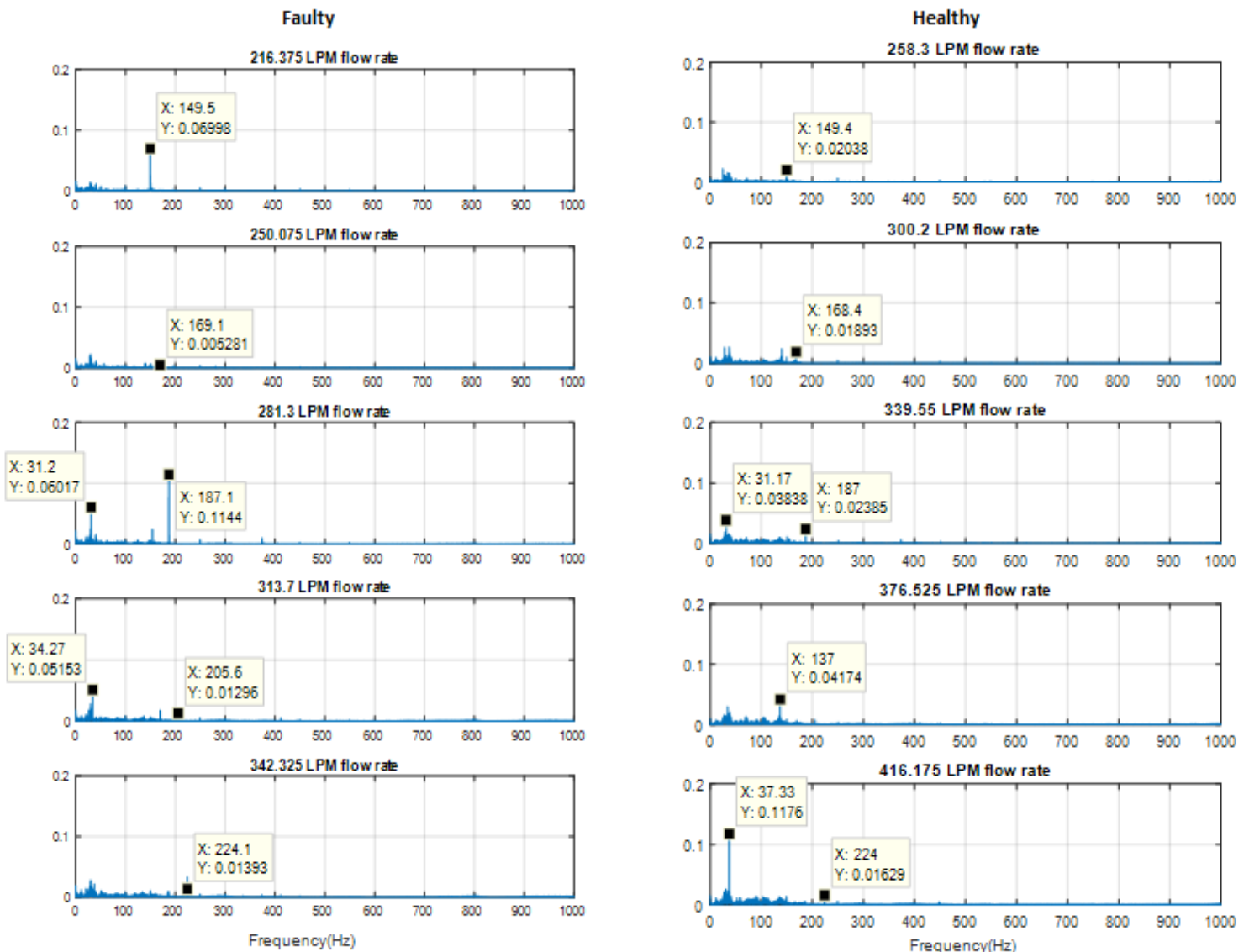
Figure 5.12(a) and (b) shows the FFT plots for the different flow rates at 60 and 80% VOPs. The signal has again been sampled at 96 kHz. Figure 5.20 shows the FFT plot of the signal for 0-1 kHz.

Figure 5.12 shows a better understanding of the dynamics of the faulty control valve as the vibration signals in time domain has been transformed into frequency domain. The peak amplitude is distinctively seen in the frequency range of 0-1000 Hz. As the flow rate increases, the peak amplitude increases.

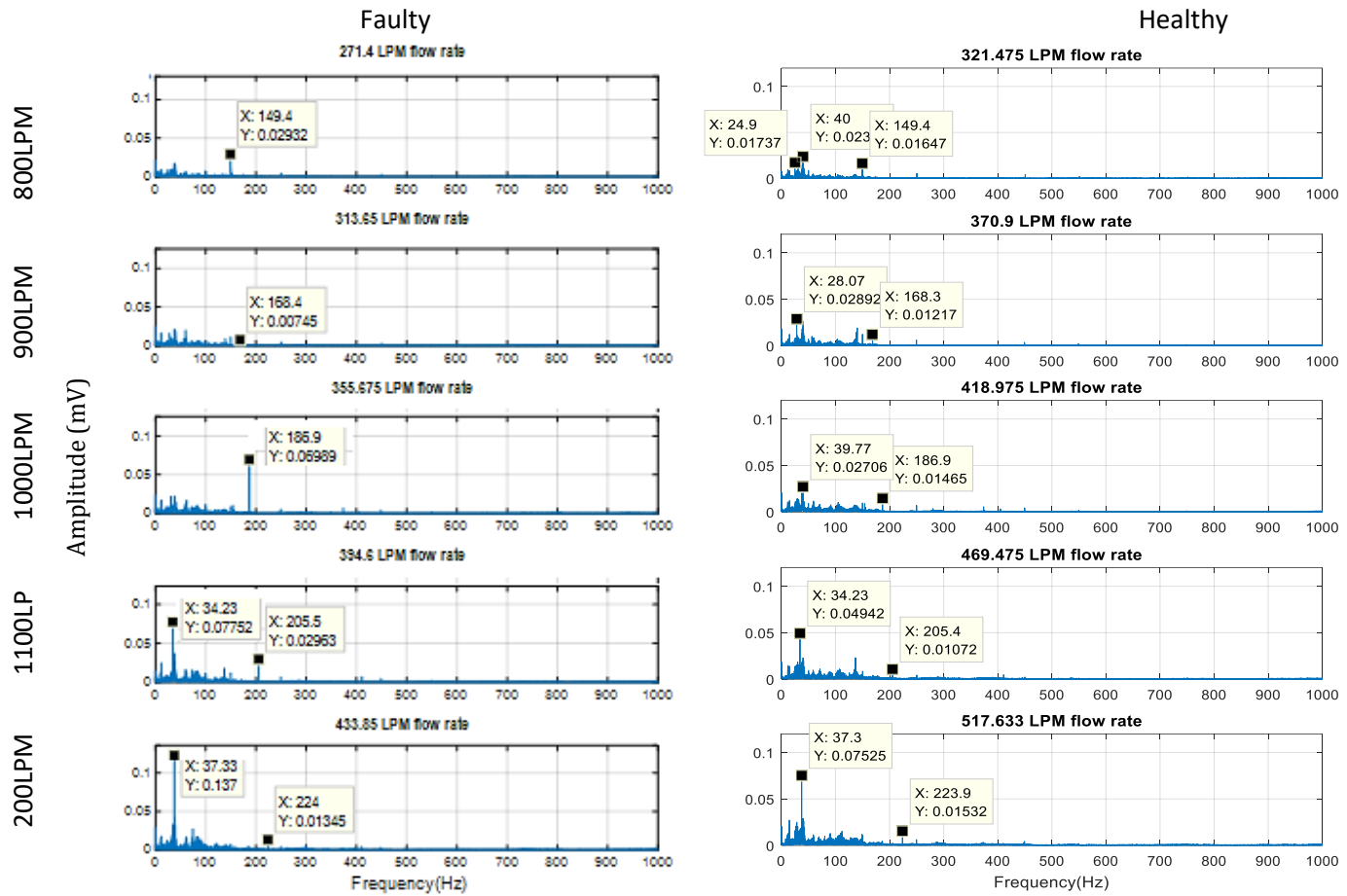
For 60% VOP, comparison has been made between faulty and healthy valve. At similar frequencies, the frequency components can be seen to increase for faulty valve condition from the healthy valve. Same set points and VOPs have been used for both faulty and healthy valve. For the same setpoints, because of the faults, the flow rate has dropped, causing changes to the flow parameters, including the vibration signatures. Ideally, for faulty valves, vibration components should increase, which is the case for most of the flow rates obtained for the faulty vibration signatures for both 60 and 80% VOPs.

The percentage frequency amplitude variation, from faulty to healthy valve, at same conditions 66.6, 72.2, 81.8, 36 and 18.7% respectively for 800, 900, 1000, 1100, 1200LPM.

At 80% VOP, the same trend is seen where faulty valve amplitude frequency increases from the healthy valve at the same flow and operating condition. The percentage variation for the different flow rates are 65.5, 30, 83.3, 65.5 and 42.3% respectively for the frequency amplitudes.



(a)



(b)

Figure 5.12. Vibration signal spectrum for the faulty and healthy valve at different flow rates (a) 60% (b) 80%

### B. Mean Frequency

Figure 5.13 shows the mean frequency from the vibration signatures for both healthy and faulty as a function of flow rate for 60 and 80% VOPs. It can be seen that across all VOPs, mean frequency can be seen to significantly vary as flow rates increase for both healthy and faulty valve. Healthy valve frequency spread across the entire frequency power spectrum of the signal, making the mean frequency very high. For faulty valve, vibration increases, making more of the vibration signal occurring at lower frequencies, hence lower mean frequencies across the flow rates.

For 60% VOP, the mean frequency is observed to decrease for the faulty valve condition from healthy valve at the rate of 73.5, 81.1, 87.5, 87 and 88% respectively across the different flow rates.

For 80% VOP, further decrease is also observed for the faulty valve condition from healthy valve for the mean frequency at the rate of 80.1, 83.7, 87.9, 92.5 and 93.6% respectively across the various flow rates.

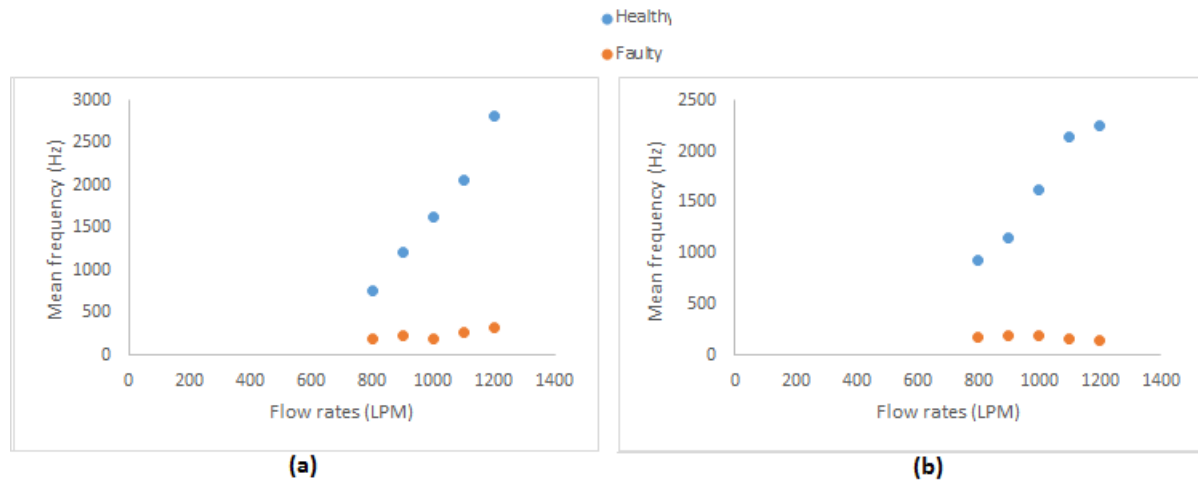


Figure 5.13. Mean frequency for the valve at different flow rates (a) 60% (b) 80%

## 5.5 DEVELOPMENT OF VIBRATION INDICATOR FOR MULTIPHASE FLOW CONDITION INSIDE A FAULTY CONTROL VALVE

This section presents data analysis for a faulty valve multiphase condition and compares with that of a healthy valve. The control valve trim have four flow paths as already described in chapter one. The faulty valve has been created by using a solid material to block one of the flow paths entirely. This blockage has had significant changes in the flow parameters, as would be seen in the analysis 5.5.1 and 5.5.2, affecting the vibration characteristics of the valve. The analysis has again be carried out in both time and frequency domain and their results compared to the healthy valve.

### 5.5.1 TIME DOMAIN ANALYSIS

For the faulty vibration characteristics, like for healthy valve, a series of experiments have been performed and the data have been collected for the different flow and operating conditions and their results compared. For single-phase condition, the faulty vibration signals have again been analysed in time domain using statistical parameters such as

RMS, peak-to-peak, kurtosis and Standard deviation. For faulty valve vibration analysis, only 60 and 80% VOPs have been analysed for different flow conditions.

Because of the blockage of one of the flow paths, vibration has increased as the flow area reduced. This has caused more vibration as the same amount of water, passing through the entire trim for the healthy valve, also needs to pass through the same trim that has one path blocked.

The RMS values have been presented in figure 5.14, comparing both healthy and faulty vibrations signals for 60 and 80% VOPs at the same pump flow rates.

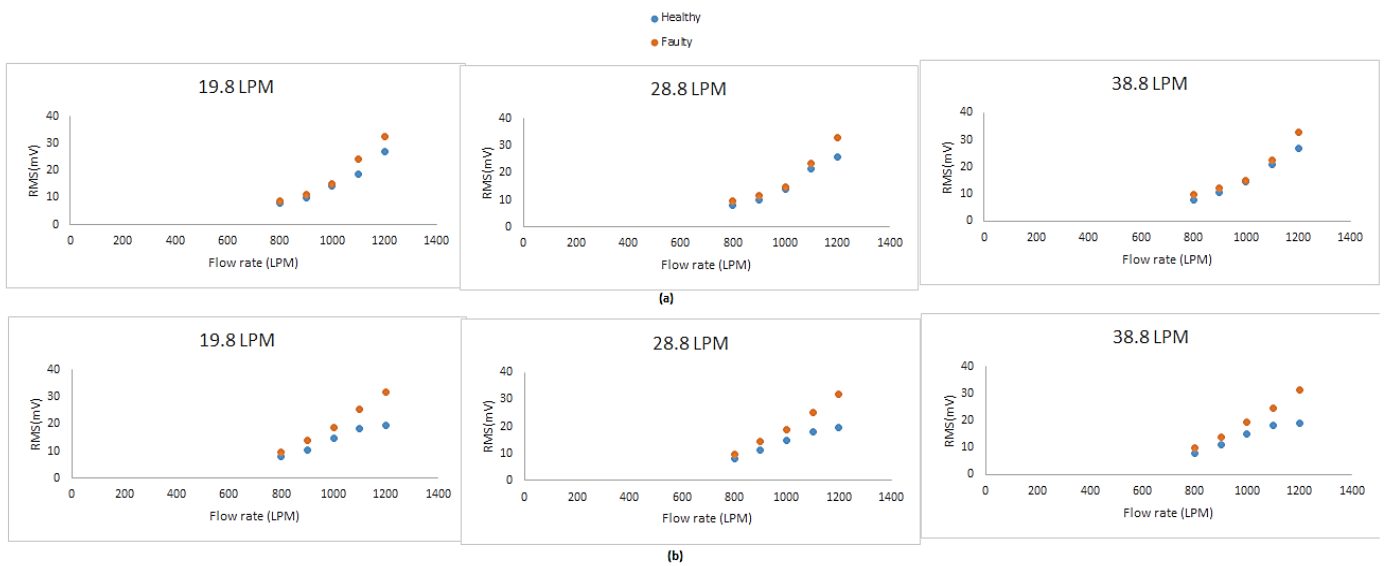


Figure 5.14: RMS value comparison between a healthy and faulty valve at different water flow rates for (a) 60% VOP (b) 80% VOP at 19.8, 28.8 and 38.8 LPM airflow rate

As seen in figure 5.14, the RMS value for the vibration signal for the different multiphase flow rates increases for faulty valve from the healthy valve for the different flow and operating condition.

At 60% VOP, for healthy valve, the vibration signal observed for the RMS values are 7.8, 10, 14.1 18.8 and 27.1mV for 800, 900, 1000, 1100, 1200LPM respectively at 19.9LPM airflow rate. For multiphase faulty valve, the vibration amplitude, in the form of RMS value increases, from healthy valve condition, at 11.6, 9.6, 5.7, 21.6 and 16.8% for the different flow rates at 19.8LPM airflow. At 28.8LPM airflow, the percentage increase from healthy to the faulty valve for the different water flow rates are 13, 15.1, 4.8, 7.9 and

21.3% respectively. For 38.8LPM airflow from the healthy valve, the percentage increase recorded are 17.4, 11.1, 3.3, 6.5 and 17.8% respectively.

For 80% VOP, from 8.02, 10.4, 14.9, 18.2 and 19.5mV for healthy valve, RMS multiphase value increases at the rate of 16.2, 25.4, 20.3, 28.3 and 38.8% for the faulty valve at 19.8LPM airflow rate. At 28.8LPM airflow, the percentage increase from healthy to faulty valve for the different water flow rates are 16, 22.9, 19.6, 27.5 and 38.5% respectively. For 38.8LPM airflow from healthy to faulty valve, percentage increase recorded are 18.1, 20.8, 21.8, 26.3 and 39.4% respectively.

Again, peak-to-peak, kurtosis and standard deviation comparisons between the healthy and faulty vibrations signals for 60 and 80% VOPs at different water and air flow rates have been analysed. They all show similar trends as that of RMS as depicted in figure 5.14. They however does not give more details as to fault detection in the vibration signals.

The next section analysed the healthy and faulty valve vibration signals and their analysis compared in frequency domain for multiphase flow as they give clearer analysis and indication of the fault.

### 5.5.2 ANALYSIS IN FREQUENCY DOMAIN

Multiphase analysis has been carried out for the same conditions as the healthy valve for the vibration signal in frequency domain. When faults occur inside the valve, the frequency components changes. These changes are significant in the analysis of vibration signal, so that when they occur, they can be detected. Again, FFT and mean frequency have been used.

#### A. Fast Fourier Transform (FFT)

Figure 5.15(a) and (b) shows the FFT plots for the different flow rates at 60 and 80% VOPs. The signal has been sampled at 96 kHz. Figure 5.25 shows the FFT plot of the signal for 0-1 kHz.

Figure 5.15 shows a better understanding of the dynamics of the faulty control valve as the vibration signals in time domain has been transformed into frequency domain. The peak amplitude is distinctively seen in the frequency range of 0-1000 Hz. As the flow rate increases, the peak amplitude increases.

For 60% VOP, comparison between faulty and healthy valve has been made. As said earlier, extra vibration, for the multiphase condition are seen between 0-40Hz. Because these vibrations are as a result of the pump rotation speed, the amplitude for the faulty valve is lesser at these frequencies when compared to that of the healthy valve, because of the lower flow rates obtained for the faulty condition caused by the fault created. From figure 5.15, the percentage increase observed for faulty to healthy valve condition are 36, 6.25, 32.4, 16.2 and 20% respectively for the different flow rates. Comparison between the healthy and faulty valve for the same condition can be seen in figures 5.15 and 5.16. Vibration signatures because of the valves' vibration can be seen at 149.4, 168.4, 187, 205 and 223Hz for the different flow rates under each condition can be seen. Figure 5.15 shows 19.8LPM airflow for the healthy and faulty valve. As said earlier, extra vibration components are seen at very low frequencies due to air injection. The amplitude at these frequencies have been compared for both faulty and healthy valve. Comparing at 19.8LPM, at similar frequencies, the amplitude at those frequencies have a percentage variation increase from healthy to faulty at the rate of 50, 39.1, 82.9, 56.7 and 60.2% respectively for the different water flow rates. At 28.8LPM airflow, 7.6, 7.1, 12.5, 1 and 12.5% respectively have been observed for the different flow rates from the healthy to faulty valve. For 38.8LPM airflow, 38.4, 42.8, 33.3, 14.2 and 30% respectively have been observed from healthy to faulty valve condition.

For 80% VOP, figure 5.16 shows 28.8LPM airflow for the healthy and faulty valve. As said earlier, extra vibration components are seen at very low frequencies due to air injection. The amplitude at these frequencies has been compared for both faulty and healthy valve. Again for all the air and water at the different VOPs (60 and 80%), the amplitude between 0-40Hz is higher for the faulty condition when compared to the healthy valve condition. Again, vibration as a result of the valve can be seen at around 149.4, 168.4, 187, 205 and 223Hz across the different flow rates. Comparing at 19.8LPM, at similar frequencies, the amplitude at those frequencies have a percentage variation increase from healthy to faulty at the rate of 26.6, 1.7, 24.4, 69.2 and 30% respectively for the different water flow rates. At 28.8LPM airflow, 28.1, 30, 32.6, 1 and 40.6%, respectively for the different flow rates. For 38.8LPM airflow, 12.5, 22.8, 36, 23 and 1% respectively have been observed from healthy to faulty valve condition.

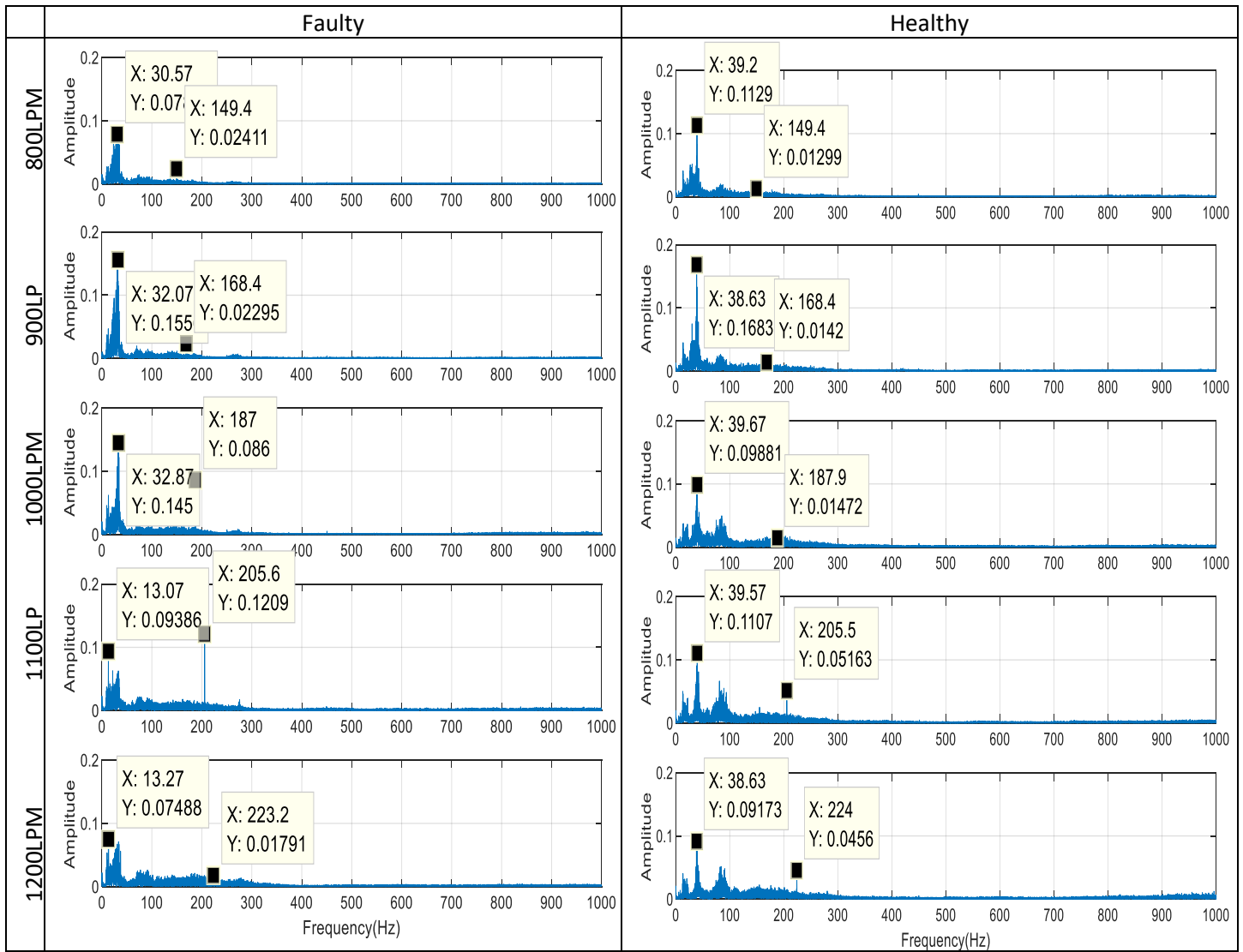


Figure 5.15: FFT for 19.8LPM airflow, comparing healthy and faulty valve at different water for 60% VOP

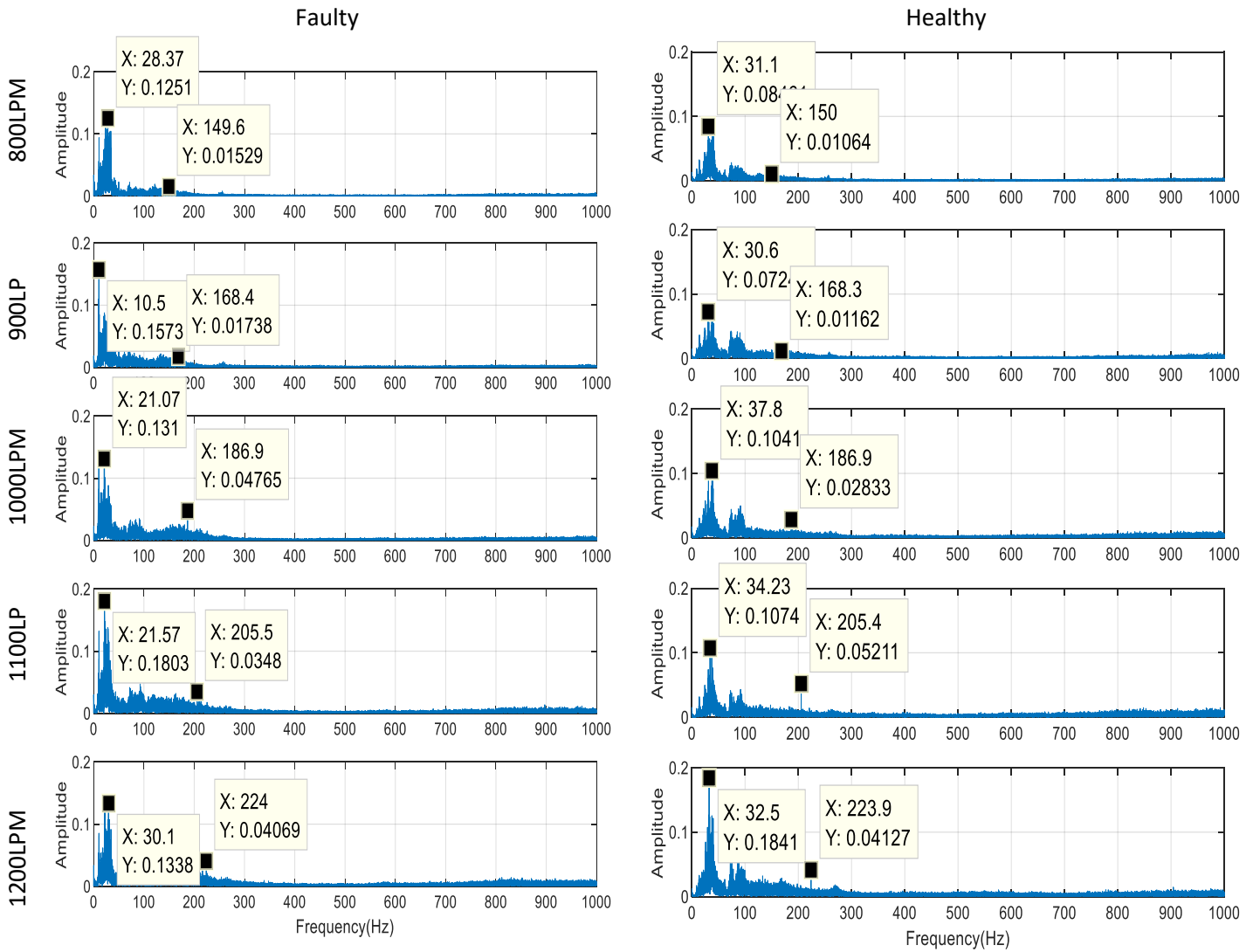


Figure 5.16: FFT for 28.8LPM airflow, comparing healthy and faulty valve at different water for 80% VOP

### B. Mean Frequency

Figure 5.17 shows the mean frequency from the vibration signatures comparison between healthy and faulty control valve as a function of flow rate. Again, higher frequency components are found at lower frequencies, making the mean frequency to be far less than for healthy valve, across both VOPs. While FFT comparison shows what component are on each frequency and how much amplitude they have, the mean frequency shows the average frequency for the signal across the frequency spectrum. Figure 5.17 (a) and (b) shows the healthy and faulty valve mean frequency for the different flow rates at 60 and 80% VOPs respectively.

For 60% VOP, the multiphase mean frequency decreases from healthy to the faulty valve for all flow rates. Mean frequency decreases at 93, 96.2, 96.3, 90.6 and 90.66% respectively across the different flow rates for 19.8LPM airflow. At 28.8LPM airflow, from healthy to faulty valve, multiphase mean frequency decreases at the rate of 93.9, 93, 96.7, 93.8 and 89.19% respectively for the different water flow rates. At 38.8LPM, the percentage variations decrease observed for faulty valve from healthy valve are 95.1, 94.6, 96.6, 93.8 and 93% respectively.

For 80% VOP, the multiphase mean frequency decreases from healthy to faulty valve for all flow rates. Mean frequency for the multiphase flow comparison, between healthy and faulty vibration signal for the valve decreases at 95.5, 89.6, 90.4, 86.7 and 75.4% respectively for the different water flow rates at 19.8LPM airflow. At 28.8LPM, airflow, from healthy to faulty valve, the multiphase mean frequency decreases at the rate of 95.3, 90.1, 88.9, 88.7 and 82.6% respectively for the different water flow rates. At 38.8LPM, the percentage variations decrease observed for faulty valve from healthy valve are 95.5, 92.3, 90.8, 87.6 and 84.6% respectively.

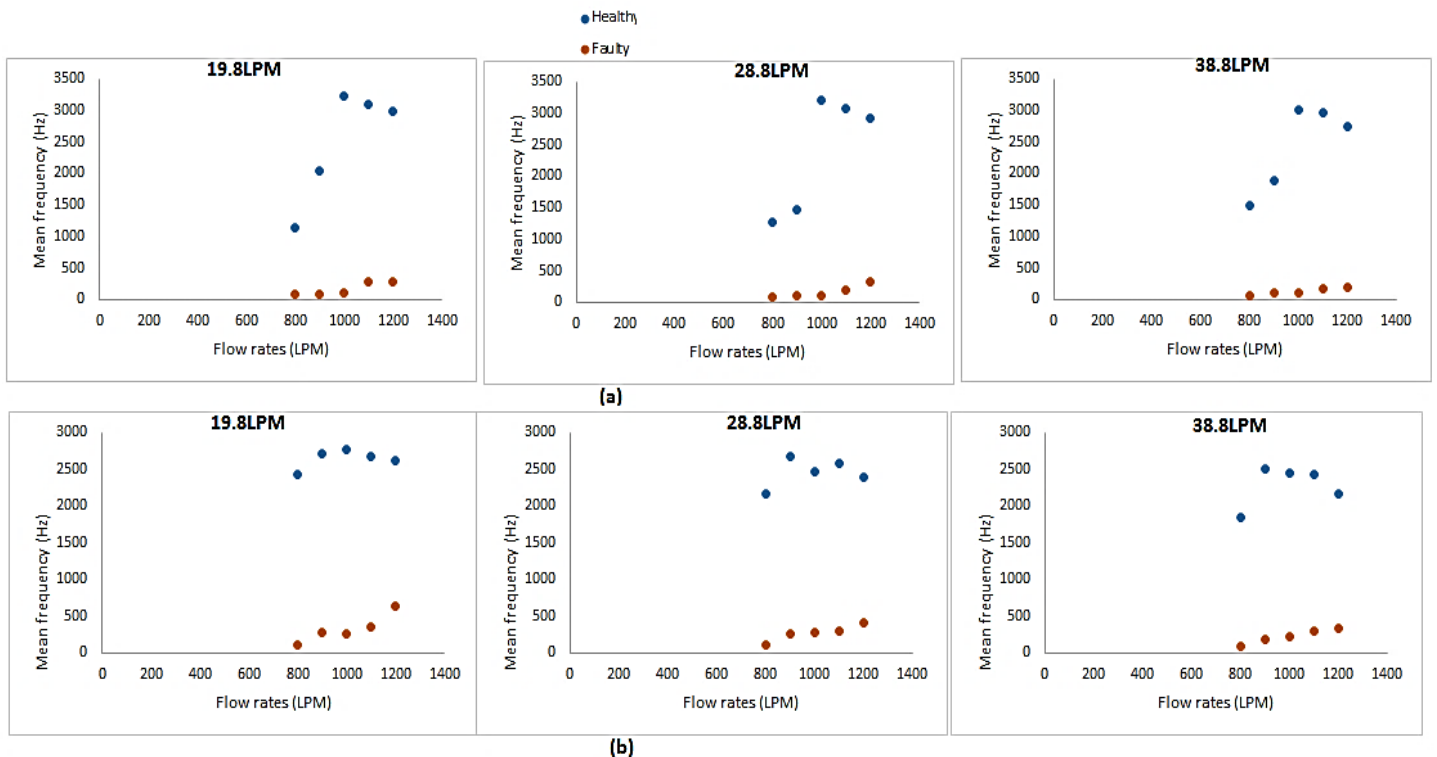


Figure 5.17. Mean frequency comparison for healthy and faulty valve condition at different flow rates (a) 60% (b) 80%

## 5.6 SUMMARY

This chapter has established the vibration behaviour of the control valve for different flow and operating condition and for single and multiphase conditions, and using vibration indicators in detecting faults when they occur. The advantages of the vibration technique have been described with setbacks that are likely to occur. It has also been seen that the probe placed at various heights and lengths inside the valve do not effect the vibration characteristics when flow and operating conditions remains the same. The vibration signals have been analysed for different flow and operating conditions in both time and frequency domain, using RMS, peak to peak, kurtosis and standard deviation in time domain, FFT and mean frequency in frequency domain. The results have also been analysed for single and multiphase flow and the flow regime change from single to multiphase have been established for different flow rates and VOPs. Multiphase flow has been created by injecting air at different airflow rates.

Finally, faults have been created inside the valve, where vibration indicators have been used to distinguish the faulty valve from healthy valve condition and to establish how their vibration behaviour changes with such indicators and how this technique can be used to detect such faults.

## CHAPTER SIX

### 6.0 ACOUSTIC BEHAVIOUR OF THE VALVE UNDER VARIOUS FLOW CONDITIONS FOR SINGLE PHASE AND MULTIPHASE FLOW

---

*This chapter establishes acoustic signals for the control valves to easily identify and evaluate the valve performance when incipient faults occur while in their early stage of development under normal operating conditions. Using acoustic signatures behaviours from the microphone can establish how the flow should behave under such conditions. Results obtained from both time and frequency domain in achieving a holistic understanding regarding fault detection have been analysed on the valve. Also in this chapter, different flow and operating conditions effect on the valve such as various flow rates, various VOPs, air injection and probe lengths and heights have been investigated and established, using several statistical features in both time and frequency domain. For cross-referencing ease, this chapter follows the same structure as in Chapter 5.*

## 6.1 ADVANTAGES AND DISADVANTAGES OF USING ACOUSTIC TECHNIQUE

One key advantage of using acoustic signals is that they are airborne, making the microphone sufficient in capturing this type of signal. Microphones can be relatively quick and easy to replace when any change is required and can be installed remotely, unlike pressure sensors and accelerometers. Another advantage is that they can be very sensitive in capturing acoustic signals, real-time condition monitoring, and can detect any faults or defects on any machine that they are being used [100, 101, 102, 103, 104]. Both analyses in time and frequency domain of airborne signals have been known to give vital information and detect the onset or severity of faults in control valves.

However, microphones can tend to be a little expensive when compared to accelerometers.

In a typical industrial environment, acoustic signals are likely to be contaminated by the background noise from their environment. In practice, it is highly likely that noise from the environment would require measures such as the enclosure of noisy centrifugal pump that can likely cause interference with the measured signal data.

## 6.2 ESTABLISHING FLOW CHARACTERISTICS FOR SINGLE PHASE FLOW CONDITION INSIDE A HEALTHY CONTROL VALVE

Again, unlike with the pressure probes where local flow parameters are being analysed, flow parameters inside the flow field can vary (sometimes slightly) for what the probe measures at different heights and lengths. Again, like the vibration signal analysis in chapter 5 and  $C_v$  in chapter 4, which is a global performance parameter measured from static pressure at 2D and 6D, the different pressure probe heights and lengths does not have any effect on the  $C_v$  and vibration signals as they remain the same as long as the flow and operating conditions are the same.

### 6.2.1 TIME DOMAIN ANALYSIS

Again, before analysing the acoustic signals for the different flow and operation conditions in this chapter, again figure 6.1 and 6.2 establishes the similarity in the acoustic signal for different heights of same probe length and again for different probe lengths of same height respectively, with a similar or same flow and operating condition.

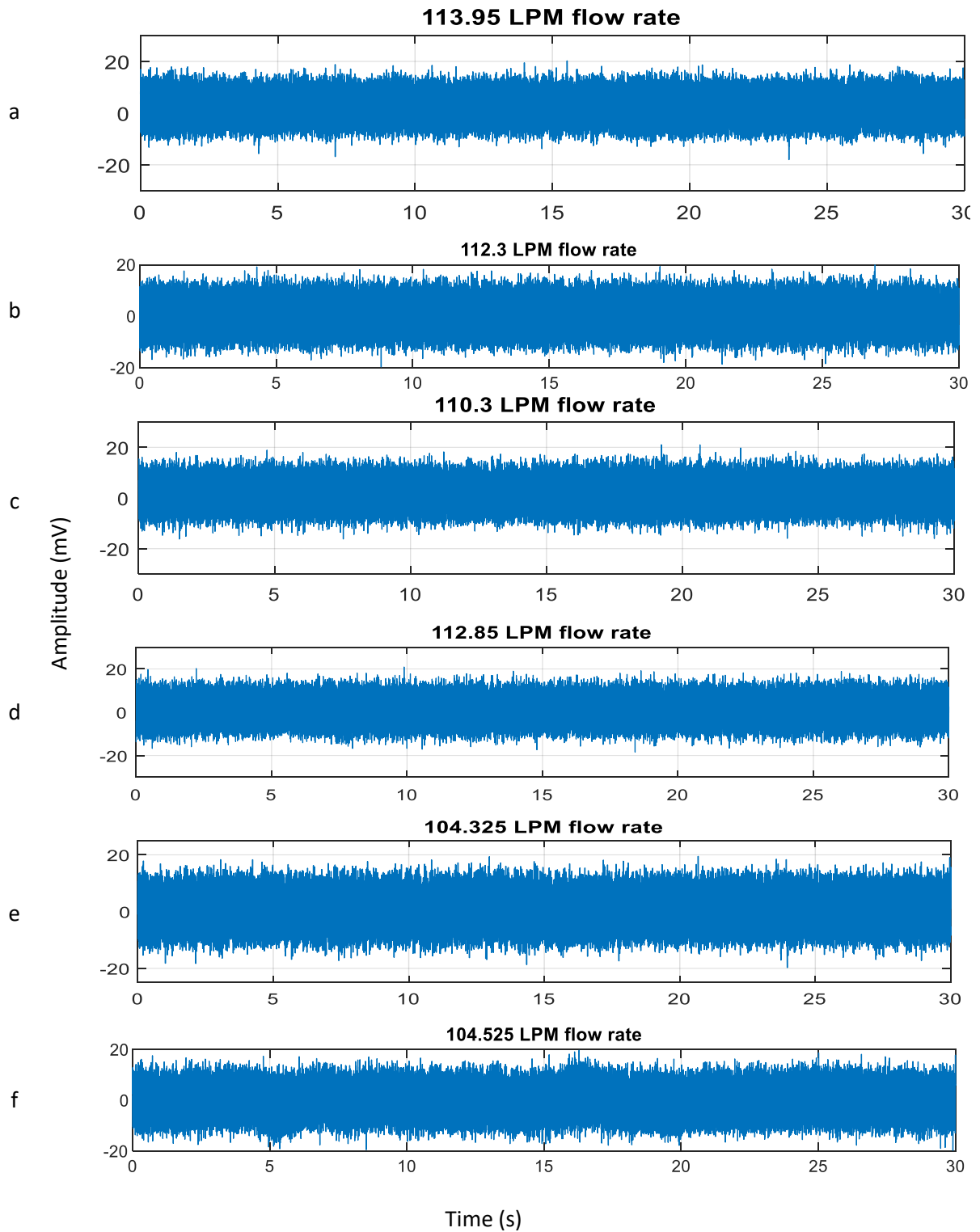


Figure 6.1: Acoustic signals for various probe height for the same length 1 probe position (a) Height 1 (b) Height 2 (c) Height 3 (d) Height 4 (e) Height 6 (f) Height 7

As said earlier, the probe inside of the valve does not have effect on the global acoustic signatures of the control valve. It is seen from figure 6.1 that the acoustic amplitude are similar for the same height at different probe lengths. This has shown that the acoustic

features will also be similar in both time and frequency domain even though there are slight differences in flow rates, which fall between 104 and 113.95LPM. The various flow rates have again, been chosen for convenience to demonstrate the acoustic signatures as the flow rate changes. The flow condition used for figure 6.1 are 20% VOP, running at 800LPM pump setpoint. The RMS values, which signifies the strength of the acoustic signals, are 4.27, 4.37, 4.17, 4.13, 4.03 and 4.52mV for height 1, height 2, height 3, height 4, height 6 and height 7 respectively. Figure 6.2 depicts the similarity in the acoustic signatures for same probe height positions at different probe lengths.

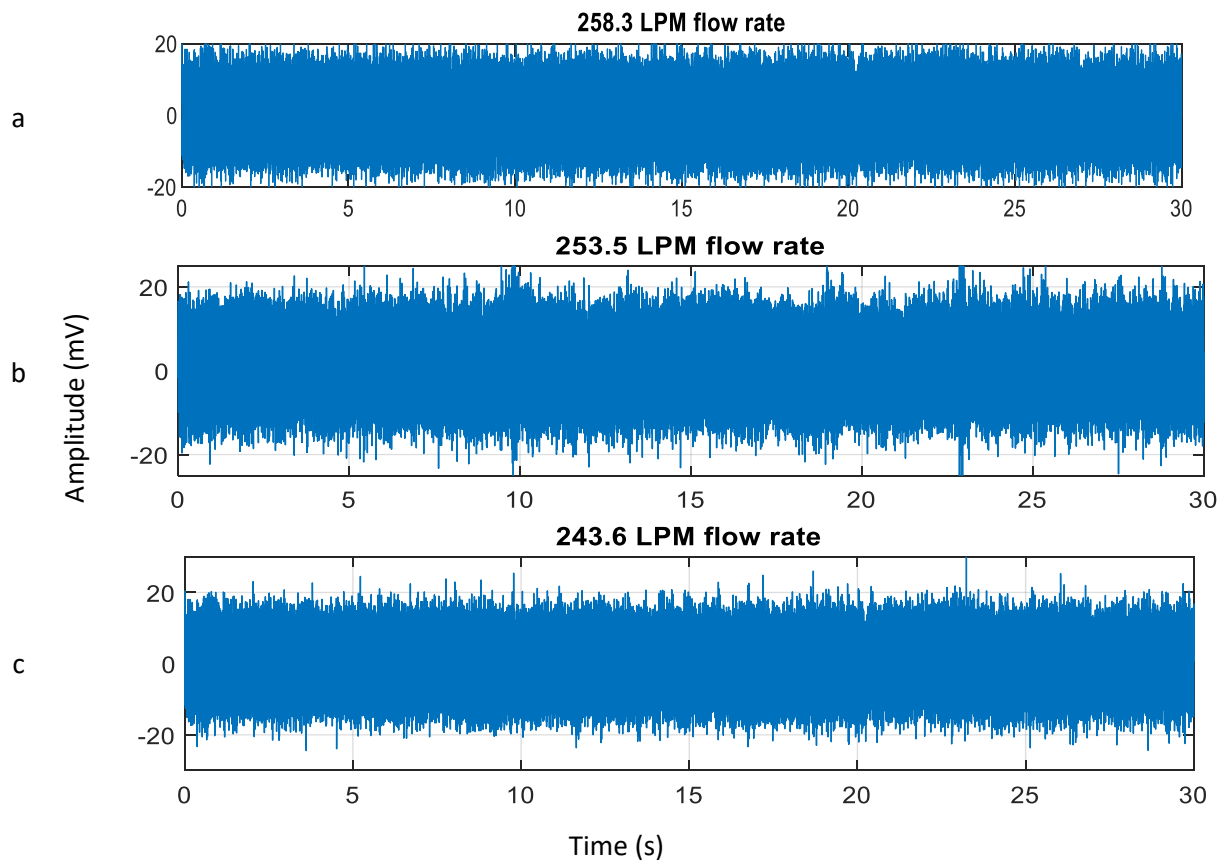


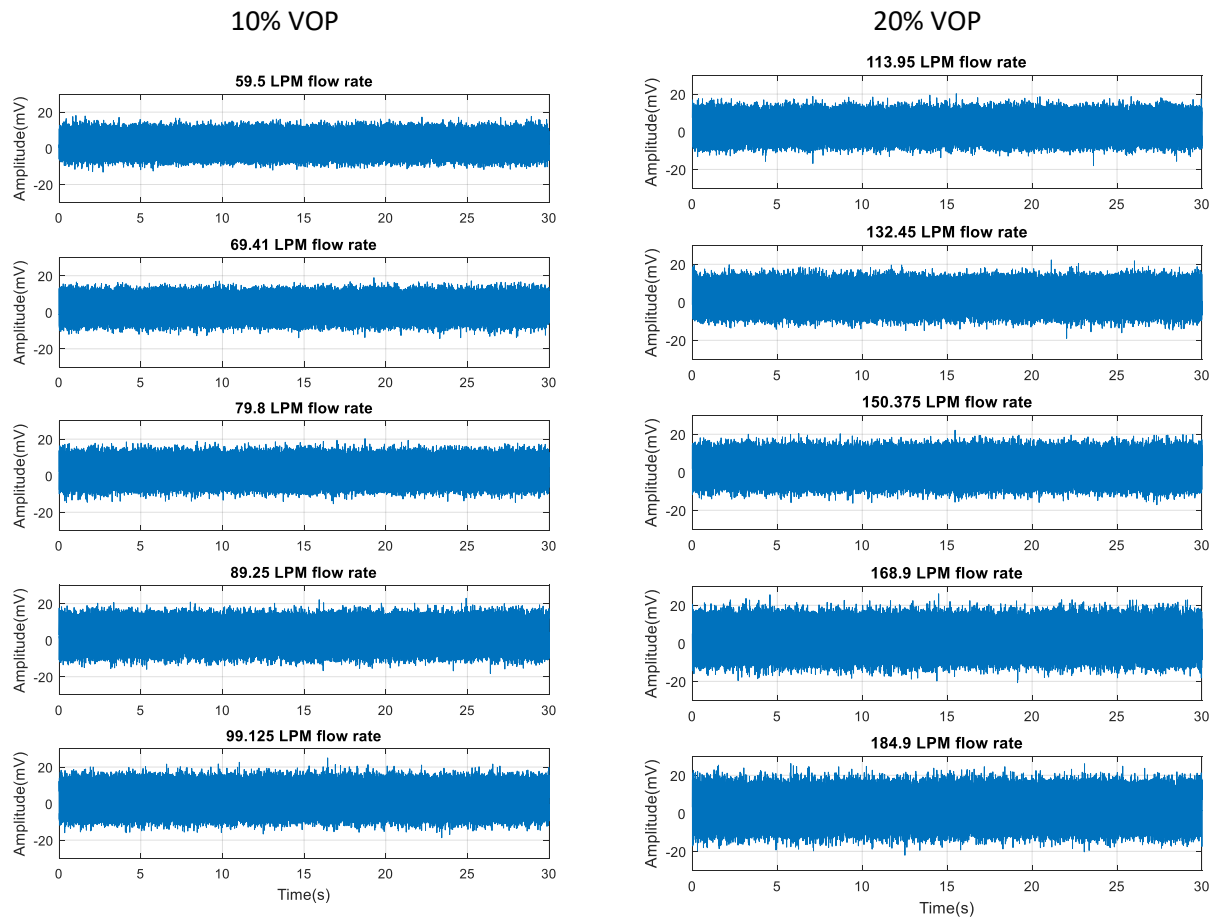
Figure 6.2: Acoustic signal amplitude similarities for same probe height and different probe lengths (a) length 1 (b) length 2 (c) length 3

The acoustic signal seen in figure 6.2 has been taken for 60% VOP and at 800 LPM pump set points for the different probe lengths. The RMS values, which again signifies the strength of the vibration signals are 5.48, 5.16 and 5.15mV for length 1, length 2 and length 3 respectively.

Time domain and frequency analysis for both the healthy and faulty valve would be used in determining the valve conditions using the acoustic monitoring technique. In the

following section, statistical parameters again such as RMS value, Peak-to-peak, standard deviation and kurtosis are analysed to identify trends of acoustic signals in time domain. Five different VOPs (10, 20, 40, 60 and 80%) have again been used in this research at different flow rates because of different pump set points, which are 800, 900, 1000, 1100, and 1200 LPM.

### 6.2.1.1 RAW ACOUSTIC SIGNALS



ESTABLISHING ACOUSTIC BEHAVIOUR OF THE CONTROL VALVE UNDER VARIOUS FLOW CONDITIONS



Figure 6.3: Single-phase raw acoustic signals for varying flow rates at different VOPs

The raw acoustic signals for the different flow rates, for all the various VOPs have been depicted in figure 6.3. The figure shows the relationships that exists between time and the acoustic amplitude for various flow rates. At the different VOPs, the acoustic signatures increases slightly as the flow rate increases. The acoustic signals have again been taken for a 30 seconds sampling time and a sampling frequency of 96 KHz. Similar conditions and analysis used in chapter five have also been used in this chapter for the acoustic signals. The next section presents the analysis for the different statistical features used previously in chapter five.

### 6.2.1.2 VARIOUS STATISTICAL PARAMETERS

#### A. RMS Values

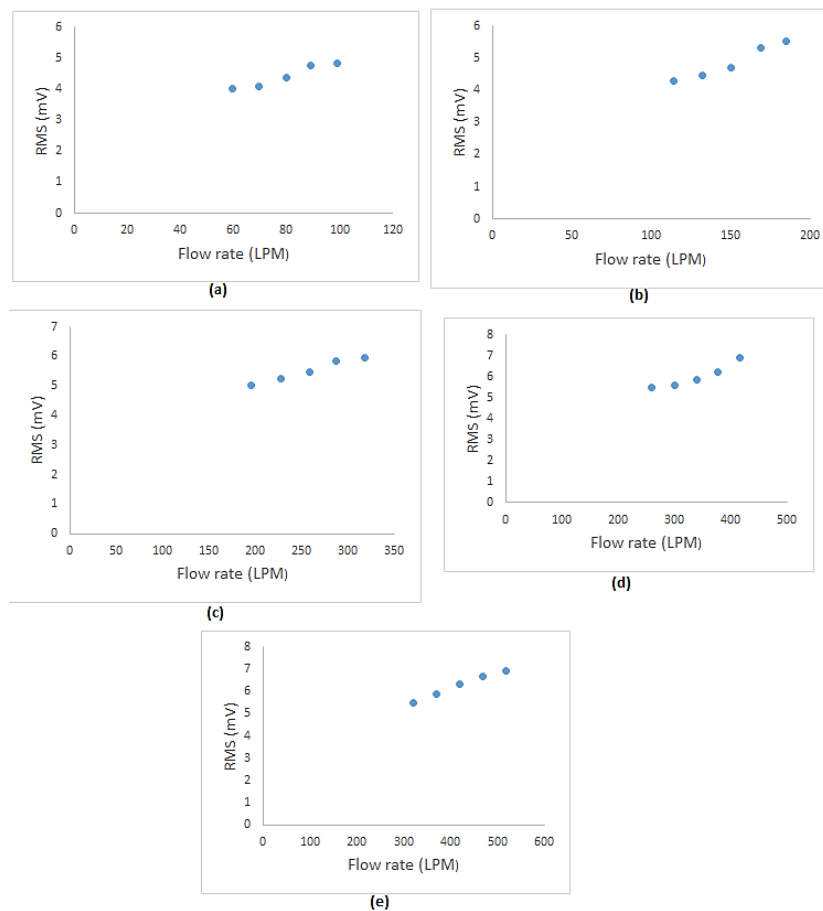


Figure 6.4: RMS variation for various flow rates at the different VOPs (a) 10% VOP (b) 20% VOP (c) 40% VOP (d) 60% VOP (e) 80% VOP

RMS shows the level of acoustic signal produced at the valve, indicating the signal strength. Therefore, at any flow changes that affect the valve, the RMS of the acoustic

signal will change. Figure 6.4 shows the RMS values variation for the various flow rates at 10, 20, 40 60 and 80% VOPs. The figure show an increasing trend for RMS at all the different VOPs as the flow rate increases.

As VOP increases, RMS of the acoustic signal increases. This is because the level of acoustic strength increases as the flow passage area (VOP) experienced during the experiments increases. The trends for RMS is seen because acoustic amplitude increase as flow rates increases as shown in figure 6.3. For 10% VOP, acoustic signal in mV increases by 2.2% from 4mV, as flow rate increases from 59.5 to 69.4 LPM. As flow rate increases to 79.8, 89.1 and 99.1LPM, percentage variation increase observed at these flow rates are 6.1, 8.2 and 1.6% respectively.

20%, 40%, 60% and 80% VOPs for the RMS value show an increase in the signal strength as the VOP increases.

Peak to Peak, standard deviation and Kurtosis analyses have also been conducted as they show similar trends. Kurtosis however, for the acoustic signal, unlike the vibration signal, are close to the normal distribution as the kurtosis values obtained are around 3 with slight variations. Higher kurtosis values signify that there are more peaks that are greater than  $3\sigma$  (peaks greater than 3 times the RMS). The drop in kurtosis values simply means that the number of peaks present in the signal for the maximum flow rate drops, hence there is a drop in kurtosis value [112] for the different flow rates from 60% at the rate of 0.2, 5.8, 8.2, 7.9 and 0.49% respectively.

After time domain analysis have been carried out for single-phase condition, for a healthy valve, the next section presents analysis carried out on acoustic signal in frequency domain using FFT and mean frequency.

### 6.2.2 ANALYSIS IN FREQUENCY DOMAIN

As mentioned earlier, the acoustic amplitude level of the signal depends on the operating and flow conditions inside the control valve. The results seen from analysis in time domain showed that when the valve is operated under low VOP and lowest flow rate, minimum level of acoustics occur. When the control valve is working at higher VOPs and maximum flow rates, higher level of acoustics occur. This can be attributed to several reasons; one is because of impeller blades interaction within the pumps. Another reason

is the increase in turbulent flow inside the valve, which causes the acoustic level to rise. One other key reason is the flow passage area due to the VOPs causing increase in the flow rate and sound levels.

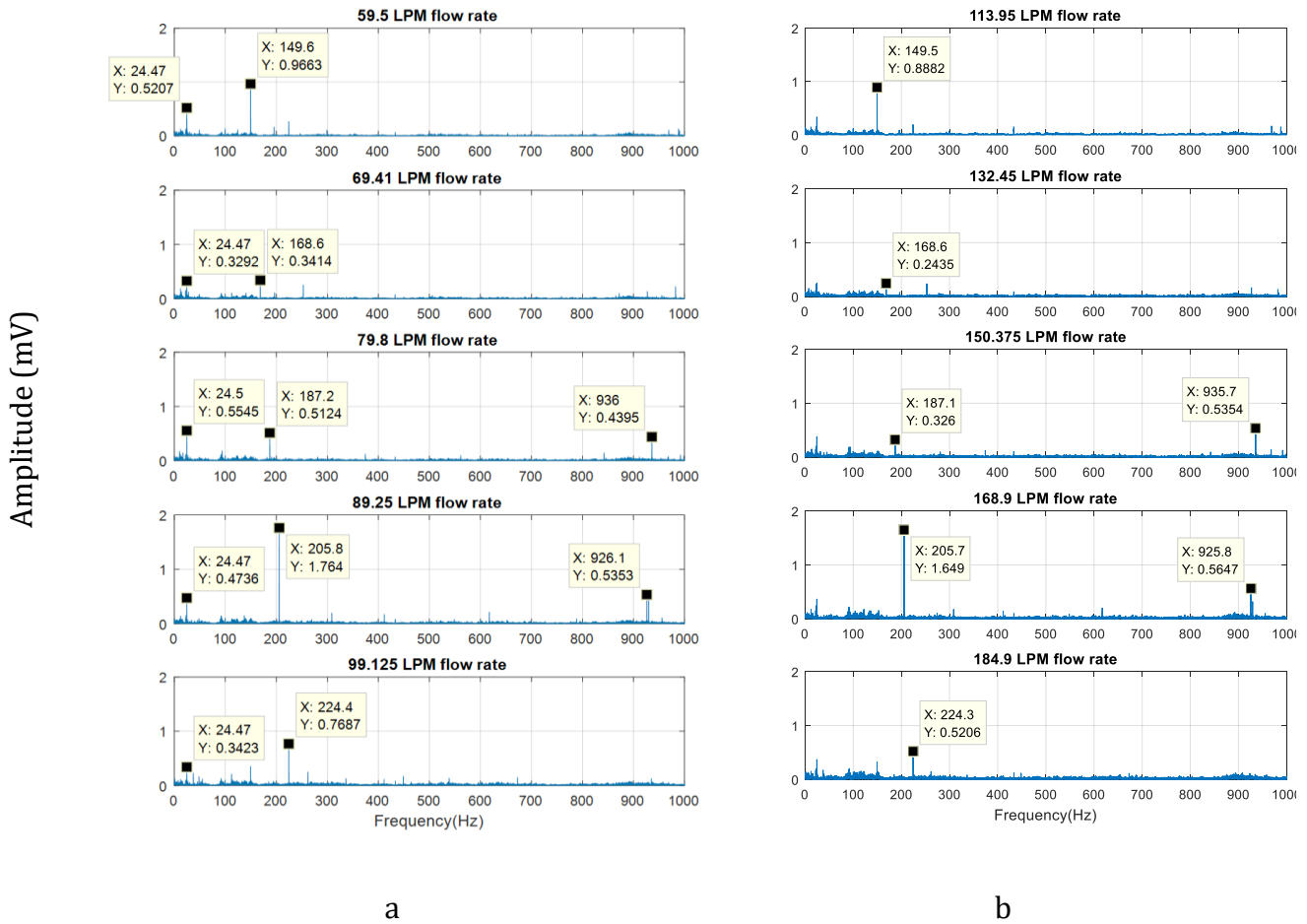
### A. Fast Fourier Transform (FFT)

An FFT plot displays the frequency components that are present in the acoustic signal. It shows how much power is present at a particular frequency. If the acoustic signal increases, the magnitude of that particular frequency component will increase. So for this section, FFT has been used to see how the magnitudes of these frequency components change when the flow regime changes, and by how much they increase or decrease. Figure 6.5 shows the FFT plots for the different flow rates at 10, 20, 40, 60 and 80% VOPs. The signals have again been sampled at 96 kHz. Figure 6.5 shows the FFT plot of the signal for 0-1 kHz.

Figure 6.5 shows a better understanding associated with the dynamics of the control valve, as the acoustic signals in time domain have been transformed into frequency domain using FFT. The peak amplitude can be seen distinctively in the frequency range of 0-1000 Hz. As the flow rate increases, the peak amplitude increases.

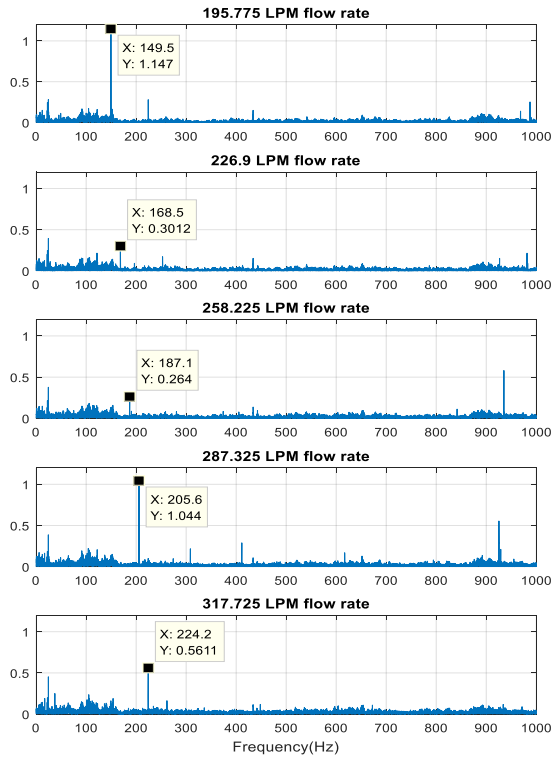
This increase in acoustic amplitude is because of flow rate increase. Regardless of the VOP, the amplitude peaks for the different flow rates occur at similar frequency and at similar pump rotation speed. They show the discrete characteristic components that are present within the entire frequency spectrum causing the flow periodicities, due to pump rotation speed and the blade interactions. Therefore, at every pump set points, the peaks occur at similar frequencies. For 10% VOP, the maximum peak is seen to initially decrease before increasing as flow rates increase, before dropping back at maximum flow rate. It can be also seen that the amplitude occurred at similar frequencies. Frequency amplitude recorded for 10% VOP were 0.9, 0.34, 0.5, 1.7 and 0.76mV respectively. Again, for 20% VOP, same trend as 10% VOP has been recorded. Maximum peak recorded were 0.88, 0.24, 0.32, 1.64 and 0.52mV respectively. At 40% VOP, maximum peak recorded are 1.4, 0.3, 0.26, 1.04 and 0.56mV respectively for the different flow rates. For higher VOPs, additional frequency components can be seen at higher frequencies. For 60% VOP, 0.59, 0.32, 1.12, 0.89 and 0.34mV respectively for the different flow rates. The highest peak

values for 80% VOP are 0.55, 0.37, 1.09, 0.88 and 0.55mV occurring at 149, 168, 186, 205 and 223Hz. The frequencies for the highest peak increases as flow rate increases.

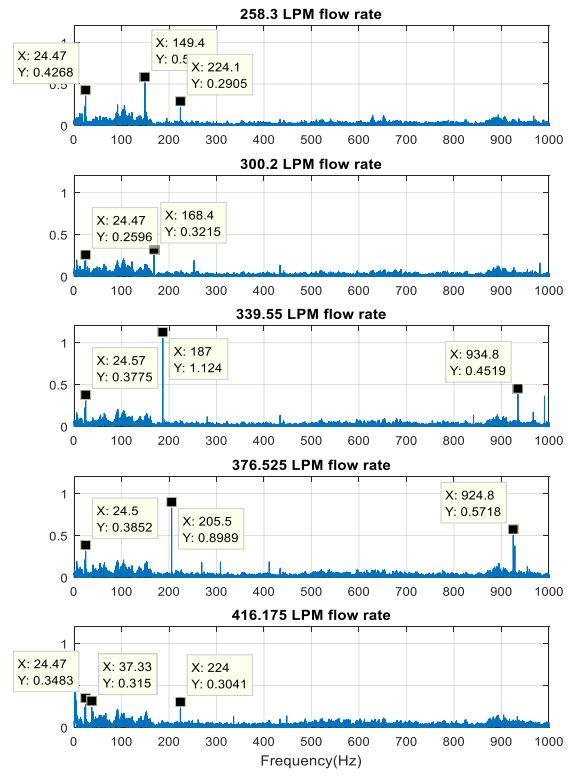


ESTABLISHING ACOUSTIC BEHAVIOUR OF THE CONTROL VALVE UNDER VARIOUS FLOW CONDITIONS

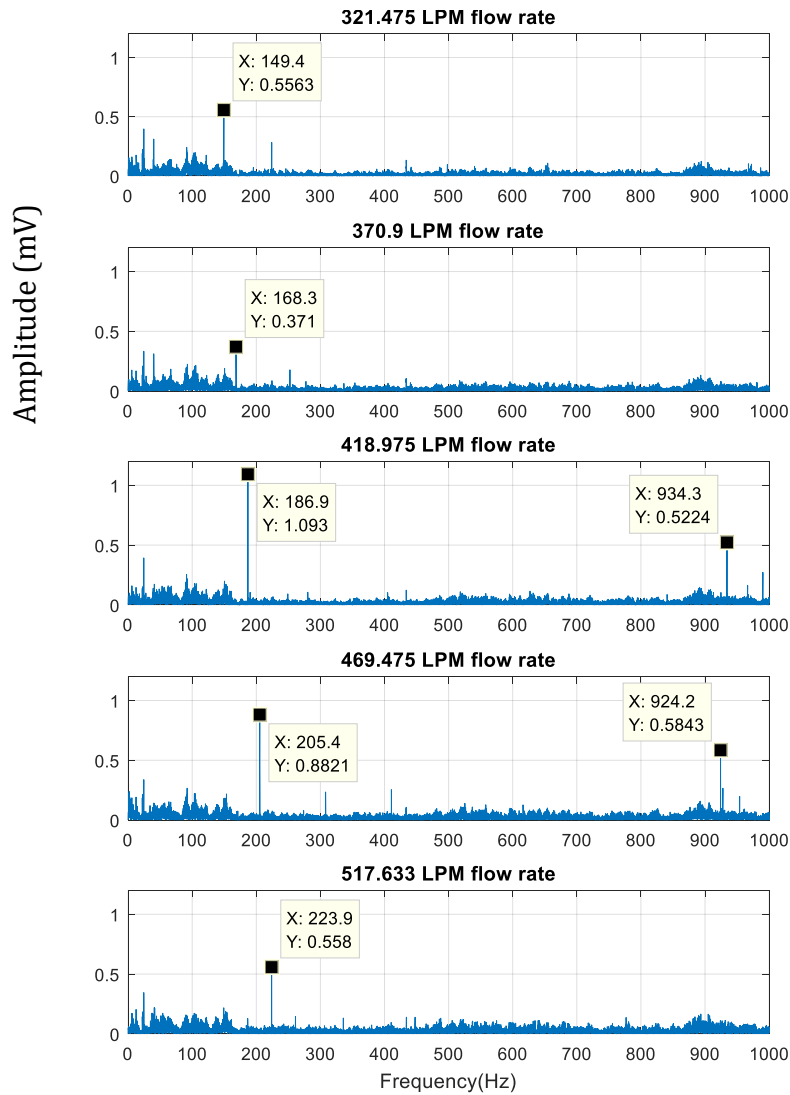
Amplitude (mV)



c



d



e

Figure 6.5. Acoustic signal spectrum for the valve at different flow rates (a) 10% (b) 20% (c) 40% (d) 60% (e) 80%

### B. Mean Frequency

Figure 6.6 shows the mean frequency from the acoustic signatures as a function of flow rates. It can be seen that at across all VOPs, mean frequency increases as flow rates increases. This is because as the flow rates increases, the signal strength increases, and in turn, have an increasing effect on the mean frequency across the entire acoustic frequency spectrum. While FFT shows you what component on each frequency and how much amplitude they have, the mean frequency shows the average frequency for the signal across the frequency spectrum.

Figure 6.6 (a), (b), (c), (d) and (e) shows the mean frequency for the different flow rates at 10, 20, 40, 60 and 80% VOPs respectively.

For 10% VOP, mean frequency increases from 368.36 Hz at low flow rates to 690.25 Hz at the maximum flow rate. Mean frequency increases at 16.5, 17.1, 6.3 and 17.6% respectively across the different flow rates.

20, 40, 60 and 80% VOPs, for similar flow condition, follows the same trend as 10% VOP where mean frequency increases as the flow rate increases. This is because of the increase in the valve flow area, causing increase in the frequency spectrum of the signal as seen in figure 6.6.

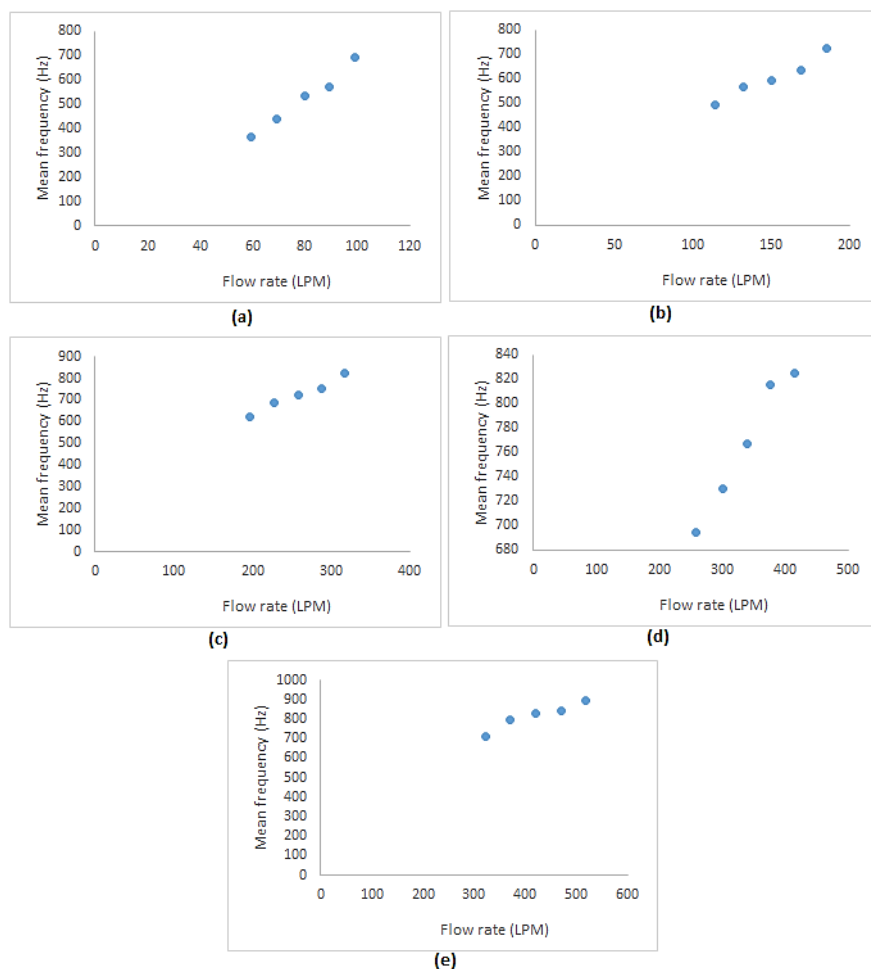


Figure 6.6. Mean frequency for the valve at different flow rates (a) 10% (b) 20% (c) 40% (d) 60% (e) 80%

### 6.3 DEVELOPMENT OF ACOUSTIC INDICATORS FOR MULTIPHASE FLOW CONDITION INSIDE A HEALTHY CONTROL VALVE

A wide range of operating conditions have been selected for tests in the laboratory. These conditions, again, correspond to the actual operating conditions for this valve in real life as discussed in chapter five. Again, because of the construction features present within the valve, there may be likelihood of cavitation and flashing occurrence. In simulating this condition, air has been injected in the pipe loop creating the multiphase flow conditions. Three different air flow rates for acoustic analysis, like vibration, have been used in these conditions to understand dependence of air flow rates on the level of acoustics obtained with a view to establish effectiveness of acoustic measurement as a technique for flow regime change identification.

Again, for the multiphase experiments in this chapter, the airflow rates used are 19.8 LPM, 28.8 LPM and 38.8 LPM in this present investigation. In a control valve, during its operation, the valve opening may change depending on the process requirement. In the present investigation, for multiphase flow tests, only 60% and 80% VOPs have been properly analysed because for lower VOPs, gas accumulates at the valve upstream for a certain period, causing uncertainties in the measured data.

Again, for multiphase flow condition, analysis have been carried out in both time and frequency domain using same features.

#### 6.3.1 TIME DOMAIN ANALYSIS

Figure 6.7 shows the RMS values variation respectively for the multiphase flow at different flow rates for 10, 20, 40, 60 and 80% VOPs. The trends for RMS show an increasing RMS values as the flow rate increases as depicted in figure 6.7 (a), (b), (c), (d) and (e). These trends are similar to that of single-phase condition. 80% VOP generates higher RMS for lower flow rates. However, at higher flow rates, 60% VOP generates higher RMS values. 10% VOP at the lowest flow rate generates the least amount of acoustic signal generated. As the VOP increases, the sound levels increases. For same flow rate and VOP, peak to peak for other VOPs (10, 20, 40 and 60%) vary due to the amount of acoustic levels caused by the air injection as the VOP changes. Again, these values are to be expected as acoustic amplitude increases with flow rate increase as shown in figure 6.13 at 19.8 LPM, 28.8 LPM and 38.8 LPM airflow rates.

The trends for RMS (Figure 6.7) at 10, 20, 40, 60 and 80% VOPs show an almost linear trend, with the values increasing as flow rates increase. The acoustic level generated for multiphase flow conditions decreases and increases slightly for 60% and 80% VOPs respectively. The RMS of the acoustic signals for single-phase (60% VOP) for the flow rates (pump set point variation) are 5.4, 5.5, 5.8, 6.2 and 6.8mV. Comparatively, for multiphase flow conditions with the lowest airflow rate (19.8 LPM), the values decreases slightly to 5.2, 5.4, 5.8, 6.1 and 6.5mV respectively for similar flow rates of water. The results have been seen to deviate from single to multiphase by 4.9, 2.2, 0.5, 0.9 and 4.1% respectively.

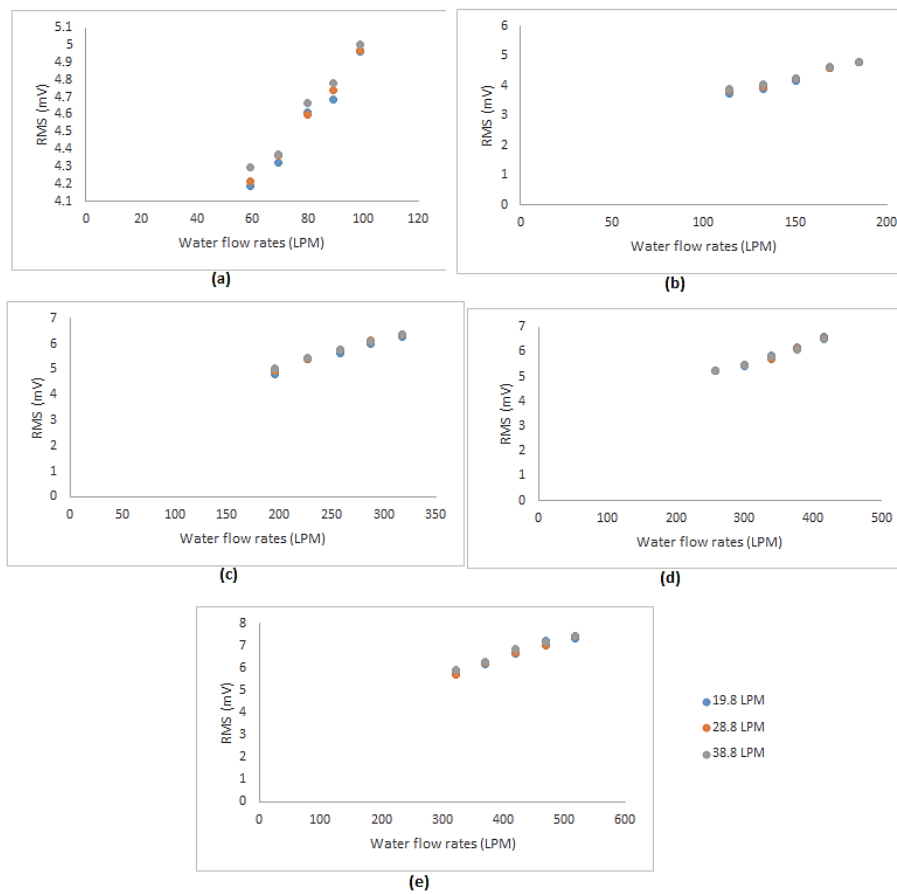


Figure 6.7: Multiphase RMS variation for the different flow rates at (a) 10% (b) 20% (c) 40% (d) 60% (e) 80% VOP

This shows how the acoustic signal changes due to the flow regime change from single to multiphase. The decrease (which is also seen for 20 and 40% VOPs) is because of the decrease in water volume fraction that has been filled with air, which creates the decrease in the acoustic level. Furthermore, as the airflow rate increases from 19.8 to 28.8 LPM,

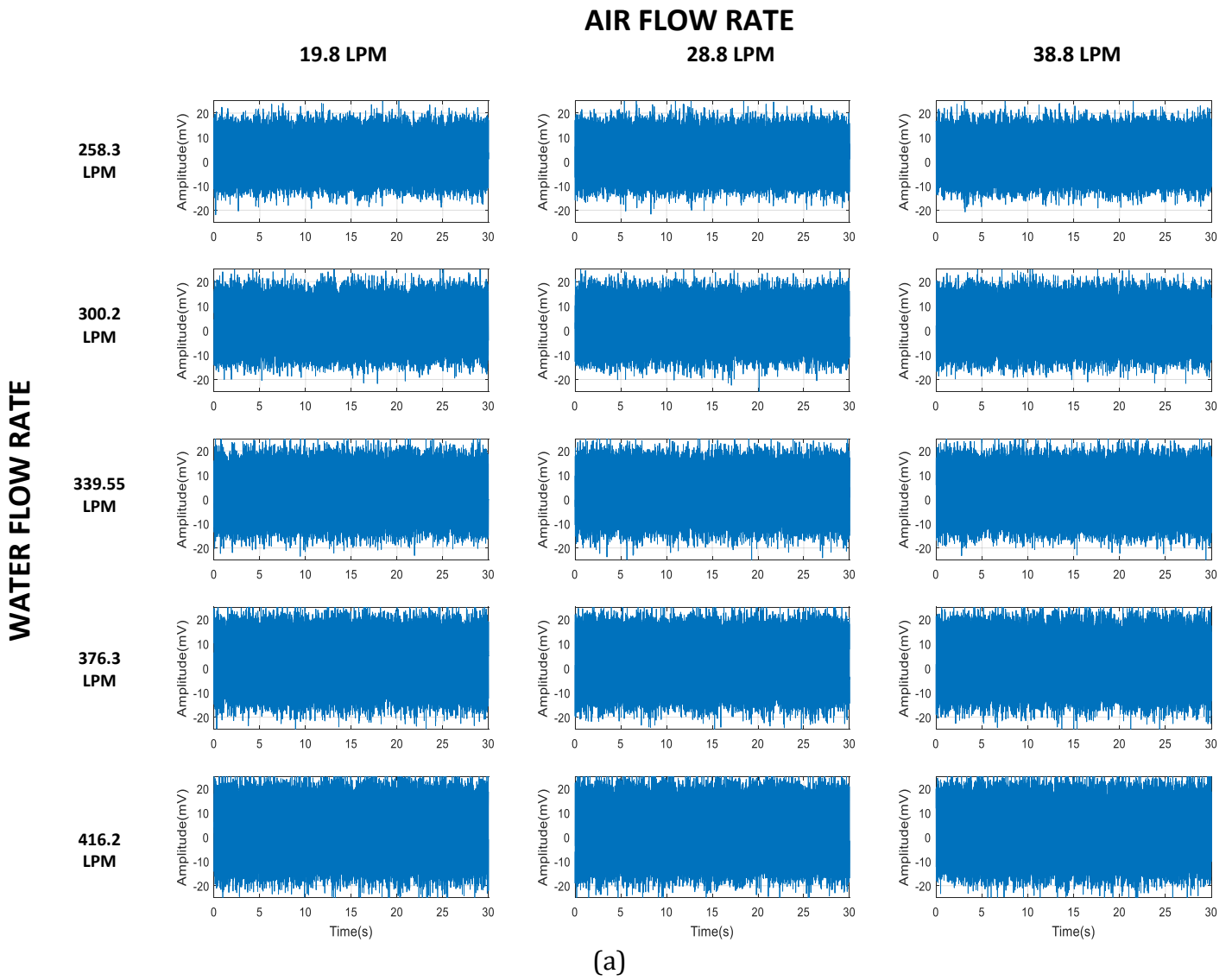
the RMS values changes slightly (remains nearly the same as the increase in the airflow rate causes very little impact) from 5.21 to 5.22mV, representing deviation of 0.19%, and from 28.8 to 38.8LPM, RMS deviates by nearly 0.0004% for lowest water flow rate. At the maximum water flow rate, from 19.8 to 28.8 LPM airflow, the RMS values deviates slightly by 0.3% and from 28.8 to 38.8LPM, RMS deviates by nearly 0.6%. The slight or no RMS values deviations is because of the impact the airflow rate increase has on the acoustic signal.

Similar trend is again, observed at 80% VOP where the RMS values of the acoustic signal goes from 5.4, 5.86, 6.3, 6.68 and 6.9mV to 5.7, 6.2, 6.6, 7.2 and 7.3mV, from single to multiphase flow conditions (19.8LPM airflow rate), representing a deviation from single-phase of 4.6, 4.7, 4.9, 7.5 and 5.4% respectively. As the airflow rate then increases from 19.8.8 to 28.8 and to 38.8, the acoustic signal RMS values deviates by 0.4 and 1.5% respectively for low flow rate, and 1.5 and 0.3% respectively for the highest flow rates.

Peak to peak, Kurtosis and standard deviation values have also been analysed for the different flow and operating condition as the results presented in RMS, as they show similar trends. For kurtosis however, the trends for 60 and 80% VOPs are very similar as that for single-phase, varying around 3. This again, shows the change in the dynamic flow behaviour as flow changes from single phase to multiphase due to the little extra acoustics in multiphase, though slightly. Furthermore, when the airflow rate increases, kurtosis values changes.

As already mentioned, figure 6.8 (a) and (b) shows the vibration signal for the different water flow rates at 19.8, 28.8 and 38.8 LPM airflow for only 60 and 80% VOPs.

In the next section, frequency domain analysis has been presented and shows a clearer understanding of how the valve behave under different flow and operating conditions.



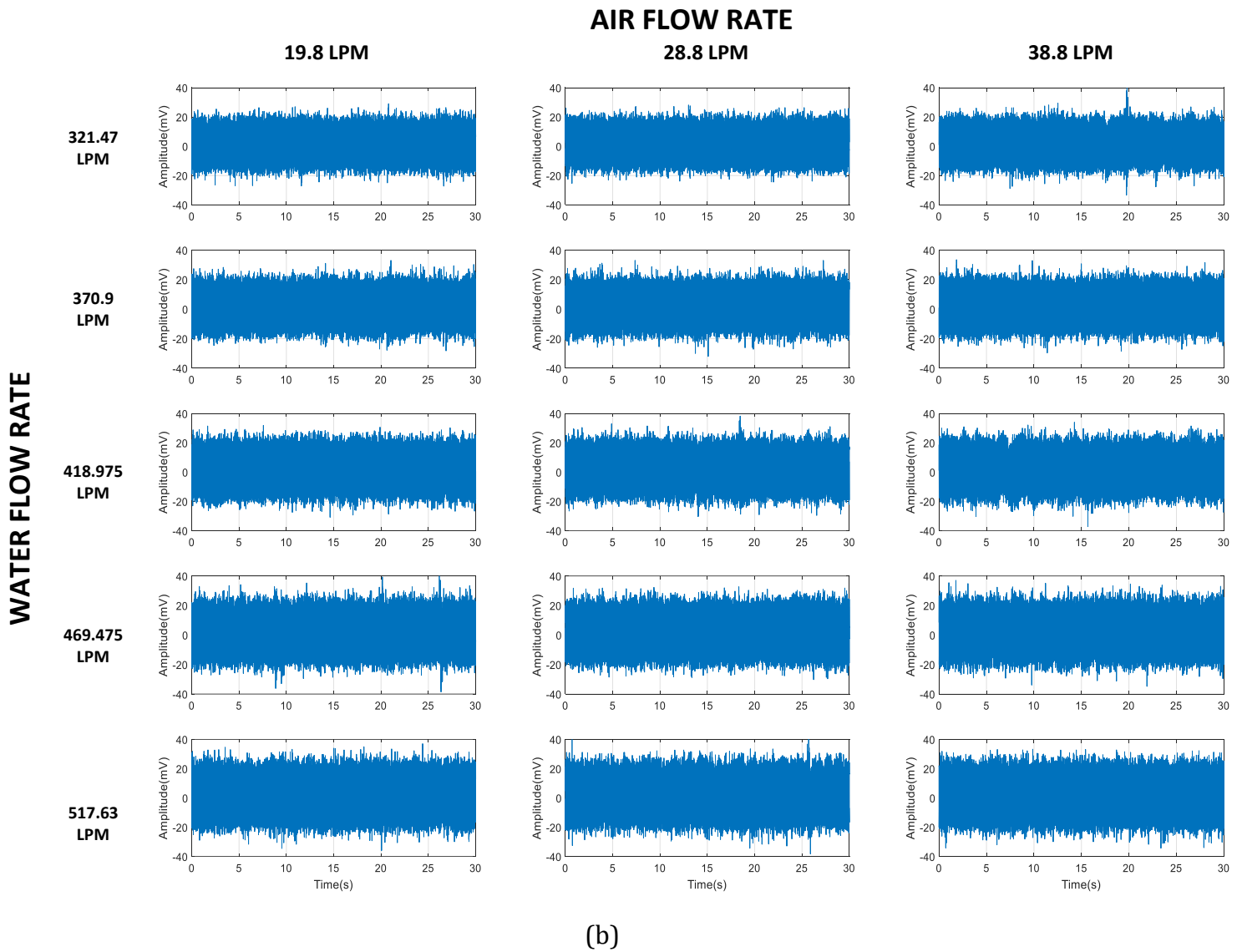
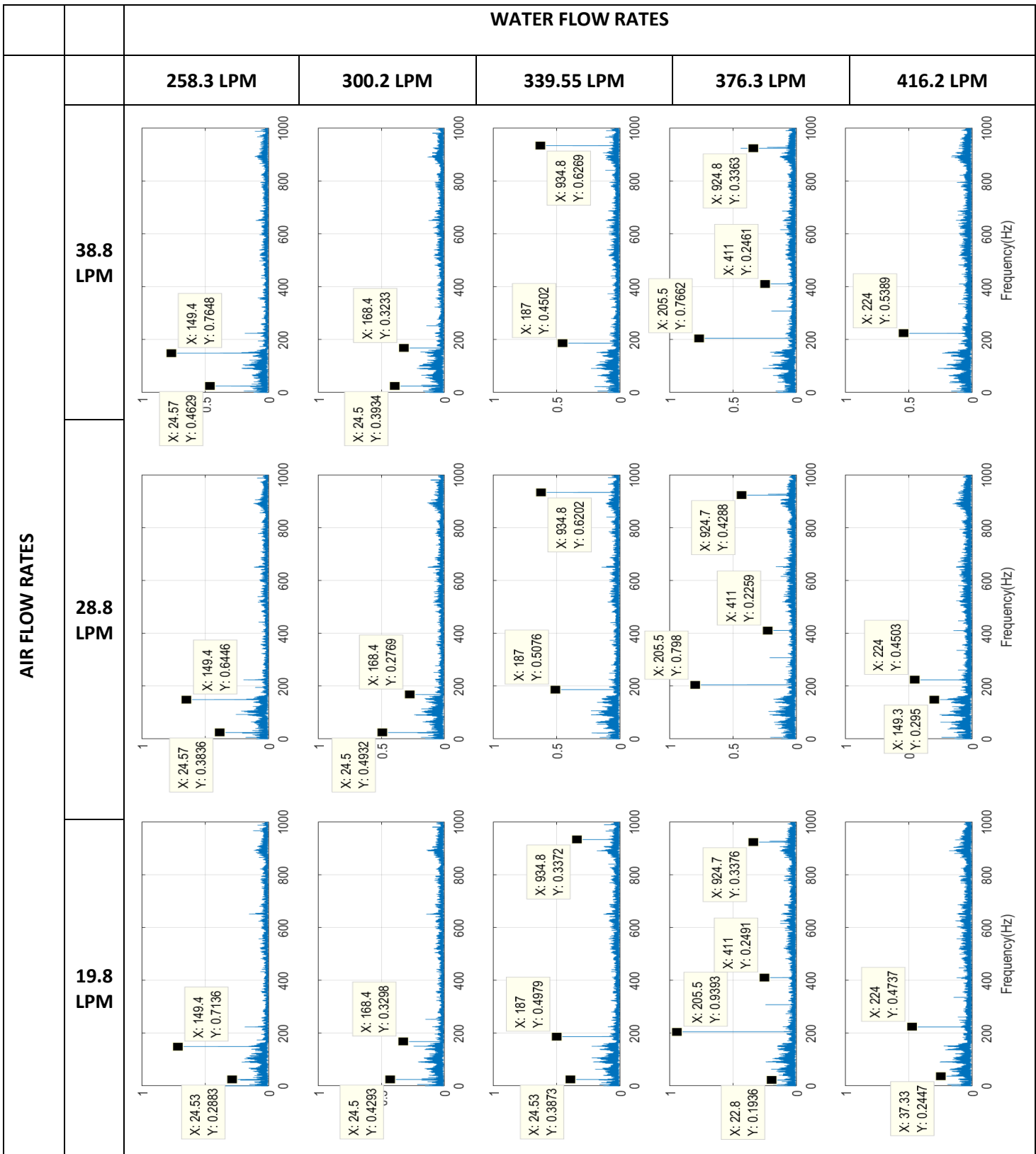


Figure 6.8. Multiphase acoustics amplitude variation for the different air flow rates for water flow rate of (a) 60% (b) 80% VOP

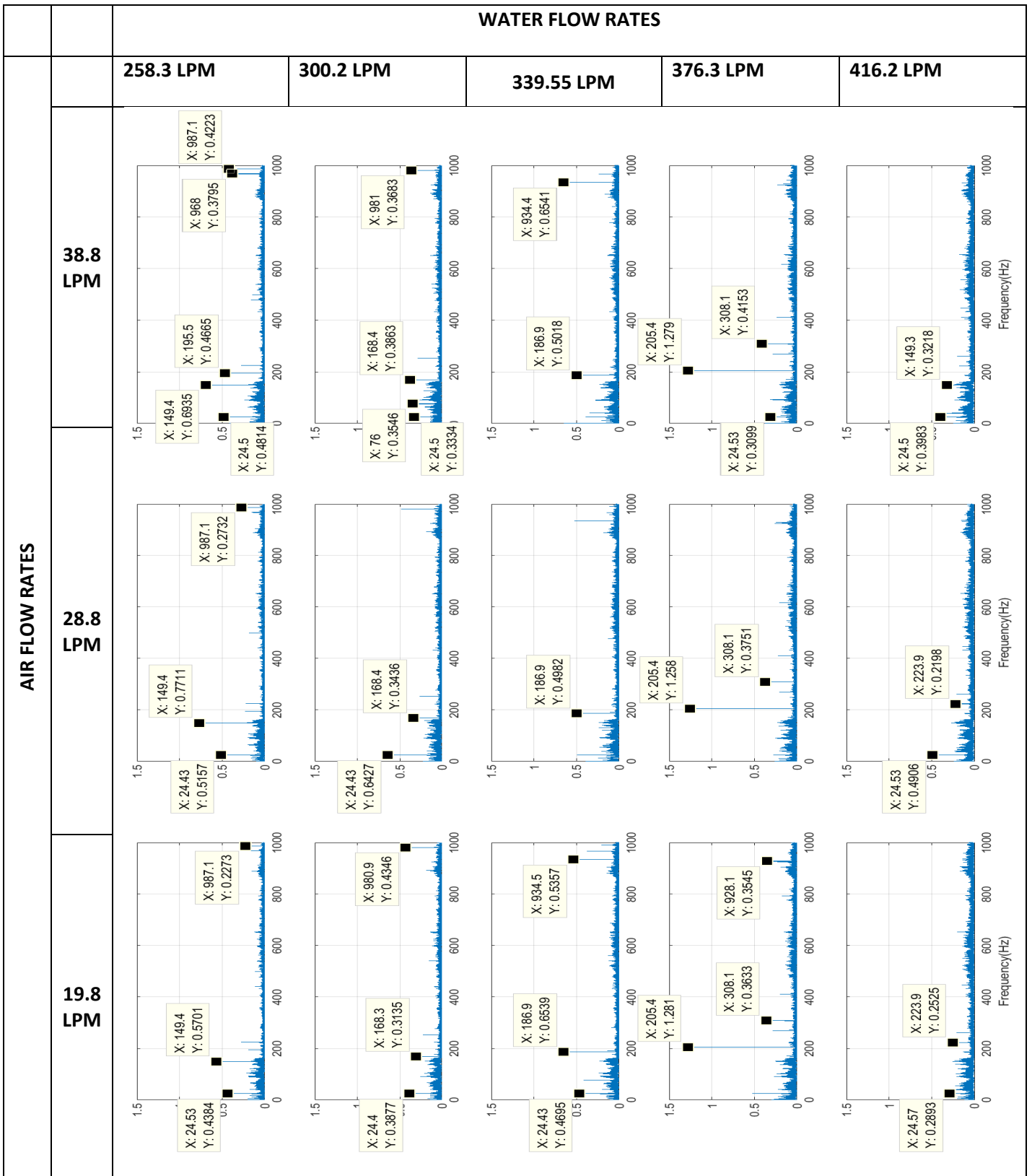
### 6.3.2 FREQUENCY DOMAIN ANALYSIS

Figures 6.9 (a) and (b) shows the FFT plots for various water flow rates at 60% and 80% VOPs respectively for the different airflow rates. The acoustic signal again, has been sampled at 96 kHz. Figure 6.13 shows the FFT plot of the acoustic signal for 0-1000Hz for 60 and 80% VOPs. This is because the dominant frequencies are observed within this region similar to that observed for single-phase flow conditions. Figures 6.9 shows a more clearer understanding into the acoustic signal for multiphase flow conditions. Figure 6.9 shows the acoustic signal FFT at different water flow rates for (a) 60% VOP and (b) 80% VOP. Again, unlike single-phase where the peaks seen at various frequencies are due to

only the flow induced sound caused by the pump, additional peaks occur at much lower frequencies (10-40 Hz) for multiphase flow for 60% and 80% VOPs.



(a)



(b)

Figure 6.9. Multiphase vibration signal spectrum for the valve at different flow rates for 19.8LPM, 28.8LPM and 38.8 LPM (a) 60% (b) 80% VOP

For single and multiphase flow condition, similar peaks but with varying amplitudes occur at similar frequencies. For 258.3, 300.2, 339.6, 376.5 and 416.2 LPM water flow rates, frequency components can be seen for single and multiphase at around 20 and 200 Hz. For 60% VOP, the amplitude of the frequency components is seen to deviate for the different water flow rates by 33.3, 68, 2.7, 50 and 29.4% respectively at the 20 Hz frequency from single to multiphase (19.8 LPM airflow). For 200 Hz, the amplitude frequency components deviates by 58.5, 0, 56.2, 4.3 and 27.6% respectively. However, due to the injection of bubbles to create the multiphase condition, additional frequency component can be seen at lower frequency (between 0 to 10 Hz), where they are all constant (0.39 Hz) for single-phase.

These varying peaks are due to the air bubbles present in the flow. As the airflow rate increases, the peak amplitude changes because of increase in air bubbles, which coalesce with each other or break into smaller bubbles. As a result, acoustic level changes. These also shows how the flow behaves when transitioning from single to multiphase condition in terms of how much additional acoustics is generated on the valve. Similar occurrence can be seen also for 80% VOP. For single and multiphase, similar peaks, but with varying amplitudes occur at similar frequencies. For 321, 370, 418, 469 and 517 LPM water flow rates, frequency components occur at around same frequencies as 60% for both single and multiphase conditions, with highest peaks occurring at 200 Hz. However, due to the injection of bubbles to create multiphase condition, additional varying frequency component can be seen again at lower frequency (around 20 Hz), where they are very low and in some cases, nearly absent, for single-phase. These components, from very low in single-phase to 0.05, 0.055, 0.074, 0.044 and 0.073 mV for the different water flow rates. Increase in the water flow rate causes a slight reduction in the frequency amplitude as seen in figure 6.9 (b). These values changes as air bubble injection increases from 19.8 to 28.8 and to 38.8 LPM causing the flow regime to change at these conditions.

Figure 6.10 shows the mean frequency for the acoustic signals at multiphase conditions as a function of water and the airflow rates for 60% and 80% VOPs.

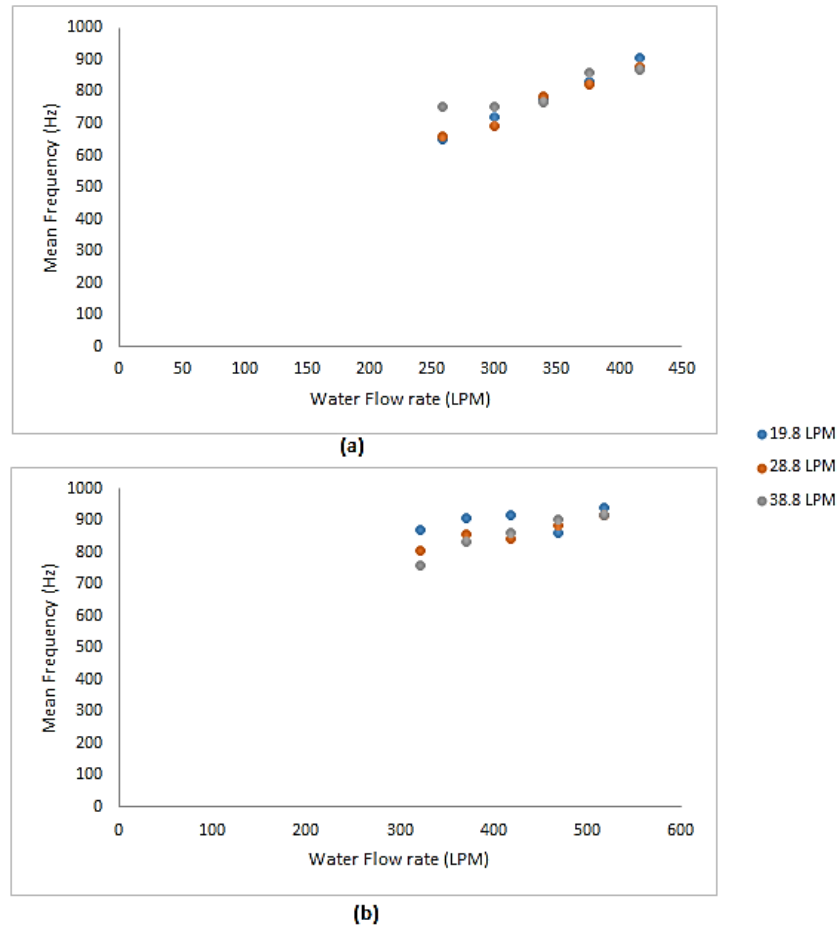


Figure 6.10: Acoustic mean frequency for the valve at different flow rates for (a) 60% VOP, (b) 80% VOP.

Figures 6.10 shows how much frequency exist in the acoustic signal spectrum for the multiphase flow conditions by calculating the mean frequencies. Figure 6.10 shows the acoustic signal mean frequency at different water flow rates for (a) 60% VOP and (b) 80% VOP. Like the vibration signal (chapter 5), the introduction of air bubbles increases the acoustic mean frequency, thereby increasing the amount of power in the frequency spectrum, from single-phase across the spectrum for both 60 and 80% VOPs.

For single-phase flow, an increasing trend was seen as flow rate increase. For the multiphase condition, mean frequency also increases as flow rate increases for 60% VOP. For 80% VOP, for low airflow rate (19.8LPM), slight drop in mean frequency can be seen as water flow rate goes from 469 to 517 LPM. This is because, at that flow rate transition, the acoustic strength slightly decreases for the low airflow rates, causing the power spectrum to decrease, making the mean frequency to decrease. It can also be because of

measurement uncertainty for this particular flow rate measurement. For 60% VOP, across water flow rates of 258.3, 300.2, 339.6, 376.5 and 416.2 LPM, mean frequency varies from 694.05 Hz to 650.8 Hz. This is from single phase to multiphase (19.8LPM), representing a decreasing deviation of 4.8%. Again, for 300.3 LPM, means frequency decreases at the rate of 4.9%. Across the remainder of the flow rates (339.6, 376.5 and 416.2 LPM), mean frequency increases with a percentage variation increase of 0.8, 1.8 and 8.9% respectively. From 19.8LPM to 28.8LPM, the frequency spectrum slightly decreases, making the mean frequency to reduce. This is because of increase in the air volume fraction (bubbles) causing the mean frequency to decrease. This percentage decrease for the lowest flow rate is about 1.5%, which can be because of one off measurement uncertainty. For the maximum flow rate, the percentage increase variation is 3%. Again, from 28.8 to 38.8LPM, mean frequency increase at flow rates (258.3, 300.2 and 376.5LPM). The percentage increase observed were 13.9, 8.6 and 4.5% respectively. For the remainder of the flow rates (339.9 and 416.2 LPM), the percentage decrease recorded were 2.6 and 1% respectively.

At 80% VOP, from single to multiphase (19.8LPM), percentage increase recorded were 18.1, 12.1, 9.3, 2.4 and 4.5% respectively across the different flow rates. Mean frequency from 19.8 to 28.8 LPM for airflow rate reduces at the rate of 7.6, 5.6, 8.2, 2.5 and 2.7%. From 28.8 to 38.8 LPM, mean frequency decreases for lower water flow rates (321 and 370LPM) at the rate of 6 and 2.7% respectively. At higher water flow rates (418, 469 and 517 LPM), the percentage increase variation from 28.8 to 38.8LPM airflow are 2, 1.9 and 0.1% respectively.

After analysis have been carried out for single and multiphase flow for a healthy valve, the next two sections discusses the acoustic characteristics for a faulty valve and comparisons made.

#### **6.4 DEVELOPMENT OF ACOUSTIC INDICATOR FOR SINGLEPHASE FLOW CONDITION INSIDE A FAULTY CONTROL VALVE**

This section of this chapter presents data analysis for a faulty valve and compares with that of a healthy valve using acoustic technique. Again, using this technique, fault used in chapter five, where one of the trims' flow path has been blocked using a solid material. This blockage have significant changes in the flow parameters, including the acoustic

characteristics of the control valve. The analysis has again been carried out in both time and frequency domain and their results compared to that of the healthy valve.

#### 6.4.1 TIME DOMAIN ANALYSIS

For the faulty acoustic characteristics, like healthy valve, series of experiments, like the one in the previous chapter have been performed and the data have been collected for the different flow and operating conditions and their results compared. For single-phase condition, the faulty acoustic signals, again, have been analysed in time domain using statistical parameters such as RMS, Peak-to-Peak, Kurtosis and Standard deviation. For the faulty valve acoustic analysis, only 60 and 80% VOPs have been analysed for different flow conditions.

The RMS values for the acoustic signal have been presented in figure 6.11, comparing both healthy and faulty valve conditions for 60 and 80% VOPs at same pump flow rates.

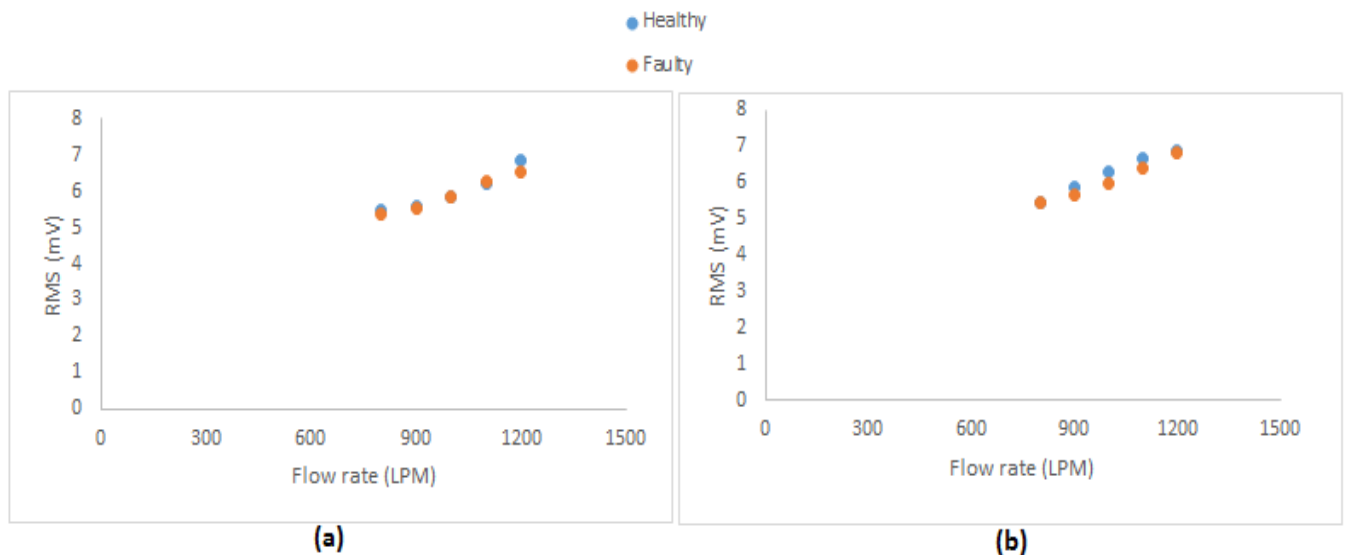


Figure 6.11: RMS value comparison between healthy and faulty valve at different flow rates for (a) 60% VOP (b) 80% VOP

As seen in figure 6.11, the RMS value for the acoustic strength of the signal decreases for faulty valve, from healthy valve for the different flow and operating condition. An increasing trend for both condition is observed.

At 60% VOP, for healthy valve, RMS value for the acoustic signal observed are 5.48, 5.57, 5.8, 6.2 and 6.8mV for 800, 900, 1000, 1100, 1200LPM respectively. For faulty valve, the

RMS value for the acoustic signal decreases, from healthy valve condition, at 2.2, 0.6, 0.4, 0.3 and 4.8% for the different flow rates.

For 80% VOP, from 5.47, 5.8, 6.3, 6.7 and 6.9mV for healthy valve, RMS value decreases at the rate of 0.2, 3.4, 5.3, 4.4 and 1% for the faulty valve.

Peak-to-peak, standard deviation and Kurtosis comparison between the healthy and faulty acoustic signals for 60 and 80% VOPs at same flow rates were also made. Similar trends where faulty valve show higher values were also observed for both 60 and 80% VOPs.

The next section analysed the healthy and faulty valve acoustic signals and their analysis compared in frequency domain for multiphase flow condition.

#### **6.4.2 ANALYSIS IN FREQUENCY DOMAIN**

Again, for faulty valve, analysis have been carried out for same conditions as healthy valve for the acoustic signal, this time in frequency domain. When faults occur inside the valve, the frequency components changes. These changes are significant in the analysis of acoustic signal, so that when they occur, they can be detected and acted upon. In this research, for faulty valve analysis in frequency domain, FFT and mean frequency have again been used.

##### **A. Fast Fourier Transform (FFT)**

Figure 6.12(a) and (b) shows the FFT plots for the different flow rates at 60 and 80% VOPs. The acoustic signal has again been sampled at 96 kHz. Figure 6.12 shows the FFT plot of the signal for 0-1 kHz.

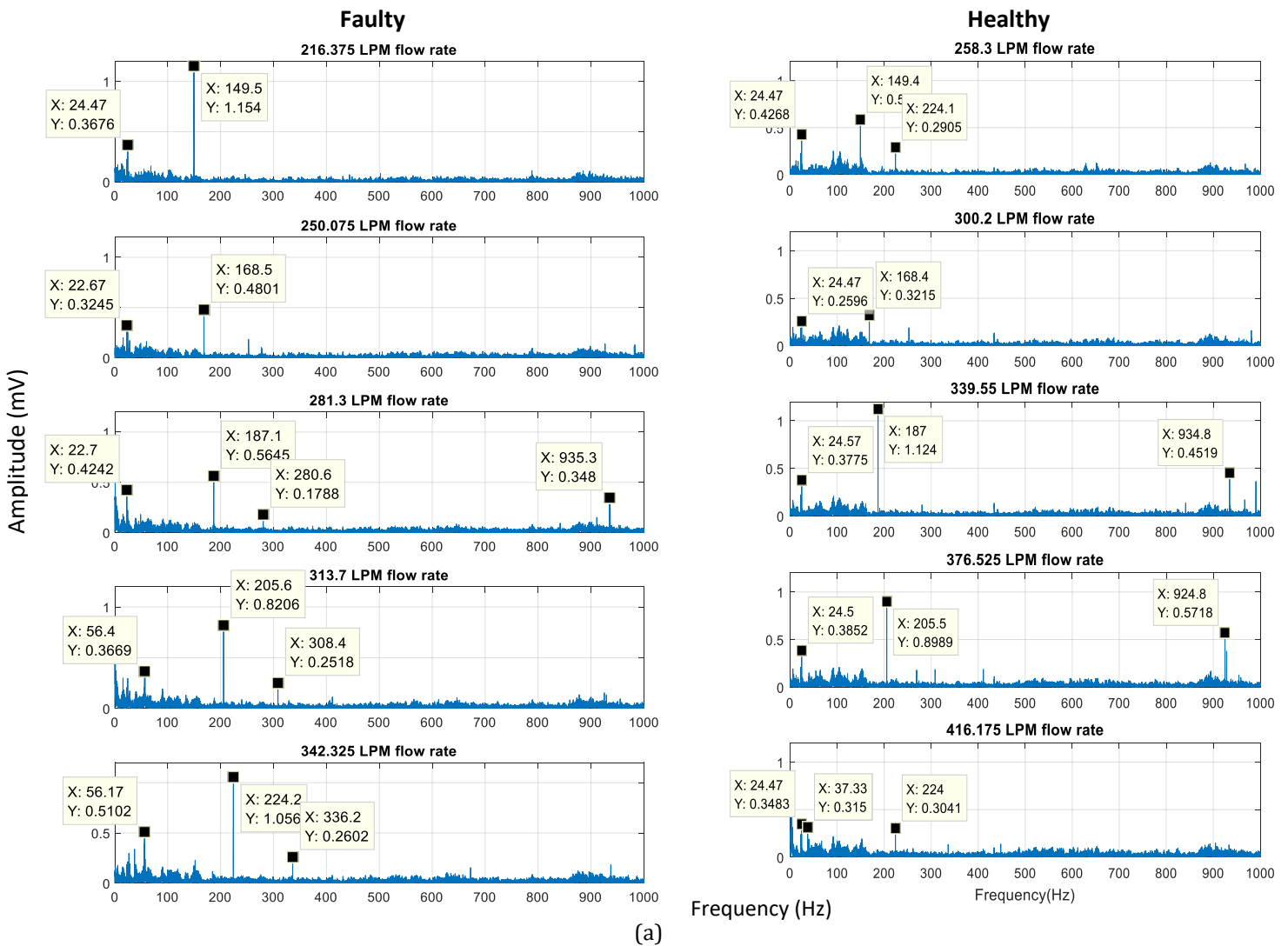
Figure 6.12 shows a better understanding of the faulty control valve dynamics as the acoustic signals in time domain have been transformed into frequency domain. The peak amplitude is distinctively seen in the frequency range of 0-1000 Hz. As the flow rate increases, the peak amplitude increases.

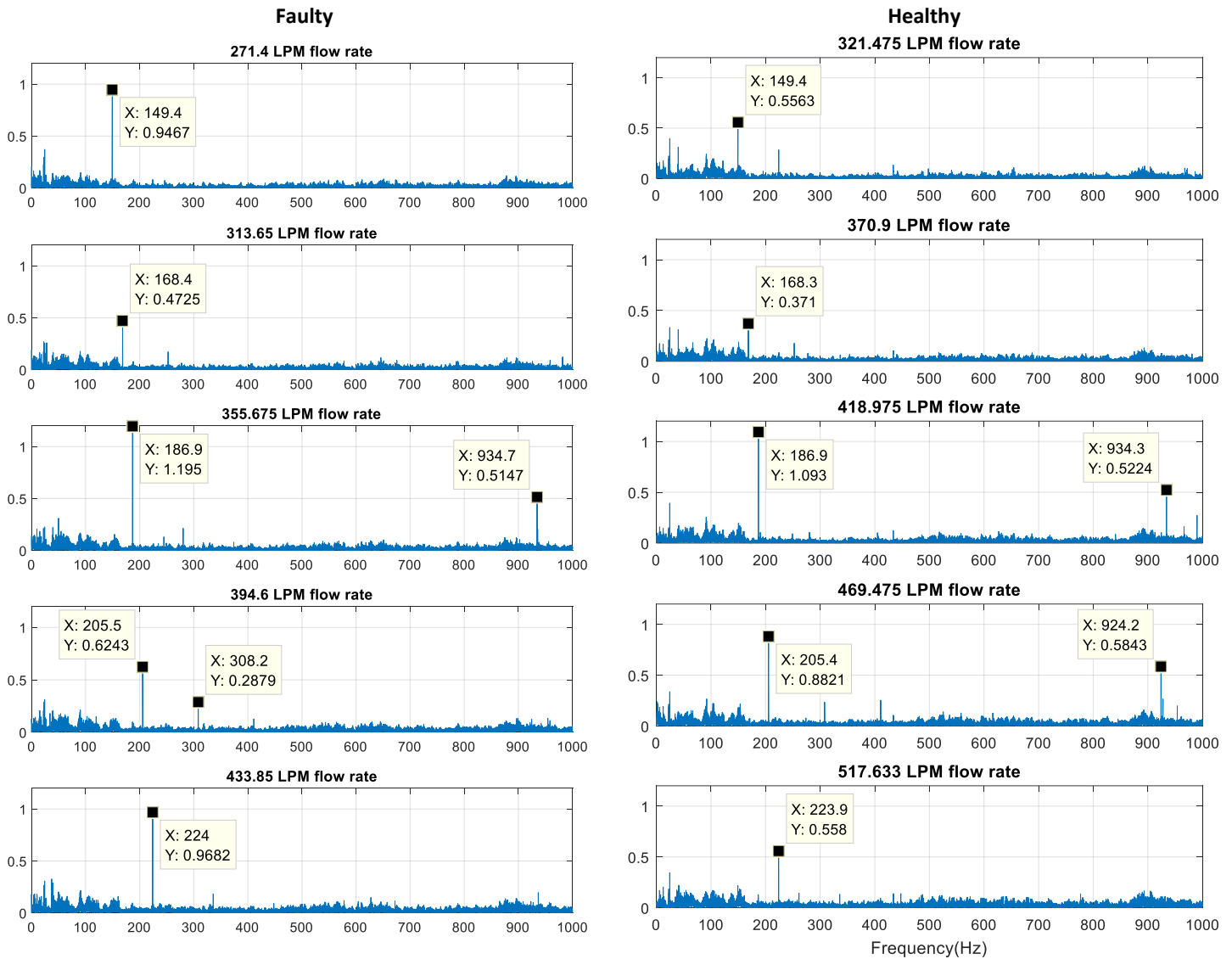
For 60% VOP, comparison for the acoustic signal have been made between faulty and healthy valve conditions. At similar frequencies, the frequency components can be seen to increase for faulty valve condition from the healthy valve. Same set points and VOPs have been used for both faulty and healthy valves. For same set points, because of the

fault, the flow rate has dropped, causing changes to the flow parameters, including the acoustic signatures. Ideally, for faulty valves, acoustic components should increase, which is the case for most of the flow rates obtained for the faulty acoustic signatures for both 60 and 80% VOPs.

The percentage frequency amplitude variation, from the faulty to healthy valve, at similar conditions for similar frequencies, are 54.7, 33.3, 54.8, 7.8 and 71% respectively for 800, 900, 1000, 1100, 1200LPM flow rates respectively for 60% VOP.

For 80% VOP, same trend is seen where faulty valve amplitude frequency increases from the healthy valve at same flow and operating conditions. The percentage variation for the different flow rates are 41, 21.5, 8.5, 29.2 and 42.4% for 800, 900, 1000, 1100, 1200LPM flow rates respectively.





(b)

Figure 6.12. Acoustic signal spectrum for the faulty and healthy valve at different flow rates (a) 60% (b) 80%

### B. Mean Frequency

Figure 6.13 shows the mean frequency from the acoustic signatures as a function of flow rates for the healthy and faulty valves, at 60 and 80% VOPs. It can be seen that at across both VOPs, mean frequency increase from the healthy to faulty valve for just the low flow rates. This can be due to lesser acoustics obtained for the faulty valve at the low flow rates, therefore expanding the entire frequency spectrum for these flow rates. If the acoustic frequency components are higher, which is experienced at lower frequencies,

the mean frequency becomes lower. Secondly, the reason might be due to one off experimental uncertainty from the measured data.

Figure 6.13 (a) and (b) shows the acoustic mean frequency for the healthy and faulty valves at different flow rates for 60 and 80% VOPs respectively.

For 60% VOP, the mean frequency from healthy to faulty valve is seen to only increase at 800 and 900LPM by 3.4 and 10.8% respectively. At higher flow rates (100, 1100, 1200LPM) decrease at the rate of 12.7, 26.3 and 12.5% respectively from healthy to faulty valve condition were observed.

At 80% VOP, mean frequency is seen to decrease from the healthy to faulty valve, except for the lowest flow rate (800LPM). For this flow rate, mean frequency decrease at 7.1%. Again, this can be due to lesser acoustic signals obtained for the faulty valve at the low flow rates, therefore expanding further, the entire frequency spectrum for this flow rates. Secondly, the reason might be due to one off experimental uncertainty from the measured data. For higher flow rates (900, 1000, 1100, 1200LPM), mean frequency, from healthy to faulty valve, is observed to decrease at the rate of 4.1, 9, 4.2 and 9.3% respectively across the different flow rates.

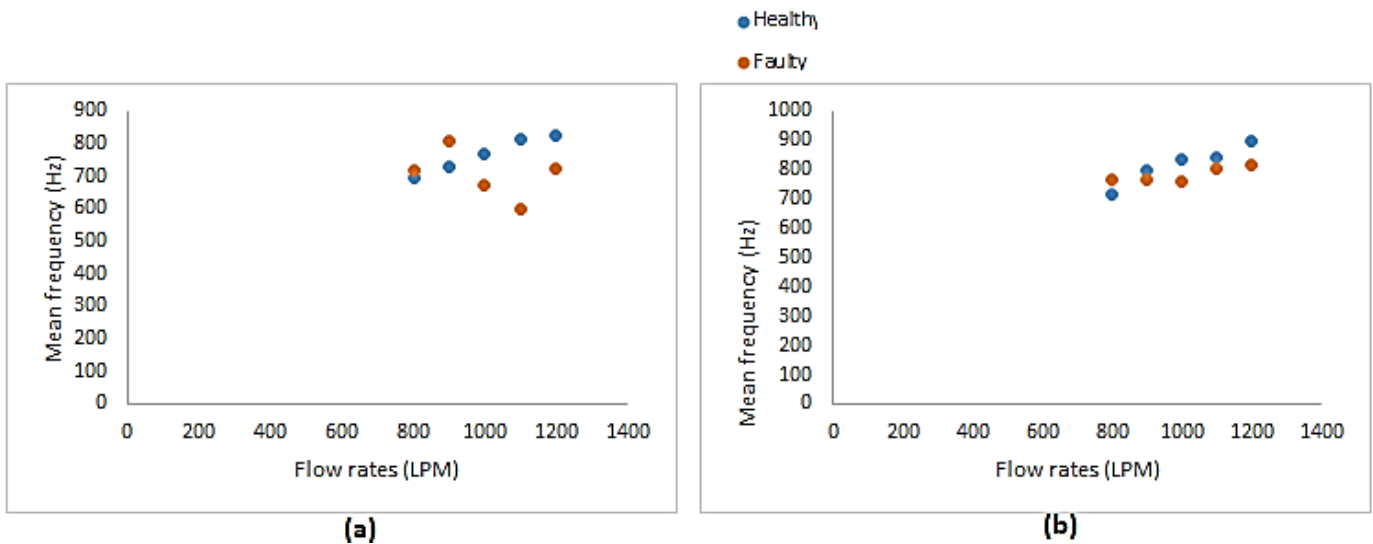


Figure 6.13: Acoustic mean frequency for faulty and healthy valves at different flow rates (a) 60% (b) 80% VOPs

## **6.5 DEVELOPMENT OF ACOUSTIC INDICATORS FOR MULTIPHASE FLOW CONDITION INSIDE A FAULTY CONTROL VALVE**

This section presents acoustic signal analysis for a faulty valve multiphase condition and compares with that of a healthy valve. The control valve trim have four flow paths as already described in chapter one. The faulty valve has been created by blocking one flow path using a solid material. This blockage has had significant changes in the flow parameters, as would be seen in the analysis in sections 6.5.1 and 6.5.2, affecting the acoustic characteristics of the valve. These analysis have again be carried out in both time and frequency domain and their results compared to the healthy valve.

### **6.5.1 TIME DOMAIN ANALYSIS**

For the faulty acoustic characteristics, like healthy valve, data have been collected for the different flow and operating conditions and their results compared. For multiphase condition, the faulty acoustic signals have been analysed in time domain using statistical parameters such as RMS, Peak-to-Peak, Kurtosis and Standard deviation. For faulty valve acoustic analysis, only 60 and 80% VOPs again, have been analysed for different flow conditions.

Acoustic characteristics have varied because of the blockage of one of the flow paths. For multiphase airflow comparisons between the healthy and faulty valves, acoustic characteristics have been seen to increase for the RMS value for 60%, as extra acoustics is developed as one flow path is blocked. The reverse is the case for 80% VOP as more flow passage area is available. This time, multiphase flow for the valve acoustic, as water volume fraction reduces, produces less sound when compared to the healthy valve.

The RMS values have been presented in figure 6.14, comparing both the healthy and faulty acoustic signals for 60 and 80% VOPs at same pump flow rates.

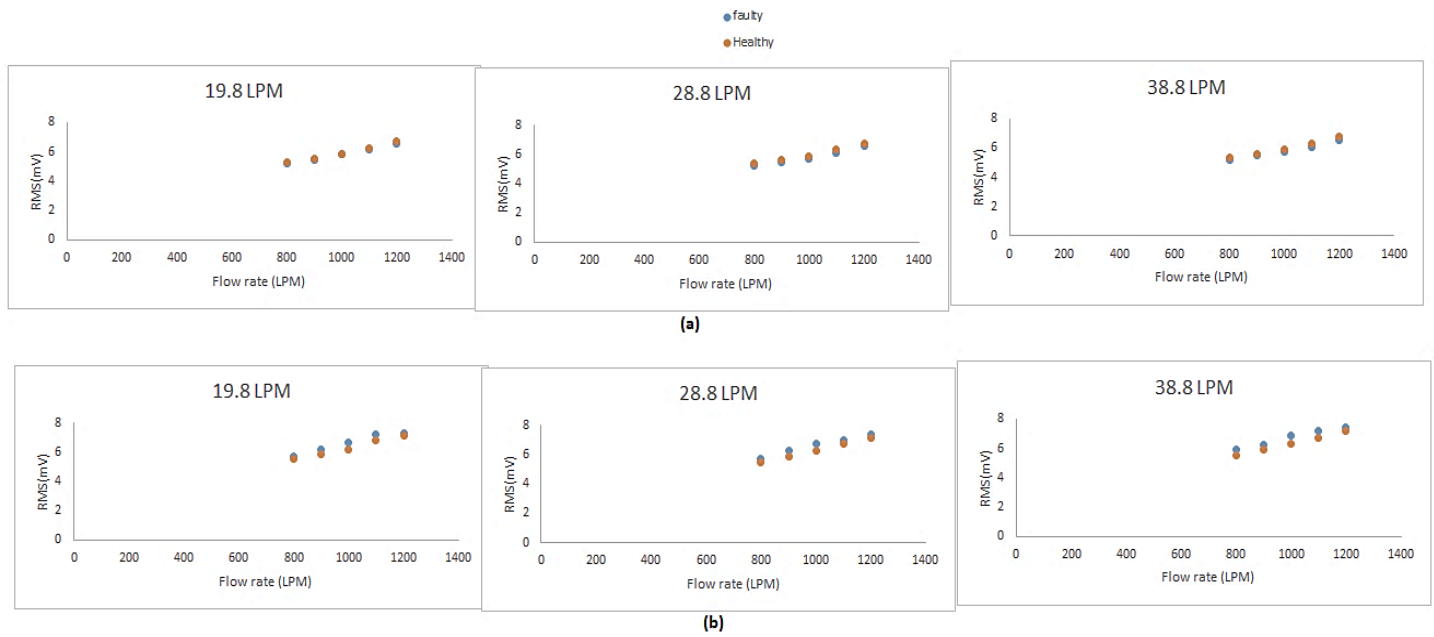


Figure 6.14: RMS value comparison between the healthy and faulty valves at different water flow rates for (a) 60% VOP (b) 80% VOP at 19.8, 28.8 and 38.8 LPM airflow rates

As seen in figure 6.14, the RMS values for the acoustic signals for the different multiphase flow rates increases for faulty valve from healthy valve for different flow and operating conditions.

At 60% VOP, for the healthy valve, the acoustic signal observed for the RMS values are 75.21, 5.44, 5.8, 6.17 and 6.58mV for 800, 900, 1000, 1100, 1200LPM respectively at 19.8LPM airflow rate. For multiphase faulty valve, the RMS acoustic amplitudes increases, from the healthy valve condition, at 1.5, 1.5, 0.3, 1.2 and 1.6% for the different flow rates at 19.8LPM airflow. At 28.8LPM airflow, percentage increase from the healthy to faulty valve for the different water flow rates are 2.3, 2.6, 2.59, 2.7 and 2.4% respectively. For 38.8LPM airflow from healthy valve, percentage increase recorded are 2.1, 1.9, 1.9, 3.1 and 3.3% respectively.

For 80% VOP, from 5.73, 6.16, 6.6, 7.2 and 7.3mV for healthy valve, RMS multiphase value decreases for 19.8LPM airflow at the rate of 3.8, 5.3, 6.8, 6.2 and 2.5% from the faulty valve. At 28.8LPM airflow, percentage variation from the healthy to faulty valve for the different water flow rates are 4.2, 6.2, 6.9, 3.4 and 4% respectively. For 38.8LPM airflow from healthy to faulty valve, percentage variation recorded are 6.8, 5.9, 8.2, 7.1 and 4% respectively.

Again, as said earlier, Peak-to-Peak, Kurtosis and standard deviation analysis have also been carried out for similar conditions as the one presented for RMS values. Their analysis all show similar trends where faulty valve, using peak-to-peak, standard deviation and kurtosis are distinctively different from healthy valve condition.

The next section analysed the healthy and faulty valve acoustic signals and their analysis compared in frequency domain for multiphase flow, where fault detection can be clearly understood.

### 6.5.2 ANALYSIS IN FREQUENCY DOMAIN

Multiphase analysis has been carried out for same conditions as healthy valve for the acoustic signal in frequency domain. When faults occur inside the valve, the frequency components change. These changes are significant in the fault analysis of acoustic signal, so that when they occur, they can be properly diagnosed. Again, FFT and mean frequency have been used.

#### A. Fast Fourier Transform (FFT)

Figure 6.15(a) and (b) shows the FFT plots for the different flow rates at 60 and 80% VOPs. The acoustic signals have been sampled at 96 kHz. Figure 6.15 shows the FFT plot of the signal for 0-1 kHz.

For 60% VOP, comparison between the faulty and healthy valves has been made. Figure 6.15 shows 19.8LPM airflow for the healthy and faulty valve. The amplitudes at these frequencies have been compared for both faulty and healthy valve. Comparing at 19.8LPM, at similar frequencies, the amplitude at those frequencies has a percentage variation increase from healthy to faulty at the rate of 33, 23.8, 37.9, 10.7 and 27.6% respectively for the different water flow rates. At 28.8LPM airflow, 36, 22.8, 56, 19.3 and 32.8% respectively for the different flow rates have been observed. For 38.8LPM airflow, 17.3, 37.2, 76.2, 9.5 and 29.3% respectively have been observed from the healthy to faulty valve condition.

For 80% VOP, figure 6.16 shows acoustic signatures for 28.8LPM airflow for the healthy and faulty valve. As said earlier, extra acoustic components are seen at very low frequencies due to air injection for both the healthy and faulty valve conditions. The amplitude at these frequencies has been compared for both faulty and healthy valve.

Comparing at 19.8LPM, at similar frequencies, the amplitude at those frequencies have a percentage variation from the healthy to faulty at the rate of 21, 31.4, 5.2, 33.3 and 57.6% respectively for the different water flow rates. At 28.8LPM airflow, 30, 42.3, 50, 0.2 and 70.8% respectively for the different flow rates were observed. For 38.8LPM airflow rate, between the healthy and faulty valve conditions, 30.1, 32.1, 66.6, 44.5 and 38.4% variations respectively have been observed from healthy to faulty valves condition.

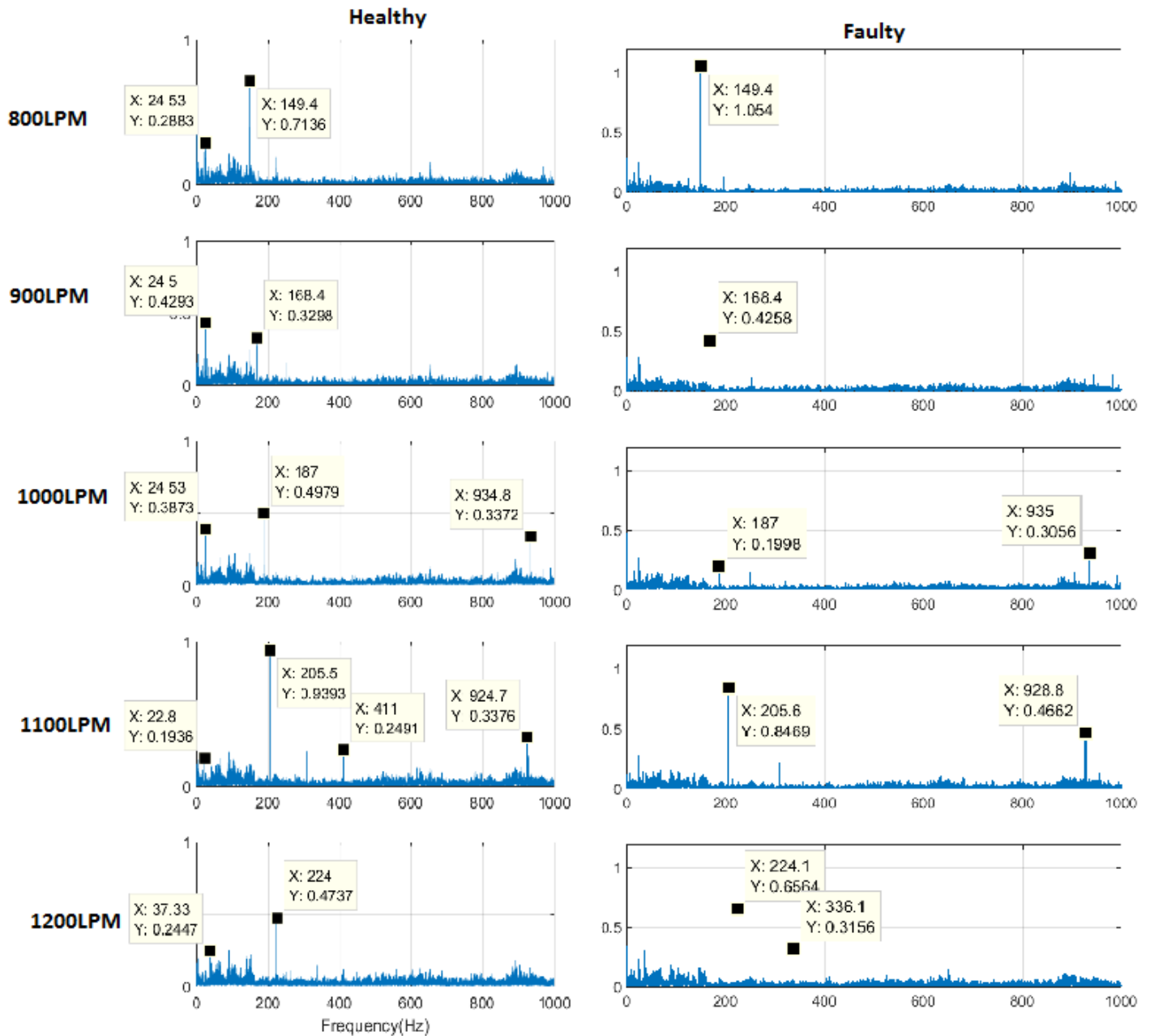


Figure 6.15: FFT for 19.8LPM airflow, comparing healthy and faulty valve at different water for 60% VOP

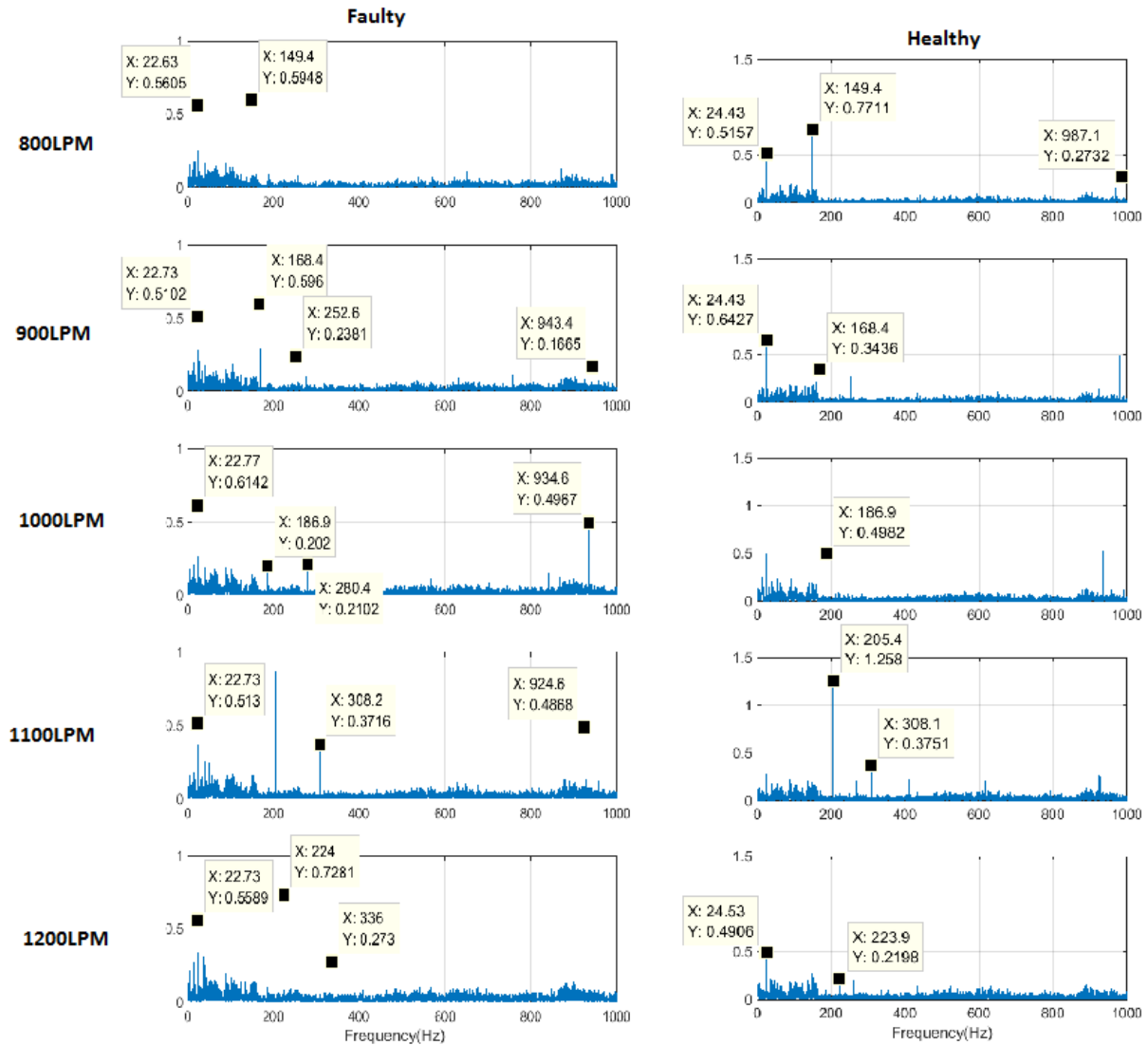


Figure 6.16: FFT for 28.8LPM airflow, comparing healthy and faulty valve at different water for 80% VOP

### B. Mean Frequency

Figure 6.17 shows the acoustic mean frequency as a function of flow rates for faulty and healthy valves condition. For 60% VOP, the acoustic mean frequency can be seen to increase slightly from the healthy to faulty valve for just the low flow rates. This can again be due to lesser acoustics obtained for the faulty valve at the low flow rates, therefore expanding further the entire frequency spectrum for these flow rates. If the acoustic frequency components are higher, which is experienced at lower frequencies, the mean frequency becomes lower. Secondly, the reason might be due to one off experimental uncertainty from the measured data.

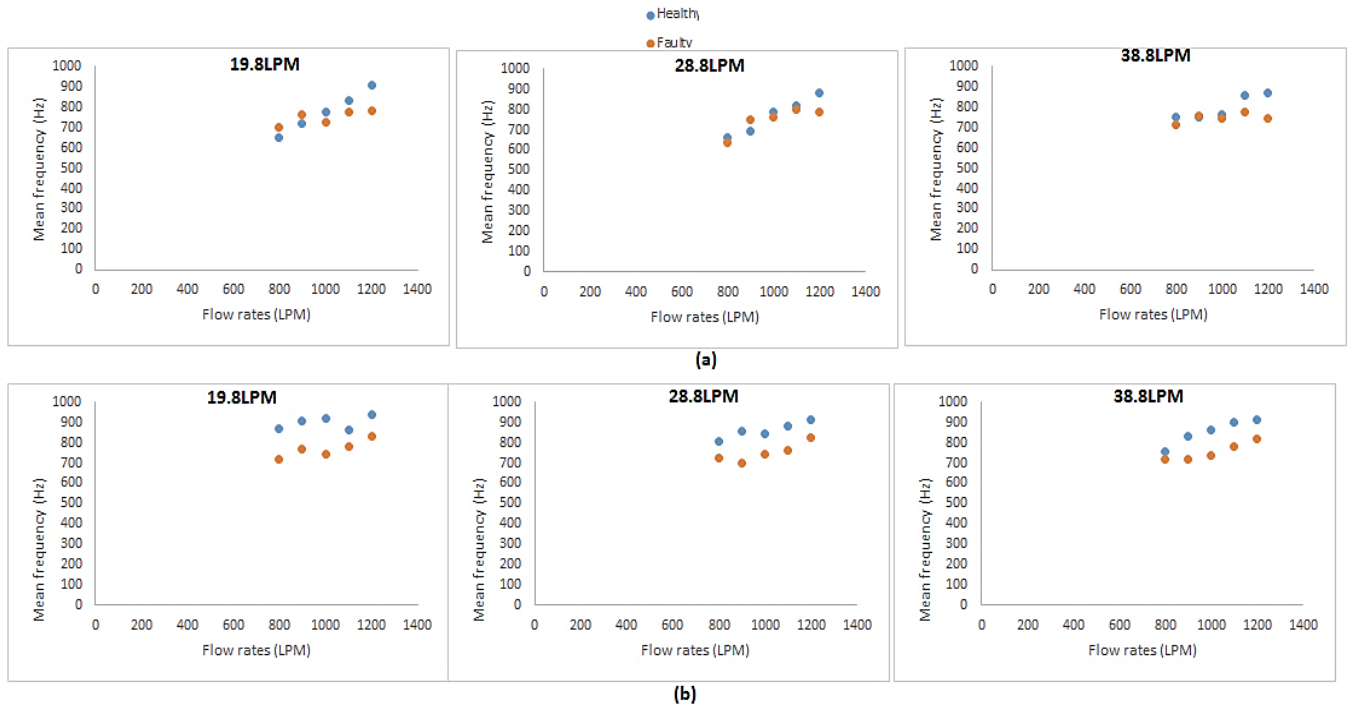


Figure 6.17. Mean frequency for the valve at different air flow rates (a) 60% (b) 80%

For 60% VOP, acoustic multiphase mean frequency decreases from healthy to faulty valve for higher flow rates. At lower flow rates (800 and 900LPM), mean frequency slightly increases at 7.9 and 5.8% respectively for 19.8LPM airflow. For 1000, 1100 and 1200LPM, the percentage decrease from the healthy to faulty valve condition observed are 5.8, 6.6 and 13.2% respectively. At 28.8LPM airflow, from the healthy to faulty valve, multiphase mean frequency increases at the rate of 8.1% for 900LPM and 3.4, 3, 2.6 and 10.3% for 800, 1000, 1100, and 1200LPM water flow rates respectively. At 38.8LPM, the percentage variation decrease from healthy to faulty valve observed are 4.9, 0.6, 2.3, 9.7 and 14.4% respectively across the different water flow rates.

For 80% VOP, multiphase mean frequency for the acoustic signal decreases from the healthy to faulty valve for all airflow rates, across the different water flows. Acoustic mean frequency for the multiphase flow comparison, between the healthy and faulty acoustic signal for the valve decreases at 17.4, 15.4, 19.3, 9.2 and 11.3% respectively for the different water flow rates at 19.8LPM airflow. At 28.8LPM air flow, from healthy to faulty valve, multiphase mean frequency decreases at the rate of 9.6, 18.2, 11.8, 13.5 and 9.9% respectively for the different water flow rates for the acoustic signals. At 38.8LPM,

the percentage variation decrease observed from healthy to faulty valve are 4.7, 13.7, 14.5, 13.6 and 10.7% respectively for the different water flow rates.

## 6.6 SUMMARY

This chapter has established the acoustic behaviour of the control valve for the different flow and operating conditions, for single and multiphase condition, and using acoustic indicators in detecting faults when they occur. The advantages of this technique have been described with setback that are likely to occur in using this technique. It has been shown that the probe placed inside the valve have no effect on the acoustic signatures for similar conditions. The acoustic signals have been analysed in in both time and frequency domain, using RMS, Peak-to-Peak, Kurtosis and standard deviation in time domain, FFT and mean frequency in frequency domain. The results have also been analysed for single and multiphase flow and the flow regime changes from single to multiphase have been established for different flow rates and VOPs. Multiphase flow have been created by injecting air at different airflow rates.

Finally, faults have been created inside the valve, where acoustic indicators have been used to distinguish the faulty valve from healthy valve condition and to establish how their acoustic behaviour changes with such indicators and how this technique can be used to detect such fault.

## CHAPTER SEVEN

### 7.0 CONCLUSION AND FUTURE WORK

---

*In this chapter, the different conclusions drawn from this research have been presented with explanations provided for each objectives listed in chapter two and how they were achieved. This chapter evaluates and compares the various techniques that have been used in establishing flow characteristics behaviour and fault detection inside the control valve. Also, included in this chapter are the achievements, knowledge contributions and the research novel aspects. The major results have been obtained in condition monitoring and flow diagnostics using the MHP and vibro-acoustic techniques on the control valves.*

*Finally, recommendation for future work on flow diagnostics and condition monitoring of the control valve have been given that would, in the opinion of the author, improve the control valve health and performance monitoring, and flow diagnostics.*

## 7.1 SYNOPSIS TO THE RESEARCH PROBLEMS

Many researchers, over the past few decades, have used numerical techniques (CFD) in studying the local and global flow behaviour inside the control. Most researches, using CFD have only done simplified 2D flows and simple valve/trim geometries. The valves are used for different applications in oil and gas, chemical, water, power plant industries, etc. Ensuring that the valve performs optimally at all times, it is therefore paramount to monitor the condition in diagnosing how flow features behaves in order to improve and detect faults in the control valve. In order to simulate real life effect of cavitation, air bubbles have been injected in order to investigate and understand how flow regime changes from single to multiphase flow conditions. The air injection causes the noise and vibration characteristics to change, causing flow instability, leading to fluctuations in the pressure signals. Based on these conditions, different techniques have been used. Local and global parameters have been analysed using different techniques for fluid diagnostics and CM in order to increase the valve life span. These techniques include using the MHP for local flow analysis, while vibration and acoustics under various operating and flow conditions are used for global flow analysis. . In this chapter, the main aim and objectives have been summarised along with their contributions and achievements.

## 7.2 MAIN AIM AND ACHIEVEMENTS REVIEW

The contributions and achievements that have been made during this research have been described in this section. Emphasis on fluid diagnostics and CM of the control valve have been made. Both numerical and experimental studies have been carried out on MHP, vibration and acoustic techniques in investigating flow behaviour for the control valve, under different flow and operating conditions. The recorded achievements established for this research have been presented.

**Research Aim: The Investigation and Establishments of flow characteristics and detection of fault on the control valve under various flow and operating conditions using intrusive and non-intrusive techniques.**

This aim has been divided into three main achievements because of the three different intrusive and nonintrusive techniques used. The techniques includes Multihole probe (intrusive), vibration (nonintrusive) and acoustic (nonintrusive).

**Achievement # 1:** In this research, the MHP (Multihole probe) has been used to investigate the flow structure inside the control valve for single-phase condition. In this study, numerical simulations, using CFD, has been used to first investigate the different effects of different MHP heads inside the flow domain, before being applied experimentally. Before the simulation was conducted, the model was first validated with experimental data. Also, numerical simulation has also been carried out, as to validate, for the different probe placement positions, how average velocity increases as flow rate increases. The third aspect corresponds to the probe calibration (invasively), where different calibration coefficients have been obtained for flow parameters calculations in an unknown stationary flow field. The MHP has been used due to their durability and robustness, easier to use and lower cost. This will allow for the extraction of the valve flow parameters, including the quantification of the flow behaviour from inlet to outlet of the valve for single-phase condition, healthy and faulty conditions. Global (2D and 6D) and local (position 1, 2 and 3) valve performances of the valve have been analysed where pressure drop have been obtained, and their different  $C_v$  calculated, for different flow rates and at different VOPs. Across each probe position, seven measurements heights across that position have been made in order to determine the velocity profile and see how flow parameters vary. Furthermore, the current study provides local flow variation for several flow parameters as flow area inside the valve changes from inlet to outlet, and how these parameters changes for a healthy valve, in comparison to a faulty valve. These parameters, when accurately obtained can be used in detecting faults and help to better design the control valve for improved performance. In using this technique,

- Complex flow inside the control valve can be determined
- Help improve the valve design
- Durable and very robust
- Inexpensive

**Achievement # 2:** This research has provided detailed results of the condition monitoring on the control valve using vibration as a tool. As explained earlier in chapter five, vibration technique in the past, has been widely used in monitoring machines.

Analysis of the valve performance and behaviour have been carried from the experimental results under different flow and operating condition and detect fault inside

the control valve using vibration as a tool for both single and multiphase condition. For the control valve reliability to be increased for fault detection, vibration technique as a tool can be very effective. Combined use of the vibration technique with MHP can give a better holistic fault detection including the underlying mechanism. Based on the thorough investigation, experimentally, the control valve vibration signals have been obtained and analysed. The results obtained from experiment for the control valve setup have shown that the vibration signals vary highly with different flow and operating conditions. The results analysed have showed that the multiphase or fault detection using vibration depends on the flow rate and VOPs and it increases when the flow rate increases and VOP decreases. The results seen in this research have shown that when faults occur, flow parameters change, causing inaccuracy of what was to be expected and reduction in the valve performance. It can also lead to reduction in the life span and can cause deterioration of the valve as the vibration signals have been seen to change as flow and operating condition changes when compared to the healthy valve. This has shown that the signals are very sensitive to any valve slight changes. The valve vibration signal amplitude can be seen to increase as flow rate increase, making time and frequency domain analysis a good indication in predicting any valve faults. Several statistical features analysis used for this research have shown that the measured vibration signal can be efficient in valve diagnosing and monitoring faults. Furthermore, the results also showed that FFT and the mean frequency are also effective for fault detection in the control valve.

**Achievement # 3:** This study has provided detailed condition monitoring (CM) using acoustic technique as a tool for the control valve with detailed explanation given in chapter six. This technique has been widely used in monitoring complex machines because of their importance. Their advantages and disadvantages have been given in chapter six technique. Because of how sensitive they are to the surrounding noise from other machines, all measurements from the experiment have been carried out in surrounding where no other machine is in operation in the lab.

This sub aim has analysed and predicted the valve behaviour for both healthy and faulty valve experimentally, using acoustic technique under different flow and operating conditions, for single and multiphase conditions. Based on the detailed measurements obtained experimentally, the control valve acoustic signals have been analysed. In

increasing the reliability and fault detection in the valve, the acoustic technique has been used for this purpose. A combination of different techniques (MHP, vibration and acoustic techniques) gives a more holistic analysis of detecting faults inside the valve. The acquired acoustic signals for the valve have been analysed in time domain using statistical features as those mentioned in chapter five for the vibration signal. In addition, the acquired acoustic signals have been analysed using FFT and mean frequency in the frequency domain to obtain detailed information regarding flow regime changes and when fault in the valve has occurred, and how to differentiate between a healthy and faulty valve signal. The results have showed that when the faults occur inside the control valve, the level of the noise slightly increases, leading to an increase in the amplitude of the acoustic signals. In addition, when flow regime changes from single to multiphase, acoustic signature changes in both time and frequency domain features, as their level increases. All of these results have showed that acoustic techniques, as an indicator, can be effective in predicting faults and detecting flow regime changes inside the valve.

### 7.3. THESIS CONCLUSIONS

A holistic investigation has been conducted to support existing literatures regarding the fluid diagnostics and condition monitoring of the control valve using different techniques, under various flow and operating conditions, in order to provide and improve the current understanding of flow behaviour inside the valve and fault prediction, in improving the valve performance. The key conclusions from each of the objectives for this research have been summarised as follows:

**Research Objective # 1: To investigate the effect of the different probe lengths and heights on the control valve flow characteristics under single-phase condition from inlet to outlet using the Multihole probe (MHP).**

From the obtained MHP results, investigations regarding the control valve flow behaviour and fault detection analysis based on single-phase flow condition have been conducted. This objective has been divided into three main sections. The first section including the mesh independence test, valve model validation with experimental data and effect of different probe heads on the valve flow fields. The result showed that for the model validation between CFD and experimental data, an average of 11.3% difference was obtained, making the model results acceptable. Also, hemispherical head show a

closer percentage difference of 3.2% as compared to 3.9% for conical head in comparison to the reference geometry. After the probe head has been chosen from CFD, the chosen probe head (hemispherical head) then needs to be calibrated. Detailed experimental calibration procedure have been given in chapter three. The third section requires using the obtained calibration coefficients to determine the local flow parameters inside the valve. The results from the calibration showed that both yaw and pitch angle validation fall within the  $\pm 10\%$  range from the verified angles. The inlet pressure have been seen to increase as flow rates increases while the outlet pressure remains nearly the same, causing increase in the pressure drop. As the flow rate increase for 10% VOP,  $\Delta P$  from position 1 to 2 and from 2 to 3 goes from 15.5 to 14.98 to 14.48PSI, representing 3.5 and 3.38% reduction respectively. All other VOPs show similar decrease for MHP lengths effect on the pressure drop. As pressure drop reduces, the  $C_v$  increases. From global to position 1, to position 2 and to position 3,  $C_v$  values increases from 4.53 to 4.62 to 4.75 and to 4.84 respectively for 10% VOP. Again, same trend is seen for the other VOPs.

For the  $C_v$  of the entire control valve system, the percentage increase from 10 to 20, 20 to 40, 40 to 60 and from 60 to 80% VOP obtained are 29, 17.5, 6.1 and 2.7% respectively across the different VOPs. Furthermore, regression analysis with multiple variables have been carried out on the results presented in this objective. A percentage error of 4.8% was obtained, making the equation capable of predicting the  $C_v$  as a function of VOP with more than 96% accuracy.  $K$  values has also been obtained for this objective across the different VOPs.  $K$  values increase as the VOP increases. The percentage increase from 10% to 20% VOP observed for  $K$  values are 2.4, 3, 36.4, 25.8 and 20.2% respectively across the different measurement positions. Similar trend is also seen for 20 to 40%, 40 to 60% and 60 to 80% VOPs. Novel  $K$  values have also been obtained as a function of Reynolds number for the different sections of the valve for various flow rates. At 800LPM, 1.5, 3.1, 3.09 and 3.12 have been recorded for  $k_1$ ,  $k_2$ ,  $k_3$  and  $k_4$ , Reynolds number calculated are 10098, 8918.6, 7667.4 and 7845.4 respectively for 10% VOP.  $K$  value increases as VOP increase from 10 to 20% VOP, 20 to 40%, 40 to 60%, 60 to 80% VOP as Reynolds number increases. Similar increase was recorded for the other flow rates. Again,  $K$  value for the control valve system ( $K_{\text{control valve system}}$ ) as a function of the Reynolds number and valve opening positions (VOPs) using regression analysis with multiple variables have been carried out on the results. A percentage error of 2.25% was observed,

making the equation capable of predicting the K value as a function of Reynolds number and VOP with more than 97% accuracy.

**Research Objective # 2: Development of flow measurement indicators in establishing flow behaviours and detecting fault under Single-phase flow condition inside a control valve using the MHP.**

This study has provided a detailed investigation using the MHP on the flow diagnosis and fault detection inside the control valves. This has shown how local and global flow varies for healthy and faulty valve for different flow and operating condition for the valve. The study uses the experimental facility and same procedure as healthy valve, except that fault has been created inside the valve by blocking one of the four trim flow path. The data have been analysed for different flow rates in order to study flow parameters effects for wide flow rate ranges at different VOPs. The results for the faulty valve analysis have been compared, for similar conditions, to that of healthy valve. The results show that for same MHP position, pressure drop increases from healthy to faulty valve across the various flow rates. For 60% VOP, the MHP was able to detect pressure drop difference across the entire flow rate range from healthy to faulty valve at a percentage increase of 3.1, 2.4, 2.6, 2.2 and 1.8% respectively. For 80% VOP, percentage increase of 1.7, 2, 2.1, 2.2 and 2% respectively was observed for the same flow rates from healthy to faulty valve. Because of this increase of local and global pressure drop from healthy to faulty valve; this has made the valve Cv to decrease from healthy to faulty valve. As the Cv increases from 16.4 for faulty to 18.7 for healthy value, representing a 12.16% increase for 60% VOP. At 80% VOP, global Cv increases from 20.69 for faulty to 23.66 for healthy value, representing a 12.53% increase. This fault has caused, for same VOP, the flow rate to reduce, creating more flow restrictions. Again, MHP has been able to detect fault for local sectional pressure drop of an average of 1.53% for the entire flow rates from a healthy valve. Finally, as the local Cv increases from 17.07 for faulty to 19.245 for healthy value, representing an 11.3% increase for 60% VOP. For 80% VOP, local sectional Cv increases from 21.2 for faulty to 24.2 for healthy value, representing a 12.53% increase.

**Research Objective # 3: Development of vibration indicators in establishing fault in a control valve under single-phase condition.**

Even though it could not be 100% ascertained that some sort of cavitation has occurred in the valve, additional fault was created using the valve trim inside the control valve. Based on this fault, vibration characteristic have been established for single-phase and compared with vibration signals from a healthy valve. Again, investigations have been carried out in time and frequency domain. Investigations regarding the effect of different VOPs and flow rates on the performance and fault prediction inside the control valve using vibration as a tool have been presented. It can be concluded that the vibration features in time domain increases when compared to healthy valve for similar flow and operating condition. This is because flow restriction reduces, causing the same amount of fluid to pass through the same trim, this time, with less flow area, causing the vibration to increase. Analysis in time domain for the vibration signal using different statistical features such as RMS, Peak-to-Peak, Kurtosis and SD, all provided good indications in fault detection inside the valve under different VOPs and flow rates. For the faulty valve, the vibration amplitude, in the form of RMS value increases, from healthy valve condition, at 34.9, 32.9, 27.6, 27 and 5.3% for 60% VOP and 44.8, 38.2, 32.2, 30.5 and 55.1% for 80% VOP for the different flow rates with Peak-to-peak, standard deviation and Kurtosis showing similar trends in time domain. In addition, the vibration signal analysed in frequency domain in investigating the vibration behaviour can satisfactorily detects the inception and development of faults inside the valve for different flow rates and VOPs. In frequency domain, the percentage maximum frequency amplitude variations, from faulty to healthy valve, at same conditions were 66.6, 72.2, 81.8, 36 and 18.7% respectively for 60% VOP and 65.5, 30, 83.3, 65.5 and 42.3% respectively for 800, 900, 1000, 1100, 1200LPM at 80% VOP. For 60% VOP, the mean frequency is observed to decrease for the faulty valve condition from healthy valve at the rate of 73.5, 81.1, 87.5, 87 and 88%, and 80.1, 83.7, 87.9, 92.5 and 93.6% respectively for 80% VOP across the various flow rates.

**Research Objective # 4: Development of vibration indicators in establishing fault in a control valve under Multi phase condition.**

Again, based on this fault, vibration characteristic have been established for multiphase flow conditions and compared with multiphase vibration signals for a healthy valve. Investigations for the multiphase flow condition have been carried out again in time and frequency domain. Investigations regarding the effect of different VOPs and flow rates on the performance and fault prediction inside the control valve using vibration as a tool

have been presented. It can be concluded that the vibration features in time domain increases for multiphase condition, when compared to healthy valve for similar flow and operating conditions. Analysis in time domain for the vibration signal for multiphase condition using different statistical features such as RMS, Peak-to-Peak, Kurtosis and SD, all provided good indications for fault detection inside the valve under different VOPs and flow rates. At 60% VOP, for 19.8LPM airflow, the results showed that RMS value increases, from healthy valve condition, at 11.6, 9.6, 5.7, 21.6 and 16.8% for the different flow rates. At 28.8LPM airflow, percentage increase from healthy to faulty valve for the different water flow rates are 13, 15.1, 4.8, 7.9 and 21.3% respectively and finally for 38.8LPM airflow from healthy valve, percentage increase recorded are 17.4, 11.1, 3.3, 6.5 and 17.8% respectively. Similar trend is again seen for 80% VOP for the different air and water flow rates. Again, peak-to-peak, kurtosis and standard deviation all show similar trends as that of RMS. In addition, the multiphase flow vibration signal analysed in frequency domain in investigating the vibration behaviour can satisfactorily detects the inception and development of faults inside the valve for different flow rates and VOPs. 50, 39.1, 82.9, 56.7 and 60.2% respectively for the different water flow rates for the faulty condition were observed using the vibration technique at 19.8LPM airflow. At 28.8LPM airflow, 28.1, 30, 40.6, 32.6 and 1% respectively for the different flow rates and for 38.8LPM airflow, 38.4, 42.8, 33.3, 14.2 and 30% respectively have all been observed from healthy to faulty valve condition. Again, similar trend were observed for 80% VOP for similar air and water flow rates conditions. For mean frequency analysis, at 60% VOP, mean frequency decreases at 93, 96.2, 96.3, 90.6 and 90.66% respectively across the different flow rates for 19.8LPM airflow, 93.9, 93, 96.7, 93.8 and 89.19% respectively for airflow of 28.8LPM, and 95.1, 94.6, 96.6, 93.8 and 93% respectively for 38.8LPM airflow. Similar trend was observed for 80% VOP.

**Research Objective # 5: Development of acoustic indicators in establishing fault in a control valve under single-phase condition .**

Acoustic characteristic have been established, based on the fault created, for single-phase and compared with acoustic signals from a healthy valve. Investigations have been carried out in both time and frequency domain. Investigations regarding the effect of different VOPs and flow rates on the performance and fault prediction inside the control valve using acoustic as a tool have been conducted. It can be concluded that the acoustic

features in time domain slightly increases when compared to the healthy valve for similar flow and operating condition. Analysis in time domain for the acoustic signals using different statistical features such as RMS, peak-to-peak kurtosis and SD, all provided good indications in fault detection inside the valve under different VOPs and flow rates. For 60% VOP, RMS value for the acoustic signal decreases, from healthy valve condition, for the faulty valve at 2.2, 0.6, 0.4, 0.3 and 4.8% for the different flow rates and 0.2, 3.4, 5.3, 4.4 and 1% at 80% VOP. Peak-to-peak, standard deviation and Kurtosis comparison between the healthy and faulty acoustic signals for 60 and 80% VOPs at same flow rates showed similar trends as that of RMS values. In addition, the acoustic signal analysed in frequency domain in investigating the acoustic behaviour can satisfactorily detects the inception and development of faults inside the valve for different flow rates and VOPs. Again, from faulty to healthy valve, at similar conditions, the microphone was able to measure a percentage difference of 54.7, 33.3, 54.8, 7.8 and 71% respectively for 60% VOP and 41, 21.5, 8.5, 29.2 and 42.4% respectively at 80% VOP for 800, 900, 1000, 1100, 1200LPM flow rates. For 60% VOP, the mean frequency from healthy to faulty valve is seen to only increase at 800 and 900LPM by 3.4 and 10.8% respectively. At higher flow rates (1000, 1100, 1200LPM), mean frequency decreases at the rate of 12.7, 26.3 and 12.5% respectively from healthy to faulty valve condition. At 80% VOP, mean frequency decreases from healthy to faulty valve, except for the lowest flow rate (800LPM) at 7.1%. Again, this can be due to lesser acoustic signals obtained for the faulty valve at the low flow rates, therefore expanding further, the entire frequency spectrum for this flow rates. It can also be due to one off experimental uncertainty from the measured data. For higher flow rates (900, 1000, 1100, 1200LPM), 4.1, 9, 4.2 and 9.3% respectively was observed for the mean frequency, from healthy to faulty valve.

**Research Objective # 6: Development of acoustic indicators in establishing fault in a control valve under Multi phase condition.**

Again, based on this fault, acoustics characteristic have been established for multiphase flow condition and compared with multiphase acoustic signals for a healthy valve. Investigations for the multiphase flow condition have been carried out again in time and frequency domain. Investigations regarding the effects of different VOPs and flow rates on the performance and fault prediction inside the control valve using acoustics as a tool have been established. It can be concluded that the acoustic features in time domain

slightly increases for multiphase condition for faulty valve, when compared to healthy valve for similar flow and operating conditions. Analysis in time domain for the acoustic signal for multiphase condition using different statistical features such as RMS, Peak-to-Peak, Kurtosis and SD, all provided good indications for multiphase fault detection inside the valve under different VOPs and flow rates. For 60% VOP, for multiphase faulty valve, the RMS acoustic amplitude increases, from healthy valve condition, at 1.5, 1.5, 0.3, 1.2 and 1.6% for the different flow rates at 19.8LPM airflow. At 28.8LPM airflow, 2.3, 2.6, 2.59, 2.7 and 2.4% respectively was observed and for 38.8LPM airflow from healthy valve, percentage increase recorded are 2.1, 1.9, 1.9, 3.1 and 3.3% respectively.

For 80% VOP, RMS multiphase value decreases for 19.8LPM airflow at the rate of 3.8, 5.3, 6.8, 6.2 and 2.5% for the faulty valve. At 28.8LPM airflow, 4.2, 6.2, 6.9, 3.4 and 4% respectively was observed and for 38.8LPM airflow from healthy to faulty valve, percentage variation recorded are 6.8, 5.9, 8.2, 7.1 and 4% respectively for the different flow rates. Peak-to-Peak, Kurtosis and standard deviation analyses have also be carried out for similar conditions as the one presented for RMS values.

In addition, the multiphase flow acoustic signals analysed in frequency domain in investigating the acoustic behaviour can satisfactorily detects the inception and development of faults inside the valve for different flow rates and VOPs. For 60% VOP, at 19.8LPM, the maximum amplitude at those frequencies have a percentage variation increase from healthy to faulty at the rate of 33, 23.8, 37.9, 10.7 and 27.6% respectively for the different water flow rates. At 28.8LPM airflow, 36, 22.8, 56, 19.3 and 32.8% respectively for the different flow rates were observed. For 38.8LPM airflow, 17.3, 37.2, 76.2, 9.5 and 29.3% respectively have been observed from healthy to faulty valve condition.

For 80% VOP, the maximum amplitude at these frequencies have been compared for faulty and healthy valve. Comparing at 19.8LPM, at similar frequencies, the maximum frequency amplitude percentage variation from healthy to faulty at the rate of 21, 31.4, 5.2, 33.3 and 57.6% respectively were observed. At 28.8LPM airflow, 30, 42.3, 50, 0.2 and 70.8% respectively were observed and at 38.8LPM airflow rate, between healthy and faulty valve condition, 30.1, 32.1, 66.6, 44.5 and 38.4% variations respectively have been observed for the different flow rates. For 60% VOP, acoustic multiphase mean frequency

decreases from healthy to faulty valve for higher flow rates. At lower flow rates (800 and 900LPM), mean frequency slightly increases at 7.9 and 5.8% respectively for 19.8LPM airflow. For 1000, 1100 and 1200LPM, the percentage decrease from healthy to faulty valve condition observed were 5.8, 6.6 and 13.2% respectively. At 28.8LPM air flow, from healthy to faulty valve, multiphase mean frequency increases at the rate of 8.1% for 900, 1000, 1100 and 1200LPM, 3.4, 3, 2.6 and 10.3% were observed. For 38.8LPM, 4.9, 0.6, 2.3, 9.7 and 14.4% respectively were observed across the different water flow rates. Again, similar results at 29.8, 28.8 and 38.9LPM airflow rates for 80% VOP for the mean frequency analysis were also seen.

#### **7.4. THESIS CONTRIBUTION**

In this research, the major contributions in the field of flow diagnostics and condition monitoring of the valve in detecting faults are summarised as follows:

##### **Contribution # 1**

The first key contribution of this research is that a holistic investigation on local and global flow field characteristics on the control valve under single and multiphase conditions have been carried out for healthy and faulty valve. Literatures available regarding the static pressure, pressure drop, velocity, global and local  $C_v$ ,  $k$  value, pressure coefficients, etc. inside the control valve are limited. The MHP has been extensively used to carry out local investigations on the above-mentioned parameters inside the valve for single-phase healthy and faulty conditions. The results presented in chapter four have shown that MHP can be a very effective and useful tool to diagnose fluid flow and detect faults in order to improve the valve performance under single-phase with reasonable accuracy. In this research, fault has been created and investigations conducted in providing useful information regarding the detection of fault. These investigations, using the MHP, have been performed in establishing the inter-dependence of different flow parameters to enable for the valve performance characteristics estimation. Both qualitative and quantitative analysis have been used for the  $C_v$ , static pressure drop and velocity magnitude under single-phase condition. The influence of different probe heights and lengths placed inside the valve have been investigated for flow parameter measurements.

### **Contribution # 2**

Local Cv and k value are calculated using static pressure drop between two sections, which usually have the same flow area. In the case of the valve, flow area inside varies due the valve complex geometries. When static pressure has been used, negative Cv is obtained. Therefore, instead of using static pressure, total energy has been used by adding the dynamic pressure to the static pressure. The author believes that very limited or no literature exists where the total energy been used for Cv calculation, making it a new method due to the valve complex geometry. Regression analysis has been used in developing an equation by which the Cv for the entire control valve system can be obtained as a function of VOPs. This equation gives more than 96% accuracy in predicting this Cv, making the equation very useful for the design of control valves.

### **Contribution # 3**

One key contribution in this research has been the flow loop design for the control valve. This test rig has been designed in such a way what the holes are drilled in the valve through the valve bonnet, to allow easy access to insert the MHP, in order to be able measure flow parameters inside the control valve under different operating conditions (healthy and faulty conditions). The design and construction of the experimental setup was to determine the performance of the valve in order to detect the faults. This setup makes it easier to use several techniques for faults detection under various flow and operational conditions. This has made it easier for several techniques to be used concurrently to investigate the valve characteristics in a controlled manner using MHP, acoustics and vibration techniques. From extensive literature review, limited researchers have explored flow regime changes from single to multiphase flow using vibration and acoustics as a tool. This research has analysed those changes. It has been seen that as flow changes from single to multiphase flow, vibration characteristic increases based on the different parameters used for this research, in both time and frequency domain. As the airflow rate increases, the vibration amplitude increases because of the increase in air bubbles, which coalesce with each other or break into smaller bubbles. As a result, vibration increases. For acoustic characteristics, similar observation was noticed in both time and frequency domain. RMS, kurtosis, Peak-to-Peak and SD in time domain and FFT

and mean frequency in frequency domain have all been used in analysing these flow changes

#### **Contribution # 4**

For this research, detailed investigations have been carried out on faults characteristics inside the valve using MHP, acoustics and vibration techniques at different flow and operating conditions as seen in chapters 4, 5 and 6. This study carried out on the valve has provided a clearer understanding and vital information regarding fault detection experimentally using the techniques mentioned above. An extensive study has been made to compare and decide on an adequate technique to reliably and accurately monitor and detect faults using the above-mentioned techniques. The author believes that simultaneously using all of the three techniques for fault detection on the control valve under different flow and operating conditions is a key contribution to knowledge, as no literature exists for this purpose.

In experimentally detecting control valve faults, under different flow and operating conditions (air and water flowrates and VOPs), this research has effectively used statistical features, measurements in both time and frequency domain. Extensive research in comparing between all of these features based on both vibration and acoustic techniques have been discussed in chapters five and six respectively. A well holistic comparison can therefore be established using all these feature and a well-informed decision can be made for analysing signals in time and frequency domain, establishing their strengths and determine what feature suits what application for the valve.

#### **Contribution # 5**

For this research, vibration and acoustic experimental techniques have been used for valve fault detection in frequency domain. The valve have natural frequencies, though not readily available in literatures, occur at very low frequency. The frequency information obtained for the valve can be included for valve manufacturers' data sheet, to know what maximum vibration or acoustics produced by the valve are allowed. Any frequency above maximum allowed frequency for a particular valve condition can lead to faults and reduce the valve performance and life span. The most sensitive frequency range for the valve is seen to occur between 0-1000Hz, with the most sensitive occurring between 0-300Hz,

which are mostly flow induced. In addition, faults occurring at these frequencies increases the amplitudes when compared to a healthy valve. Using both the acoustic and vibration technique helps to decrease the computation attempts (which are expensive) and reduce the sensors cost. This research has found that the signals frequency range between 0Hz and 300Hz was more sensitive to detect the faults in the valve when compared to a healthy valve. Because of these findings, microphones and accelerometer sensors with a low frequency range have allowed for decrease in the sensor cost when compared to using sensors that have high frequency range. Another main contribution is using the different techniques explained in chapter 4, 5 and 6 towards the detecting of fault within in a control valve. As observed for this current experimental study, the use of these techniques is not only capable of detecting the occurrence of this particular fault, but can be used also for future work in detecting different fault types inside the valve.

### **Contribution # 6**

Another novel contribution is determining the  $k$  value for the different valve section and how  $k$  is varying as a function of Reynolds number for the different VOPs.  $K$  remains constant across flow rates, but varies along the valve sections and across the different VOPs. This has been seen chapter four. Because the different flow sections have different area, their hydraulic diameter then varies, and thereby increasing the Reynolds number, as dynamic viscosity and water density remains the same. As the VOP increases, Reynolds number increases, and at same VOP, Reynolds number inside the valve increases as the flow rate increases. Again, as flow goes from inlet to outlet, Reynolds number is seen to vary as the hydraulic diameter changes. This result can prove to be a vital knowledge in the design of the valve for optimum performance and longevity. Regression analysis has been carried out in developing an equation by which  $k$  value for the control valve system can be obtained as a function of Reynolds number and VOPs. This equation gives more than 97% accuracy in predicting this value, making the equation very useful for the valve designs.

## **7.5. FUTURE WORKS**

Further works relating fluid diagnosis and fault detection inside the control valve have been presented:

1. Data have been obtained using MHP in multiphase condition but have not been analysed. Calibration of the probe has only been done for single-phase. To analyse multiphase data, calibration would then need to be done in multiphase condition and obtain different sets of calibration coefficients, in order to determine flow parameters for an unknown flow field.
2. Using machine learning to identify faulty behaviour. This can be done by uploading data/signal into this code and based on the code parameters, the code can identify if the data from the control valve is a from faulty or healthy condition.
3. Also using machine-learning codes to identify volume fraction in multiphase flow conditions. Again, this code can identify, for multiphase condition, the volume fraction of water and air present in the valve.
4. Determining the faults in the valve seat and valve plug caused by erosion/cavitation. This can be detected using the different techniques used in this research, or including other techniques to detect such faults.
5. Obtaining the Cv of the seat and that of the trim, by combining both experimental and CFD techniques.
6. Investigation into other types of faults inside the valve such as bent stem, worn trims, stiction, etc. using the techniques described in this thesis or any other proven techniques.
7. Experimentally investigation on how flow behaves for different trim designs and, making comparisons, and how faults created on these trims can be detected using the different techniques used for this research.
8. Common studies using the control valves concentrates more on water as the working fluid. The control valve can also be used for many other applications including oil and gas, petroleum industries, sewage treatment plants etc. Therefore, for future work, different working fluid effect on control valve performance and detecting faults using similar techniques used in this research can also be conducted.

## REFERENCES

---

1. L. Zhang, C. Xia, J. Cao, J. Zheng (2012). Physical-based Modeling of Nonlinearities in Process Control Valves.
2. Q. Yang, Z. Zhang, M. Lui and J. Hu. " Numerical simulation of Fluid flow inside a valve". *Procedia Engineering* 23 (2011).
3. A. Yantao, C Fang (2010). "ETMD System in Vibration Control of Control Valve and Friction Compensation", International Conference on Electrical and Control Engineering.
4. R. Amirante, G. Del Vescovo, A. Lippolis (2005). Evaluation of the flow control forces on an open center directional control valve by means of CFD analysis.
5. Douglas O.J, 2001. *Instrumentation Fundamentals for process control*. Senior Applications Engineering consultant, Retired, Foxboro G.B Limited. Published by Taylor and Francis, London, EC4P 4EE.
6. IEEE Global Spec (1998). Chapter 2 – The history of control valves. Available [online] <https://www.globalspec.com/reference/13607/179909/chapter-2-the-history-of-control-valves> (Accessed 13/11/2015).
7. Fassitelli, E.F.y.L. (2016). *The History of the Valves*. <http://www.valvias.com/history.php>.
8. Borden, G (1998). *Control Valves: Practical Guides for Measurement and Control*.
9. IHS Engineerin360, 2015. Chapter 9- Control valve trim. Available online <http://www.globalspec.com/reference/13614/179909/chapter-9-control-valve-trim> (Accessed 6/12/2015)
10. DOE-HDBK-1993. Department of Energy Fundamentals Handbook. MECHANICAL SCIENCE Module 4 on Valves. Available on line [http://www.constructionknowledge.net/public\\_domain\\_documents/Div\\_15\\_Mechanical/HVAC/Valves\\_DOE\\_Fundamentals.pdf](http://www.constructionknowledge.net/public_domain_documents/Div_15_Mechanical/HVAC/Valves_DOE_Fundamentals.pdf) (Accessed 3/12/2015)
11. R. Zhao, R.Q. Xu, Z.H. Shen, J. Lu, X.W. Ni. Experimental investigation of the collapse of laser-generated cavitation bubbles near a solid boundary; *Opt Laser Technol*, 39 (2007), pp. 968–972
12. B. Carlson. Avoiding cavitation in control valves. *ASHRAE J*, 43 (6) (2001), pp. 58–63

13. F.G. Hammit. Cavitation and multiphase flow phenomena. McGraw-Hill Inc., USA (1980)
14. H. Hassis. Noise caused by cavitating butterfly and monovar valves<sup>1</sup>. J Sound vibr, 225 (3) (1999), pp. 515–526
15. H. Lee, T. Tsukiya, A. Homma, T. Kamimura, Y. Takewa, E. Tatsumi, *et al.* Observation of cavitation bubbles in monoleaflet mechanical heart valves. J Artif Organs, 7 (2004), pp. 121–127
16. L. Béla, 2008. Cavitation in control valves. Available online <http://www.controlglobal.com/articles/2008/169/>
17. Bo-Suk Y., Won-Woo H, Myung H.K, Soo Jun L., (2005) Cavitation detection of butterfly valve using support vector machines. 6 October, Pages 25–43
18. BS EN 60534-2-1:2011, Industrial Process Control Valves – Part 2.1 Flow Capacity –Sizing Equations for fluid flow under installed conditions.
19. Bernoulli, D. (1738). Hydrodynamica. Dulsecker. Consultable en ligne <http://imbase-scd-ulp.u-strasbg.fr/displayimage.php>.
20. Whittle Laboratory. Pressure probes. University of Cambridge, department of engineering. Available [online] <http://www-g.eng.cam.ac.uk/whittle/current-research/hph/pressure-probes/pressure-probes.html> (Accessed 13/11/2018).
21. Regeai M N (2007). *Helical Gearbox Fault Detection Using Motor Current Signature Analysis*. The University of Manchester: Manchester.
22. Willetts, R., *Holistic condition monitoring*. 2002, University of Manchester: Manchester. p. 247.
23. Weidong, L. (2000), *A Study of Diesel Engine Acoustic Characteristics*, in *Department of Mechanical*, Manchester School of Engineering: Manchester.
24. Liang, B. (2000), *Condition Monitoring and Fault Diagnosis of Induction Motors*, in *Mechanical Engineering*. Manchester School of Engineering: Manchester UK.
25. Matthew, J. (1987), *Machine Condition Monitoring Using Vibration Analysis*, in *Acoustic*. Australia. p. 7 13.
26. Kelly, A. (1997), *Maintenance Strategy*.
27. Goldman, S. (1999), *Vibration spectrum analysis: a practical approach*. Industrial Press Inc

28. Yih-Hsing, P., R.G. Ralph, and N.C. Ahmet (1979) *Acoustic emission and transient waves in an elastic plate*. The Journal of the Acoustical Society of America. **65**(1): p. 96-105
29. Jiang, J., et al. (2008), *Monitoring of diesel engine combustions based on the acoustic source characterisation of the exhaust system*. Mechanical Systems and Signal Processing, **22**(6): p. 1465-1480.
30. Management, I.I.f.P. *Wear Debris Analysis*. Indian Institute for Production Management ; Available [online]: <http://www.iipm.ac.in/> (Accessed 2018)
31. Huang, K. and T. Liu, (2000). *Dynamic analysis of a spur gear by the dynamic stiffness method*. Journal of Sound and Vibration, **234**(2): p. 311-329.
32. R Willetts (2002), H.c.m., PhD thesis, University of Manchester, number: M0174866MU, 247 p., *Holistic condition monitoring*. 2002, University of Manchester: Manchester. p. 247.
33. Doctor, C. *Corrosion Monitoring. Sponsored by MATCO associates*. Corrosion Doctor 1999 (Accessed 2018); Available [online]: <http://www.corrosion-doctors.org/MonitorBasics/Introduction.htm>.
34. Davies, A., *Handbook of condition monitoring: techniques and methodology*. 1998: Springer.
35. Ramroop, G., et al (2001). *Airborne Acoustic Condition Monitoring of a Gearbox System*. in *2001 5th Annual Maintenance and Reliability Conference (MARCON 2001)*.
36. Runkel, J., et al. (1996). *Condition Monitoring of Industrial Machines, Institute of Nuclear Engineering and Non-destructive Testing*: Hannover Germany.
37. Li, Z., S. Akishita, and T. Kato (1997). *Engine failure diagnosis with sound signal using wavelet transform*. SAE Technical Paper.
38. Mobley, R.K (2002). *An introduction to predictive maintenance*. Butterworth-Heinemann.
39. Adams, C.H (1982). *Recommended practice for acoustic emission testing of fiberglass tanks/vessels*. in *37th Annual Conference, Reinforced Plastics/Composites Institute*. The Society of the Plastics Industries, Inc.

40. Edwards, D.J., G.D. Holt, and F. Harris (1998). *Predictive maintenance techniques and their relevance to construction plant*. Journal of Quality in Maintenance Engineering. 4(1): p. 25-37.
41. Gu, F. and A. Ball. (1995), *Vibration Based Fault Diagnosis in Diesel Fuel Injection System*, in *IMEchE Seminar on Diesel Fuel Injection Systems*. London. p. 89-97.
42. Nandi, A. (2002) *Vibration Based Fault Detection Features Classifiers and Novelty Detection*, in *COMADEM. Proc. Condition Monitoring and Diagnostic Engineering Management: Birmingham, UK*. p. 23 - 36.
43. Troyer, D.D. and M. Williamson (1999). *Effective integration of vibration analysis and oil analysis*. in *Proceedings of the International Conference on Condition Monitoring, University College of Swansea, Swansea, UK*.
44. J Ferrari, EDF R&D, MS Loing, Z Leutwyler and Kalsi Engineering (2006). Measurements of fluid flow load on A globe valve stem under various cavitation condition.
45. A. Taimoor, M. Rakesh, C. Matthew and O. Carlos (2015). "Capacity Testing and Local Flow Analysis of a Geometrically Complex Trim Installed within a Commercial Control Valve".
46. Emerson Process management (2005). Control Valve Handbook; Fourth Edition.
47. W. S. Qu, L.Tan, S. L. Cao, Y. Xu, J. Huang and Q. H. Xu (2014). "Experiment and numerical simulation of cavitation performance on a pressure-regulating valve with different openings".
48. Fisher Controls International LLC; Researchers Submit Patent Application, "Method of Cavitation/Flashing Detection in or near a Process Control Valve", for Approval for Politics and Government Journal (Mar 26, 2015): page 12460.
49. Osterman, Aljaž et al. "Characterization of Incipient Cavitation In Axial Valve By Hydrophone And Visualization". *Experimental Thermal and Fluid Science* 33.4 (2008): 620–629.
50. A. Masjedian Jazi, H. Rahimzadeh (2009). Detecting cavitation in globe valves by two methods: Characteristic diagrams and acoustic analysis. *Applied Acoustics*, 1440-1445.
51. J Green, R Mishra, M Charlton and R Owen (2012). Validation of CFD predictions using process data obtained from flow through an industrial control valve.

52. Ned, A. A, Shang, T, Goodman, S, Hurst, A and Chivers, J. “ Fully intergrated miniature, high frequency flow probe utilizing leadless, SOI technology suitable for gas turbines”,
53. Rediniotis, O. K, Hoang, N. T, and Telionis, D. P. 1993. “The Seven-Hole Probe: Its Calibration and Use,” Forum on Instructional Fluid Dynamics Experiments, Vol. 152, pp. 21-26.
54. Zhao, X., Lucas, G., Pradhan S. (2009). Signal Processing Method in using Four-sensor Probe for Measuring the Velocity Vector of Air-liquid Two-phase Flow. Journal of the Japanese Society of Experimental Mechanics (JSEM), 9. pp. 19-24.
55. Duquesne, P, Iliescu, M, Fraser, R, Deschenes, C and Ciocan, G. D. “Calibration in a Potential water Jet of a Five-hole Pressure Probe with Embedded Sensors for Unsteady Flows Measurement” Hydraulic Machines Laboratory, University of Laval, Quebec, Canada
56. J. Kurian (2007). Chapter 5-Measurements of Pressure. Department of Aerospace Engineering, Indian institute of technology, Madras. Available [online] <http://nptel.ac.in/courses/101106040/chapter%205.pdf>
57. D. W. BRYER, D. E. WALSHE, and H. C. GARNER (1958). Pressure probes selected for three dimensional flow measurements. Aerodynamics division of N.P.L
58. Bryer, D. W., and Pankhurst, R. C., “Pressure-Probe Methods for Determining Wind Speed and Flow Direction,”HMSO, (NPL), 1971.
59. Everett, K. N., Gerner, A. A. and Durston, D. A., 1983, “Seven-Hole Cone Probes for High Angle Flow Measurements: Theory and Calibration,” AIAA Journal, Vol. 21, No. 7, pp. 992-998.
60. Rediniotis, O. K., Hoang, N. T., and Telionis, D. P (1993). “The Seven-Hole Probe: Its Calibration and Use,” Forum on Instructional Fluid Dynamics Experiments, Vol. 152, June 1993, pp. 21-26.
61. Zilliac, G. G., “Calibration of Seven-Hole Probes for Use in Fluid Flows With Large Angularity,” NASA TM 102200, December 1989.
62. Devia, F and Fossa, M. 2003. “Design and optimisation of impedance probes for void fraction measurements”, Flow Measurement and Instrumentation 139–149, DITEC, Universita` degli Studi di Genova, via all’Opera Pia 15a, 16145 Genova, Italy.

63. Kupferschmied, P, Koppel, P, Gizzi, W, Roduner, C and Gyarmathy, G. "Time-resolved flow measurements with fast-response aerodynamic probes in turbomachines", ETH Zurich (Swiss Federal Institute of Technology), Institute of Energy Technology, Turbomachinery Laboratory, CH-8092 Zurich, Switzerland.
64. Rediniotis, O. K, Johansen, E. S, Tsao, T, Seifert, A and Pack, L. G. 1999. "MEMS-Based Probes for Velocity and Pressure Measurements in Unsteady and Turbulent Flow fields," AIAA-99-0521, 37th Aerospace Sciences Meeting and Exhibit, Reno, NV, January 11-14.
65. N. Sitaram and K. Srikanth (2014). Effect of Chamfer Angle on the Calibration Curves of Five-Hole Probes. Thermal Turbomachines Laboratory, Department of Mechanical Engineering, IIT Madras, Chennai 600 036, India.
66. Paul, A. R., Upadhyay, R. R., & Jain, A. (2011). A novel calibration algorithm for five-hole pressure probe. *International Journal of Engineering, Science and Technology*, 3(2).
67. Bryant and Johnson. "Comparison of Gas Velocity Measurements and CFD Predictions in the Exhaust Duct of a Stationary Source", National Institute of Standards and Technology Gaithersburg, MD 20899.
68. Kim, S and Kang, Y. J. "Calibration of a Five-Hole Multi-Function Probe for Helicopter Air Data Sensors", Department of Mechanical and Aerospace Engineering, Gyeongsang National University, Jinju, Korea.
69. C.S Lee and N. J Wood (1986). "Calibration and Data Reduction for a Five-hole Probe", Joint Institute for Aeronautics and Acoustics, Stanford University, Department of Aeronautics and Acoustics, Stanford, CA 94305.
70. J. D. Hobeck and D. J. Inman (2015). Low-Cost Pressure Probe Sensor for Predicting Turbulence-Induced Vibration from Invasive Low-Velocity Turbulent Flow Measurements. *IEEE SENSORS JOURNAL*, VOL. 15, NO. 8.
71. Porro, A. R. (2001). Pressure Probe Designs for Dynamic Pressure Measurements in a Supersonic Flow Field.[conducted in the Glenn Supersonic Wind Tunnel (SWT)].
72. V Malviya, R Mishra, E Palmer, B Majumdar (2007). CFD based analysis of the effect of Multi-hole pressure probe geometry on flow field interference.

73. Malviya, Vihar, Mishra, Rakesh and Palmer, Edward (2010) CFD Investigation on 3-Dimensional Interference of a Five-Hole Probe in an Automotive Wheel Arch. *Advances in Mechanical Engineering*, 2010. pp. 1-19. ISSN 1687-8132
74. S. intan NAjha, I. Rosdiazli (2014). Implementation of Acoustic Emission technique in early detection of control valve seat leakage. 15<sup>th</sup> international conference on sciences an techniques of automation control and computing engineering.
75. U bogumil, P. Lorenzo, J. Tomasz (2015). Measurements and analysis of cavitation in a pressure reducing valve during operation – a case study. *Prosedian Engineering* 119 270-279.
76. L Zeng, G Lui, J Mao, S Wang, Q Yang, H Yuan, K Wang, J Zhang Y Xu (2015). Flow induced vibration and noise in control valve. *J Mechanical Engineering science*, Vol 229(18) 3368-3377.
77. W. Kaewwaewnoi, A. Prateepasen, P. Kaewtrakulpong (2010). Investigation of the relationship between internal fluid leakage through a valve and the acoustic emission generated from the leakage. *Measurement* 43 274-282.
78. BS EN 60534-2-5 British Standards BSI Part 2-5(2009): Flow Capacity – Sizing Equations for Fluid Flow through Multistage Control Valves with Interstage Recovery.
79. <http://www.cfd-online.com> (Last visit on 25-12-2015).
80. T Asim, A. Oliveira, M Charlton, R. Mishra (2019). Improved design of a multi-stage continuous-resistance trim for minimum energy loss in control valves. *Energy*. Vol 174, Pages 954-971.
81. G.S.T(Global sensor technology). *The CA-YD-1182 is a general purpose integrated electronics (IEPE) accelerometer*. 2018; Available [online]: [www.globalsensortech.com/icpe-accelerometer-ca-yd-1182](http://www.globalsensortech.com/icpe-accelerometer-ca-yd-1182).
82. G.S.T(Global sensor technology). *Free field microphone CHZ-223*. 2018; Available [online]: <http://www.globalsensortech.com/free-field-microphone-chz-223>. (Accessed 2-01-2018)
83. G.S.T(Global sensor technology). *Microphone pre-amplifier YG-201*. 2018; Available [online]: <http://www.globalsensortech.com/microphone-pre-amplifier-yg-201>. (Accessed 2-01-2018)

84. D. Telionis, Y. Yang, O. Rediniotis (2009). Recent Developments in Multi-Hole Probe (MHP) Technology. International congress of mechanical engineering, Brazil.
85. Wei, J., Chen, T., Liu, G. et al (2016). Higher-order Multivariable Polynomial Regression to Estimate Human Affective States. Sci Rep 6, 23384 Available [online] <https://doi.org/10.1038/srep23384> (accessed 14th March, 2020).
86. 16.621 Experimental project lab 1. Error analysis (Uncertainty analysis). Available [online] [https://ocw.mit.edu/courses/aeronautics-and-astronautics/16-621-experimental-projects-i-spring-2003/lecture-notes/10\\_errors03.pdf](https://ocw.mit.edu/courses/aeronautics-and-astronautics/16-621-experimental-projects-i-spring-2003/lecture-notes/10_errors03.pdf) (Accessed 29-01-2019).
87. MoreStream (2019). Measurement system analysis. Available [online] <https://www.moresteam.com/toolbox/measurement-system-analysis.cfm> (Accessed 29-01-2019).
88. C. Deziel (2018). How do I calculate repeatability? Available [online] <https://sciencing.com/calculate-xbar-8382419.html> (accessed 14th March, 2019).
89. J. Green, R. Mishra, M. Charlton, R. Owen (2012). Validation of CFD predictions using process data obtained from flow through an industrial control valve. J. Phys. Conf., 364
90. T. Asim (2013). Capacity Testing of X-stream Valves for Single-component Single-phase Flows. Technical report submitted to Weir Valves and Controls Ltd
91. M. Charlton, R. Mishra, T. Asim (2016). The effect of manufacturing method induced roughness on severe service control valve performance. 43<sup>rd</sup> National Conference on Fluid Mechanics and Fluid Power, 15-17 December, Allahabad, India
92. T. Asim, R. Mishra, M. Charlton, C. Oliveira (2015). Capacity testing and local flow analysis of a geometrically complex trim installed within a commercial control valve. International Conference on Jets, Wakes and Separated Flows, 16-18 June, Stockholm, Sweden.
93. A. Oliveira (2017). Capacity Testing of X-stream Valves for Single-component Single-phase Flows. Technical report submitted to Weir Valves and Controls Ltd

94. T. Asim, M. Charlton, R. Mishra (2017). Capacity CFD based investigations for the design of severe service control valves used in energy systems. Energy conversion and management.
95. Brüel & Kjær (2009). Kurtosis in random Vibration Control. Available [online] <https://www.bksv.com/media/doc/bo0510.pdf>
96. J Basmajian, C.J DeLuca (1985). Muscles alive: their function revealed by electromyography, Wiliams & Wilkins, Baltimore
97. B Gerdle, S Karlsson, S Day, M Djupsjöbacka (1999). Acquisition, processing and analysis of surface EMG signals U Winhorst, H Johansson (Eds.), Modern techniques in neuroscience research, Springer, Berlin, pp. 705-756.
98. P. Angkoon, T. Sirinee, H. Huosheng, P. Pornchai and L. Chusak (2012). The Usefulness of Mean and Median Frequencies in Electromyography Analysis.
99. J Diva (2018). Skew and Kurtosis: 2 Important Statistics terms you need to know in Data Science. Available [Online] <https://codeburst.io/2-important-statistics-terms-you-need-to-know-in-data-science-skewness-and-kurtosis-388fef94eeaa> (accessed 12th February, 2019)
100. Tandon, N. and B. Nakra, *Defect detection in rolling element bearings by acoustic emission method*. Journal of Acoustic Emission, 1990. **9**(1): p. 25-28.
101. Tan, C., *Application of acoustic emission to the detection of bearing failures*. 1990.
102. Yan, D., T. El-Wardany, and M. Elbestawi, *A multi-sensor strategy for tool failure detection in milling*. International Journal of Machine Tools and Manufacture, 1995. **35**(3): p. 383-398.
103. Droge, M. *Recommended practice for acoustic emission testing of fiberglass reinforced plastic piping systems*. in *Proceedings of the 1 st international symposium on Acoustic Emission from reinforced composites*. 1983.
104. Al-Ghamd, A.M. and D. Mba, *A comparative experimental study on the use of acoustic emission and vibration analysis for bearing defect identification and estimation of defect size*. Mechanical Systems and Signal Processing, 2006. **20**(7): p. 1537-1571.

## APPENDICES

### APPENDIX A

#### SENSORS AND EQUIPMENTS SPECIFICATIONS

**Table 1: Accelerometer sensor specification [98]**

Axial sensor sensitivity (20±5°C)	100mV/g
Range of the measurement sensor range (peak)	50g
Transverse of the sensor sensitivity	≤5%
Frequency response range (0.5dB)	0.5 to 15000 Hz
Mounting frequency resonance	40,000 Hz
Sensor Polarity	Positive
Operating temperature range	-40 to 120°
Sensor limit shock (±peak)	3,000 g
Operating current of the accelerometer	+2 to +10 mA (typical 4mA)
Output signal of the accelerometer	≤6V
Noise (1 to 20 kHz)	<0.5 mg
Base strain accelerometer sensitivity	0.2mg/με
Magnetic sensitivity	1.5g/T
Thermal transient of the sensor sensitivity	10mg/°C
Output accelerometer impedance	<100 Ω
Weight of the sensor	9g

**Table 2: Specifications for the microphone sensor [99]**

Acoustic microphone sensor	
Microphone diameter	12.7mm (0.50") without grid ;13.2mm (0.52") with grid
Height	16.0mm(0.63") without grid ; 17.2mm(0.68") with grid;
Weight of microphone	9g
Case	material MONEL
Mounting to amplifier	11.7 mm- 60UNS

Sensing element	Electret condenser
Sensitivity	(250Hz) 31.6mV/Pa (at 250Hz, open-circuit, -30dB±2dB ref. 1 V/Pa)
Range of frequency	20Hz to 20kHz
Dynamic range	>140dB SPL within 3% distortion
Thermal noise	<20.0dB
Temperature coefficient-0.01 within the range	-10°C and +50°C

**Table 3: Microphone YG-201 ICP preamplifier specifications [100]**

Microphone prean1plifier	
Frequency Response of the preamplifier (ref. 250Hz)	16Hz to 100 kHz, ±0.5dB
Nominal attenuation	-0.3dB
Input impedance	2GΩ, <0.4pF
Output impedance	100 Ω
Maximum output voltage	5.0Vrms(Corresponding to 134dB SPL (Sound Pressure Level) for microphone sensitivity of 50mV/Pa)
Noise	<5.0μV A-weighting <15.0μV Lin., 22.4Hz - 22.4 kHz
Power supply requirements	ICP supply, 2 to 20mA. Nominal 4mA
Type of connector	Connector type BNC
Dimensions	12.7mm(1/2") x 70mm (including connector)
Preamplifier mounting Thread	11.7mm -60UNS (for standard 1/2 inch microphones)
Range of operating temperature	-40°C to +85°C
Humidity range	0 to 98%RH

**Table 4: Pressure transducer specification**

<b>Manufacturer</b>	<b>IMP - Industrial Pressure Transmitter</b>
Type	IMP-C0053-9A4-CAV-02-000
Pressure Datum	Custom Range
Range for the pressure	-1 to +10 Bar G
Output	0.5 to 4.5V / 3-wire (ratiometric)
Transducer Accuracy (Combined NL&H)	<±0.25% / FS
Transducer Accuracy (Thermal Zero Shift)	<±0.04% / FS / °C
Electrical Connection	Industrial PVC cable (IP66)
Process Connection	G 1/4" male DIN 3852
Material of the O Ring	Viton
Length of the Cable (Metres)	2 (industrial PVC)
Specials Code	No Special Requirements
Material for the Diaphragm	Aluminum Oxide 96% (Ceramic Al <sub>2</sub> O <sub>3</sub> )
Material for the Process Connection	303 Stainless Steel
Media Temperature	-20 to +135°C
Operating Temperature	-20 to +80°C
Supply Voltage	5V dc

**Table 5: Turbine flow meter technical specification for the OMEGA-WE-SDC series**

Flow meter manufacturer	Bells flow system
Model	OMEGA-WE-SDC
Contact type	NA
Size	100mm (4 inch)
Accuracy	Class B
Maximum flow	125m <sup>3</sup> /h
Minimum flow (L/H)	1250
Working Pressure	16 Bar
Temperature class	T30/T50
Maximum reading	2 m <sup>3</sup> /h
L	250mm

H	282mm
Position	Central
Max power	3W
Maximum Voltage	28 VDC
Max Current	0.11 Amps
Maximum contact resistance	200 milli ohms
Maximum contact Capacity	0.2 Pico Farad
Insulation resistance	1000 ohms
Maximum frequency	5 KHz
Minimum insulation rupture voltage	200 V

**Table 6: Technical specification for the FMA air mass flow meter series**

Air flow meter	
Flow meter accuracy	±1.5% of full scale
Pressure coefficient	0.01% of full scale per psi (0.07 bar)
Response time	800 msec time constant; 2 sec (typical) to within ±2% of set flow rate over 25 to 100% of full scale
Power supply requirement	12 to 26 Vdc power @200 mA max.
Maximum pressure gas	1000 psig (70 kg/cm <sup>2</sup> gauge)
Ambient and gas temperature.	0 to 50°
Materials in fluid contact	Aluminium models: Anodized aluminium, 316 SS, brass and FKM O-rings Stainless steel models: 316 SS and FKM O-rings
Output air flow meter signal	Linear 0 to 5 Vdc: 1000 ohm minimum load 4 to 20 mA: 50 to 250 ohm loop resistance
Power of the transducer	12 Vdc @ 200mA maximum
Weight of air flow meter	1.1 kg

**Table 7: Power supply unit specification**

PSU Manufacturer	Rapid Electronics
Model	Dual Rail 1A
Input Voltage	230V ac
Supply frequency	50 Hz
Maximum Power	50 Watts

Panel fusing rating	2A quick blow
Mains plug fuse rating	3A
Output Voltage	+/- 5v, 12v, 15v smoothed and regulated dc
Maximum output current	1A per rail
Dimension	140 x 125 x 240mm

**Table 8: The YE6232 -16 CHANNEL DAQ Technical specifications**

Manufacture	Global Sensor Technology (GST) which was made by Sinocera Company
A/D bits	24bit ( $\Sigma$ - $\Delta$ )
Channels	16/32(Selectable)
Range of the signal frequency	DC-30kHz (-3dB $\pm$ 1dB)
Input DAQ Mode	V/IEPE (Integrated Electronics Piezo Electric)/TEDS (Transducer Electronic Data Sheet)
Range of the signal input	$\leq \pm 10VP$
Filter	Independent Anti-filtering
Power supply	AC220V50Hz/110V60Hz
Accuracy of the DAQ	$\pm 0.5\%$
Type of software	YE7600 Software used for general test and analysis
Maximum sample rate	96kHz/CH, Parallel
Cable	interface cable, Input cable, and power cable
Type of interface	USB2.0
Weight of the DAQ	4Kg
Modes of trigger	Signal trigger; external trigger
DAQ Dimensions (mm)	426W $\times$ 88H $\times$ 300D
Operating temperature	0 to 50°C;
Humidity Range	20 to 80% RH

**Table 9: NI DAQ technical specification**

Manufacture	National Instrument
Model	NI 6363 X series

<b>ANALOGUE INPUT</b>	
Number of channel	32 single ended or 16 differential
ADC Resolution	16 bits
Maximum sampling rate	2MS/s for single channel and 1MS/s for multichannel
Timing accuracy	50 ppm of sample rate
Timing resolution	10 ns
Input coupling	DC
Input range	$\pm 10$ V, $\pm 5$ V, $\pm 2$ V, $\pm 1$ V, $\pm 0.5$ V, $\pm 0.2$ V, $\pm 0.1$ V
Maximum working voltage for analogue inputs (signal + common mode)	$\pm 11$ V of AI GN
Input impedance when device ON (AI+ to AI GND)	$>10$ G $\Omega$ in parallel with 100 pF
Input impedance when device ON (AI- to AI GND)	$>10$ G $\Omega$ in parallel with 100 pF
Input impedance when device OFF (AI+ to AI GND)	820 $\Omega$
Input impedance when device OFF (AI- to AI GND)	820 $\Omega$
Input bias current	$\pm 100$ pA
crosstalk (at 100 kHz) for non-Adjacent channels	-95 dB
Crosstalk (at 100 kHz) for Adjacent channels	-75 dB
Small signal bandwidth (-3 dB)	1.7 MHz
Input FIFO size	4,095 samples
Overvoltage protection (AI <0..31>, AI SENSE, AI SENSE 2) when Device on	$\pm 25$ V for up to two AI pins
overvoltage protection (AI <0..31>, AI SENSE, AI SENSE 2) when Device off	$\pm 15$ V for up to two AI pins
Input current during overvoltage condition	$\pm 20$ mA max/AI pin

<b>ANALOGUE OUTPUT</b>	
Number of channel	4
Output impedance	0.2 $\Omega$
Output current drive	$\pm 5$ mA
Overdrive protection	$\pm 25$ V
Overdrive current	26 mA
Power-on state	$\pm 5$ mV
<b>DIGITAL I/O/PFI</b>	
Number of channel	48 total, 32 (P0.<0..31>), 16 (PFI <0..7>/P1, PFI <8..15>/P
Port/sample size	Up to 32 bit

## APPENDIX B

## RISK ASSESSMENT FORM FOR THE EXPERIMENTAL WORK

## UNIVERSITY OF HUDDERSFIELD - GENERAL HEALTH AND SAFETY RISK ASSESSMENT FORM

(To be completed for intended and proposed activities)

<b>Brief description of activity: Operation of Flow Loop</b>				
Location: T4-09		Assessment by: Airede Yusuf		Assessment date: 20-07-2018
Assessment reference:				
<b>SPECIFIC TASK/ASPECT OF ACTIVITY: Student Laboratory Work</b>				
Hazards identified	Risks to health and safety	People at risk	Measures to manage the risks effectively	
Water Leaks (From pipes, valves, the pressure probes, water tank overflow or tubes used to connect the pressure probes and the pressure transducers. Also, water overflow from the drainage system)	Slips & Falls (Low Risk)	Operator	Run Rig to check for leaks prior to any experimentation being carried out.  Any leaks to be repaired and spillages cleaned up.  All Pipework is within a separate bund area. Students are not permitted within this area. Only staff allowed within the bund area where pipes, brackets, Pressure probes and wires could result in trips and falls. No such problem exists outside this area.	
Pipe Failure	Water under pressure (Low Risk)	Local Area	System Checks as described. Event unlikely. Pipe sizes would result in a rapid dissipation of water pressure. All electrical circuits on circuit breakers which would switch power off to any live instrumentation. Power outlets within the bund are water proof.	
<b>SPECIFIC TASK/ASPECT OF ACTIVITY: Using Electrical Devices</b>				
Hazards identified	Risks to health and safety	People at risk	Measures to manage the risks effectively	
Water near Electrical Devices including the microphone and the accelerometer	Short Circuits (Low Risk)	Operator	Electrical Supplies within the flow loop area itself were specified by Estates Services for this environment to be water safe.  All Circuits protected through circuit breakers, RCD, MCB, Fuse etc.  PAT carried out on all 240v equipment.	

Also, a lot of pressure sensors are being used for this experiment (about 10). Lot of wires are being used to connect the transducers up to where there are being powered and connected to the data acquisition.	Trip from wires or overhead contacts with the wires	Operator	All the wires are safe connected and away from the walking area to avoid any accident	
--	---	----------	---	--

SPECIFIC TASK/ASPECT OF ACTIVITY: Working within the Bund Area				
Hazards identified	Risks to health and safety	People at risk	Measures to manage the risks effectively	
Pipes & Brackets running across the floor.	Trip & Fall (Medium – High Risk)	Operator	Restricted access – Approved Staff & Contractors Staff to be authorized by their Supervisor/Manager.	
Water Leaks	Slip & Fall		Normally only occurs when changing sections of pipe. Appropriate non-slip footwear advised. Spills to be cleaned up immediately.	

SPECIFIC TASK/ASPECT OF ACTIVITY: Valve and Pipe installation						
Hazards identified	Risks to health and safety	People at risk	Measures to manage the risks effectively	Action by:		
				Who	When	Completed
Dropping the valve while moving it or the pipe while removing and placing new pressure probes	Feet/hand injuries	Operators	The installation should be done by three persons to reduce the weight and the risk of dropping the valve. Ideally a crane should be used.  Ideally a crane should be used  Use work gloves and boots  At least two people should be working on this			

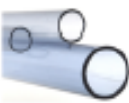
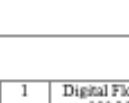
SPECIFIC TASK/ASPECT OF ACTIVITY: Using the Pump						
Hazards identified	Risks to health and safety	People at risk	Measures to manage the risks effectively	Action by:		
				Who	When	Completed

Version: September 2006

Pressurized Water Lines	Leaking Pipes/Joints resulting in slip hazard on Vinyl Floor. Water spurting out. Burst Pipes.  Low Risk.	Operator	Sealed system with water running back to an open tank. Low pressures within pipe circuit. Any spills to be immediately cleaned up. Apparatus checked by staff (Research/Academic)			
-------------------------	--	----------	--	--	--	--

## APPENDIX C

## Details of piping system components

Item	No	Description	Cost	Photo
Clear PVCu Pipe	2	PVCu Clear Pipe 16 BAR 2.5m Length 32mm	£ 41.802	
Clear PVCu Pipe	1	PVCu Clear Pipe 16 BAR 1.25m Length 50mm	£ 34.668	
Short Radius Bend 90°	2	PVCu Bend 90 Swept Plain 2"	£ 32.448	
Elbow 90°	2	PVCu Elbow 90 Plain 1 1/4"	£ 4.44	
Tee 90°	1	PVCu Tee 90 Plain 2 1/2"	£ 9.384	
Reducing Bush	1	PVCu Reducing Bush Plain 2 1/2" x 2"	£ 2.984	
Reducing Bush	2	PVCu Reducing Bush Plain 1 1/2" x 1 1/4"	£ 2.424	
Ball Valves	1	Brass Ball Valve NPT F/F 1 1/4"	£ 20.676	
Ball Valves	1	Brass Ball Valve NPT F/F 2"	£ 66.852	
Adaptor Plain F / BSP M	2	PVCu Adaptor Female Plain x Threaded Male 1 1/4"	£ 4.824	
Adaptor Plain F / BSP M	2	PVCu Adaptor Female Plain x Threaded Male 2"	£ 8.4	
Socket	4	PVCu Socket Plain 1 1/4"	£ 5.328	
Socket	5	PVCu Socket Plain 2"	£ 11.1	
Union	1	PVCu Union Plain x Threaded 1 1/4"	£ 9.775	
Union	1	PVCu Union Plain x Threaded 2"	£ 12.855	

Flow Meter Plain Inch	1	Digital Flow Meter 38 to 380 LPM Plain 1 1/2"	£ 322.992	
PVCu Solvent Cement	1	Solvent Cement for PVCu 500ml Tin	£17.436	
Cleaning Fluid	1	Cleaning Fluid For PVCu And ABS 500ml Tin	£12.584	
PTFE Tape	1	PTFE Tape 12m Roll Pack of 10	£6.516	
Thread	1	Studding 1M	£1.56	
Galv Back Plate	5	THREADED BACK PLATE GALV	£2.12	
RUBBER LINED CLIPS	3	110 mm EPDM RUBBER LINED CLIPS	£ 17.4	
sheet steel metal	1	dimensions (70cm*60cm*1cm)	£ 90.5	

## APPENDIX D

## Calibration chart for the microphone sensor

**Calibration Chart for  
Prepolarized Free-field  
1/2" Microphone**

**Type CHZ-223**

**Serial No: 2453**

**Open-circuit Sensitivity Level:**

- 29.7 dB re 1 V/Pa  
or 32.6 mV/Pa

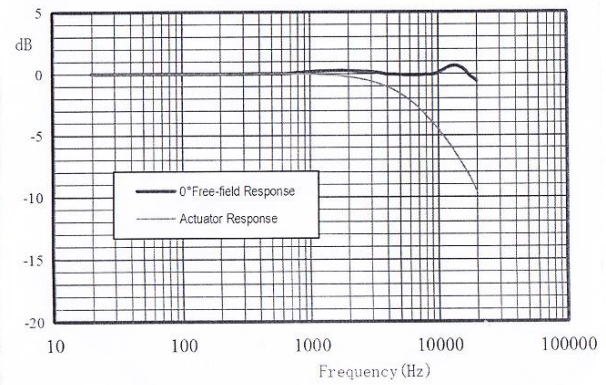
**Conditions of Test:**

Polarization Voltage: 0 V  
Frequency: 250 Hz  
Barometric Pressure: 101.3 kPa  
Relative Humidity: 45 %  
Temperature: 18 °C  
Date: 2017.05.23  
Signature:

Beijing AcousticSensing Technology Ltd

**Specifications:**

**Outside Diameter:**  
13.2 mm with protecting grid  
12.7 mm without protecting grid  
**Mounting Thread:**  
11.7 mm 60 UNS 2  
**Frequency Response Characteristic:**  
20–20kHz 1/2 IEC61672 Class 2  
**Ambient Pressure Coefficient:**  
-0.010 dB/kPa for 10% pressure  
change at 250 Hz  
**Temperature Coefficient:**  
-10°C to +50°C  
-0.010 dB/°C at 250 Hz  
**Dynamic Range:**  
SPL. blow which the total harmonic  
distortion remains less than 3%: 146dB



## APPENDIX E

## Specification for the ICP microphone preamplifier

**ICP MICROPHONE PREAMPLIFIER**

Type YG-201      Serial No:101170

## Specifications:

Frequency Response (re 250Hz): 16Hz to 100kHz,  $\pm 0.5$ dB

Attenuation: -0.3dB (Typical)

Input Impedance:  $9G\Omega \approx 0.4PF$ Output Impedance:  $100\Omega$ 

Maximum Output Voltage: 5.0Vrms

(Corresponding to 134dB SPL for microphone sensitivity of 50mV/Pa)

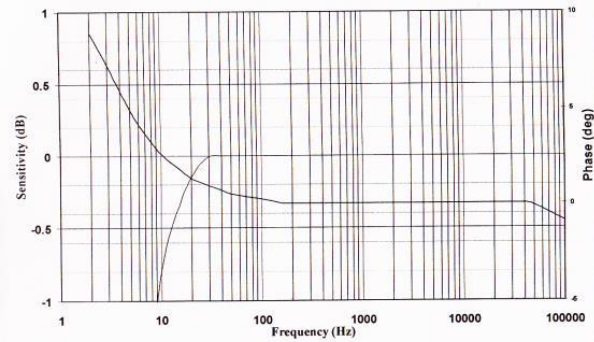
Noise: A-weighting  $< 3.0\mu V$       22.4Hz-22.4kHz  $< 7.0\mu V$  Lin

Power Requirements: ICP supply, 2 to 20mA. Nominal 4.0 mA

Connector Type: BNC Socket

Dimensions:  $\varnothing 12.7mm \times 70mm$  (including connector)

Thread for Preamplifier Mounting: 11.7mm-60UNS (For standard 1/2 inch microphones)

Operating Temperature Range:  $-40^{\circ}C$  to  $+85^{\circ}C$ ; Humidity: 0 to 98%RH**Beijing AcousticSensing Technology Ltd**

Typical Frequency and Phase Response Curves  
for Preamplifier Type YG-201





## APPENDIX H

### Flow meter Calibration process.

1. Through the pressure regulator, 4 Bar is sent to the knife valve in order to close the valve. The pressure regulator can be seen in figure H1. It is recommended that the valve is set at a normally closed (NC) position.



Figure H1: Pressure regulator

2. The PLC unit is turned ON for the PLC display to be initialised as shown in figure H2. Once this initialization is complete, the hopper static weight will be seen on the display making the PLC ready to be used.



Figure H2: PLC unit

3. The PLC unit is connected to the university network in order to be accessed on the PC in the lab by a software named DOP4.
4. Once the PLC is still powered ON and the software is launched from the PC, change the hardware to serial LAN, change the IP address to 10.71.56.171. Click on test device. After the device has been found, select the device and the set to channel 1. You can show the hopper weight by clicking on the start the test stream button to be able to read the hopper net weight as seen in figure H3.

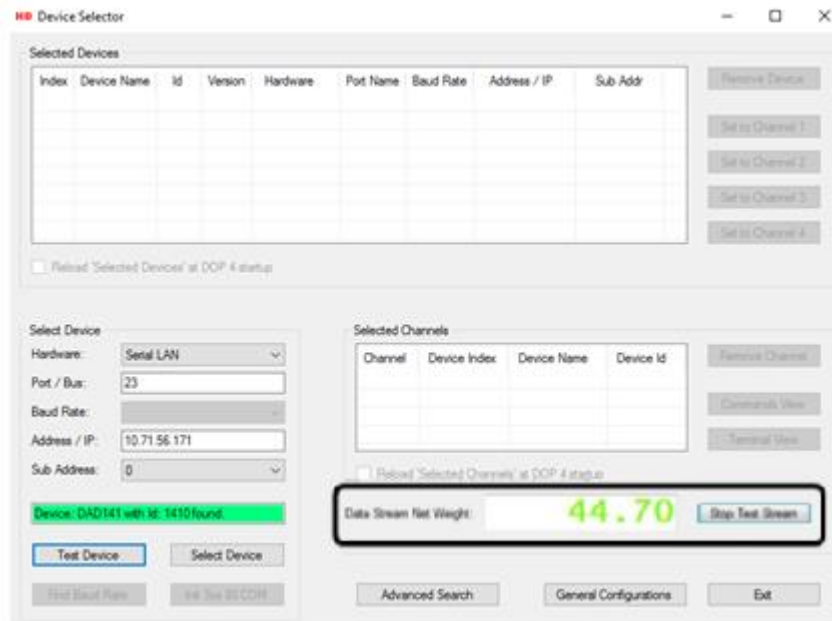


Figure H3: PLC to DOP4 data transmission

5. After the test has been carried out, the “stop test screen” button is clicked. The command view button clicked in order to view the “sequencer” as shown in figure H4.

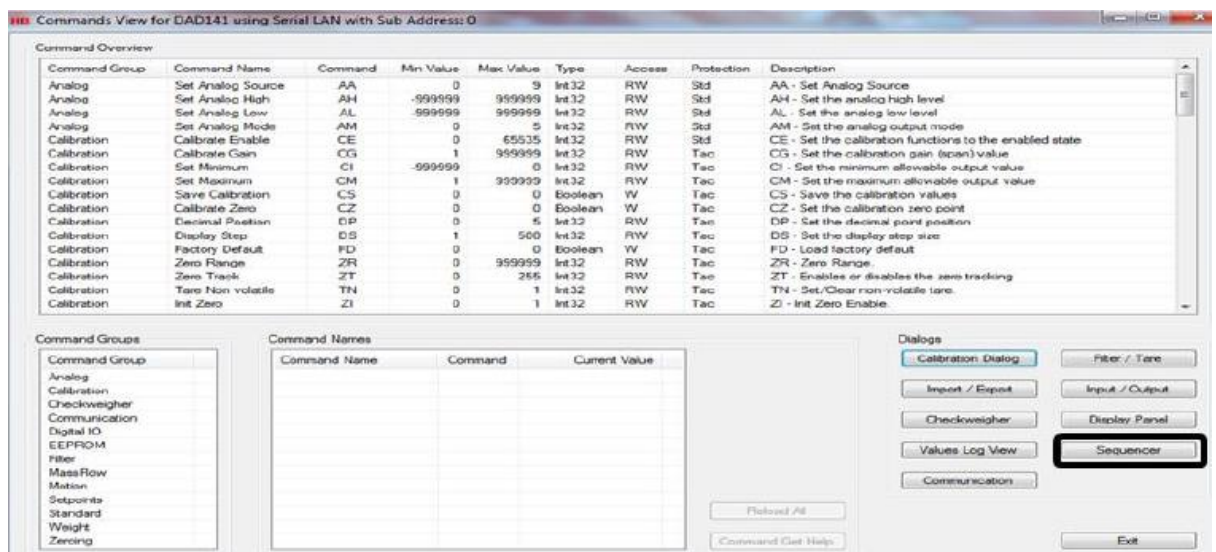


Figure H4: Command view window

6. After the clicking the “sequencer” button, the window in figure H4 opens where the “load” button is clicked to load the program file for the sequence. The file named Test\_Sq1.dsd can be found on the desktop under the folder named LoadCellSequencer.
7. After the file has been loaded, the pre-programmed sequence on the sequence command window can then be viewed. The “Run” button is then clicked in order

to execute the sequence. The “Add/Edit” button is used in order to edit any command by selecting that command as seen in figure H5.

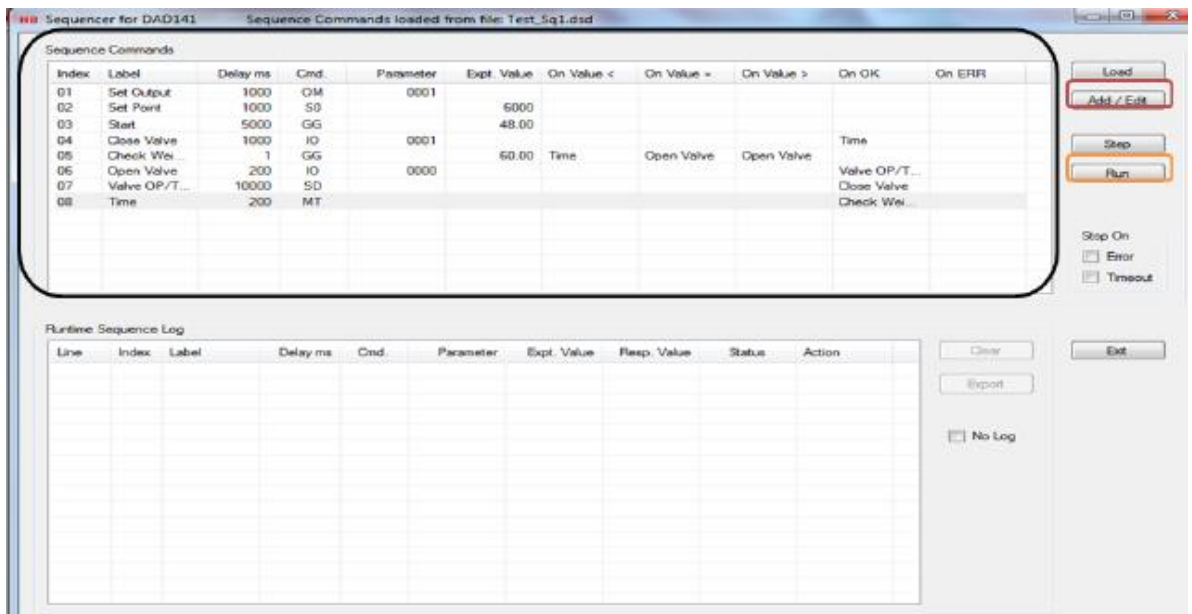


Figure H5: The Sequence command window

8. A runtime log is seen after the start of the sequence as seen in figure H6.

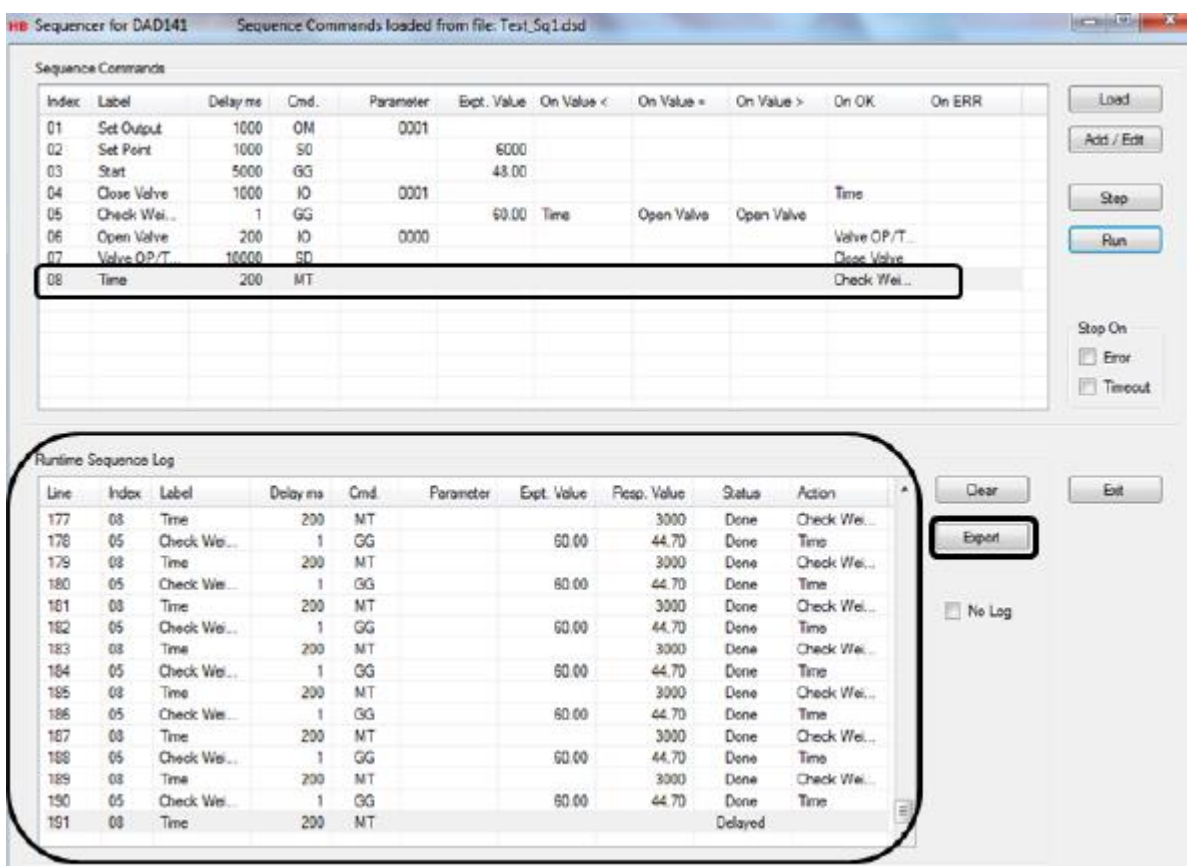


Figure H6: The Runtime sequence Log

This runtime log is used in creating a .csv file via the export button. Each sample measuring time interval can be reset by editing the time command. This time is the time the PLC takes in measuring between each readings from the load cell. The time is currently set at 0.2seconds.

9. After clicking the export button, a pop up window appears where the place to save the data in the preferred drive for post analysis. Ensure that the file is saved in .csv type as seen in figure H7.

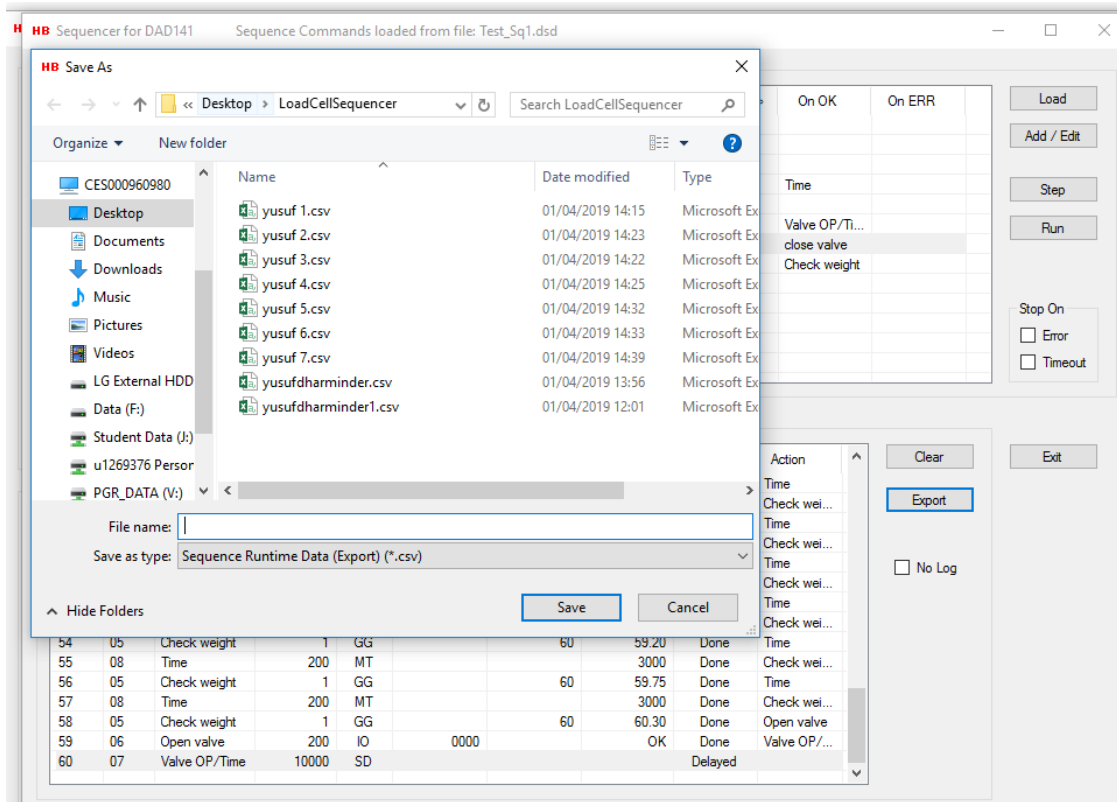


Figure H7: Window for saving the data

10. After saving the file, the test can then be repeated after clicking the “clear” button.

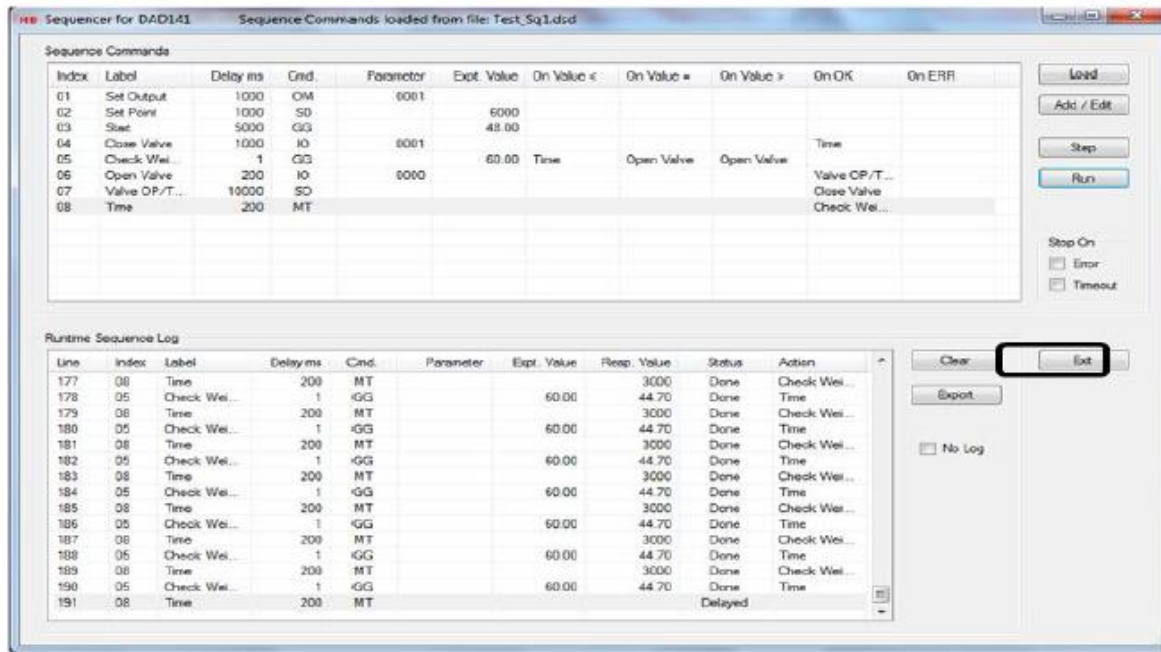


Figure H8: Repeating of the test procedure

After the process of calibration have been completed, the post processing of the data can then commence. For each of the (.csv) file already saved, same post processing process is conducted as follows:

- Open the .csv excel file which should look like figure H9.

Line	Index	Label	Delay ms	Cmd.	Parameter	Expt. Value	Resp. Value	Status	Action
1	1	7 Valve OP/Time	10000	SD			0	Done	Close Valve
2	2	4 Close Valve	1000	IO	1		OK	Done	Time
4	3	8 Time	200	MT			1000	Done	Check Weight
5	4	5 Check Weight	1	GG		60	47.85	Done	Time
6	5	8 Time	200	MT			1000	Done	Check Weight
7	6	5 Check Weight	1	GG		60	48.1	Done	Time

Figure H9:.csv excel data

- Create a time column of 100ms (0.1sec) interval from the first data collected, to the last data for a particular sequence.

Index	Label	Delay ms	Cmd.	Parameter	Expt. Value	Resp. Value	Status	Action	Time
8	Time	200	MT			1000	Done	Check Weight	0.1
5	Check Weight	1	GG		60	47.45	Done	Time	0.2
8	Time	200	MT			1000	Done	Check Weight	0.3
5	Check Weight	1	GG		60	47.55	Done	Time	0.4
8	Time	200	MT			1000	Done	Check Weight	0.5
5	Check Weight	1	GG		60	47.75	Done	Time	0.6
8	Time	200	MT			1000	Done	Check Weight	0.7
5	Check Weight	1	GG		60	48.7	Done	Time	0.8
8	Time	200	MT			1000	Done	Check Weight	0.9
5	Check Weight	1	GG		60	49.4	Done	Time	1
8	Time	200	MT			1000	Done	Check Weight	1.1
5	Check Weight	1	GG		60	49.95	Done	Time	1.2
8	Time	200	MT			1000	Done	Check Weight	1.3
5	Check Weight	1	GG		60	50.35	Done	Time	1.4
8	Time	200	MT			1000	Done	Check Weight	1.5

Figure H10: Creating timing interval at 0.1 sec

- Next step is to filter the label column by using the sort and filter button and then click on filter from the home tab. A drop down arrow is created. Uncheck the time row from the drop down.
- After unchecking the time, the new interval of 200ms Or 0.2sec is created from the time column as it has been already set earlier from the program. The resp. value column indicates the weight rise over the time of collection of the calibration data.
- Extra columns are needed for the calculation in order to calculate the flow rates in LPM as seen in the table H1.

Table H1: Calibration conversion

Absolute time secs	Absolute weight kg	kg/s	load cell l/min	Flow meter reading l/min	Difference (%)
2.8	13.25	4.732142857	284.4976	285.15	0.229

- To calculate the absolute time, subtract initial time from final time,  $2.9 - 0.1 = 2.8$ sec
- Absolute weight is equal to the subtraction of the initial from the final weight  $60 - 47.35 = 13.25$ Kg
- The mass flow in kg/s is then calculated by dividing the absolute weight and the absolute time which is  $\frac{13.25}{2.8} = 4.73 \text{ kg/s}$
- To convert from Kg/s to LPM,  $\frac{4.73 \times 1000}{998} = 284.497 \text{ LPM}$
- The percentage difference between the calculated LPM and the flow meter LPM can then be found by  $(\frac{285.15 - 284.497}{285.15}) \times 100 = 0.229\%$

After the calculation of each of the data collected for the test and converting to LPM as shown in the process above, the data are then plotted against what the turbine flow meter is reading. Figure H11 displays the calibration curve for the flow meter. It is seen that there is a good agreement between what has been calculated and what the flowmeter is reading, signifying a reasonable calibration results. An average of 1.17% is the difference between what has been calculated and the flow meter reading.

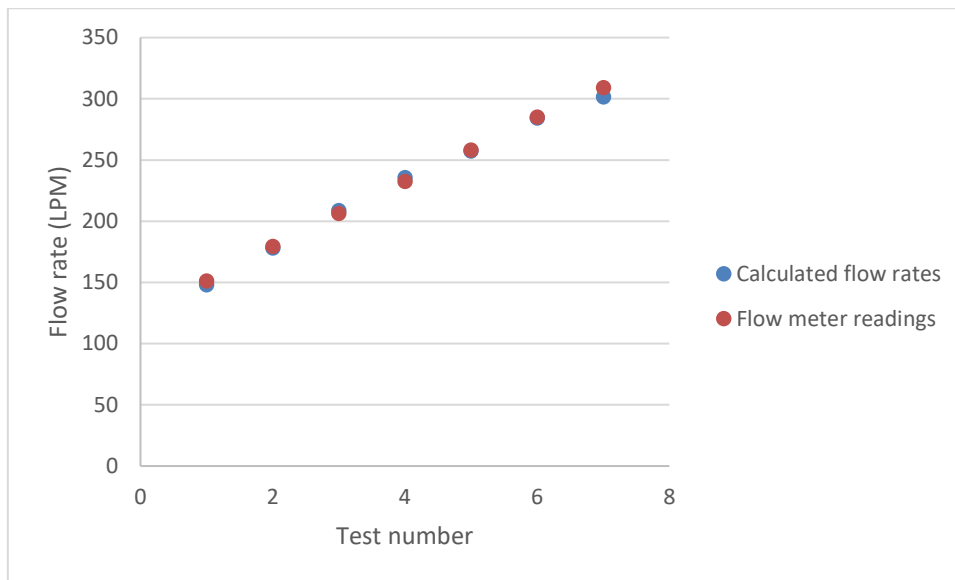


Figure H11: Turbine flow meter calibration curve